

FACULDADE DE ENGENHARIA DA UNIVERSIDADE DO PORTO

# Aluminium FSW joints under high strain rate tensile testing

Soraia Carvalho Constantino



Master in Mechanical Engineering Dissertation

Supervisor: Dr. Pedro Miguel Guimarães Pires Moreira  
Co-supervisor: Prof. Dr. Mário Augusto Pires Vaz  
Daniel Filipe Oliveira Braga

September 05, 2016



# Acknowledgments

I would like to express my thank to my supervisor, Dr. Pedro Moreira, for giving me the opportunity to work on this experimental field, for his guidance through all the difficulties I encountered throughout this work and for all the motivation he gave me.

I also thank my co-supervisor, Prof. Mário Vaz, for letting me use LOME facilities in order to perform my work and for his kindness.

I'm grateful to my co-supervisor, Daniel Braga, for his guidance, help, advices, reviews, availability for clarify all my doubts and his participation in this work.

I also would like to thank to engineer Nuno Viriato who offered me his time and availability to help me during this work, for all his patience and for all the things he taught me.

To engineer Jorge Reis whose participation in this work was essential concerning the acquisition system, since he spent a lot of time helping me with the circuit that was used to acquire data. Without him, I wouldn't be able to proceed my work.

I would like to express my gratitude to Dr. Jaime Monteiro for helping me with the strain gauges installation.

To my family, to all my colleagues and friends for their support, friendship and encouragement I express my gratitude.



# Resumo

O principal objectivo deste trabalho foi o estudo do comportamento mecânico de juntas de alumínio obtidas através de *Friction Stir Welding* submetidas a testes de tensão de alta taxa de deformação. Uma vez que existem pesquisas decorrentes dentro do grupo de trabalho, este trabalho servirá como o primeiro passo no sentido de caracterizar um novo tipo de ligação estrutural que inclui *Friction Stir Welding* combinado com *Adhesive Bonding*. Como esta tecnologia é projectada para uma possível aplicação na indústria aeronáutica, primeiro é necessário caracterizar as juntas FSW. Esta caracterização inclui o estudo das propriedades mecânicas em função das diferentes condições de taxa de deformação. Assim, para a caracterização dinâmica das juntas FSW foi proposto o uso da *split Hopkinson tensile bar* existente no LOME.

Como a instalação experimental *split Hopkinson tensile bar* existente não permitia a realização de testes usando juntas sobrepostas, havia necessidade de desenvolver uma instalação experimental nova. Para a instalação experimental desenvolvida todas as peças foram totalmente projectadas e desenvolvidas, com o sistema de amarração sendo o projecto de maior destaque devido à sua versatilidade. Sendo assim, o sistema de amarração é composto por dois conjuntos diferentes. O primeiro permite o teste de material de base e juntas topo a topo com provetes de espessura até 2 mm. O segundo permite o teste de juntas de sobreposição com provetes de espessura até 4 mm. De forma a adquirir dados, um novo amplificador de sinal capaz de filtrar o ruído do laboratório foi desenvolvido a partir do zero numa *breadboard*. Depois, os dados foram adquiridos e analisados utilizando o software *SUREPulse* cuja fiabilidade é apresentada neste trabalho.

Provetes de material de base foram testados e a influência da direcção de carga com a direcção de laminagem foi analisada. Posteriormente, os resultados foram comparados com os resultados quasi-estáticos e foi concluído que a liga de alumínio estudada não apresentava sensibilidade à taxa de deformação. Depois, testes utilizando provetes topo a topo foram realizados com a soldadura colocada transversalmente e axialmente. Foi observado que a colocação da soldadura e subsequentemente a colocação do provete na SHTB desenvolvida não mostravam qualquer influência nos resultados adquiridos para tensão. Contudo, provetes com a soldadura colocada axialmente atingiram valores de deformação maiores. Em seguida, os resultados foram comparados com os quasi-estáticos e não foi observada qualquer sensibilidade à taxa de deformação. Quando os resultados foram comparados com os do material de base, foi concluído que o material de base mostrou maiores valores de tensão. Finalmente, as juntas FSW sobrepostas foram testadas e comparadas com os resultados quasi-estáticos. Foi observada uma discrepância entre os dois resultados. Tal aconteceu por causa do comprimento reduzido do braço do provete e conseqüentemente, o seu comprimento livre. Esta redução causou no provete um maior carregamento de corte do que arrancamento. A tensão remota atingida no teste dinâmico foi superior à antigida no quasi-estático. Em contraste, o deslocamento foi menor. Os provetes FSW de juntas sobrepostas mostraram menores valores de taxa de deformação em comparação com todos os outros.



# Abstract

The main goal of this work was the study the mechanical behaviour of aluminium joints obtained through Friction stir welding under high strain rate tensile testing. Since there are ongoing researches within the workgroup, this work will serve as the first step in order to characterise a new type of structural joining which includes Friction stir welding combined with Adhesive bonding. As this technology is designed for a possible application in the aeronautical industry, first it is necessary to characterise FSW joints. This characterisation includes the study of the mechanical properties as a function of the different strain rate loading conditions. Thus, for dynamic characterisation of FSW joints was proposed the use of the existing split Hopkinson tensile bar in LOME.

Since the existing split Hopkinson tensile bar set up didn't allow the performance of tests using the overlap joint configuration, there was a need to develop a new set up. For the set up developed all parts were fully designed and developed, with the gripping system being the most outstanding design due to its versatility. Therefore, the gripping system is composed of two different sets. The first set allows the testing of base material and butt joints with specimens with thickness up to 2 mm. The second set allows the testing of overlap joints specimens with thickness until 4 mm. In order to acquire data, a new signal amplifier conditioner capable of filtering the laboratory noise was developed from scratch in a breadboard. Then, data was acquired and analysed using *SUREPulse* software whose reliability is shown in this work.

Base material specimens were testing, and the influence of loading direction with the rolling direction was analysed. Thereafter, results were compared with the quasi-static results and it was concluded that the studied aluminium alloy showed no strain rate sensitivity. Then, tests were performed using butt joint specimens with the weld placed crosswise and axially. It was observed that the weld placement and the subsequently specimen placement on the SHPB developed didn't show any influence on the acquired results for stress. However, the specimens with the weld placed axially achieved greater values of strain. Afterwards, results were compared with the quasi-static and it wasn't observed any strain rate sensitivity. When the results were compared with the base material, it was concluded that base material showed greater values of stress. Finally, FSW overlap joints were tested and compared with quasi-static results. A discrepancy was observed between the two results. Such happened because of the reduced length of the specimen arm and consequently, its free length. This reduction caused the specimen to be more loaded in shear than peel. The remote stress achieved in the dynamic test was greater than the achieved in the quasi-static. In contrast, the displacement was lower. The FSW dynamic tested specimen showed lower values of strain rate compared to all the others.





# Contents

<b>1</b>	<b>Introduction</b>	<b>1</b>
1.1	Background and Motivation . . . . .	1
1.2	Dissertation Synopsis . . . . .	2
<b>2</b>	<b>State Of The Art</b>	<b>5</b>
2.1	Introduction . . . . .	5
2.2	Base material: Aluminium . . . . .	6
2.3	Manufacturing Processes . . . . .	12
2.3.1	Friction Stir Welding . . . . .	13
2.3.1.1	Process Parameters . . . . .	15
2.3.2	Adhesive bonding . . . . .	17
2.3.2.1	Adhesives classification . . . . .	17
2.3.3	Weldbonding . . . . .	18
2.4	High strain characterisation . . . . .	18
2.4.1	Test methods and testing equipments . . . . .	19
2.4.1.1	Servo hydraulic testing machine . . . . .	19
2.4.1.2	Drop weight test . . . . .	20
2.4.1.3	Rotating wheel test . . . . .	22
2.4.1.4	Expanding ring . . . . .	22
2.4.1.5	Split Hopkinson pressure bar . . . . .	23
2.4.2	Base material characterisation . . . . .	26
2.4.3	Friction stir welded joints characterisation . . . . .	38
2.4.4	Adhesive bonding characterisation . . . . .	43
2.4.5	Weldbonding characterisation . . . . .	58
<b>3</b>	<b>Experimental Methods Fundamentals</b>	<b>65</b>
3.1	The split Hopkinson bar testing . . . . .	65
3.1.1	The split Hopkinson pressure bar analysis . . . . .	66
3.1.1.1	Wave propagation in cylindrical bars . . . . .	67
3.1.1.2	Mechanical Impedance . . . . .	69
3.1.1.3	Incident, reflected and transmitted pulse under the specimen in stresses and strains calculus . . . . .	71
3.1.2	Practical Aspects of The Split Hopkinson Pressure Bar . . . . .	74
3.1.3	Pulse time-shifting . . . . .	77
3.1.4	Wave dispersion . . . . .	78
3.1.5	Data acquisition . . . . .	81
3.2	Digital Image Correlation . . . . .	81
3.2.1	DIC fundamentals . . . . .	82

<b>4</b>	<b>The Experimental Test Set Up</b>	<b>87</b>
4.1	Tensile Split Hopkinson Pressure Bar . . . . .	87
4.2	Experimental Set Up Design . . . . .	88
4.2.1	Gas gun . . . . .	89
4.2.1.1	Breech and bushing . . . . .	90
4.2.1.2	Holdings . . . . .	92
4.2.2	Striker . . . . .	94
4.2.2.1	Striker bushings . . . . .	95
4.2.3	Bars . . . . .	96
4.2.3.1	Bars holders and bushings . . . . .	98
4.2.4	Gripping System . . . . .	99
4.2.4.1	Development of the gripping system . . . . .	101
4.2.5	Energy dissipation system . . . . .	108
4.3	Strain gauges design . . . . .	109
4.4	Signal processing . . . . .	109
4.4.1	Signal conditioners . . . . .	109
4.4.2	Data acquisition . . . . .	112
4.4.3	Trigger . . . . .	112
<b>5</b>	<b>Experimental Work</b>	<b>113</b>
5.1	Introduction . . . . .	113
5.2	Data analysis with the <i>SUREPulse</i> software . . . . .	116
5.3	Considerations and Results . . . . .	119
5.4	Dynamic characterisation of materials . . . . .	126
5.4.1	Dynamic characterisation of base material . . . . .	127
5.4.2	Dynamic characterisation of butt joints obtained through FSW . . . . .	129
5.4.3	Dynamic characterisation of overlap joints obtained through FSW . . . . .	135
<b>6</b>	<b>Concluding Remarks</b>	<b>141</b>
<b>7</b>	<b>Future Work</b>	<b>145</b>
<b>A</b>	<b>Technical drawings of the SHTB components</b>	<b>157</b>
<b>B</b>	<b>Technical drawings of the SHTB components for testing single lap joints</b>	<b>183</b>

# List of Figures

2.1	Evolution of the aluminium consumption in Europe . . . . .	7
2.2	Honda NSX . . . . .	7
2.3	NSX weight reduction . . . . .	8
2.4	Alcoa-Audi A8 Body in white . . . . .	8
2.5	Alcan-Ford Aluminium intensive vehicle . . . . .	8
2.6	International Congress Centre of Rio de Janeiro at Brazil . . . . .	9
2.7	Roof of a Colombian swim pool . . . . .	9
2.8	Sport Hall of Quito at Ecuador . . . . .	10
2.9	Memorial Pyramid in La Baie, Canada . . . . .	10
2.10	Schematic drawing of FSW . . . . .	13
2.11	Microstructure of a friction stir weld . . . . .	14
2.12	Tools designed at TWI . . . . .	16
2.13	Experimental set-ups for different strain rate regimes . . . . .	19
2.14	Servo hydraulic machine VHS 8800 High strain rate systems by INSTRON® . . . . .	20
2.15	Drop weight test . . . . .	21
2.16	CEAST 9350 Drop weight tower by INSTRON® . . . . .	21
2.17	Flying wheel set up . . . . .	22
2.18	Different configurations of the SHB . . . . .	24
2.19	“Top-hat” specimen used by Lindholm et al. . . . .	25
2.20	Split Hopkinson Tensile Bar used by Nicholas . . . . .	25
2.21	Threaded specimen used by Nicholas . . . . .	26
2.22	Strain rate and work hardening rate dependence of AA6061 alloy . . . . .	27
2.23	Inverse of the flow stress as function of work-hardening rate of AA6061 alloy deformed at 25°C and different strain rates . . . . .	27
2.24	Strain rate sensitivity and activation volume as a function of the work hardening stress . . . . .	28
2.25	Split Hopkinson pressure bar configuration . . . . .	28
2.26	Dynamic tensile stress-strain curve for AA6061-T6 . . . . .	29
2.27	Dynamic compressive stress-strain curve for AA6061-T6 . . . . .	30
2.28	Dynamic log strain rate vs. maximum stress for AA6061-T6 . . . . .	30
2.29	Split Hopkinson tensile bar . . . . .	31
2.30	Representative true stress versus true plastic strain curves proving the plastic anisotropy of the 6xxx series tested . . . . .	31
2.31	Representative true stress versus true plastic strain curves showing the strain-rate sensitivity of the 6xxx series tested . . . . .	32
2.32	Split Hopkinson tensile bar . . . . .	32

2.33 Comparison between experimental and simulated results for alloys AA6060-T6 and AA6082-T6 in three directions . . . . .	33
2.34 Split Hopkinson Pressure Bar used by Fan et. al . . . . .	34
2.35 Split Hopkinson tensile bar . . . . .	35
2.36 Frames from high-speed camera records for AA606-T6 at room temperature . . . . .	35
2.37 Results at room temperature. Dots on curve correspond to high-speed camera . . . . .	35
2.38 Results in different high strain rates at room temperature . . . . .	36
2.39 Frames from high-speed camera records for AA6061-T6 at -170°C . . . . .	36
2.40 Comparison between low and room temperatures . . . . .	36
2.41 Tensile Hopkinson bar . . . . .	37
2.42 Non contact method mounting with heat shield . . . . .	37
2.43 Stress-strain curves for quasi-static, medium strain rate and high strain rate tests . . . . .	38
2.44 Stress-strain curves at three strain rates for AA2024-T3 . . . . .	39
2.45 Stress-strain curves at two strain rates for AA7075-T7351 . . . . .	39
2.46 Yield stresses vs. strain rate . . . . .	39
2.47 Compressive true stress-strain and true strain-rate relation for weld nugget in thickness direction; True compressive strain (%) . . . . .	40
2.48 True compressive stress-strain curves for base material and different weld nuggets at low and high strain rates . . . . .	41
2.49 Effect of strain rate on flow stress for base material and different weld nuggets . . . . .	41
2.50 Yield stress for the three dynamic tests performed . . . . .	42
2.51 Calculated strain rate by varying the tracer position in FSW . . . . .	43
2.52 ASTM Block Impact Test . . . . .	44
2.53 Three loading cases for ASTM Block Impact Test . . . . .	44
2.54 Energy absorbed for the tested adhesives in ASTM Block Impact . . . . .	45
2.55 Energy absorption variation with the square of the specimen width for different specimens . . . . .	45
2.56 Stress-strain curves for quasi-static (a) and high strain rate (b) tests . . . . .	46
2.57 Reflected energy vs thickness . . . . .	46
2.58 Set up of testing machine for combined high rate loading . . . . .	47
2.59 Specimen and Hopkinson bar configuration and dimensions . . . . .	47
2.60 Dynamic and static strength joints comparison . . . . .	48
2.61 Used specimen geometry . . . . .	48
2.62 Effect of the loading rate on the tensile strength (a) and effect of the loading rate on the absorbed energy (b) . . . . .	49
2.63 Compressive dynamic comparison of stress-strain curves after the elastic range for hot curing (a) and compressive dynamic comparison of stress-strain curves after the elastic range for cold curing (b) . . . . .	50
2.64 Tensile test for hot cured specimens (a) and tensile test for cold cured specimens (b) [1] . . . . .	50
2.65 Specimen geometry (mm) . . . . .	51
2.66 Experimental set up and the connection between specimen and bars . . . . .	51
2.67 Average shear stress-time curve . . . . .	52
2.68 Broken specimen . . . . .	52
2.69 Shear stress as a function of temperature and striker's velocity . . . . .	52
2.70 Variation of strength in function of loading rate in adhesive joint . . . . .	53
2.71 Average shear strength variation of the adhesive bonded lap joint with overlap area . . . . .	54

2.72	Tested specimens with different loading angles . . . . .	54
2.73	Hat-shaped joint specimen . . . . .	55
2.74	Modified SHTB . . . . .	55
2.75	Butt joint and lap shear specimen geometry . . . . .	56
2.76	Split Hopkinson bar design . . . . .	56
2.77	Speckle pattern and DIC deformation field on butt joint (left) and lap shear (right) specimens . . . . .	56
2.78	Deformation measurement base on SHPB and DIC: butt joint and lap shear test . . . . .	57
2.79	Stress-deformation curves according to SHPB and DIC data reduction for butt joint and lap shear tests . . . . .	57
2.80	Stress-deformation relations in tensile direction . . . . .	57
2.81	Stress-deformation relation in the shear direction . . . . .	58
2.82	Hybrid joint specimen (a) and scheme of the hybrid joint geometry (b) . . . . .	58
2.83	Comparison between experimental and numerical results for rivet joints, adhesive bonded joints and hybrid joints . . . . .	59
2.84	Strength, stiffness and energy absorption for homogeneous joints . . . . .	59
2.85	Stress distribution in the lap zone for weld bonded and spot welded joints . . . . .	60
2.86	Stresses distribution over the lap length for weld bonded and adhesive bonded joints . . . . .	61
2.87	Major principal stress distribution for three models . . . . .	61
2.88	Minor principal stress distribution for three models . . . . .	62
2.89	Strength comparison between spot welded and weld bonded joints . . . . .	62
2.90	Damping capacity of spot welded and weld bonded joints . . . . .	63
2.91	Natural frequency of spot welded and weld bonded joints . . . . .	63
2.92	Ultimate load for the different types of joints tested . . . . .	64
3.1	Pressure bar differential element . . . . .	67
3.2	Wave propagation between two different bars . . . . .	70
3.3	Expanded view of incident bar-specimen and specimen-transmitted bar interface . . . . .	71
3.4	1-wave and 2-wave stress curves for the response of 304 stainless steel . . . . .	76
3.5	True stress-true strain curve for a high-purity lead, comparing the 1- and 2-wave analysis . . . . .	76
3.6	Lagrange-diagram for FEUP's SHPB TD16 . . . . .	77
3.7	Time-shifting of the bars strain waves . . . . .	78
3.8	Solution of Pochhammer-Chree's equation showing the variation of phase velocity with wavelength for the first three vibrational modes for a material with Poisson's ratio of 0.29 . . . . .	80
3.9	Scheme of the possible forms to employ the pulse shaping technique on a tensile apparatus . . . . .	80
3.10	2D DIC method set up . . . . .	82
3.11	Reference image with red facet used to track its centre point motion and yellow grid intersection points represent the points to be calculated (a) and the calculated displacement vectors to impose on the deformed image (b) . . . . .	83
3.12	Reference facet (reference subset) and deformed facet (target subset) . . . . .	84
4.1	Tensile split Hopkinson bar with a tubular striker . . . . .	88
4.2	LOME original SHPB apparatus . . . . .	88
4.3	LOME split Hopkinson tensile bar developed . . . . .	89

4.4	Trigger controller . . . . .	90
4.5	Breech . . . . .	91
4.6	Breech and barrel . . . . .	91
4.7	Breech bushing . . . . .	92
4.8	Bushing assembled on breech holders . . . . .	92
4.9	Breech holders . . . . .	93
4.10	Barrel lower support . . . . .	93
4.11	Holders assembled . . . . .	94
4.12	Striker with the four bushings assembled . . . . .	96
4.13	Striker's bushings . . . . .	96
4.14	Threaded hole to attach the grip (a) and threaded end (b) . . . . .	97
4.15	Non standard lock nuts (a) and their attachment to the threaded end of the incident bar (b) . . . . .	97
4.16	Bars holders . . . . .	98
4.17	Bar's bushing (a) and assembled holders with bushing (b) . . . . .	99
4.18	Axis symmetric specimen with threaded ends used by Chen et. al . . . . .	99
4.19	Specimen and gripping system used by Huh et. al . . . . .	100
4.20	Tensile specimen (a) and its positioning at SHPB (b) . . . . .	100
4.21	Adhesively bonded specimen to threaded metallic endcaps . . . . .	101
4.22	Gripping system which uses screws to fix specimens with respective holes . . . . .	101
4.23	Grip serrated surface detail . . . . .	102
4.24	Form-fit gripping system . . . . .	102
4.25	Adhesively bonded specimen with threaded metallic grips . . . . .	103
4.26	Nominal stress strain curves for the three different mounting systems considered . . . . .	103
4.27	Strain rate with the different systems . . . . .	104
4.28	First variant of the chosen gripping system . . . . .	105
4.29	Second variant of the chosen gripping system . . . . .	105
4.30	Third variant of the chosen gripping system . . . . .	106
4.31	Grippings . . . . .	107
4.32	Gripping (a) and grip cover (b) . . . . .	107
4.33	Compensator . . . . .	108
4.34	Gripping (a) and grip cover (b) for overlap joints . . . . .	108
4.35	Used breadboard circuit to acquire data . . . . .	111
4.36	Voltage power supply . . . . .	111
4.37	<i>PicoScope</i> USB oscilloscope . . . . .	112
5.1	Threaded part . . . . .	114
5.2	Threaded part dimensions . . . . .	115
5.3	Wave recorded with the calibration part . . . . .	115
5.4	<i>SUREPulse</i> menu . . . . .	116
5.5	Creating a bar setup in <i>SUREPulse</i> . . . . .	117
5.6	Creating a sample on <i>SUREPulse</i> . . . . .	118
5.7	Analyzing samples on <i>SUREPulse</i> . . . . .	119
5.8	Specimen . . . . .	120
5.9	Specimen dimensions . . . . .	120
5.10	Specimen to be tested after the parameters determination . . . . .	121
5.11	Torque wrench used for tighten the screws . . . . .	122
5.12	Recorded waves for the first test . . . . .	123

5.13	Stress vs strain curve obtained for one of the first samples . . . . .	123
5.14	Time-shifted waves . . . . .	124
5.15	Stress vs strain curve for the calculated results . . . . .	125
5.16	Comparison between the software and the calculated results . . . . .	125
5.17	Specimen rupture . . . . .	126
5.18	Base material specimen placed on the grips . . . . .	127
5.19	Stress vs strain curves for the 0°, 45°, 90° rolling directions . . . . .	127
5.20	Base material specimen rupture at 45° . . . . .	128
5.21	Comparison between quasi-static and dynamic results for base material . . . . .	129
5.22	Butt joint specimen with the welding crosswise and its placement on the grips, positioned with the AS to the incident bar . . . . .	130
5.23	Butt joint specimen with the welding crosswise and its placement on the grips, positioned with the RS to the incident bar . . . . .	130
5.24	Stress vs strain curves for the specimens with the cross wise weld . . . . .	131
5.25	Butt joint specimen with axial welding placement on the grips, advancing-retreating side . . . . .	131
5.26	Butt joint specimen with axial welding placement on the grips, retreating-advancing side . . . . .	132
5.27	Stress vs strain curves for the specimens with the axial weld . . . . .	133
5.28	Broken butt joint specimens for the second kind of tests . . . . .	133
5.29	Comparison between quasi-static and dynamic results for FS welded butt joints .	134
5.30	Comparison between FS welded butt joints and base material . . . . .	135
5.31	Grips for testing overlap joints assembled on the bars . . . . .	136
5.32	FSW overlap specimen dimensions . . . . .	136
5.33	Overlap joint specimen on the grips . . . . .	137
5.34	Overlap joint specimen placement on the gripping system . . . . .	137
5.35	Remote stress vs displacement curve for overlap joints obtained through FSW .	138
5.36	Comparison between the quasi-static and dynamic results for overlap joints ob- tained through FSW . . . . .	139
5.37	Overlap specimen rupture . . . . .	139





# List of Tables

2.1	Different compositions for wrought aluminium alloy series . . . . .	11
2.2	Basic designations for thermal treatments . . . . .	11
2.3	Strain-hardening treatments specification . . . . .	12
2.4	Degree of strain-hardening specification . . . . .	12
2.5	Thermal treatments “T” specification . . . . .	12
4.1	AISI 303 Steel chemical composition . . . . .	94
4.2	AISI 303 Steel mechanical properties . . . . .	95
5.1	Chemical composition of AA6082-T6 aluminium alloy . . . . .	113
5.2	Properties of AA6082-T6 aluminium alloy . . . . .	113



# Acronyms and Symbols

## Symbols

$\alpha$	Transmission coefficient
$\beta$	Reflection coefficient
$\eta_1$	First order shape function for displacement component v
$\rho_1$	Volumetric mass density of bar 1
$\rho_2$	Volumetric mass density of bar 2
$\xi_1$	First order shape function for displacement component u
$A_1$	Cross section area of bar 1
$A_2$	Cross section area of bar 2
$A_s(t)$	Area of the specimen
$c_1$	Elastic longitudinal wave velocity of bar 1
$c_2$	Elastic longitudinal wave velocity of bar 2
$N$	Axial strength at a section
$R_b$	Bridge resistance
$R_s$	Shunt Resistance
$V_s$	Simulated output at signals leads
$\Delta l_{SG1}$	Geometrical distance between the incident bar strain gauge and the specimen
$\Delta l_{SG2}$	Geometrical distance between the specimen and the transmitted bar
$\Delta_x$	First order displacement gradient in x direction
$\Delta_y$	First order displacement gradient in y direction
$\delta$	Phase angle
$\dot{\epsilon}_n(t)$	Nominal specimen's strain rate
$\dot{\epsilon}_{true}(t)$	True strain rate

$\eta_0$	Zero order shape function for displacement component v
$\rho_{striker}$	Density of the striker
$\sigma_b$	Bar stress
$\sigma_I$	Bar stress caused by the incident wave
$\sigma_R$	Bar stress caused by the reflected wave
$\sigma_{striker}$	Striker stress
$\sigma_{true}(t)$	True stress
$\sigma_T$	Bar stress caused by the transmitted wave
$\sigma_{yb}$	Yield strength of the bars material
$\sigma$	Stress
$\varepsilon_b$	Bar strain
$\varepsilon_e(t)$	Strain on the incident bar
$\varepsilon_I$	Incident wave
$\varepsilon_n(t)$	Mean strain of the specimen
$\varepsilon_{true}(t)$	True strain
$\varepsilon$	Strain
$\Lambda$	Pulse length
$\xi_0$	Zero order shape function for displacement component u
$A_0$	Fourier coefficient
$A$	Cross section area
$c_n$	Elastic longitudinal wave velocity of the angular frequency component
$c_s$	Wave velocity of the specimen
$d_{bar}$	Barrel diameter
$d_b$	Diameter of the bar
$D_n$	Fourier coefficient
$E$	Young's modulus
$F(x, t)$	Non harmonic function which propagates in opposite ways in x direction with the wave propagation velocity
$G(x, t)$	Non harmonic function which propagates in opposite ways in x direction with the wave propagation velocity

$l_{bar}$	Length of the barrel
$l_b$	Length of the bar
$l_{striker}$	Length of the striker
$l_s$	Length of the specimen
$n\omega_0$	Angular frequency
$Q_p$	Particulates movement's quantity
$Q_{striker}$	Striker movement's quantity
$t_{\varepsilon_I}^{specimen}$	Time that the incident wave actuated on the specimen
$t_{\varepsilon_R}^{specimen}$	Time that the reflected wave actuated on the specimen
$t_{\varepsilon_T}^{specimen}$	Time that the transmitted wave actuated on the specimen
$t_{SG1}$	Time of the signal of the incident bar strain gauge
$t_s$	Transit time of specimen's longitudinal wave
$t_t$	Transit time
$T$	Pulse duration
$t$	Time
$u(x, t)$	Displacement in x direction
$u_x$	First order displacement gradient of u in x direction
$u_y$	First order displacement gradient of u in y direction
$u$	Displacement in longitudinal bar direction
$v(x, t)$	Particulates' velocity of a bar with infinite dimensions
$v_e(t)$	Displacement velocity at the top of the incident bar
$v_p$	Particulates' velocity
$v_{striker}$	Striker's velocity
$v_s(t)$	Displacement velocity at the specimen-transmitted bar interface
$v_x$	First order displacement gradient of v in x direction
$v_y$	First order displacement gradient of v in y direction
$Z_0$	Intrinsic impedance of the material
COD	Crack opening displacement
$f(t)$	Fourier series expansion for a whole pulse

NDTT	Nil-ductility transition temperature
P	Desirable pressure on the gas gun
R	Radius of the expanding ring
Z	Mechanical impedance
z	position along the pressure bar

**Acronyms**

AS	Advancing side
ASTM	American society for tests and materials
BM	Base material
CCD	Charge-coupled device
DIC	Digital image correlation
DIN	Deutsches institut für Normung
FSW	Friction stir welding
HAZ	Heat affected zone
IADES	International alloy designation system
MIG	Metal inert gas
NZ	Nugget zone
PTFE	Polytetrafluoroethylene
RS	Retreating side
RSW	Resistance spot welding
SHB	Split Hopkinson bar
SHPB	Split Hopkinson pressure bar
SHTB	Split Hopkinson tensile bar
SZ	Stir zone
TMAZ	Thermo mechanically affected zone
TWI	The welding institute

# Chapter 1

## Introduction

### 1.1 Background and Motivation

Crashworthiness of vehicles and aircraft becomes an important topic when new demands of restricting the emission of pollutants to the atmosphere emerged. Such demands can be tailored with the use of lightweight materials, resulting in the rising application of aluminium alloys. This material is preferred over steel since it has good mechanical properties and it is lighter, maintaining safety at low cost. However, crashworthiness events as well as many applications (e.g.: ballistics, bird strike events) are characterized as impact events. In its turn, impact events occur at high strain rates, since the material suffers fast deformations. Therefore, the materials employed should present a good impact resistance and their dynamic mechanical properties must be determined.

The most commonly performed tests are the quasi static tests, at very low strain rates wherein the material is slowly deformed. These tests allow the obtainment of static mechanical properties of the materials. As aforementioned, crashworthiness and impact events happen at very high strain rates where the materials are quickly deformed. Thus, high strain rate tests are required to characterize materials subjected to impact loadings and evaluate the response presented to determine if the material meets the needed requirements. Strain rates of practical events can reach up to  $5 \times 10^3/s$  and the split Hopkinson pressure bar technique is known for achieving high values for strain rates. The technique has been the subject of several studies, specially in the tensile loading. The configuration of the apparatus for performing tensile tests has many variations towards the tensile pulse generation, gripping system and it is not fully explored, a still very experimental field.

This dissertation is linked to the development of split Hopkinson pressure bar equipment and the measurement of dynamic mechanical properties of the materials, especially aluminium.

There are developments of manufacturing processes, more specifically Friction stir welding and Adhesive bonding which combined result in Weldbonding to produce overlap joints. The Friction stir welding is a solid welding technique and was purposely developed for aluminium alloys. Adhesive bonding has been used for several years in the automotive and aeronautical industry. Though this technique distributes loads uniformly over a wide area and absorbs more energy, it has some restrictions regarding the exposure environments and thus, service life. Both techniques when are combined as Weldbonding, produce joints with higher mechanical properties.

As there are no studies on overlap joints obtained by Weldbonding and exposed to impact loading conditions, the author feels motivated to study their mechanical behaviour. Specially

when this kind of process is being an area of interest in aircraft industries. For this, a new split Hopkinson apparatus was developed in order to first study the dynamic mechanical properties of aluminium, overlap joints produced by Friction stir welding, then produced by Adhesive bonding and last, produced by Weldbonding. This work aims to establish the bridge between the quasi-static and dynamic properties of the aluminium material using the different manufacturing processes mentioned previously. Furthermore, it aims to determine if the overlap joints obtained by Weldbonding are reliable for the aircraft industry.

## 1.2 Dissertation Synopsis

During this master thesis, several researches were made in order to develop a split Hopkinson tensile bar apparatus. In its turn, this apparatus could perform impact tests on two different kind of specimens.

This dissertation is composed of seven different chapters. The first chapter presents the background and motivation of the work, including a short summary of the applied strategy to achieve the main goals. It also presents the thesis content.

After gathering all the existing information related with this master thesis work through an extensive literary research, the second chapter emerges. This chapter contains a brief introduction where it is mentioned why impact tests at high strain rate are so important, which is followed by a literature review of the base material. The manufacturing processes that are subject of study are mentioned, described and categorized. The advantages and disadvantages regarding each other are presented and some important parameters are referred. Besides, several concepts such as strain hardening, strain rate hardening and strain rate sensitivity are briefly explained. Thereafter, different test methods and equipments are shown for different values of strain rate, including the split Hopkinson pressure bar. The different existing results for base material, Friction stir weld joints, Adhesive bonding joints and Weldbonding joints are exhibited.

The third chapter presents the theory and fundamentals behind the experimental methods supposed to be used in this work. The first section presents the split Hopkinson pressure bar analysis, with the working principle and its conditions. These conditions are responsible for assuring a correct analysis via the 1D propagation theory, which follows. The mechanical impedance and its change are also mentioned, due to its inherent importance to the analysis. Then, the weight of the incident, reflected and transmitted pulse under the specimen in stresses and strains calculus is shown. Some practical aspects are mentioned, before explaining the pulse time-shifting and the wave dispersion correction with reference to the data acquisition system parameters. Thereafter, the digital image correlation method is presented, with a short mention to its history. Its working principle with its fundamentals are also presented. Finally, the digital image correlation theory can be observed.

The fourth chapter is dedicated to the experimental set up design. The parts of the set up are fully described with their design criteria. The gripping system has the most outstanding description due to the several studied solutions. The strain gauges design is showed, followed by the signal processing. Besides the gripping system, the data acquisition system inserted in the signal processing section also should be highlighted since unmeasured problems appeared. Lastly, the trigger is mentioned.

In fifth chapter, a short explanation of the data analysis software used in this work is made. After, some important considerations which include the best parameters ascertained to obtain the best results are listed. The results obtained with the software using the experimental ap-



paratus developed during this work for the first specimens are presented. In order to validate those results, calculations were made so that a comparison between the software and calculated values is showed. With that validation, the dynamic characterisation of the base material, butt joint and overlap specimens obtained through Friction stir welding are displayed.

The sixth chapter refers important conclusions regarding the first strategy defined in this work, states all the difficulties that were overcame and point out why some topics first established weren't approached. Important conclusions towards the obtained results for the different specimens tested are presented.

In the last and seventh chapter, future works within this area are proposed, along with future improvements in the set up.



## Chapter 2

# State Of The Art

### 2.1 Introduction

Dynamic loading conditions are present in so many different events and applications such as those found in vehicle collision, bird-strike events, mishandle of electronic devices and terminal ballistics. As such, it becomes important to characterize materials mechanical behaviour very accurately under realistic test conditions in order to assure product's quality and reliability in those numerous applications. Consequently, their inherent mechanical properties (e.g. yield strength, tensile strength, Young's modulus, Poisson's ratio and so forth) must be characterized too. However, these mentioned mechanical properties are usually obtained by performing tests in quasi-static loading conditions, according to the standard procedures (DIN, ASTM, etc). Generally, mechanical properties obtained through quasi-static loading conditions are listed in several books and so they are easy to find. Nevertheless, these type of tests are performed at very low strain rates, in the order of  $10^{-4}$  to  $10^0/s$ , and therefore the material in study is deformed slowly.

A large number of practical events in engineering and even certain manufacturing processes like explosive forming, blast loading, metal working, high speed machining and plastic forming, present strain rates which vary from  $100/s$  to  $5 \times 10^3/s$ . This important parameter has a great influence on the materials mechanical properties. Thus, the magnitude of such strain rate, specially in metals, has been the study topic of countless researchers since 1950 [2].

The present restrictions imposed in polluting emissions and the need to reduce the transportation cost demand new design solutions such as the use of advanced materials and manufacturing processes to build lighter structures. Although, this weight reduction must not be accompanied by a decrease in comfort or safety. So, the interest in aluminium alloys has been increasing due to its strength-to-weight ratio, aesthetics and costs reduction, despite traditionally, the strain rate sensitivity of these allows be considered low [3].

The development of solid state joining techniques, such as Friction Stir Welding (FSW), in which there is no phase transformation, has the potential to recrystallize the grain uniaxially, producing good mechanical properties. This solid state technique allows the welding of aluminium alloys that are not usually weldable as well the joining of different alloys: magnesium, copper, titanium and steel. It is capable of producing high strength welds, being considered an efficient process, versatile and environmentally friendly, with increasing importance in the automotive and aerospace industries. Nevertheless, the weld nugget resulting from lap, L-joint and T-joint configurations, display notches on both sides which are responsible for increasing concentration factors and reducing fatigue life. Due to the formation of "hook" defect, joints

in lap configuration are inherently weaker. Besides, FSW can not seal the gaps between both joint components. These gaps are the result of a mismatch between the two interfaces of the materials to be welded, causing the escape of material from the processing zone.

Another important technique, Adhesive Bonding, has been used to produce light weight structures in the automotive, aerospace and nautical industries. Adhesives provide a better stress distribution, resulting in a more uniform stress distribution towards the bonded area and therefore, a stiffness increase. They also can be used to replace mechanical fasteners in order to eliminate drilling holes. With the number of researches increasing, its employment have increased exponentially. However, their service life depends on the conditions of the exposure environment and hence, seeing their life limited to upper temperature service [4].

These two powerful joining methods can be combined into a hybrid joining technique, Weldbonding, which seeks to overcome the disadvantages of each process alone and to satisfy certain specifications, with improved mechanical properties [5]. The hybrid technique results in improved damage tolerance (more than one independent failure mode) and improvements in mechanical properties and resistance to environmental degradation [6].

Furthermore, this groundbreaking type of joining requires, in addition to conventional mechanical tests, to be characterized under dynamic loading conditions, in order to potentiate its adoption in various structural applications.

## 2.2 Base material: Aluminium

Throughout the years, specially the 1950s, 60s and 70s, several investigations in the area of product development were made. These investigations allowed a better understanding on the microstructure, processing, properties and permitted to establish important relations amongst them. They also constituted an important mark on aluminium's history, since they are responsible for increasing its application on the most varied industries and fields such as the automotive, aerospace, shipping, construction, sports and leisure [7].

Although, this remarkable increase of the use of aluminium alloys occurred due to its strength-to-weight ratio, low density, thermal and electrical conductivity, durability, ductility, corrosion resistance and recyclability, in other words, its good mechanical properties and its short design cycle improved over time. The manufacturers main goal was to produce transports with better fuel economy and in order to achieve that goal, lightweight materials that also present good mechanical properties are required. With the environmental restrictions imposed to reduce air pollution and global warming, if lesser fuel was consumed, lesser pollutants gases were emitted to the atmosphere. Hence, steel and cast irons had been gradually replaced by aluminium alloys and researches comparing both materials, specially the formability factor had emerged [8].

Furthermore, casting aluminium alloys have been used in transmission housing and heads also with the aim to reduce engine weight. They began to replace other materials in chassis applications, suspension components and road wheels [9]. Nevertheless, efforts had been made with the intent to increase the number of applications which concerns wrought aluminium alloys including transmission, seat frames, pneumatic systems, air bag housing and bumper reinforcements too. In Figure 2.1 the evolution of the aluminium consumption in Europe is well displayed.

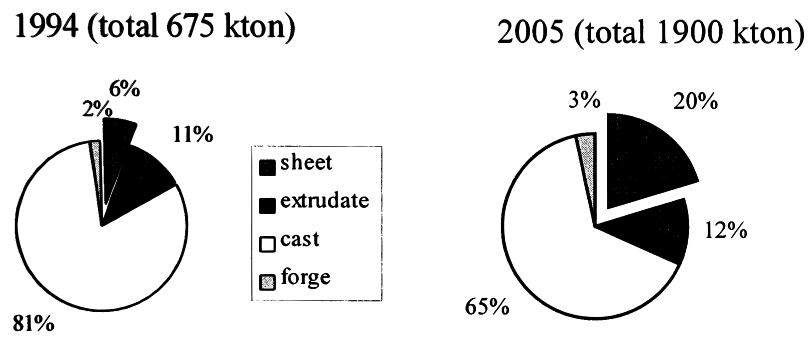


Figure 2.1: Evolution of the aluminium consumption in Europe [10]

Honda NSX, which is shown in Figure 2.2, was the first production car with an all-aluminium automotive body. Muraoka and Miyaoka [11] reported the main technical issues regarding manufacturing processes and the new technologies introduced to overcome those technical issues. This car was seen as an avant-gardist automotive design, since its aerodynamics were based on the concept of the F-1, presented a weight reduction of 200 kg towards steel (Figure 2.3).

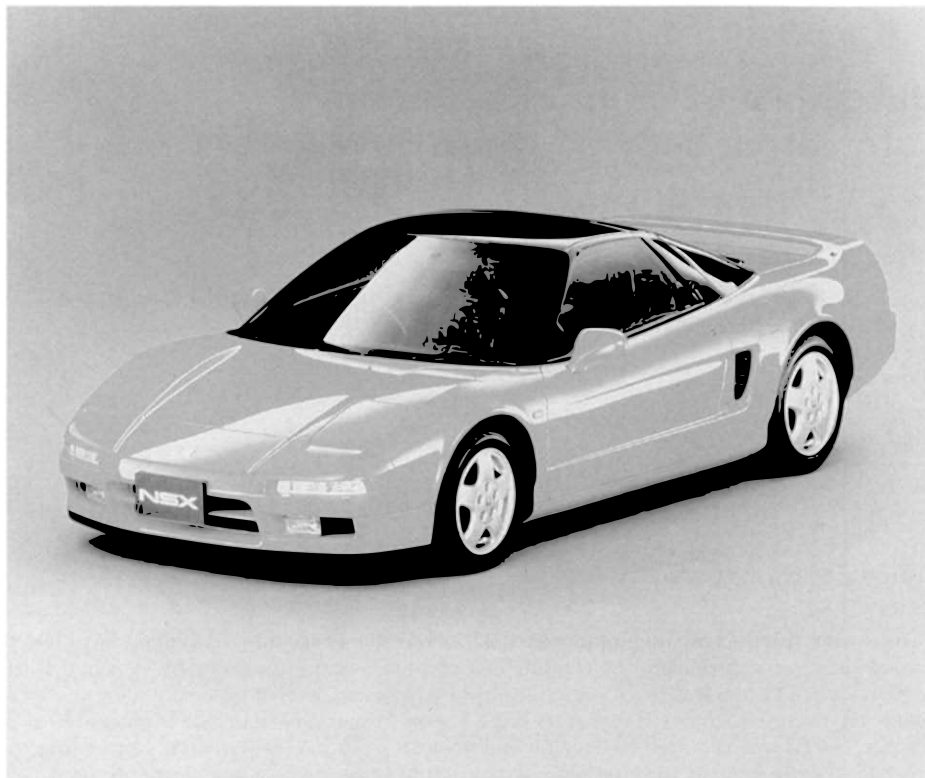


Figure 2.2: Honda NSX [11]

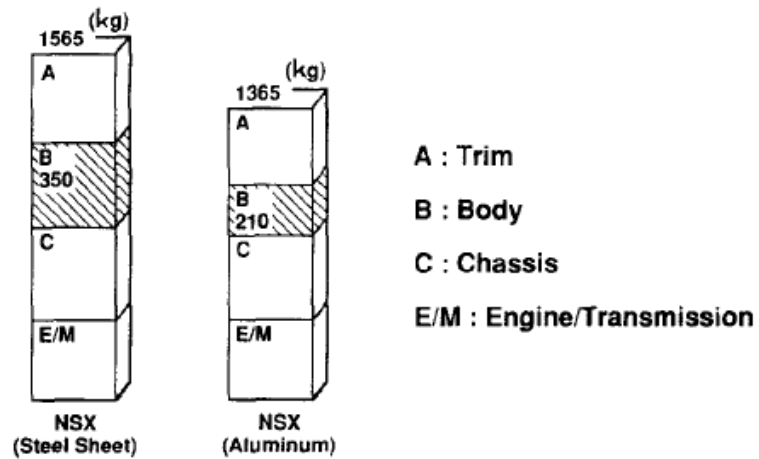


Figure 2.3: NSX weight reduction [11]

Alcoa-Audi A8 (Figure 2.4) is an example of a body in white application while Alcan-Ford (Figure 2.5) is an example of an aluminium intensive vehicle. The body in white application could aim for bigger weight reductions due to the extruded space frame. However, the Alcan-Ford had a sheet monocoque architecture.

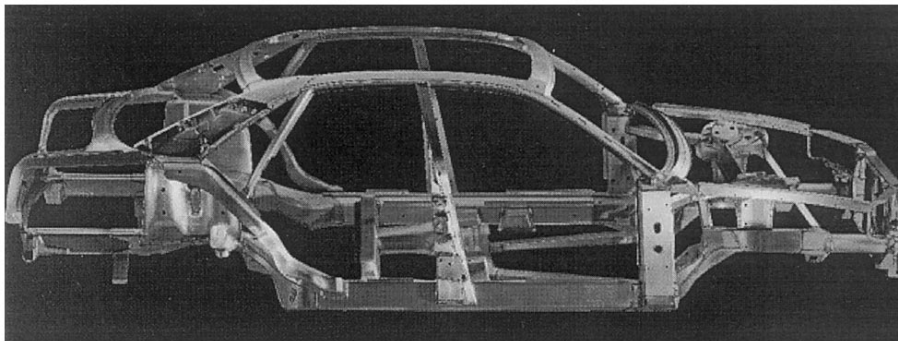


Figure 2.4: Alcoa-Audi A8 Body in white [10]

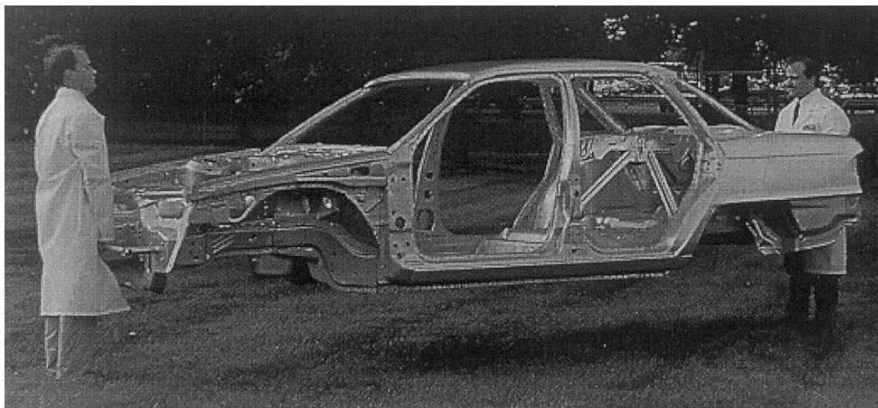


Figure 2.5: Alcan-Ford Aluminium intensive vehicle [10]

Likewise, the American automotive industry started to gain ground when a large production of aluminium engine blocks was put in practice, including engines like GM's lost Foam Cast Saturn, ZR-1 Corvette, Ford's 4.6L Continental, 2.5L Countor/Mystique/Mondeo and Chrysler's Viper [12].

In the early days of the aircraft industry, wooden was the principal structural material braced by wires and treated with varnishes. There were almost no metal parts, except the engine, fasteners and wires. The main focus was to reduce weight, not only in airframes but also in propulsion systems due to the limitations imposed by the latter. So, the most effective way to reduce weight was to use a lower density material as aluminium, for instance. The great impulse was given by Alfred Wilm when he discovered the precipitation hardening process, leading some innovators designers to realize diverse experiments [13]. With the aircraft industry evolution, new manufacturing processes, designs and materials arose to meet the crescent demands, and contemplating the lessons learned from structural failures that occurred along the way, such as the fatigue failure on Comet airplane disasters. Aluminium became the material of choice to construct airframes, since this material demands a lower production cycle, substitution risk and existing production infrastructures can be used [14].

In civil engineering, aluminium alloys applications have been growing also because of its mechanical properties and its low mass weight which facilitates transportation. A considerable number of movable bridges, helicopter decks on offshore platforms and also metallic buildings employing aluminium were constructed, since there are a large variety of design rules and an existing standard procedure "Eurocode 9: Design of Aluminium Structures". Regarding metallic structures, aluminium has been revolutionizing the entire area, enabling the construction of lightweight structures and the access to structures located in inaccessible places by easing the structures raising and material transportation. This material is also known for requiring low maintenance. Reticular structures of great importance are found on the roof of a Colombian swim pool (Figure 2.7) or at the International Congress Centre of Rio de Janeiro, Brazil (Figure 2.6). Aluminium is also used as a sheet to cover reticular roofs, for instance: Sport Hall of Quito, Ecuador (Figure 2.8) and the Memorial Pyramid in La Baie, Canada (Figure 2.9) [15].



Figure 2.6: International Congress Centre of Rio de Janeiro at Brazil [15]

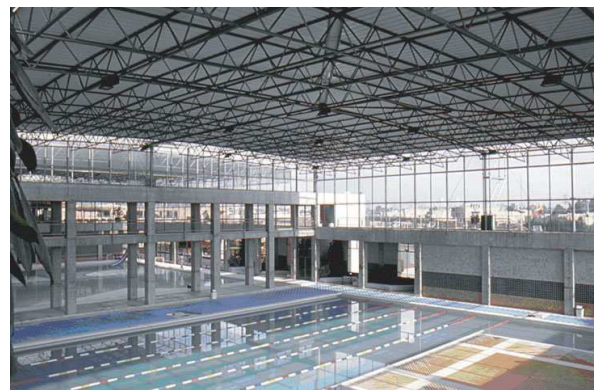


Figure 2.7: Roof of a Colombian swim pool [15]



Figure 2.8: Sport Hall of Quito at Ecuador [15]



Figure 2.9: Memorial Pyramid in La Baie, Canada [15]

Shipping construction was marked by the first ship, “Mignon”, constructed with aluminium in 1891, France. The first aluminium ship that owned an engine was called “Diana” and was used by the British Royal Navy during the Second Great War and continued to the 1960s. Despite being used for yachts and sail boats construction, this metal only is applied for unit constructions, while fibre glass is used for mass production. As mentioned before, aluminium is a ductile and tenacious material which improves its resistance to lower temperatures when compared to steel [16].

With all these dramatic increases of aluminium alloys in several industries, Aluminium Association developed a four-system identification for wrought alloys whose acceptance has been widely established all around the world. The nomenclature is known as IADS (International Alloy Designation System) [13]. Aluminium alloys can be categorized in groups based on particular characteristics of the material and its ability to respond to thermal and mechanical treatments and the primary element added to the aluminium alloy.

The first digit denotes the primary alloying element, also used to describe the alloy series as shown in Table 2.1. The second digit, if different from 0, indicates a change in the alloy. The third and fourth digits are arbitrary numbers assigned to identify a specific alloy in the series, e.g.: in the alloy 5183, the number 5 indicates that belongs to the series of magnesium alloys, the number 1 shows that’s the first modification to the original alloy 5083 and 83 identifies it in the 5xxx series. The only exception appears to the 1xxx series, pure aluminums, wherein the last 2 digits provide the minimum percentage of aluminium higher than 99%, for instance: Alloy 1350, 99,50% minimum of aluminium. The prefix F is used if the alloy in case is in an experimental process of development.



Series	Elements of the principal alloy
1xxx	99% Minimum of aluminium
2xxx	Copper
3xxx	Manganese
4xxx	Silicon
5xxx	Magnesium
6xxx	Magnesium and Silicon
7xxx	Zinc
8xxx	Other elements (including Lithium)
9xxx	Reserved for future use

Table 2.1: Different compositions for wrought aluminium alloy series [17]

Considering the different series of aluminium alloys, there are considerable differences in their characteristics and consequent applications. There are two distinct types of aluminums within the aforementioned series: the heat-treatable aluminium alloys, whose resistance increases through heat addition and the non heat-treatable aluminium alloys. Accordingly, the series 1xxx, 3xxx e 5xxx are non heat-treatable, the series 2xxx, 6xxx e 7xxx are heat-treatable and, finally, the series 4xxx can be or not heat-treatable. Depending on the treatment suffered, the alloys have a designation which characterizes them, considered an extension to the numbering system and consisting of a series of letters and numbers connected by a hyphen, for example: 6061-T6. This designation is shown in the following table:

Letter	Meaning
F	No treatments, applied to products resulting of forming processes in which there is no kind of thermal control or application of hardening conditions
O	Annealed, applied to products that were heated to produce conditions of lower resistance in order to improve their ductility and dimensional stability
H	Strain Hardened, applied to products that are hardened through cold-working. May be followed of supplementary thermal treatments. The letter "H" is usually followed by 2 or more digits (see table 2.3 e table 2.4)
W	Solution Heat-treated, applied only to alloys that overage spontaneously at room temperature
T	Thermally treated, to produce stable tempers besides F, O or H. Applied to products which were thermally treated, sometimes with supplementary cold-working. "T" is always followed by 1 or more digits (see table 2.5)

Table 2.2: Basic designations for thermal treatments [17]

Apart these basic designations for thermal treatments, there are two sub-categories: one for "H" treatment and other for "T" treatment:

Type	1st digit specification
H1	Only strain hardened
H2	Strain hardened and partial annealed
H3	Strain hardened and stabilized
H4	Strain hardened and lacquered or painted

Table 2.3: Strain-hardening treatments specification [17]

Type	2nd digit meaning
Hx2	Quarter hard
Hx4	Half hard
Hx6	Three Quarters hard
Hx8	Full hard
Hx9	Extra hard

Table 2.4: Degree of strain-hardening specification [17]

Type	1st digit specification
T1	Naturally aged after cooling from elevated temperatures
T2	Cold worked after cooling from elevated temperatures and naturally aged
T3	Solution heat-treatable, cold working and naturally aged
T4	Solution heat-treatable and naturally aged
T5	Artificially aged after cooling from elevated temperatures
T6	Solution heat-treatable and artificially aged
T7	Solution heat-treatable and stabilized (overaged)
T8	Solution heat-treatable, cold working and artificially aged
T9	Solution heat-treatable, artificially aged and cold working
T10	Cold worked after cooling from elevated temperatures and artificially aged

Table 2.5: Thermal treatments “T” specification [17]

Additional digits indicate stress relief, for instance: TX51, stress relief by stretching or TX52, stress relief by compression [17].

## 2.3 Manufacturing Processes

Constant and continuous developments in the industries mentioned in Section 2.2 and others as well, besides requiring the use of lighter materials, also require the improvement of bonding technologies and methods. Further, new hybrid bonding techniques have been gaining ground, with the power to combine the advantages of each technique alone and with the aim to produce bondings with better mechanical properties, in order to tailor the safety and performance requirements. In this master thesis, the author will focus on three manufacturing processes. First

Friction stir welding and Adhesive bonding. When combined, these two techniques result in a hybrid-bonding technique named Weldbonding.

### 2.3.1 Friction Stir Welding

Friction Stir Welding (FSW) is an innovative welding process, invented and patented in 1991 by The Welding Institute (TWI) [18, 19], being specifically developed and initially used in aluminium alloys hard to join through fusion welding [20]. This process represents possibly the most significant development of the decade in the area of metallic joining. It is commonly known for being a welding process in solid state because it is carried out at temperatures below the melting temperature, producing a plasticized region of material, using only mechanical energy. Hence, the joints produced have higher tensile strength to weight ratio and a finer microstructure free of defects. This process proved to be suitable to join a large number of materials, e.g.: titanium and aluminium, magnesium and aluminium, magnesium and steel, copper-nickel and steel, aluminium and steel, dissimilar steels, dissimilar aluminium alloys and aluminium with composites.

This process consists in a non-consumable rotating tool composed of two main-parts: cylindrical shoulder and pin (Figure 2.10). The material of the components to be welded is mixed by the latter, while the necessary heat to plasticize the material is generated by the shoulder at the joint line. The tool is moved along that line, always rotating which will continue to frictionally heat the materials to high temperatures, leading to the materials' plastification. The localized heat softens the material around the pin, forcing it to flow around the tool, forming a weld behind it as the stirred material is consolidated [21]. As the plastification is so intense due to elevated temperatures, the grains become finer and equiaxed recrystallized [22]. The "advancing side" (AS) is coincident with the direction of the rotating tool's movement towards the traversing direction, while the "retreating side" (RS) is opposite to the traversed direction and supports all the deformed material that is extruded. At the end of the welding, the tool's retreat leaves a keyhole of the pin's diameter size. Regarding butt joint configuration, it is important the length of the pin is only lightly less than the thickness of the plate.

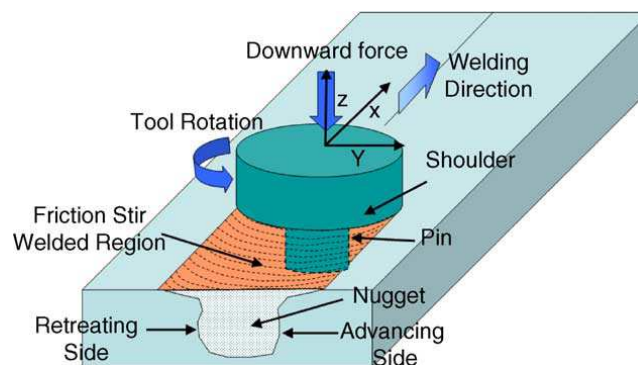


Figure 2.10: Schematic drawing of FSW [22]

In addition, friction stir welded joints present an excellent chemical composition and mechanical properties, the temperature achieved is lower than melting temperature, eliminating defects inherent to fusion such as: porosity, cracks and inclusions and minimizes the distortion and warpage index. The process in itself doesn't require specialized welding skill nor shielding gas or filler wire and it is tolerant to poor quality of weld preparations. Further, it is energy efficient and environmentally friendly since there's no formation of smoking or splashes [23].

However, as the process is fully mechanised, its use is not trivial when access or weld shape is complex. Also, work piece restraining needs a well designed clamping which may require large down forces [24].

Friction stir welds exhibit a microstructure which is affected by rotational and traverse speed, materials, tool geometry and pressure, displaying a unique morphology due to the lack of melting when compared to other welding processes. Intense plastic deformation, high temperature exposure of the stirred zone results in recrystallization, development of texture, precipitate dissolution and coarsening within and around it, influencing the grain size, character and boundary and the resulting mechanical properties.

The resulting microstructures can be divided into four different zones as it is shown in Figure 2.11:

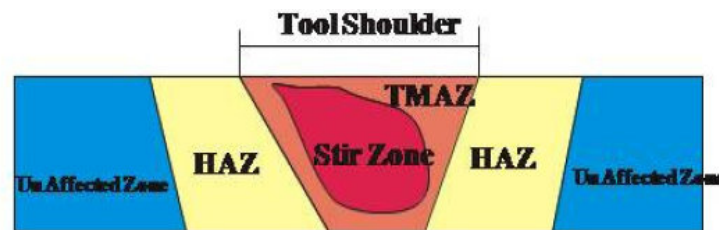


Figure 2.11: Microstructure of a friction stir weld [25]

- Unaffected zone also known as base material (BM) is not affected by the heat generation and consequently, doesn't suffer deformation or any change in its microstructure and material's properties;
- Weld nugget also known as stir zone (SZ) and nugget zone (NZ) which suffers modifications due to the pin's action. Thus, there's an increase in temperature responsible for recrystallization: grain size becomes smaller;
- Thermo mechanically affected zone (TMAZ) counting on the weld's centre is the next zone to the weld nugget. Due to the tool's action, a high plastic deformation followed by heating occurs. Plastic deformation with or without partial recrystallization might happen between weld nugget and TMAZ;
- Heat affected zone (HAZ) is the region closer to the weld centre, does not experience plastic deformation but it has experienced a thermal cycle responsible for mechanical properties' loss.

As in "the advancing side" the traverse speed and rotation speed are on the same way, TMAZ/HAZ limit is more nitid when compared to "the retreating side" where the limit is wider. Counting from the SZ to "the advancing side", concentric rings may be observed on the inferior part of the SZ. Some considered them as the result of threaded tool and indicate good weld quality, Instead, others considered them as the result of grain size change orientation. These considerations arise because of the asymmetry morphology of the joint between the AS and the RS [26, 22, 27].

### 2.3.1.1 Process Parameters

#### Tool geometry

Tool geometry is considered to be one of the most important parameters on FSW, given that its geometry influences directly the material flow, assuring the needed pressure on the weld's interior and governing the traverse speed along the line of joint, heat generation, plastic flow, the weld uniformity and the required power. As stated above, tool is composed by a shoulder and a pin and has two primary functions: localized heat and material flow. Pin design has a crucial role in material flow and regulates the welding speed of the process, while the shoulder is responsible for heat generation and also prevents the escape of the plasticized material from the work-piece. Sidhu et. al [23] concluded despite of the role played by the pin profile in material flow, it is also assumed pin and shoulder are both responsible for affecting the material flow.

Aiming for weld improvement, several researches emerged overtime, resulting in different designs and consequently, on a large variety of shoulders and pins, in order to attend the diverse needs of materials to be joined. For example: Whorl<sup>TM</sup> and MX Triflute<sup>TM</sup> developed by the TWI. The Whorl<sup>TM</sup> tool has a threaded conical pin, doesn't allow inverse rotation and is generally used for butt welding with less torsion effort. On the other side, the MX Triflute<sup>TM</sup> tool has a conical threaded pin with three grooves, doesn't allow inverse rotation and it is suitable for butt welding with much less torsion effect. Both tools have pins with inferior volume, when compared to others. Furthermore, their designs reduce the displayed volume and are believed to reduce welding force, enable easier flow of plasticized material, facilitate the downward augering effect and increase the interface between pin and the plasticized material and additionally, increase heat generation [22].

However, these tools are not recommended for lap welding, where the excessive wear of superior plate might occur while the adherent oxide is purveyed between the lap surfaces, leading to significantly reduced bend properties. So, Flared Triflute<sup>TM</sup> and A-skew<sup>TM</sup> were developed in order to assure a better joining than usual in lap joints and to assure the interfacial layer of oxide fragmentation. The Flared triflute<sup>TM</sup> tool has a tri-fluted pin with flutes being flared out, doesn't allow inverse rotation and it is suitable for lap joints with less thinning on the superior plate. On the other hand, A-skew<sup>TM</sup> has cylindrical threaded pin which is inclined relatively to the machine axis, doesn't allow inverse rotation and it is suitable for the same type of joints of Flared Triflute<sup>TM</sup>. Their designs increase the swept volume of the pin, causing an expansion of the welding region, improve the mixing action, resulting in a bigger union and in successful lap joints [22, 28]. Comparing these two tools with the previous tools aforementioned, its pin resulted in: an improvement in welding speed superior to 100% , a 20 % reduction in axial force, a larger welding region and a reduction in upper plate thinning [29].

Nevertheless, regarding the rotation and translation movements of the tool, an asymmetry is introduced on the material's flow and heat through the pin. As the material flows mainly on the "retreating side", a new tool was developed by the TWI: Re-Stir<sup>TM</sup> whose application consists on a periodical rotation inversion responsible for eliminating the most part of problems related to the asymmetry previously mentioned. Its pin is cylindrical and threaded [26].




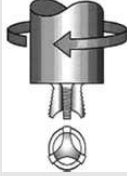
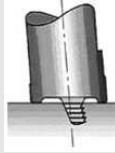

Tool	Cylindrical	Whorl™	MX triflute™	Flared triflute™	A-skew™	Re-stir™
Schematics						
Tool pin shape	Cylindrical with threads	Tapered with threads	Threaded, tapered with three flutes	Tri-flute with flute ends flared out	Inclined cylindrical with threads	Tapered with threads
Ratio of pin volume to cylindrical pin volume	1	0.4	0.3	0.3	1	0.4
Swept volume to pin volume ratio	1.1	1.8	2.6	2.6	Depends on pin angle	1.8
Rotary reversal	No	No	No	No	No	Yes
Application	Butt welding; fails in lap welding	Butt welding with lower welding torque	Butt welding with further lower welding torque	Lap welding with lower thinning of upper plate	Lap welding with lower thinning of upper plate	When minimum asymmetry in weld property is desired

Figure 2.12: Tools designed at TWI [26]

### Welding parameters

The fundamental welding parameters are: tool rotation speed, in clockwise or counter clockwise direction, tool traverse speed along the line of joint and axial force. Temperature rises with the increase of the tool speed, responsible for stirring and mixing the material around the rotating pin, due to the elevated friction and the heat thus generated. Besides, the advancing movement of the tool leads the plasticized material of the advancing side to the retreating side of the tool, causing the slowly decrease of temperature in function of the increase of tool traverse speed.

Meanwhile, other important parameters should be referred: the angle of spindle or tool tilt, regarding the workpiece surface. This parameter is responsible for assuring the shoulder holds the stirred material and moves effectively the material from the front to the back of pin, In order to produce sound welds, the insertion depth of pin into the workpiece should be taken into account and it's obviously associated with the pin's height. This way, welds with inner channel of surface groove due to a shallow insertion depth or concave welds, with local thinning of the welding plates due to a deep insertion depth won't be produced.

For materials with high melting points, the rotation movement of the tool may not be enough to soften plasticize the material. In cases like these, it is recommended to preheat or add a external source of heating in order to help the material flow. Nevertheless, for materials with lower melting points, it is recommended to cool in order to reduce or even prevent the extensive growth of recrystallized grains and dissolution of strengthening precipitates on the stirred zone [22, 26].

### 2.3.2 Adhesive bonding

Adhesive history is relatively long and ancient, dating back thousand of years. But, only 100 years ago the majority of them resulted of mucous body fluids derived from animals such as: insects, fish, birds and even plants along with other natural products such as: milk, bones, skin, water and so on. In 1900, adhesives based on synthetic materials like polymers have been introduced to the industry. Nowadays, they have reached to a level the world can't live with their absence at quite different levels: industry, construction, transportation and many more, due to its mechanical properties, cost and its ability to reduce weight.

Although its relatively long history, in the recent years the use of adhesive bonding technique has increased since it has been the target of study of many researchers. When an adhesive is applied between two dissimilar surfaces, it is with the intent to join them permanently through interfacial contact after the adhesive cure and to improve resistance. Relatively to its structural purpose, adhesives may be classified into two different categories: structural and non-structural. As the name implies, structural bonding is used when two different structures experience stresses which they must be able to transmit without losing integrity. Thus, in order to categorize as a structural adhesive, it must have a shear strength greater than 7 MPa [30], plus ageing resistance. On the other hand, non-structural bonding is required to hold light-weight materials in their place, without supporting substantial loads. However, both must have equal duration of their service life.

Adhesives also improve resistance to fatigue loading, can be used for sealing since they're not attacked by gases or liquids and can be used for mechanical clamping too [30], they allow the joining of similar and dissimilar materials with any shape or thickness. They also improve resistance to corrosion when dissimilar materials are joined, reduce weight and cost, provide a uniform stress distribution, resulting in a wider stress-bearing area and finally, thermal or electrical conductivity may be adjusted when desired to. On the other hand, a careful surface preparation is needed, curing may be a longstanding process, upper temperature service is limited and service life is dependent on the environment of exposure. Natural adhesives are often attacked by living organisms and special equipment like presses, ovens, autoclaves and holding fixtures are required [30]-[32].

#### 2.3.2.1 Adhesives classification

Adhesive classification varies depending on the consulted literature, application, resistance, function, performance, costs, chemical composition, materials to be joined, working conditions and many others.

They can be categorized considering their nature:

- Polymer base: natural or synthetic;
- Polymer "backbone" functionality: thermoplastic or thermoset;
- Physical forms: one or more components, films;
- Chemical families; epoxy, silicon;
- Functional types; structural, hot melting, water-base, pressure sensitive, etc [31, 30].

More information about adhesive classification and further characterization can be consulted on the proposed bibliography [31, 30].

### 2.3.3 Weldbonding

Weldbonding is a hybrid technique, given that combines different types of joining: welding, e.g.: spot-welding (RSW), hybrid laser plasma welding or recently friction stir welding; and adhesive bonding, to attach two materials, which can be or not of a different composition. It was originally developed to avoid noises and vibrations for aircraft, rail-way carriages and to improve automotive production so structural crashworthiness, corrosion resistance and fatigue performance could be increased. Other techniques regarding hybrid joints were developed and investigated, such as: bonded-riveted, bonded-screwed, bonded-clinched and bonded-bonded. First, Weldbonding was applied by the Russians to their planes: first the parts were welded together and then, they forced the adhesive to flow into the joint. Meanwhile, Americans used weld-through method which consists on applying an adhesive to the parts to be joined, followed by spot welding and left to cure [33].

When adhesives of polymeric nature are used, considerations must be made because of their resistance to harsh environments, principally concerning temperature and humidity and also their durability. On overlap joints, the stress distribution lies at their ends, leading to concentration of stress and therefore, leading to premature failures. This technique was introduced with the aim to overcome several issues when it comes to welding and Adhesive Bonding, producing final joints with improved mechanical properties when compared to those of each process alone.

Although for FSW there's scarce information, generally hybrid joints improve fatigue and static strength, stiffness, corrosion resistance, energy absorption, load distribution and therefore, stress concentration. Sealing operations are eliminated and manufacturing costs are reduced [33]-[35]. However, the co-existence of the weld nugget and adhesive layer, stress and strain analysis become complex resulting in lack of information regarding failure processes and fracture prediction. Hereupon, it is hard to point the disadvantages of the process [36].

Due to its improved mechanical properties, Weldbonding has gained a lot of ground with the number of involved applications increasing and seeing its degree of acceptance enhances in the most diverse areas.

## 2.4 High strain characterisation

As stated in Section 2.1, most materials mechanical properties are listed in diverse books. Nonetheless, these properties are obtained through quasi-static tests in which the specimen is under quasi-static loading conditions. Therefore, the deformation the specimen suffers is very low and so, the strain rate. To fully characterise materials, their behaviour must be completely studied and after, understood.

In addition, materials submitted to different manufacturing processes also need to be tested, not only to be fully characterized as materials but also for continuous improvements. Accordingly, manufacturing processes cause transformations in the materials. Thus, strain hardening is the strengthening of a material caused by a plastic deformation. Such occurs because there's a dislocation of the material crystal structure. It is used to characterise the increase in flow stress which is directly proportional with the increase of the strain. Further, strain rate hardening is used to characterize the increase in flow stress with the increase of strain rate. By increasing strain rate, it can be observed if a material presents strain rate sensitivity or not.

Then, the performance of dynamic tests in which the specimen is under dynamic loading conditions and it is quickly deformed at high strain rates is required.



### 2.4.1 Test methods and testing equipments

In order to characterize materials mechanical response at different loading conditions, several tests and respectively equipments were developed. Their major goal is to reproduce as close as possible real loading conditions and therefore, static and dynamic loading conditions. Besides, with the emergence of innovative materials and bonding processes, structural behaviour must be completely understood. In addition, important improvements can be applied to tailor different ranges of applications.

Strain rate has an important role on the ductile-fragile transition regarding the material of study. To well define its properties or its strain rate dependence, the material needs to be subjected to different ranges of strain rate. However, when a material is exposed to high strain rates, difficulties in measuring specimen load and strain arise due to the loading conditions application in a short period of time, similar to an impulse. For very high strain rates, these variables can only be measured when wave propagation analysis is considered. Observing the Figure 2.13, distinct equipments can be applied when different strain rate regimes are required.

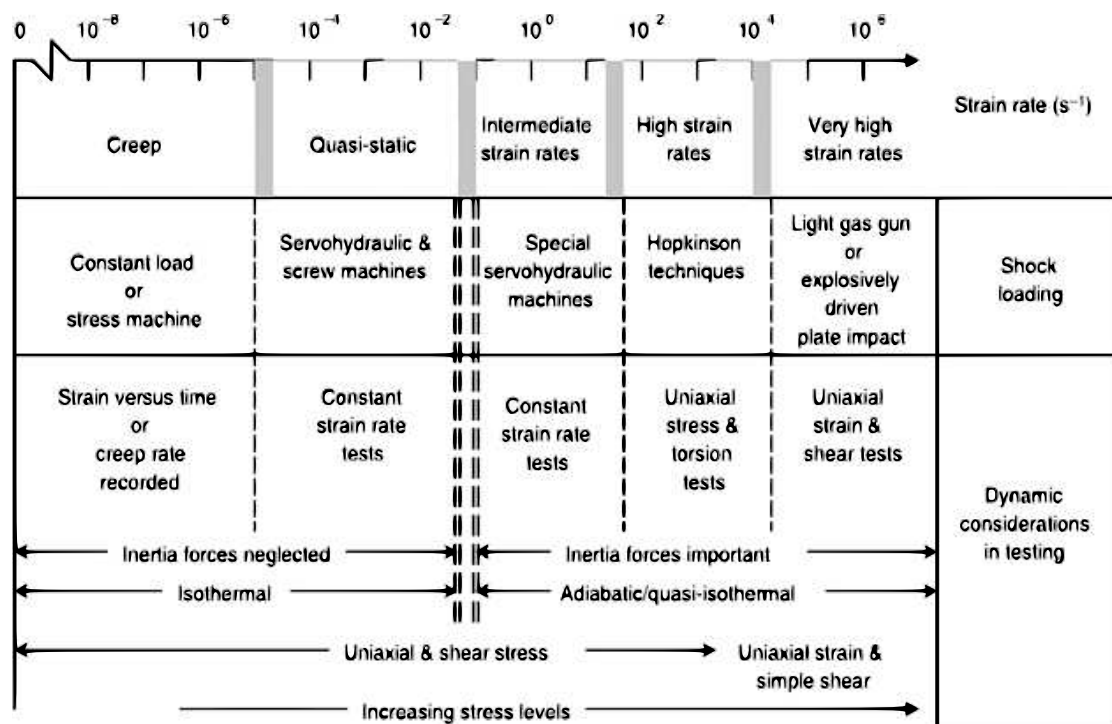


Figure 2.13: Experimental set-ups for different strain rate regimes [37]

#### 2.4.1.1 Servo hydraulic testing machine

Servo hydraulic machines, as the own name says, are constituted by a hydraulic piston, with dual or simple function, triggering the cylinder head down and up. These kind of machines operate in a closed loop cycle wherein a servo controller is responsible for regulating and adjusting electronically the servo-valve. Sometimes, procedures like these in standard systems may occur 10000 times per second. Likewise, the servo-valve controls oil flow, guide position, velocity and force whose measurement is made by a load cell [38].

These machines have a large range of test cases, considering the mechanical test to be performed: tensile and compressive, creep, fatigue for low and high cycles, crack opening dis-

placement (COD) tests or even constant strain rate tests. The performed tests may be performed at strain rates up to 200/s, due to the limitations introduced by the indirect measurement of load and displacement.

In Figure 2.14, a servo hydraulic machine for performing high strain rates tests by INSTRON® is presented. This particular machine has a capacity of 40 kN to 100 kN, it is capable of velocities up to 25 m/s, operates at a 280 bar resulting in higher acceleration and loading performance and has specialized measurement transducers [39].



Figure 2.14: Servo hydraulic machine VHS 8800 High strain rate systems by INSTRON® [39]

#### 2.4.1.2 Drop weight test

The drop weight test was developed at the United States Naval Research Laboratory with the intent to determine the nil-ductility transition temperature (NDTT). NDTT represents the test temperature in explosion bulge test, where the crack propagation occurs in the presence of only elastic strains. The test procedure is described in ASTM E 208 [40].

A specimen with a rectangular shape is placed on two rounded end supports. These rounded end supports are part of a stop block where the specimen is welded down (Figure 2.15). The brittle weld bead deposited on one face contains a notch which is responsible for the crack propagation or arrest when an impact loading is applied to the specimen. Different tests with temperature variation are carried out. After the impact, examinations on the specimen are made to determine if it has fractured or not. If the observed crack is extended to one or both sides of the specimen surface towards the weld bead, the specimen is considered broken. In order to admit the test validity, a complete deflection must occur [37].

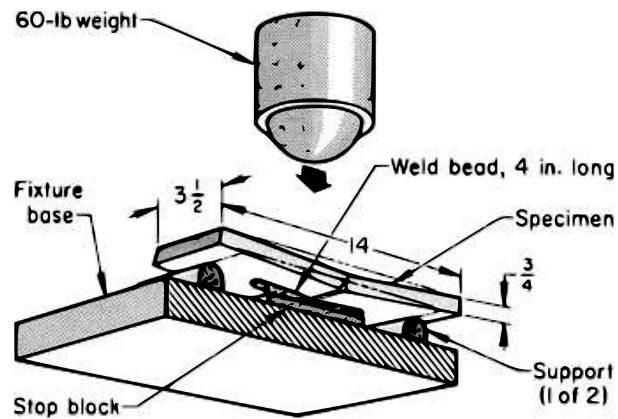


Figure 2.15: Drop weight test [37]

### Drop weight tower

This equipment is composed by a suspended mass, which is responsible for generating an impulsive force over the specimen when it is dropped. By increasing mass weight it is possible to perform tests with elevated loadings. Strain rates on the order of 200/s can be achieved. Sometimes, impact velocities on the order of 7m/s can be reached and therefore, solid foundations are required to endure impact and to maintain the inferior plate stiffness. The superior plate is fixed on a guide rail, with an adequate alignment considering the specimen and the plates. Meanwhile, the inferior plate is mounted on a spherical base and a load cell is placed under it. In order to maintain the equipment integrity, the mass is decelerated by anvils when it is close to its maximum course. Plus, the impact generated by the suspended mass is transmitted to the specimen through the guide rail aforementioned. Figure 2.16 shows a drop weight tower produced by INSTRON®.

Nevertheless, this test presents some disadvantages because it is incapable to impose a constant strain rate and a constant loading rate. The specimen geometry and behaviour influence the impact velocity and the energy of the suspended mass. This equipment is also used to evaluate the effect of different load ranges, generally inferior to rupture load [41].



Figure 2.16: CEAST 9350 Drop weight tower by INSTRON® [42]

### 2.4.1.3 Rotating wheel test

The equipment used to perform the rotating wheel test consists of a rotating wheel with claws or noses, stroking a yoke containing test pieces. Introducing load-measuring gages as close as possible to the gage length is responsible for measuring elastic strains, converting to stresses using the Young's modulus of the material. This technique allow records of stress-strain up to velocities of 30 m/s, in other words, allows strain rates on the order of 2500/s, using a specimen with 10.5mm of gage length and 3.5 mm of diameter.

As the rotating wheel has a energy content 10 higher than the specimen's fracture energy, almost no influence of the tested materials towards velocity or strain rate is observed, even if they are high strain hardened or highly deformable. Electro-optical cameras and non contact laser interferometers are used if strain rate measurement is required so that calculation is avoided.

If short specimen lengths are required, a wave transmitter bar is connected to it after a careful evaluation of impedance transference between them. This procedure is most suitable for high and very high strain rates of welded-joints, since screwing and brazing result in stress-time diagrams of bad-quality [37, 41].

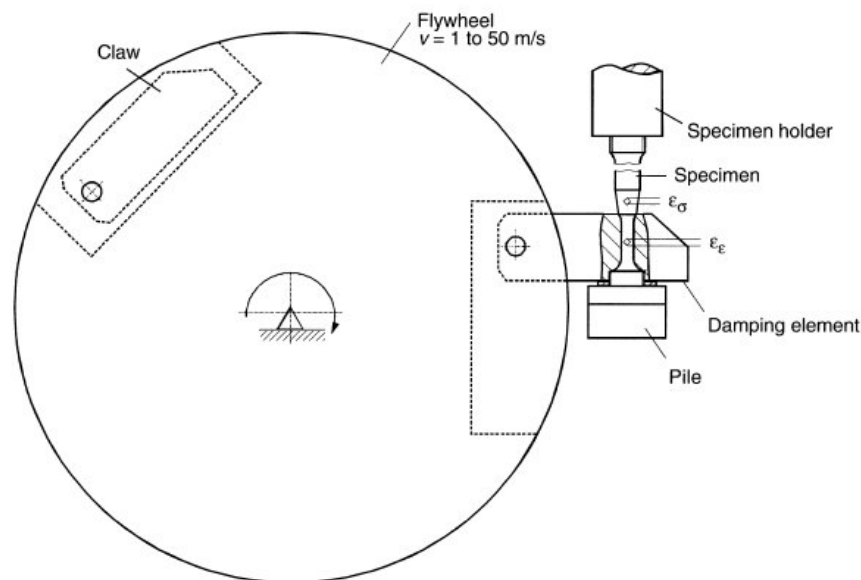


Figure 2.17: Flying wheel set up [41]

### 2.4.1.4 Expanding ring

The expanding ring test demands the application of an impulsive radial load of short duration, in a specimen with a thin ring geometry and it is employed when strain rates over  $10^4$ /s are required. Applying an intense magnetic field or by detonating an explosive load, the specimen is radially expanded, with high acceleration. The ring expands as a free body, subjected to its own inertia, decelerating due to the hoop stress effect. This phenomena usually happens after a short period of time. However, this theory can only be applied to rings with thin walls. For this reason, the specimens used have typical dimensions: 25mm of diameter and walls with 0.8mm of thickness. Hoop stress can be obtained using the Equation 2.1:

$$\sigma = -\rho R \frac{d^2 R}{dt^2} \quad (2.1)$$

where  $R$  is the radius and  $\rho$  is the density of the ring.

In addition, as strain is proportional to change in radius, it can be obtained by the following equation:

$$\varepsilon = \ln \frac{R}{R_0} \quad (2.2)$$

where  $R_0$  is the initial radius of the ring.

Although it is based in a simple principle, the test requires specialized equipment and a sophisticated technique. The use of high speed cameras, streak cameras or interferometry pulsed techniques are required to measure the radial displacement of the ring's walls during the test, whose duration is very small, during millisecond fractions.

The material is subjected to a state of dynamical uniaxial stress without any problems towards wave propagation which are present on other high strain rate tests. Furthermore, the available strain rate is higher than in any common tension tests with large strain rates involved. However, the major difficulty of this method relies on the need to measure radial displacement with enough precision for its temporal variation of second order to be acceptable. The interior pressure caused by detonation is responsible for engender compressive tensions in the radial direction, which surpass the yield stress [37, 41].

#### 2.4.1.5 Split Hopkinson pressure bar

The split Hopkinson pressure bar technique was named for Sir Bertram Hopkinson in 1914 [43]. His studies were primarily intended to characterize the impact generated by explosives. For that, he used the induced-wave propagation in a long elastic metallic bar in order to measure the resulting pressure of the dynamic events, performing his tests with different momentum traps, varying their lengths. In metallic rods, stress pulses propagated and then, the form and evolution of stress pulses could be studied, enlisting the variable time.

Nowadays, there are many variants of this equipment thanks to researches initially made by Davies [44] and Kolsky [45]. As such split Hopkinson tensile bar is also know as Kolsky's bar. The well known and widely used form of equipment consists on an impact bar and two bars: the incident and transmitted bar, placed in series with a specimen sandwiched between them, so that the dynamic response of the material under consideration can be studied. There's a gas gun which accelerates the impact bar, which in its turn shocks against the incident bar with an incident wave propagation. Part of this wave is reflected in the specimen-bar interface to the incident bar, while the remaining part is transmitted to the transmitted bar and therefore, gets the name of transmitted wave. This particular configuration is used to characterize the behaviour of materials subjected to compressive high strain rates, up to the order of 5000/s. With the three waves registered, three equations can be used to determine the strain rate and the relation between tension and strain:

$$\sigma(t) = E_b \frac{A_b}{A_{s0}} \varepsilon_T(t) \quad (2.3)$$

$$\varepsilon(t) = \frac{-2c_0}{l_{s0}} \int_0^t \varepsilon_R(t) dt \quad (2.4)$$

$$\dot{\varepsilon}(t) = \frac{-2c_0}{l_{s0}} \varepsilon_R(t) \quad (2.5)$$

where  $E_b$  is the Young's modulus of the bar,  $A_b$  is the bar's cross section,  $A_{s0}$  is the initial cross section of the specimen,  $l_{s0}$  is the initial length of the specimen,  $c_0$  is the wave velocity propagation,  $\varepsilon_T$  is the transmitted wave and  $\varepsilon_R$  is the reflected wave.

On the other side, there are different configurations of the split Hopkinson bar equipment, given that materials also need to be characterized under uniaxial tensile, torsion and bend loads.

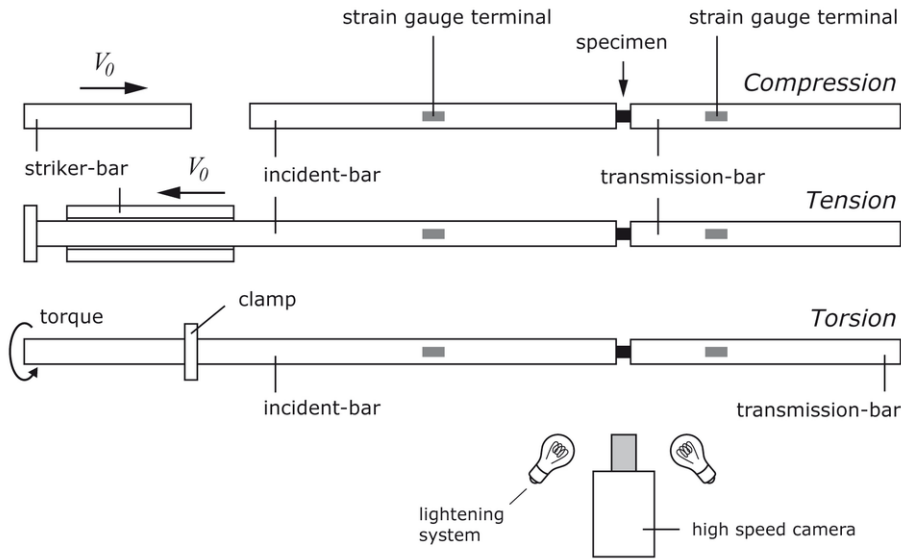


Figure 2.18: Different configurations of the SHB [46]

There are three different methods for measuring tensile pulses in the incident and transmitted bar. First method developed by Lindholm et al. [47] uses a hollow transmitted bar with a "top-hat" specimen (Figure 2.19). Second method consists on applying a direct tensile loading (see Figure 2.18 for tensile configuration) on the incident bar and several geometries of specimen can be used: an axisymmetric one with threaded ends, a flat specimen gripped to both bars and a dumb-bell one, attached through flanges. Third and last method consists on the reflection of the compressive pulse at the free end of the transmitted bar. This reflection is responsible for loading the specimen in tension, with the coexistence of a collar whose importance is utmost because it protects the specimen from the initial compressive pulse. In Figure

2.20, an experimental set up based on this method used by Nicholas [2] is introduced, with special detail for the collar. In addition, in Figure 2.21 the specimen used is exhibited.

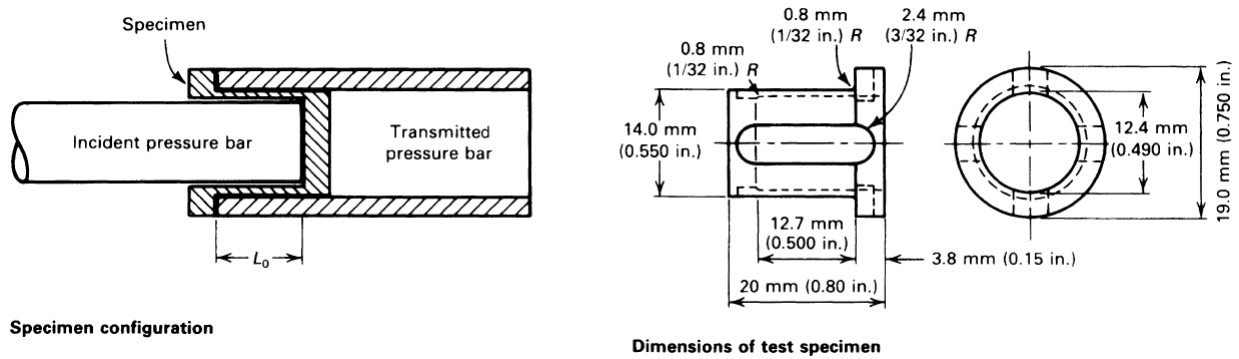


Figure 2.19: "Top-hat" specimen used by Lindholm et al. [41]

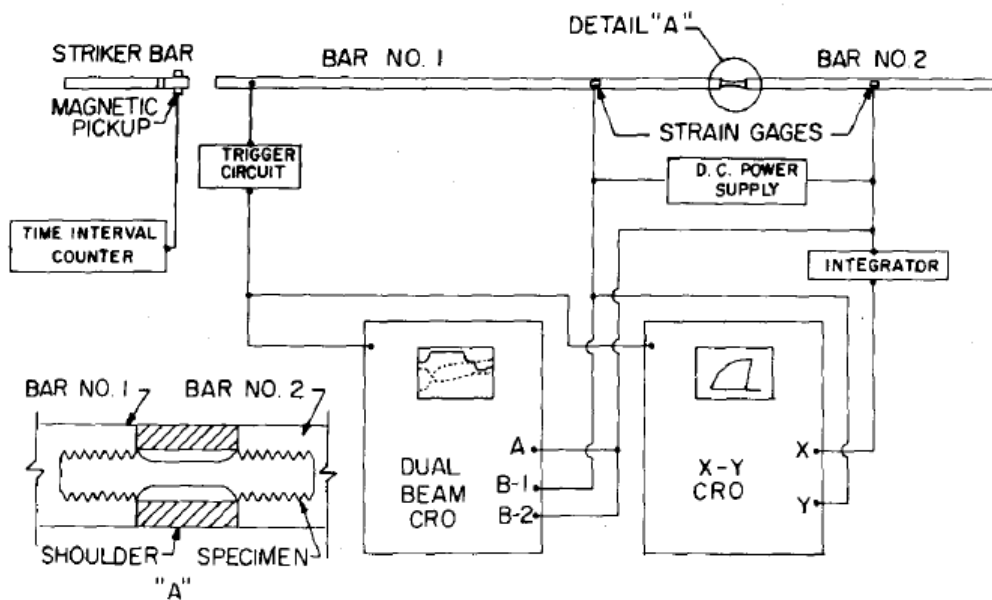


Figure 2.20: Split Hopkinson tensile bar used by Nicholas [2]

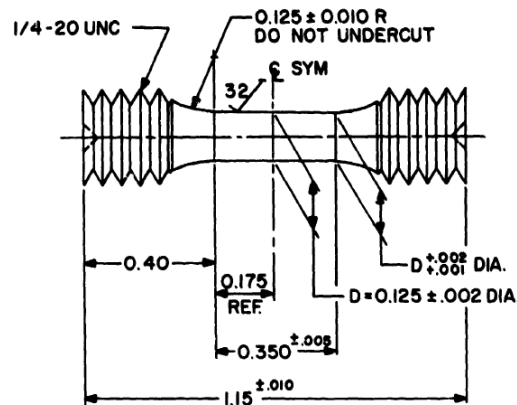


Figure 2.21: Threaded specimen used by Nicholas [2]

Subsection 3.1 provides an extensive analysis and further details of the split Hopkinson pressure bar.

#### 2.4.2 Base material characterisation

Shi and Meuleman [48] studied the strain rate sensitivity variation in the tensile test, the effects of strain hardening and strain rate hardening for different ranges of aluminium alloys and, finally, the dependence of elongations on strain hardening and strain rate hardening. The tensile tests were performed at strain rates between  $1 \times 10^{-7}$  and  $1 \times 10^2$ /s. The authors found strain rate hardening was dominantly responsible for increasing tensile strength and it was more evident at low strain levels than at high strain levels. Moreover, increasing strain rate led to an increase of yield strength but on the other hand, led to a decrease of elongation. Last, strain rate decreases when uniaxial stress was increased.

It is well known and recognized that materials generally respond in a different form at high strain rates when compared to quasi-static or static loading conditions. Since there is an increase of strain rate from the quasi-statics tests to the dynamics, conditions change from isotherm to fully adiabatic. This results in a strain rate increase and in a gradual decrease in strength [49, 50]. The material's flow stress depends not only on the strain and strain rate but also on its microstructure at the displacement level. In order to combine flow micro mechanisms in the formation of constitutive macroscopic relationships, there is a need to comprehend the microstructural changes that occur during deformation. Lee et. al [51] studied the impact response that the deformed AA6061 alloy presents at different strain rates which were varied between  $10^3$  and  $4 \times 10^3$ /s and, continuously, investigated the displacements configurations and densities thus generated. The authors concluded that the impact response of that same alloy was strongly affected by the applied strain rate, leading in variations of work hardening rate, strain rate sensitivity and activation volume. Work hardening rate decreased with strain and strain rate (Figure 2.22) and it was linearly related with the flow stress inverse (Figure 2.23).



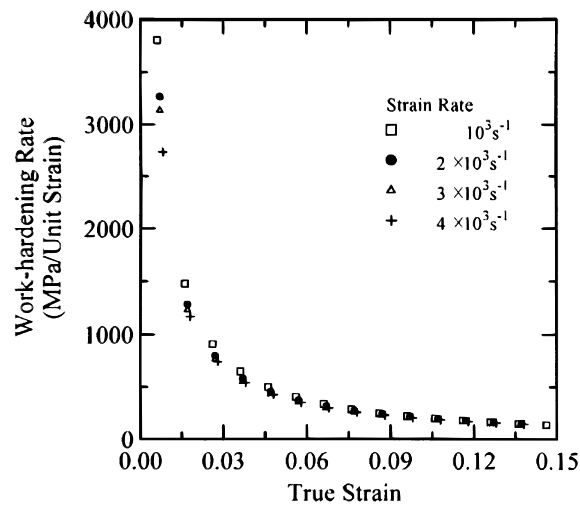


Figure 2.22: Strain rate and work hardening rate dependence of AA6061 alloy [51]

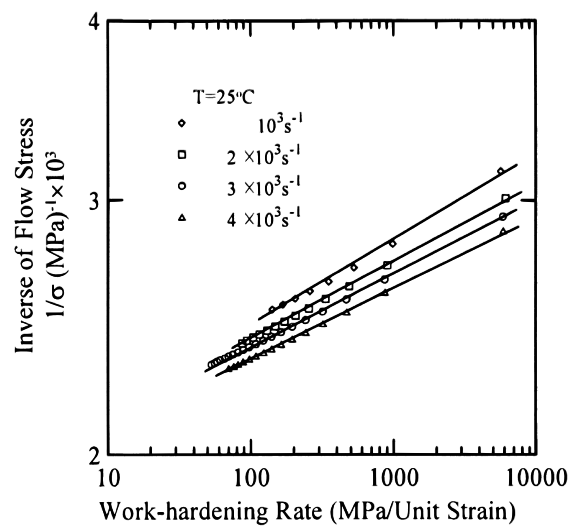


Figure 2.23: Inverse of the flow stress as function of work-hardening rate of AA6061 alloy deformed at 25°C and different strain rates [51]

As can be seen, strain rate sensitivity increased with work-hardening stress. However, for the activation volume, the situation was reversed (figure 2.24).

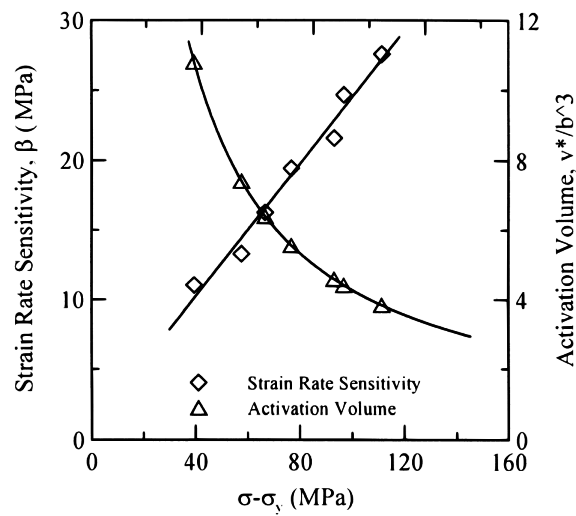


Figure 2.24: Strain rate sensitivity and activation volume as a function of the work hardening stress [51]

The strain rate sensitivity of two commercial aluminium alloys: AA6082-T6 at peak temper and AA7108-T79 aged, was analysed by Oosterkamp et al. [52]. It was expected that these alloys presented a relatively low strain rate sensitivity, since they were hardened by precipitation. Their response to fast loadings has been tested for a wide range of strain rates, from 0.1 to 3000/s, at room temperature, as well as 375 and 515°C temperatures for the AA6082 alloy and at room temperature, as well for 280 and 340°C temperatures for the AA7108 alloy. The cylindrical shape specimens were cut from a planar extruded section and were tested for uniaxial compression state with the strain axis parallel to the extrusion direction. For high strain rates greater than 500/s, tests were performed on a conventional split Hopkinson pressure bar (SHPB), whose configuration can be seen in Figure 2.25.

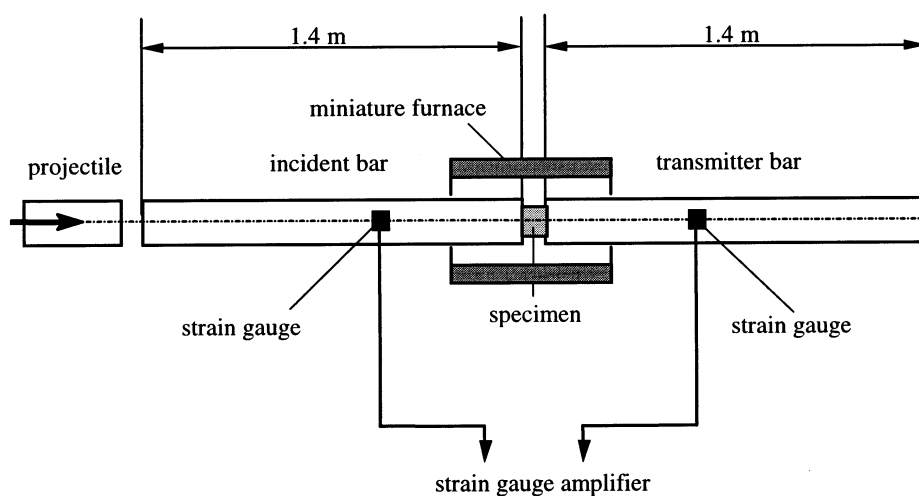


Figure 2.25: Split Hopkinson pressure bar configuration [52]

In SPHB tests, uniform strains and stress in the specimen can only be considered at lower

velocities of impact and as such some inaccuracies may be introduced. Therefore, a numerical simulation was performed. The results achieved by the authors confirmed the expected: the strain rate sensitivity of both alloys was very low since, as mentioned above, they were aged artificially by precipitation and tested in peak temper. A tendency of negative strain rate sensitivity to strain rates above 2000/s was observed. Might be a consequence of the strain localisation on a microscopic scale. Different stress-strain curves were obtained, for different geometries tested. These same curves also satisfied the inherent material properties. Furthermore, it was also verified the discrepancy obtained between the numerical solution and the experimental solution decreased with the increase of specimen diameter/thickness ratio. This observation also means that when testing the commonly accepted specimen geometry in which diameter/thickness ratio is approximately equal to 2, an over estimation of the flow stress occurs. In the flow stress vs. strain rate in logarithmic form, this event was recognized through a sudden change of the strain rate sensitivity.

Lee and Kim [53] conducted an experiment using SHPB technique with a special experimental apparatus so the materials mechanical properties under high strain rates for both compressive and tensile loading could be obtained. The authors subject of study were the following alloys: AA2024-T4, AA6061-T6 and AA7075-T6. For compressive tests, the specimens geometry was set in order to minimize the inertia effect. As a result, they had 5mm thickness and 10 mm diameter. On the other hand, for tensile tests specimens with 34, 4 and 12 mm whole length, diameter and gauge length respectively were used. The tensile specimens had a screw shape on both ends, for better fixing in incident and transmitted bars. It was noticed that the superposed wave of the reflected and the transmitted waves were almost the same as the incident waves. Also, for both compressive and tensile loading there were pronounced effects of strain rate on the relationship of stress-strain, see Figure 2.26 and Figure 2.27. Furthermore, the material had a higher strain rate sensitivity towards tensile strength than compressive strength. Finally, the relationships between compressive/tensile strength and strain rate were found to be bilinear (Figure 2.28).

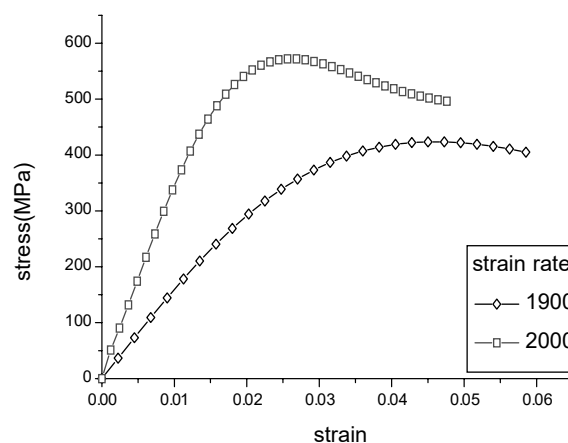


Figure 2.26: Dynamic tensile stress-strain curve for AA6061-T6 [53]

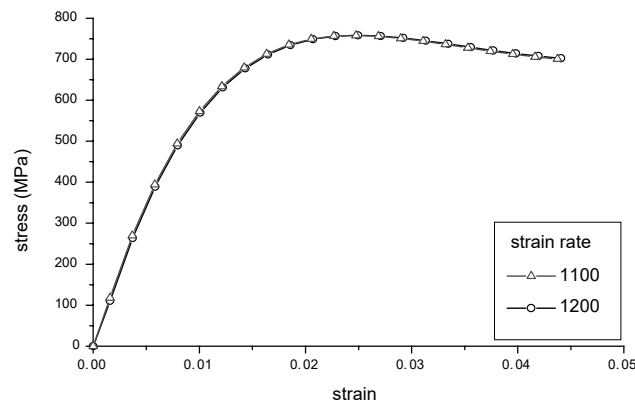


Figure 2.27: Dynamic compressive stress-strain curve for AA6061-T6 [53]

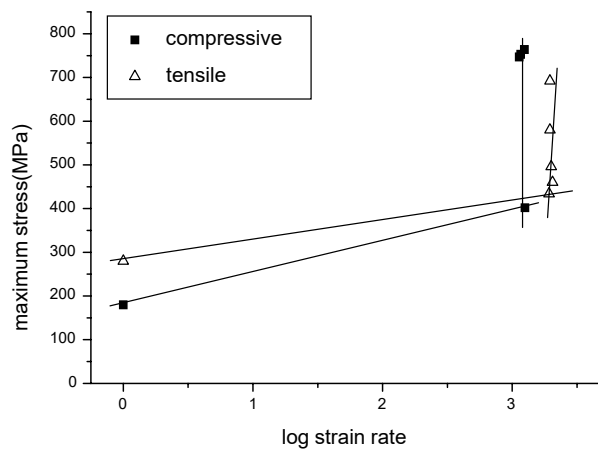


Figure 2.28: Dynamic log strain rate vs. maximum stress for AA6061-T6 [53]

Some other studies were performed on the AA6061 alloy where the effects of strain rate on its deformation behaviour were examined by Masuda et al. [54]. Tensile tests were performed at room temperature for three different ranges of strain rate conditions in which the employed specimens had a smooth and notched cylindrical geometry, machined with the tensile axis parallel to the extrusion direction (three extruded directions). Masuda et al. concluded the increase in stress triaxiality was dependent on the strength level increase but, on the other hand, there was a decrease in ductility. Plus, strain rate sensitivity grows with the increasing strain rate. The notches in specimens were responsible for the reduction of plastic constraint factor.

A more interesting case of study appeared when Chen et al. [55] conducted an investigation on aluminium alloys subjected to a wide range of strain rates wherein the selected alloys belonged to the 6xxx and 7xxx series. While tensile tests at low to medium strain rates were performed in a conventional tensile test machine, high strain rates tests were carried out in a split Hopkinson tensile bar (SHTB) at strain rates between  $10^{-3}$  and  $10^3$ /s. Even though for the 6xxx alloys the rate sensitivity had no significant role in the stress-strain behaviour, for the 7xxx alloys a moderate rate sensitivity was found. As a result, in the three tensile directions there was no significant difference between their rate sensitivity. The main goal was to identify the parameters of a thermo-viscoplastic constitutive relation for the extruded alloys, more specifically the effects of strain hardening, strain-rate hardening, thermal softening and plastic

anisotropy. Specimen geometry was a cylindrical dogbone with threaded ends which was designed to be connected between the incident and the transmitted bars. The SHTB apparatus contained a locking mechanism (A) and a hydraulic jack (B), Figure 2.29.

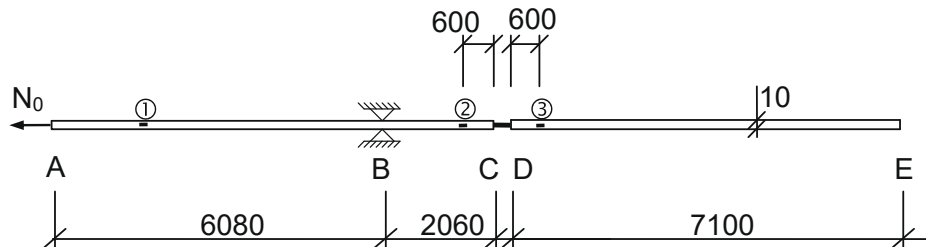


Figure 2.29: Split Hopkinson tensile bar [55]

For the three directions in which the tests were conducted ( $0^\circ$ ,  $45^\circ$  and  $90^\circ$ ), the obtained hardening curves in terms of true stress and true plastic hardening at strain rate  $10^{-3}/s$  are displayed in Figure 2.30 while the true stress plastic strain curves showcasing the hardening behaviour are plotted in Figure 2.31 for the strain rate range tested.

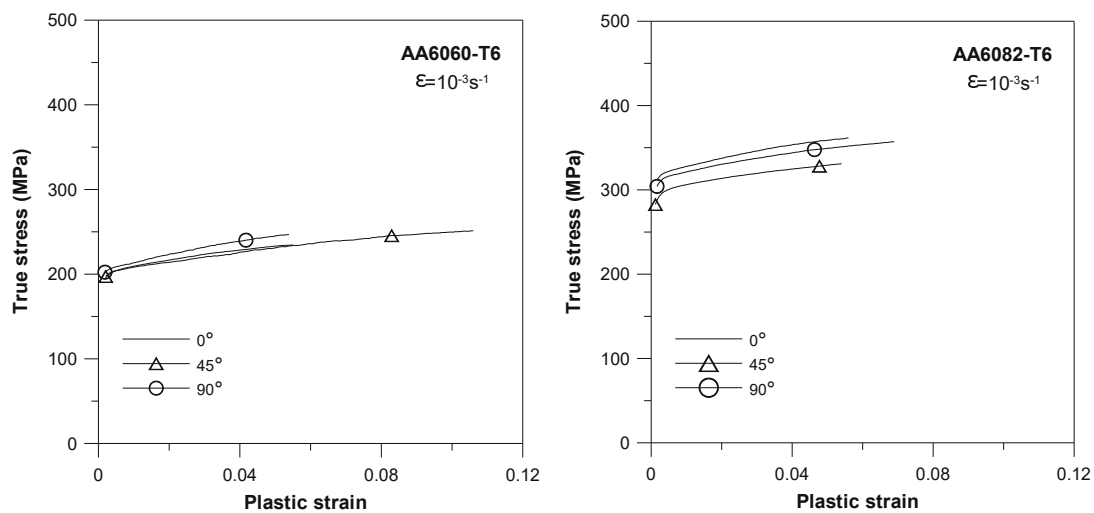


Figure 2.30: Representative true stress versus true plastic strain curves proving the plastic anisotropy of the 6xxx series tested[55]

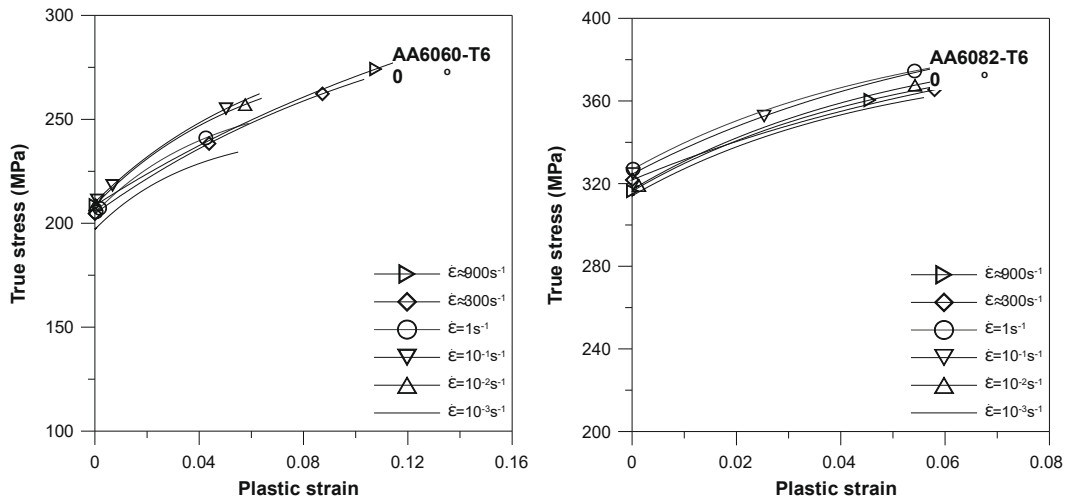


Figure 2.31: Representative true stress versus true plastic strain curves showing the strain-rate sensitivity of the 6xxx series tested [55]

Using those results, another investigation performed by Chen et. al [56] focusing on the same previous alloys was performed employing a different SHTB apparatus (Figure 2.32). The test results were employed in order to identify the parameters of an anisotropic thermoelastic-thermoviscoplastic constitutive relation and a one-parameter fracture criterion for the materials available. With all the parameters identified a implementation using finite element analysis of the SHTB tests, the experimental set-up and the stress wave propagation during the tests was made. The used SHTB apparatus had three strain gauges (1, 2 and 4) mounted diametrically on the incident bar and one strain gauge (3) also mounted diametrically on the output bar (see Figure 2.32). Strain gauges 1 and 3 were used to determine the strain, strain rate and consequently, stress in the specimen which made them the most important ones. On its turn, strain gauge 1 provided an important verification, if there was or not any dispersion present on the test while strain gauge 4 served to monitored the tension force  $N_0$ . All combined, it was possible to control the bending effects in the bar, only by considering the mean values between the two opposite gauges.

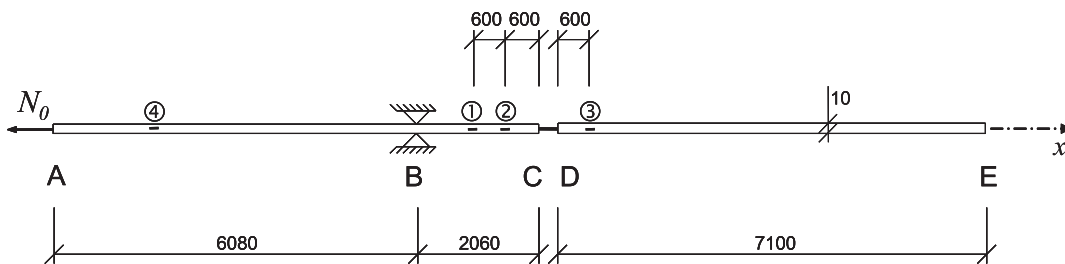


Figure 2.32: Split Hopkinson tensile bar [56]

Therefore, by using the strain gauges 2 and 3, a comparison between simulations and experiments of the strain for the three directions was made for alloys AA6060-T6 and AA7003-T6, proving the average values of the incoming strains were well predicted in all simulations. Thereafter, the authors also compared the engineering stress-strain curves from simulations and experiments, with and without use of the Bridgman correction and concluded the agreement between them was generally good, as shown in Figure 2.33.

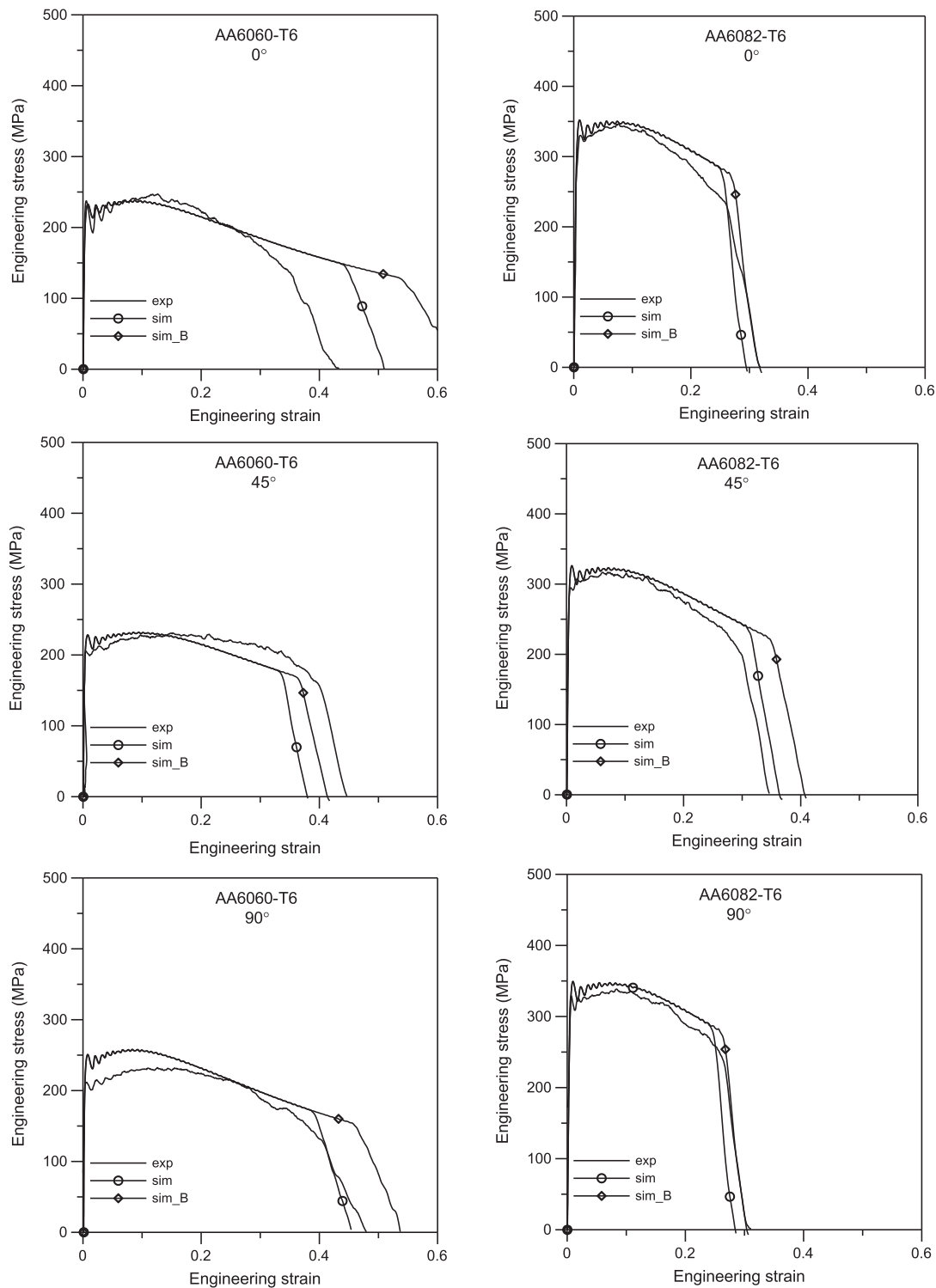


Figure 2.33: Comparison between experimental and simulated results for alloys AA6060-T6 and AA6082-T6 in three directions [56]

Fan et al. [57] investigated the compressive stress-strain relationships of AA6061 alloy over wide temperature ranges and strain rates, using an improved high temperature SHPB apparatus (Figure 2.34) to conduct the dynamic experiments. The experimental results were com-

pared with those obtained using the Johnson-Cook constitutive model. It is known temperature has a fundamental effect on the dynamical behaviour. On one hand, the dynamical behaviour depends on the temperature under low strain rates conditions or depends on the strain rate at high temperatures. The results showed that at low temperatures the effect of strain hardening is more significant, whereas at high temperatures the significant effect was due to strain rate. At elevated temperatures, the change in deformation mechanism was considered to be the crucial factor affecting the sensitivity of the strain rate. Fan et al. also found the mechanical properties of AA6061 alloy were more sensitive to the temperature than to the strain rate.

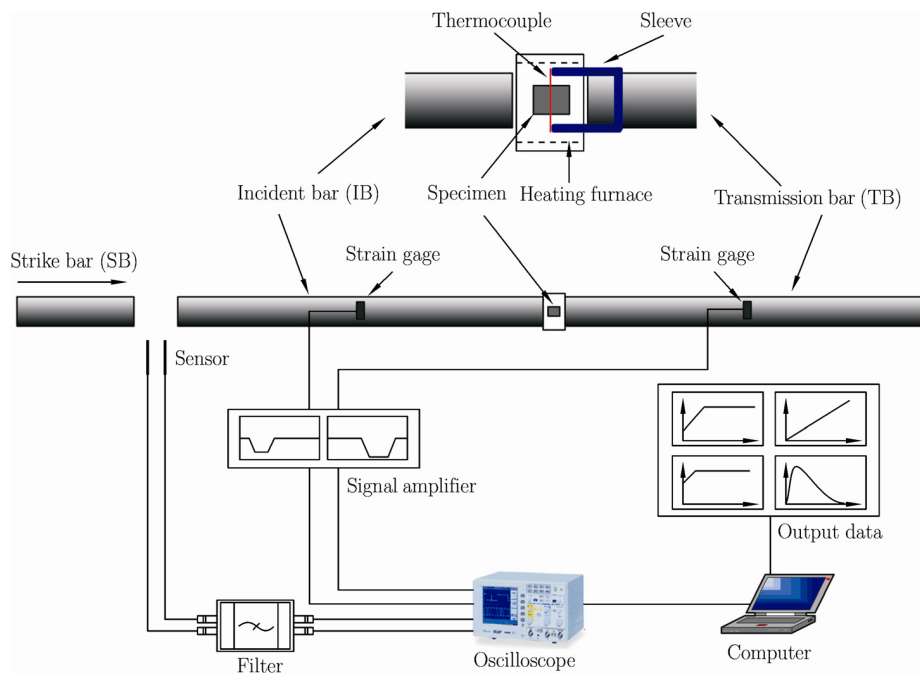


Figure 2.34: Split Hopkinson pressure bar used by Fan et. al [57]

As the information on the energy absorption of aluminum-based sandwich panels is scarce, Tang et. al [58] carried out an investigation aiming to fill this research gap. First, several tests were made for individual constituents under a wide range of strain rates for AA6061 alloys in two different heat treatments. Then, the studied alloys were tested at room and low test temperatures. The dynamics tests were conducted on a split Hopkinson tensile bar whose configuration is illustrated in the following figure:



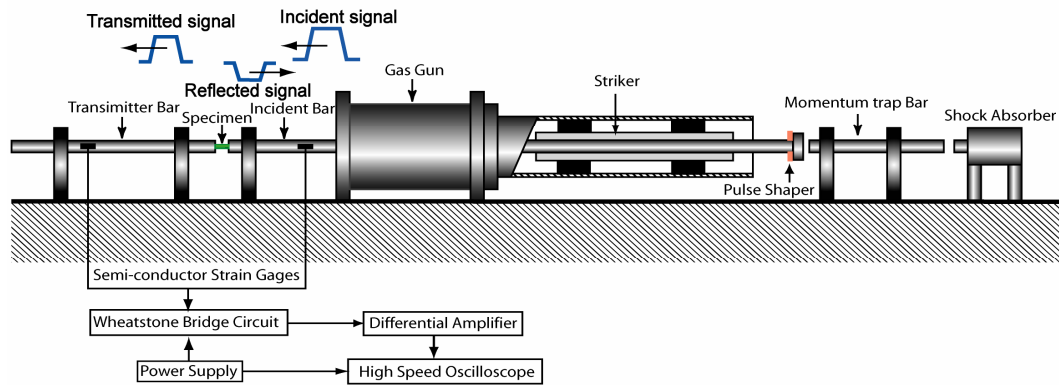


Figure 2.35: Split Hopkinson tensile bar [58]

Images taken with high-speed camera for the AA6061-T6 alloy, at a 1280/s strain rate, show the gradual elongation of the specimen until its neck fractures:

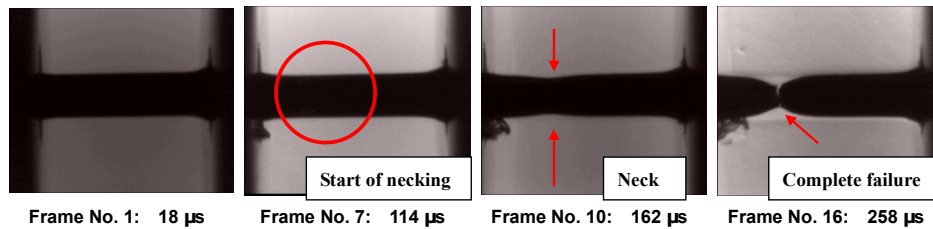


Figure 2.36: Frames from high-speed camera records for AA606-T6 at room temperature [58]

The authors observed a slightly positive strain rate sensitivity as well high work hardening after necking (Figure 2.37). When a decrease of temperature was imposed, there was a significant increase on the tensile strength.

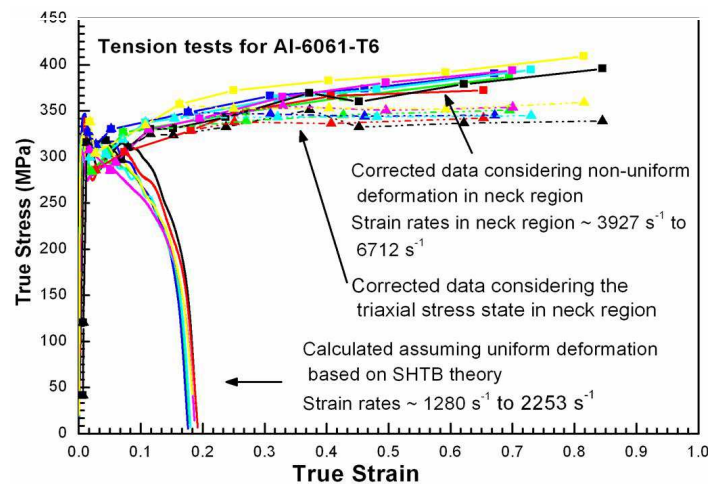


Figure 2.37: Results at room temperature. Dots on curve correspond to high-speed camera [58]

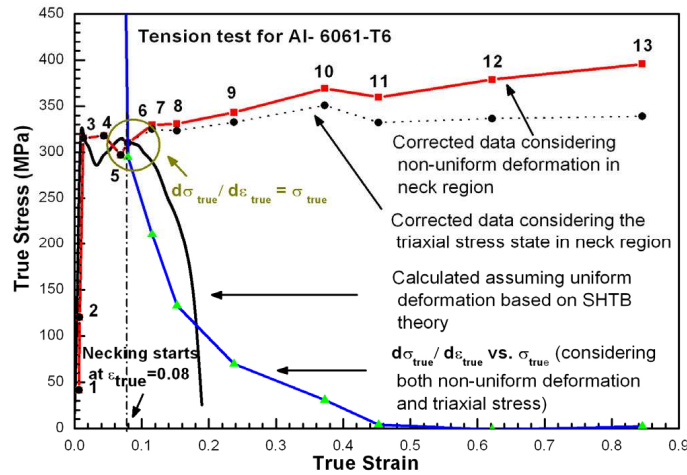


Figure 2.38: Results in different high strain rates at room temperature [58]

Observing Figure 2.39 and Figure 2.40, it may be noted that when temperature drops to  $-170^{\circ}\text{C}$ , the true stress versus true curve alters to a superior high level.

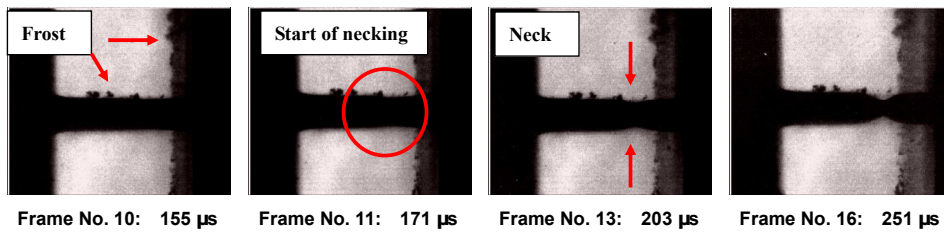


Figure 2.39: Frames from high-speed camera records for AA6061-T6 at  $-170^{\circ}\text{C}$  [58]

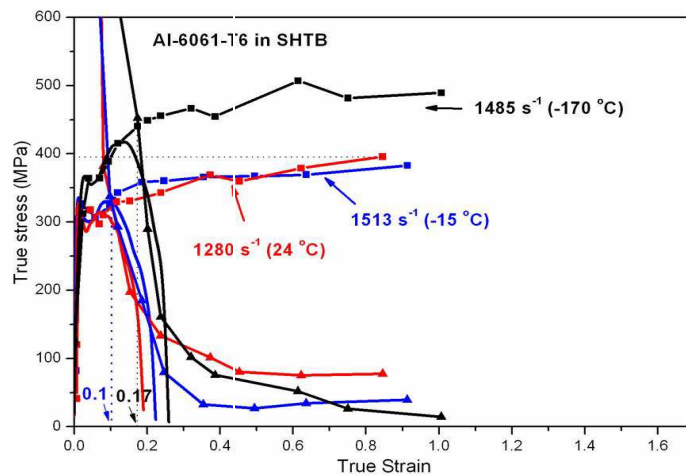


Figure 2.40: Comparison between low and room temperatures [58]

Another investigation performed by Lemanski et al. [59] emerged for characterize experimentally the AA6082 alloy at varying temperature and strain rate where high strain rate tests were realized in a tensile Hopkinson bar (Figure 2.41), at a strain rate of  $1.5 \times 10^3 / \text{s}$ . The used

specimen had a cylindrical gauge section of length 8mm and diameter 3mm with both ends screwed. However, a new non-contact method was employed to eliminate the possibility of affecting the mechanical test results by temperature measurement. This method (Figure 2.42) consisted in applying a thermocouple to measure the air temperature immediately downstream the specimen [59].

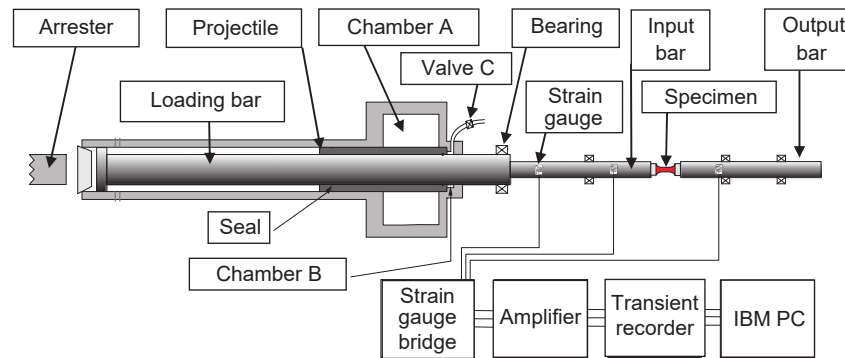


Figure 2.41: Tensile Hopkinson bar

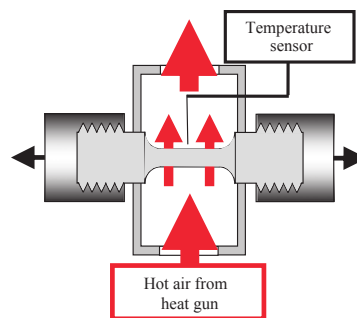


Figure 2.42: Non contact method mounting with heat shield [59]

Curves for quasi-static, medium and high strain rate loadings conditions were obtained (Figure 2.43), based on the specimens used. Lemanski et al. [59] concluded, as it was expected and as it is common for metals, there was a initial linear elastic region, which was followed by a plastic region with initial work hardening, necking and proceeded by tensile failure. Although, for medium and high strain rates, a small stress peak appeared at the beginning of yielding, as observable in the stress-strain curves. Subsequent oscillations were observed and were believed to be possibly caused by the threaded connection between the specimen and the bars. Therefore, the use of specimens with threaded ends should be avoided, to decrease the significant difference between the specimen's and bars' impedance.

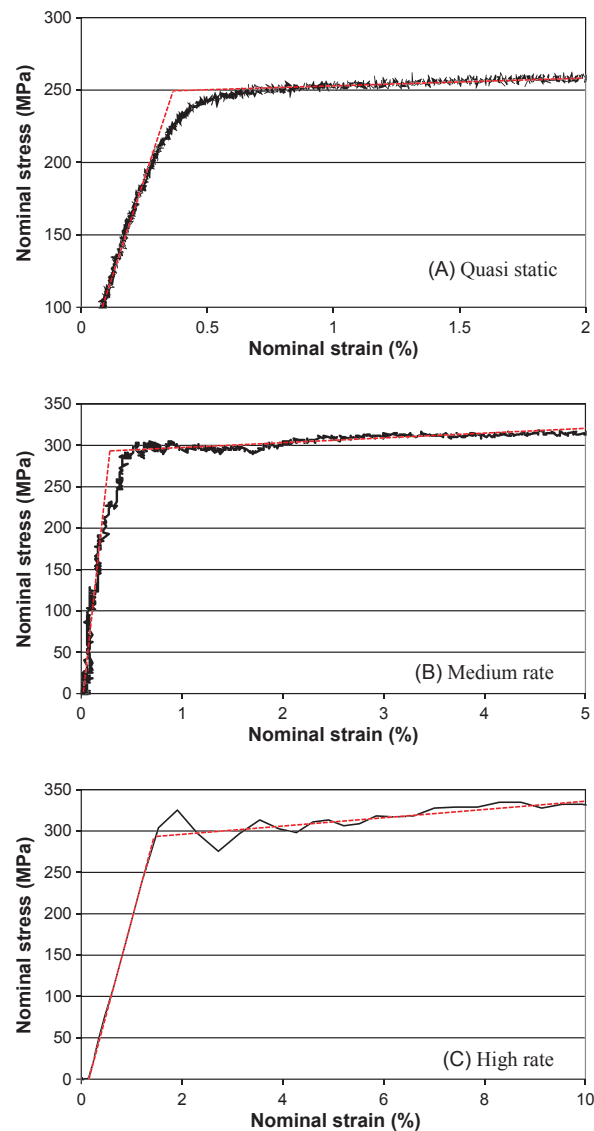


Figure 2.43: Stress-strain curves for quasi-static, medium strain rate and high strain rate tests [59]

As seen by other authors, Ng et al. [60] and Hoge [61], yield strength, peak stress, true failure stress increase with strain rate whereas yield stress and peak stress decrease with temperature, with a weak trend for true failure stress to decrease with temperature.

Additional information on the effect of strain rate, temperature, elongation, deformation mechanisms, damage and failure mechanisms in different alloys can be found in further literature [62]-[75].

### 2.4.3 Friction stir welded joints characterisation

Chao et al. [76] used a SHPB to study the effect of FSW on dynamic properties of AA2024-T3 and AA7085-T7351 alloys. The authors obtained the compressive stress-strain curves. To observe the strain rate effect, quasi-static and dynamic tests were performed using an identical specimen configuration. The high strain rate tests were performed at different strain rates:

800/s and 1200/s for AA2024-T3 and 500/s for AA7075-T7351. For the first alloy, both base and friction stir welded material exhibited yield stress sensitivity to strain rate (Figure 2.44 and Figure 2.46). For the other alloy, base metal had rate dependence. However, for the friction stir welded material, no rate effect was found at strain rate of 500/s (Figure 2.45). Besides, for both alloys FSW was considered to reduce the yield stress under high strain-rate and under quasi-static load conditions. Finally, in both materials, strain hardening was similar at various strain rates.

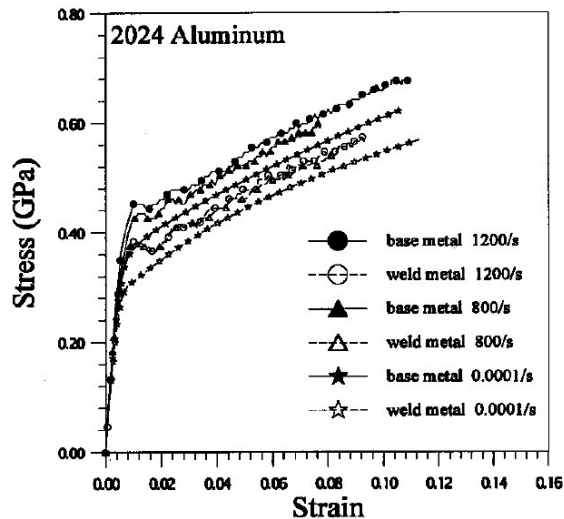


Figure 2.44: Stress-strain curves at three strain rates for AA2024-T3 [76]

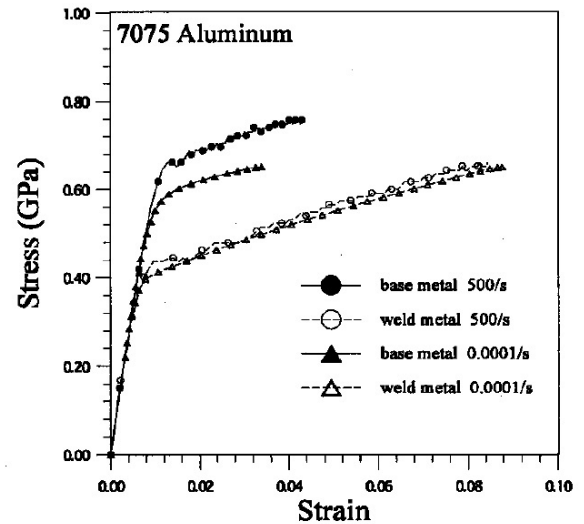


Figure 2.45: Stress-strain curves at two strain rates for AA7075-T7351 [76]

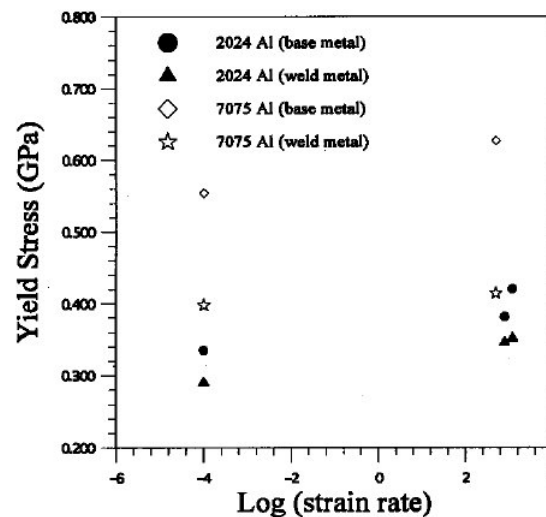


Figure 2.46: Yield stresses vs. strain rate [76]

Another study, performed by Yokoyama and Ogawa [77], with the purpose of investigating the impact tensile properties of AA60601 and SUS 304 stainless steel friction stir welded butt

joints was carried out.. The acquired results showed the effect of the loading rate on the tensile properties varies in function of the friction welding conditions applied. The tensile strength and absorbed energy increased with a rising loading rate. Joints with high tensile strength absorbed lower energy than joints with low tensile strength. The authors concluded the fracture mode and position of the joints depended on friction welding conditions and loading rate.

Yokoyama and Nakai [78] studied the response of AA 7075-T651 alloy and its welds produced by FSW to compressive high strain rates. To perform the tests the authors resorted to SHPB varying strain rate values from  $10^{-3}/s$  to  $10^3/s$ , using cylindrical specimens machined along the thickness direction of base material at room temperature. Yokoyama and Nakai found the compressive flow of the weld nugget was reduced when compared to that of the base material, displaying almost no strain rate effects when close to  $10^3/s$ . In addition, FSW conditions also were responsible of reducing the in-plane transverse tensile strength and elongation at low strain rates.

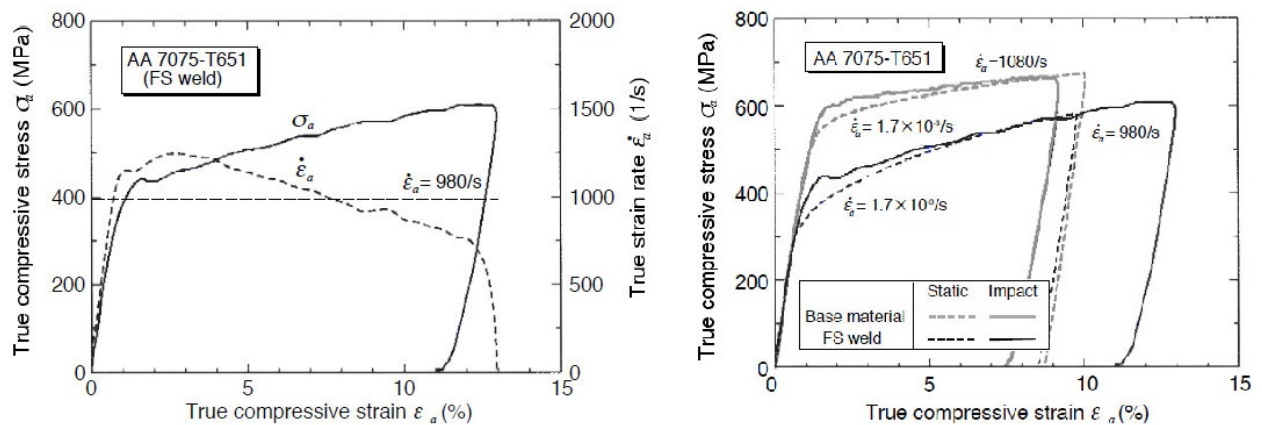


Figure 2.47: Compressive true stress-strain and true strain-rate relation for weld nugget in thickness direction; True compressive strain (%) [78]

Further, Yokoyama et al. [79] conducted a research on the compressive response of friction stir welded AA6061-T6 joints and further, the effect of welding parameters, using a conventional SHPB and cylindrical specimens machined along the thickness direction of friction stir welds, in the butt joint configuration. The obtained results showed there was a significant strain rate sensitivity regarding the weld nugget when strain rates of  $10^3/s$  were applied. After comparing strain-rate dependence between the weld nugget and base material, it was found base material showed a higher strain-rate dependence than that of the weld nugget (Figure 2.48). On the other hand, when comparing the flow stress the inverse happens (Figure 2.49): weld nugget flow stress was lower than that of base material. Furthermore, each friction stir weld had a high strain hardening rate than that of the base material, with no strain rate dependence observed.

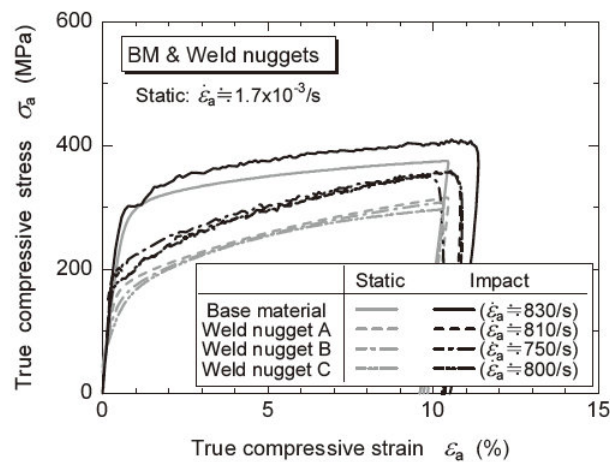


Figure 2.48: True compressive stress-strain curves for base material and different weld nuggets at low and high strain rates [79]

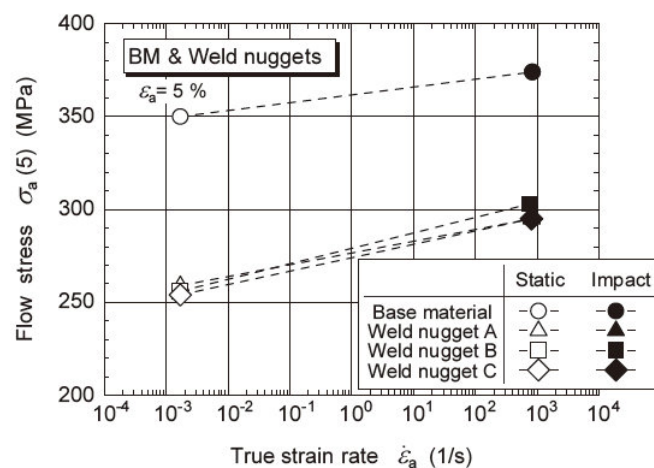


Figure 2.49: Effect of strain rate on flow stress for base material and different weld nuggets [79]

Then, an innovative method using the virtual fields method was applied by Louédec et al. [80] in order to improve data acquisition and to provide a better analysis of materials mechanical properties sparing measurement of the load. The alloy AA 5456 FSW was used in this study. First, Louédec et al. submitted cylindrical specimens to compressive high strain-rate loading using SHPB, then two different methods were used: the grid method and digital image correlation (DIC). Two set ups were used, since SHPB tests using the grid method were performed at the University of Oxford while SHPB test using DIC were performed at the University of South Carolina. Afterwards, the results focused on strain rates of the range of  $10^3$  /s. As the accelerations were at its maximum value and the first images were taken only when the transient stress wave was present, any use of SHPB analysis were dismissed.

The authors pointed the existence of a time shift between the two set-ups due to the different manner how each trigger was actuated. Louédec et al. [80] concluded that the elastic strains resulting of the elastic waves couldn't be seen due to the existence of larger plastic strains presented in the specimen. A strong localisation of strain on the impact side both in welded and homogeneous specimen was observed, noticing there was no uniform contact between it

and the impact bar. However, for welded specimens the cause was assigned to the mechanical properties gradient.

Using the Virtual Fields Method, the results obtained referred to both elastic and plastic parameters, whereas using DIC was not possible to achieve elastic parameters. Elastic parameters results were considered to be promising due to the image quality, since a linear relation between results and image quality was verified. Yet, large dispersion still exists. For identifying plastic parameters, the reference value of Young's modulus and Poisson's ratios were considered. Since all weld's areas didn't suffer the same amount of strain, different numbers of images were used for each slide. To identify the referred parameters, a minimisation process was required. Although, it was important to notice that the starting algorithm of the process had an impact on the parameters to identify. The authors plotted the evolution of the cost function towards the plastic parameters. Knowing cost function was almost insensitive to the variation of hardening modulus, the increase of the number of images could be used to overcome this problem. Since the number of images were limited, the results focused and identified only the yield stress. When slice width results were increased, convergence was restored. The final results are illustrated in the Figure 2.50.

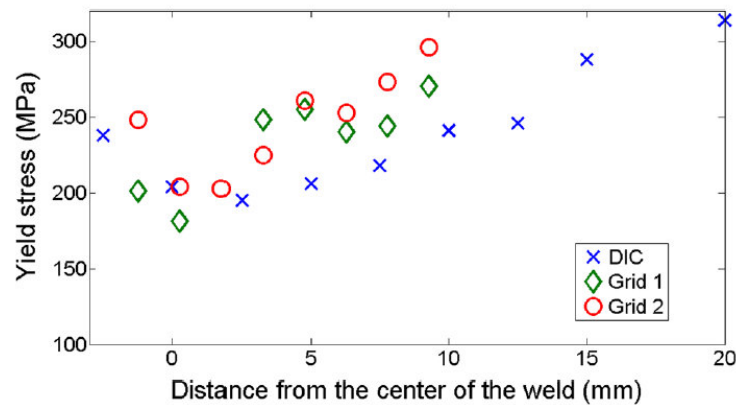


Figure 2.50: Yield stress for the three dynamic tests performed [80]

At the centre of the weld, a significant strain-rate sensitivity was observed from  $83 \mu/s$  to  $0,63 \mu/s$ .

Posteriorly, three-dimensional visualization of the material flow was studied by Morisada et al. [81] using X-ray radiography with success. Strain rate was directly obtained and calculated by the change in the material flow velocity. The results obtained concluded that changing tracer position in the SZ can be used to calculate both strain and strain-rate. In addition, in the flow zone strain rate was very small as a result of almost constant angular velocity. The estimated grain size by the highest strain rate in SZ periphery was smaller than the expected and observed by other techniques, because of the static grain growth during the FSW.



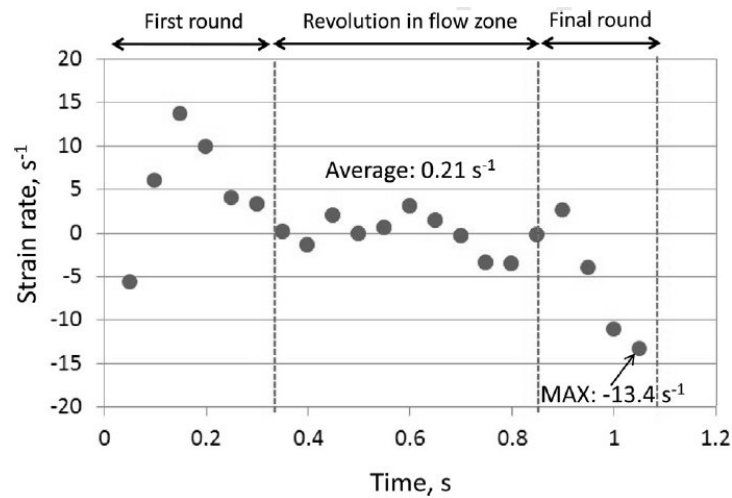


Figure 2.51: Calculated strain rate by varying the tracer position in FSW [81]

Other study of interest towards torsional response of AA7050-T7651 at elevated strain rates was conducted by Mallon et al. [82].

#### 2.4.4 Adhesive bonding characterisation

The impact strength of adhesive bonds was evaluated by Adam and Harris [83], using the block impact test (Figure 2.52). Due to the limitations of the test, the authors had difficulties to set up the specimen. Also, finite element analysis was used to determine the exact position in which the impactor shocks with the specimen. As butt joints have low strengths, low energy absorption was expected in this test. In this configuration, the adhesive is stressed in tension which is its weakest mode. As stated before, better performances are achieved when the configuration of the joint is changed to suffer shear loadings. The authors underline the fact that the impact energy measured was more a function of the geometry and test method, more precisely the rig, than adhesive properties.

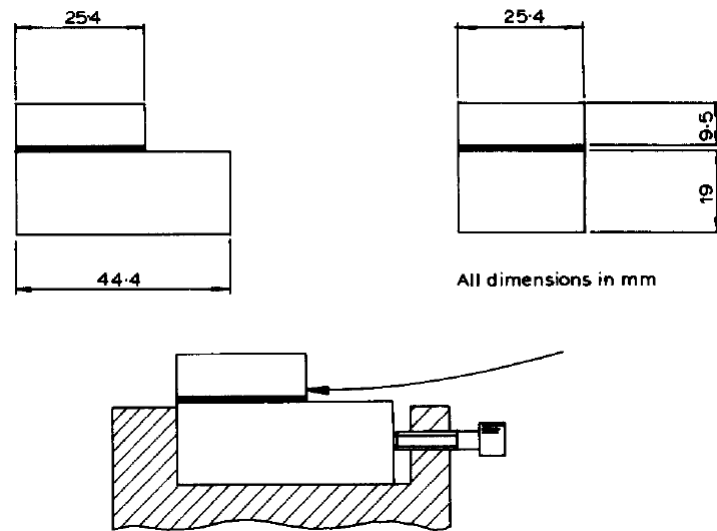


Figure 2.52: ASTM Block Impact Test [83]

Another limitation was the geometry of the test pieces which was nothing approximated to the types of joints used to describe real structures. For the finite element analysis, the authors considered three cases of loading (Figure 2.53). First, uniform loading and then, mode II and II in which specimen misalignment caused extreme loading conditions.

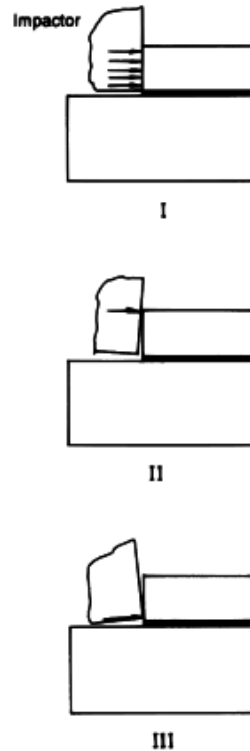


Figure 2.53: Three loading cases for ASTM Block Impact Test [83]

The results showed that for case I shear stress distribution was not uniform, since the de-

formation of struck block caused concentration of shear stress at the adhesive layer loaded end. On the other hand, for case II when the struck block bended substantial normal stresses appeared in the adhesive. The authors also concluded that the deformation of the block is less pronounced for case II than for case I. In addition, case III led to a greater shear stress concentration than case I. Experimentally, four adhesives were tested. The energy absorbed by each of them is showed in Figure 2.54.

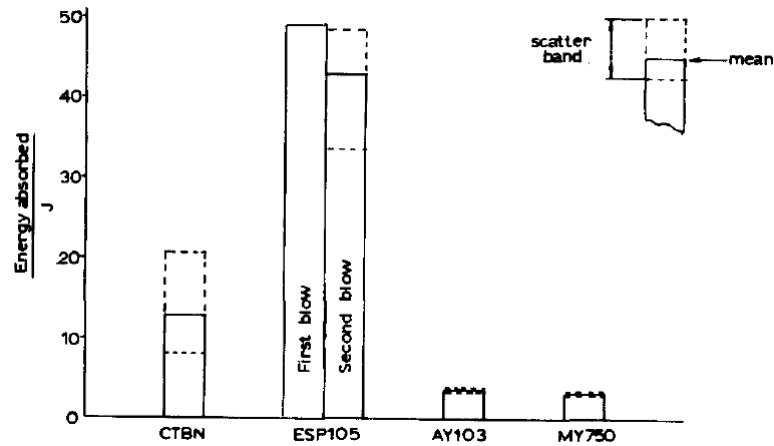


Figure 2.54: Energy absorbed for the tested adhesives in ASTM Block Impact [83]

The energies were plotted as a function of the square width, see Figure 2.55. Therefore, Adam and Harris [83] found that energy absorption was proportional to the square of the failure load. So, energy absorption was found to be a product of the elastic deformation of the test machine. If it was a product of the test piece, the total energy was directly proportional to the specimen width. Comparing numerical and experimental results, numerical results were higher than experimental.

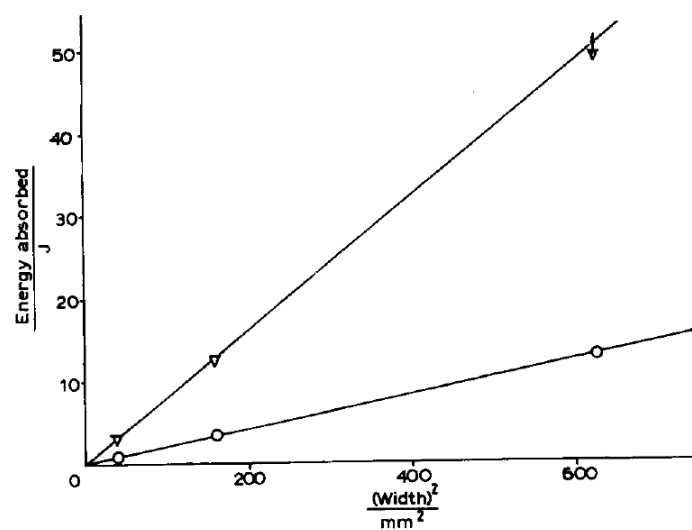


Figure 2.55: Energy absorption variation with the square of the specimen width for different specimens [83]

Martinez et al. [84] investigated the behaviour of several elastic adhesives under impact loads used to bond ceramic and metallic materials, performing compression tests at a strain rate of 1000/s on a SHPB in order to determine the stress-strain curves and, therefore, the transmitting and reflecting impact energy capability. The chosen geometry for specimen was cylindrical, with its thickness varying from 0.5 to 5mm and constant diameter. Elastic adhesives had a based composition of polyurethanes and epoxy. The authors concluded the stress-strain curve was smoother at lower rates while for high rates a slope was observed which was not totally understood (Figure 2.56) and finally, elastic adhesives reflected much more energy than any epoxy adhesive (Figure 2.57), with the larger thickness being responsible for the increase of the reflected energy and stress.

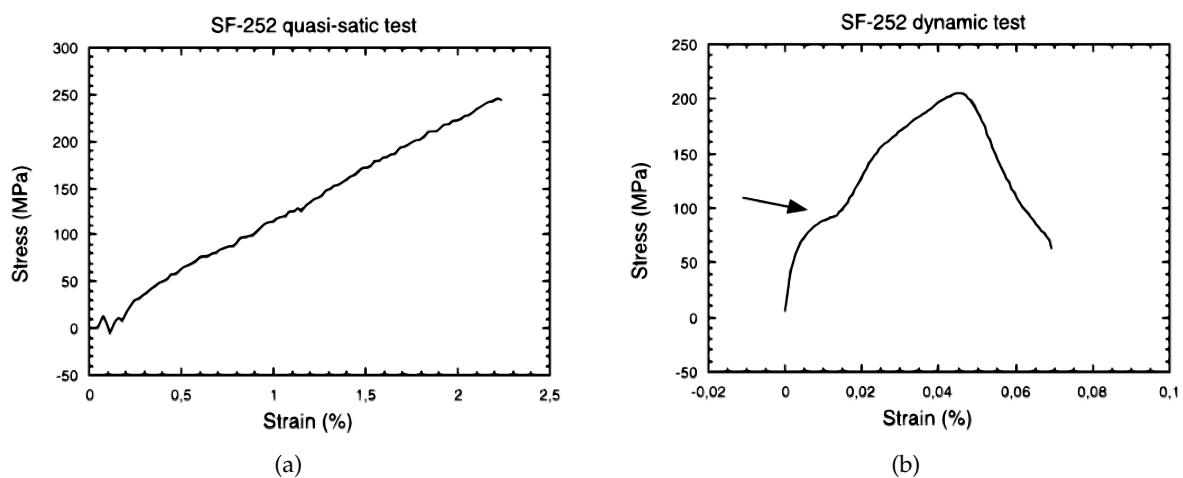


Figure 2.56: Stress-strain curves for quasi-static (a) and high strain rate (b) tests [84]

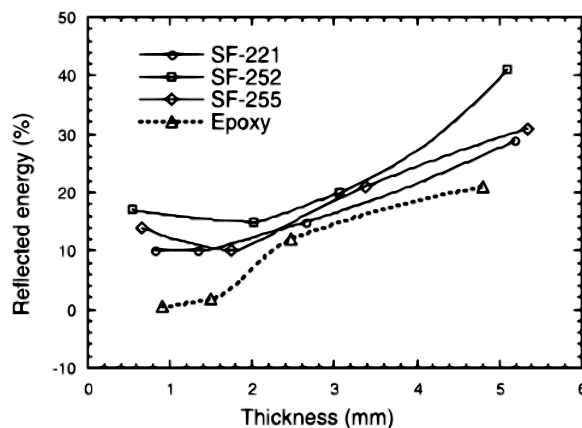


Figure 2.57: Reflected energy vs thickness [84]

Strength of adhesively-bonded butt joints of tubes under combined high rate loading was the subject of study of Sato and Ikegami [85]. The applied adhesive was an epoxy resin and the authors applied combined stress waves of tension and torsion to the specimens on a Hopkinson bar. The experimental set-up of the biaxial bar is exposed on Figure 2.58.

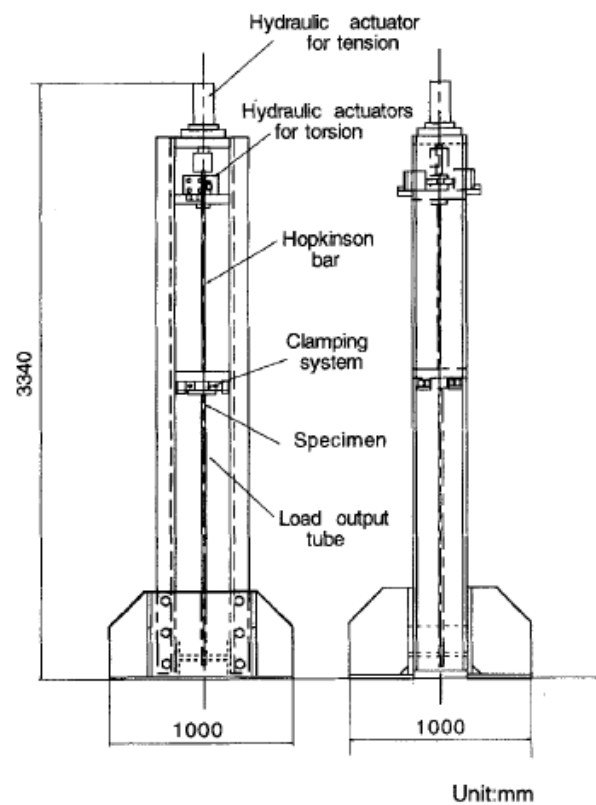


Figure 2.58: Set up of testing machine for combined high rate loading [85]

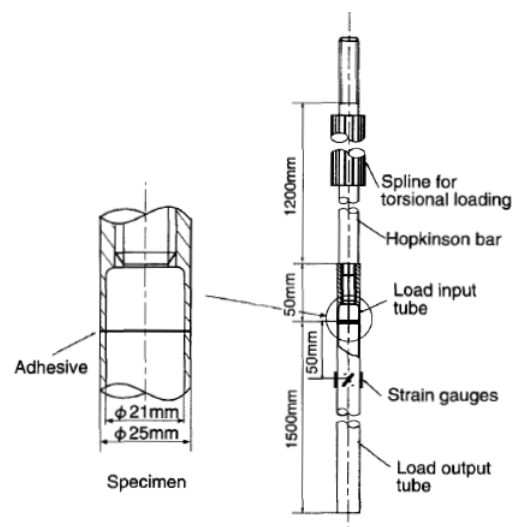


Figure 2.59: Specimen and Hopkinson bar configuration and dimensions [85]

Sato and Ikegami observed the obtained dynamic strength was twice as high as the static strength, under tensile, torsional and all other cases of combined loading (Figure 2.60) and also noticed some cohesive and visually interfacial fractures on the specimen adherend surfaces when dynamic tests were performed. However, cohesive fracture had more distinction in static tests.

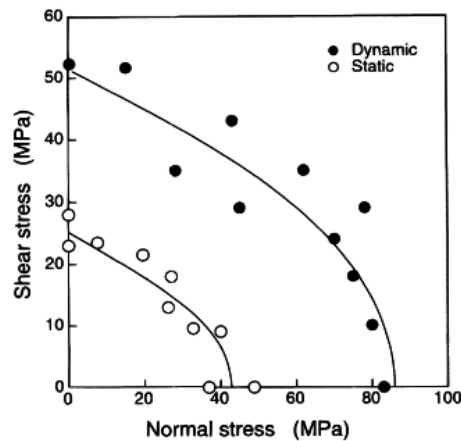


Figure 2.60: Dynamic and static strength joints comparison [85]

Yokoyama [86] determined experimentally the impact tensile properties of adhesive butt joints using a split Hopkinson bar, a cylindrical specimen (Figure 2.61), a single-component cyanoacrylate adhesive and two different adherend materials. To investigate the stress distributions in the adhesive layer an axisymmetric finite element was considered. The main goal was the determination of the effects of loading rate, adherend material and adhesive layer thickness on the tensile strength and energy absorption.

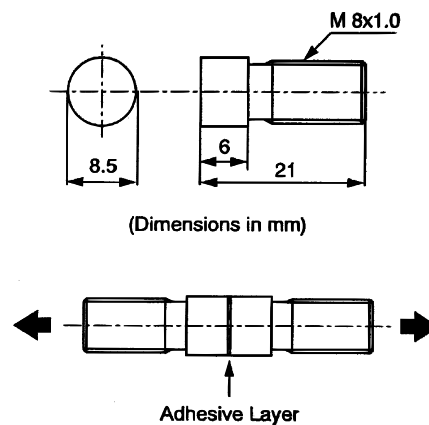


Figure 2.61: Used specimen geometry [86]

As loading rates are limited to  $\dot{\sigma}=10^6$  MPa/s, the used technique can not be applied to non-metallic adherend materials. Through the conducted experimental investigation and the obtained results, it was concluded that increasing loading rate had the effect of increasing significantly the joint tensile strength. AA aluminium alloy adherend had a lower joint tensile strength in comparison to that of the steel adherend and the energy absorption was highly influenced by the adherend materials and loading rate, see Figure 2.62. Plus, regarding only the thickness of the adhesive layer, the authors found 35  $\mu$ m was the optimum thickness for maximum joint tensile strengths at low and high rate of loading.

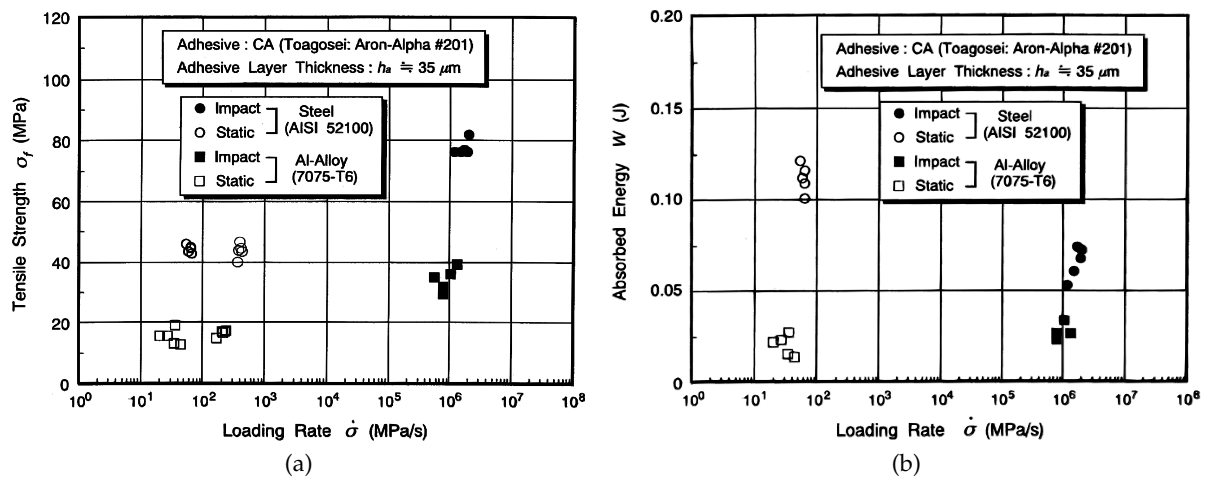


Figure 2.62: Effect of the loading rate on the tensile strength (a) and effect of the loading rate on the absorbed energy (b) [86]

A research on the dynamic mechanical behaviour and the effect of the curing temperatures of an epoxy bi-component adhesive under compressive and tension loading conditions at high strain rates was made by Goglio et al. [1]. A hydraulic universal testing machine and a tensile-compression Hopkinson bar for tests up to  $3 \times 10^3$ /s were used to perform experimental tests. For compression tests, on the SHPB standard configuration cylindrical specimens were used. Meanwhile, for tensile tests cylindrical specimens with threaded ends were used. The considered adhesive was Henkel Loctite Hysol 9466. After obtaining the experimental results, it was concluded that for compressive loading the adhesive presented a ductile behaviour while for tensile loading it presented a brittle behaviour, independently of strain-rate values and curing methods (see Figure 2.63 and Figure 2.64). Nevertheless, the adhesives cured at higher temperatures presented higher strength. It was found adhesives were very sensitive to the strain rate. To conclude, only for compression loading, a limited effect of the strain-rate on the elastic modulus was observed.

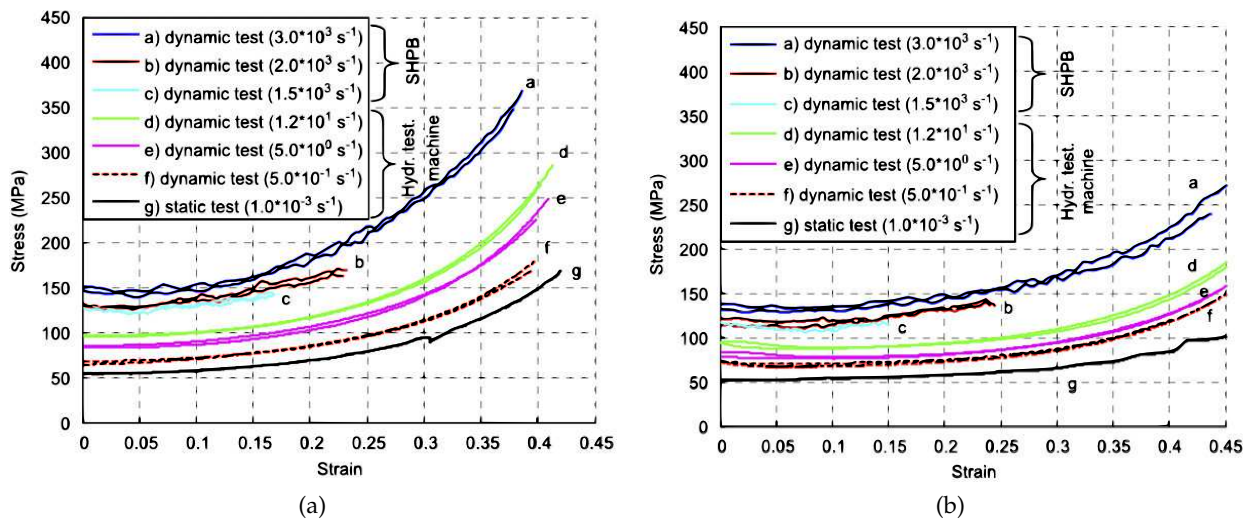


Figure 2.63: Compressive dynamic comparison of stress-strain curves after the elastic range for hot curing (a) and compressive dynamic comparison of stress-strain curves after the elastic range for cold curing (b) [1]

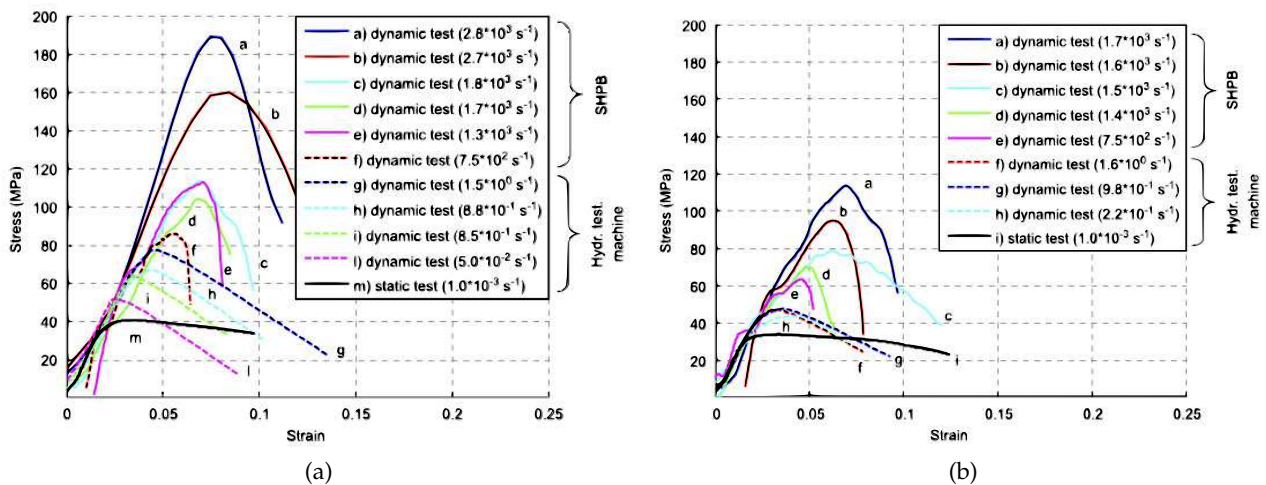


Figure 2.64: Tensile test for hot cured specimens (a) and tensile test for cold cured specimens (b) [1]

The shear strength of adhesively bonded single lap joints were evaluated by Chen and Li [87]. A SHTB was used to test two different velocities ( $20 \text{ m/s}$  and  $7 \text{ m/s}$ ) and temperatures varying from  $-40^\circ\text{C}$  to  $80^\circ\text{C}$ . The lap joints used in this experiment are illustrated in Figure 2.65. The tested adhesive was toughened epoxy adhesive and the bonded surfaces were primarily degreased with acetone before the adhesive application.



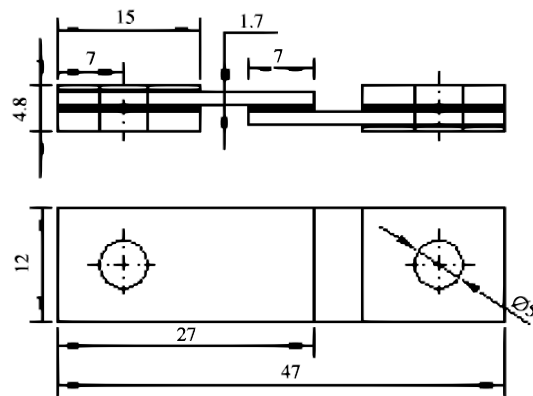


Figure 2.65: Specimen geometry (mm) [87]

The experimental set up had bars with grooves and two holes in vertical direction with the groove surface to allow the specimens fixation through the use of pins, see Figure 2.66.

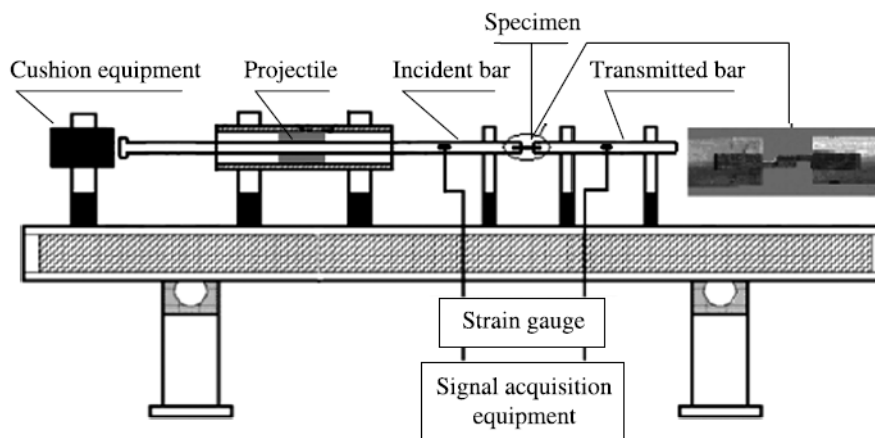


Figure 2.66: Experimental set up and the connection between specimen and bars [87]

The authors found that shear stress had non-linear behaviour up to its maximum value and sustained during certain time until it decreased again (Figure 2.71). The occurred fracture (Figure 2.68) diverged from the expected, since it occurred partially in-adhesive and partially interfacial in nature. However, the in-adhesive failure was the dominant one.

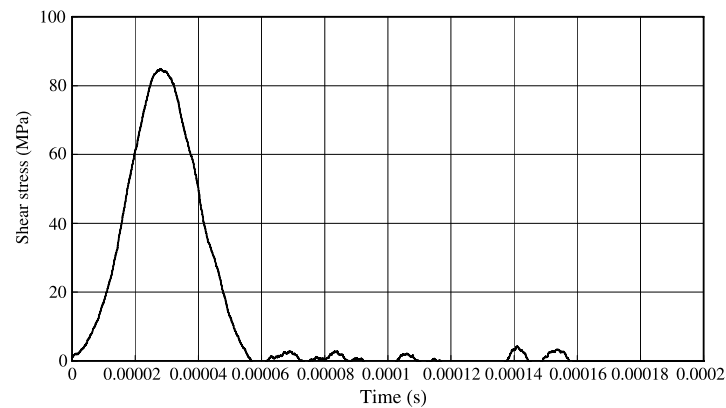


Figure 2.67: Average shear stress-time curve [87]

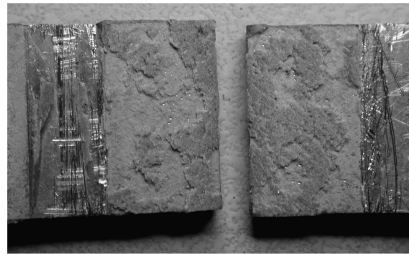


Figure 2.68: Broken specimen [87]

Further, the authors found that for  $-40^{\circ}\text{C}$  the shear strength of the specimen was maximum while for  $80^{\circ}$ , the shear strength decreased. It was also noted that the shear strength of the specimen was higher for higher velocities, see Figure 2.69. Strength degradation was more severe from room temperature to high temperature than that from low temperature to room temperature and it was independent from the loaded velocity, possibly due to the adhesives softening at high temperatures.

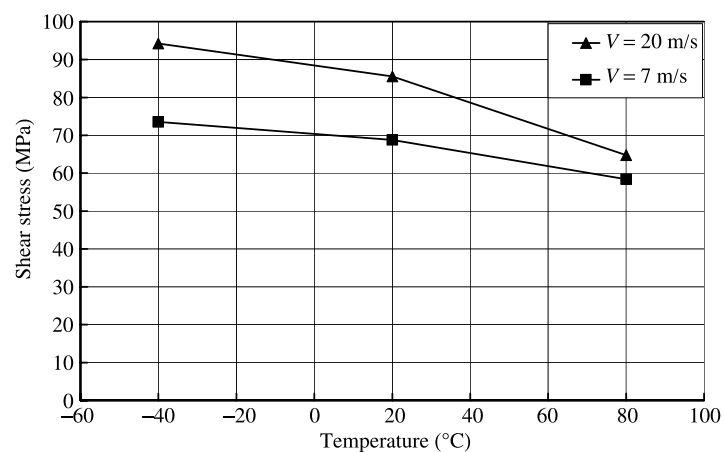


Figure 2.69: Shear stress as a function of temperature and striker's velocity [87]

The pins used to fix the specimen to the bars resulted in oscillations and affected the shear joint strength determination such as thermal and peel stresses.

Challita et. al [88] investigated the shear dynamic behaviour of double-lap adhesively bonded joints on different ranges of strain-rates, using steel substrates bonded by an epoxy adhesive and considering surface treatments like ethanol and sand shooting. The authors found strain-rate increase was responsible for shear strength increase and failure strain decreased until reaching a maximum value before dropping for very high strain-rates. Bonded assemblies were very sensitive to strain rate and sand shooting provided higher strain values than ethanol.

To determinate the dynamic strength of single lap joints using the SHB, Sen et al. [89] subjected identical metallic adherends bonded by a two-part epoxy adhesive at different loading rates, varying overlap length and adherend width, resulting in four different specimens. Next, an elastodynamic model of Sen et al. authorship was put in practice. Hereupon, the authors found only a part of adhesive layer was strained at failure. Also, maximum shear strain in the adhesive decreased when varying the adhesive width layer for a given overlap length, whereas there was an increase of adhesive's total length which was subjected to non-zero strain. An increase of the average strain regarding the entire adhesive layer was obtained, thus. However, when overlap's length was decreased this last condition suffered an alteration. Towards the authors mathematical model, it was only valid after specimen's achieved stress-equilibrium. Observing Figure 2.70, the authors concluded the joint strength increased with loading rate for the four different specimens. Moreover, observing Figure 2.71 it was concluded the shear strength was decreased due to the existence of a larger overlap area. The authors explained such fact happened because of the predictions regarding SHB theory. These predictions only give the shear stress at failure over the entire length of the joint. So, SHB values of the adhesive strength are said to be conservative. Selecting equal diameters for the adherend and bars and maintaining the overlap length as high as possible provide the most conservative values. Such means the stress-equilibrium on both faces of the joint is not affected during the experiment.

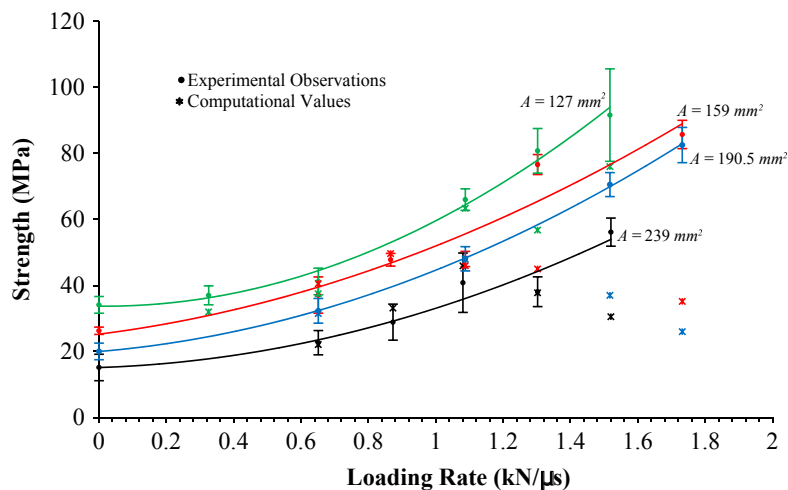


Figure 2.70: Variation of strength in function of loading rate in adhesive joint [89]

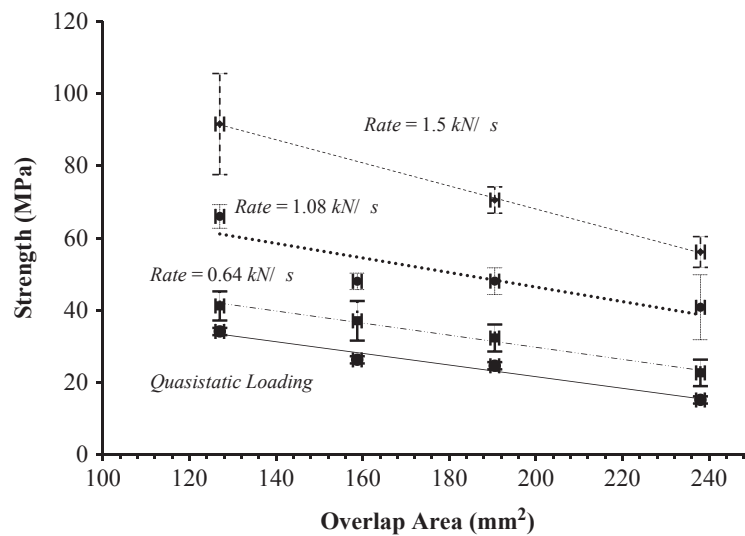


Figure 2.71: Average shear strength variation of the adhesive bonded lap joint with overlap area [89]

Hagou et al. [90] developed a new cohesive element model that can solve problems with an explicit integration time scheme which has its efficiency proven, saving calculation time. To be able to develop this model, experimental tests had to be conducted. For that, split Hopkinson bar was modified, introducing special connectors. Three different specimens with different loading angles ( $0^\circ$ ,  $45^\circ$ ,  $90^\circ$ ) were tested:



Figure 2.72: Tested specimens with different loading angles [90]

The developed model was validated, proving its efficiency and more important, its advantage compared to more accurate models. Due to its simplicity, the model can be adapted and suited to industrial needs.

Using hat-specimens (Figure 2.73) and a modified SHTB (Figure 2.74), Yokoyama and Nakai [91] conducted an experimental investigation in order to determinate the impact tensile strength of structural adhesive butt joints. Therefore, for the adhesion tests two different adherend materials were used (Al 7075-T6 alloy and pure titanium) and a two-part structural adhesive.

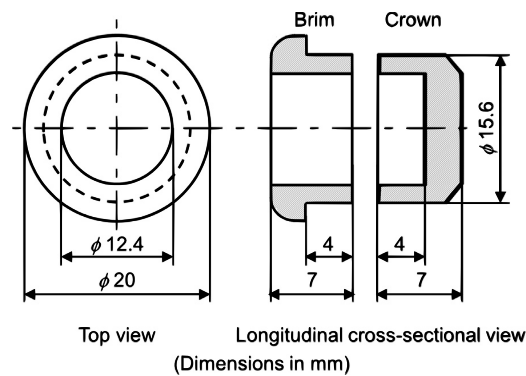


Figure 2.73: Hat-shaped joint specimen [91]

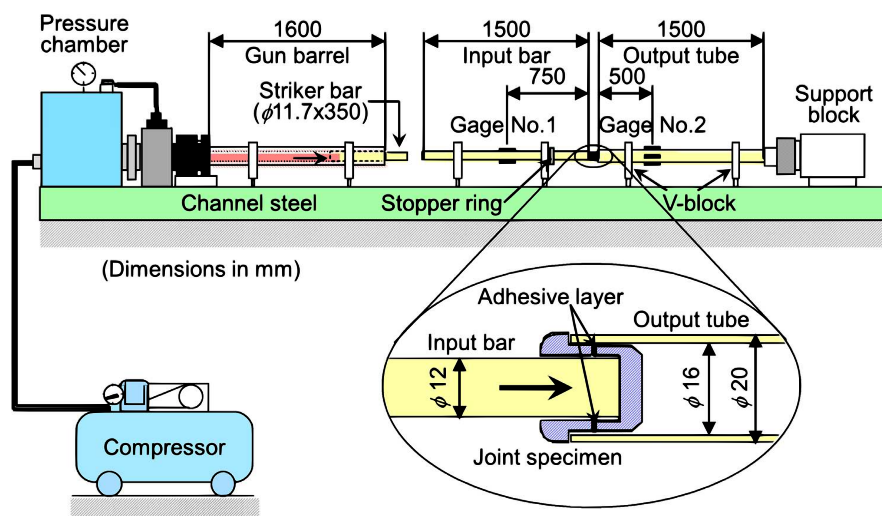


Figure 2.74: Modified SHTB [91]

Yokoyama and Nakai's conclusions were identical to those found on an earlier study [86]. Increasing loading rate led to an increase of the joint tensile strength. On the other hand, increasing adhesive thickness had the same effect on the joint tensile strength. For the Al alloy adherend, higher joint tensile strength was observed in comparison to that for pure titanium adherend for both low and high rates of loading. Furthermore, the inherent strain rate dependence of the epoxy adhesive used was totally responsible for the loading rate dependence of the joint tensile strength. Hat-shaped specimens produced reliable results until adhesive thickness of 200  $\mu\text{m}$ .

Hayashida et al. [92] studied the impact strength of joints bonded with high-strength pressure-sensitive adhesives (PSA). Two types of specimens were used: butt joint specimens and double cantilever beam (DCB), bonded by adhesives. It was found that increasing loading velocity led to a strength increase. Mode I fracture energy was measured on DCB tests. Therefore, a peak around intermediate loading velocity was observed, plus a decrease towards impact loading due to PSA started to become brittle.

An experimental determination of the tensile and shear behaviour of adhesives under impact loading was performed by Neumayer et al. [93], using a new design for SHTB proposed by Gerlach et al. [94] (Figure 2.76), a high-speed camera and DIC (see Section 3.2). Two different specimens with butt joint and lap shear geometry made of two stainless steel adherends

and bonded by an epoxy adhesive were tested, see Figure 2.75.

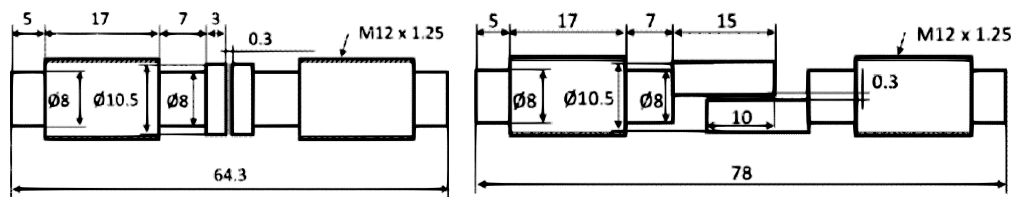


Figure 2.75: Butt joint and lap shear specimen geometry [93]

It was observed adherends had a small influence on the stress-deformation data measured. Energy absorbed showed smaller values while adhesive stiffness showed higher values with the DIC measurement (figure 2.77) for both geometries when compared to SHTB. It was proven DIC involves great accuracy of strain measurement since its use allows a correct measurement of the stress-deformation relation. Also, for both geometries DIC had a great influence on the measurement of deformation signal (Figure 2.80 and 2.81).

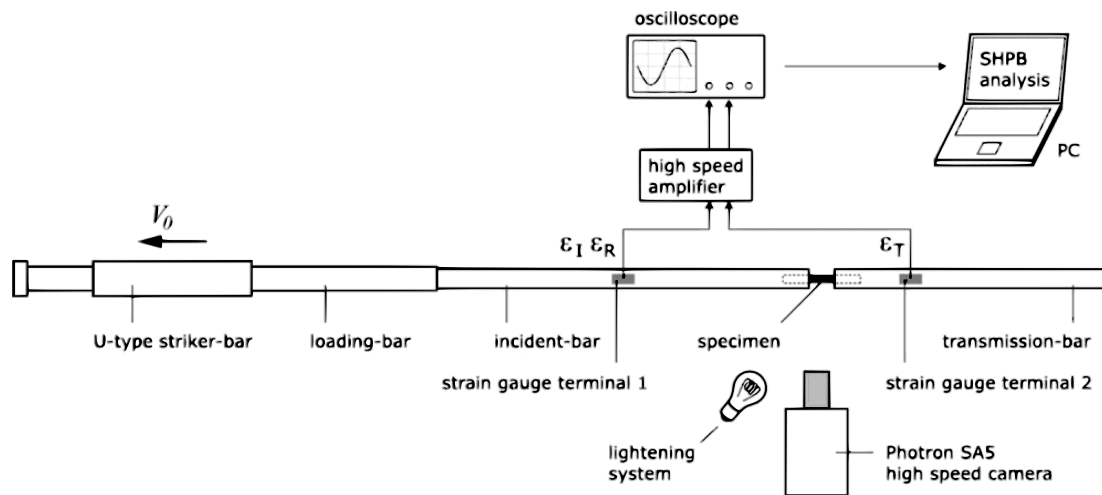


Figure 2.76: Split Hopkinson bar design [93]

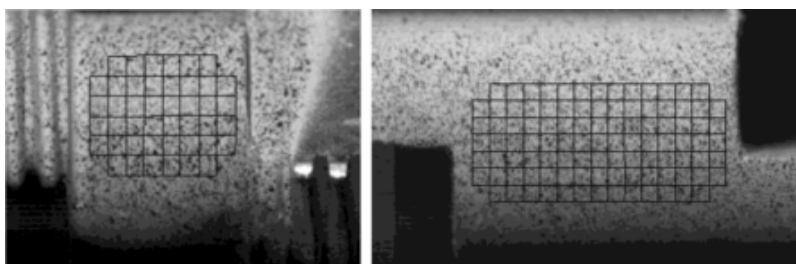


Figure 2.77: Speckle pattern and DIC deformation field on butt joint (left) and lap shear (right) specimens [93]

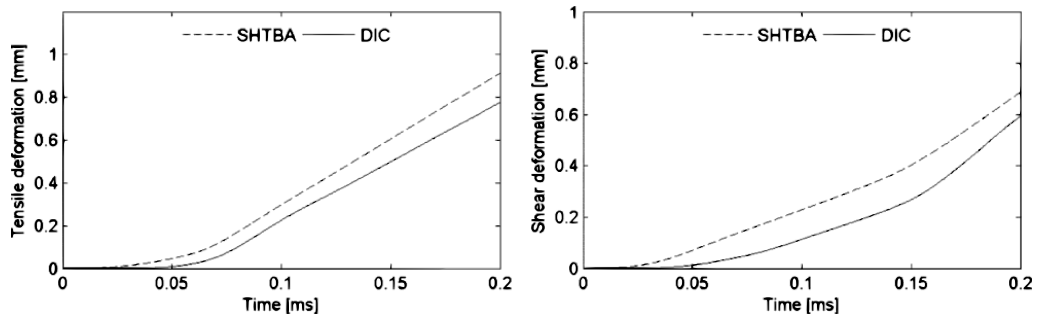


Figure 2.78: Deformation measurement base on SHPB and DIC: butt joint and lap shear test [93]

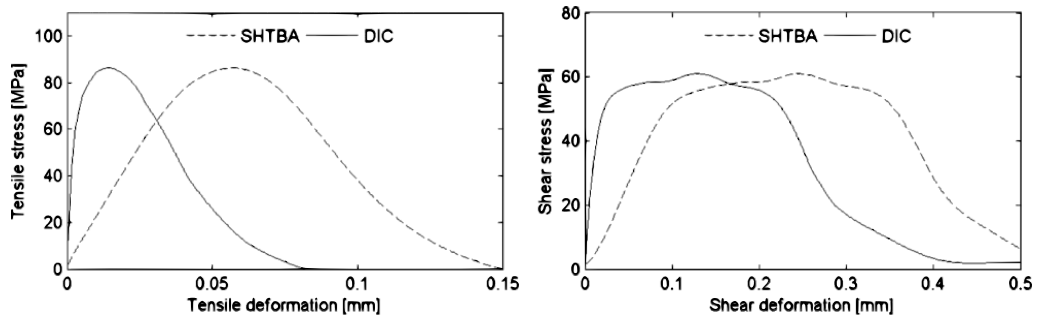


Figure 2.79: Stress-deformation curves according to SHPB and DIC data reduction for butt joint and lap shear tests [93]

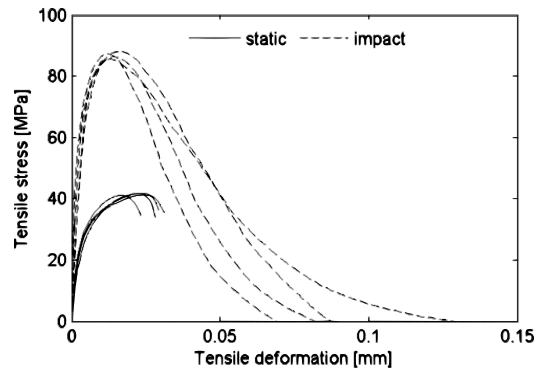


Figure 2.80: Stress-deformation relations in tensile direction [93]

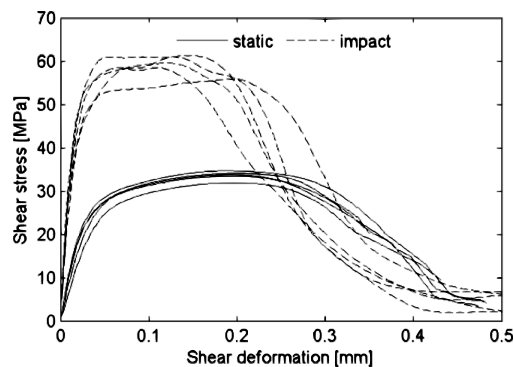


Figure 2.81: Stress-deformation relation in the shear direction [93]

Others researches of interest may be found in [96]-[69].

#### 2.4.5 Weldbonding characterisation

Since there are many types of hybrid joints, several studies [98]-[104] were made in order to understand the differences between each kind of process, so advantages and disadvantages regarding each process could be pointed out.

For instance, Sadowski et al. [98] studied the damage and failure processes of hybrid joints which consisted on adhesive bonded aluminium plates reinforced by rivets. ABAQUS was used to simulate the tensile strength of the respective joint. 3D DIC method was used in the experiments. The specimen used is illustrated in Figure 2.82. The authors found that the hybrid joint was better when compared to only rivet joint or only bonded joint, also had higher tensile strength compared to bonded joint and much more higher when compared to rivet joint. Its energy absorption increased when compared only to the adhesive joint due to the existence of rivets. In addition, higher reliability and durability was observed because of the stiffness effects on the hybrid joint, see Figure 2.83.

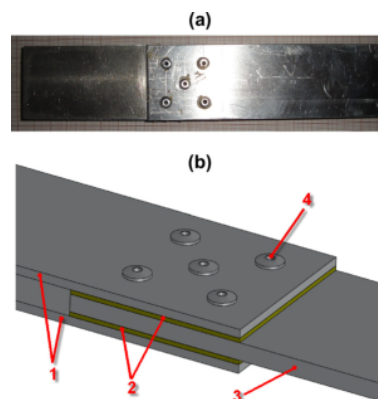


Figure 2.82: Hybrid joint specimen (a) and scheme of the hybrid joint geometry (b) [98]



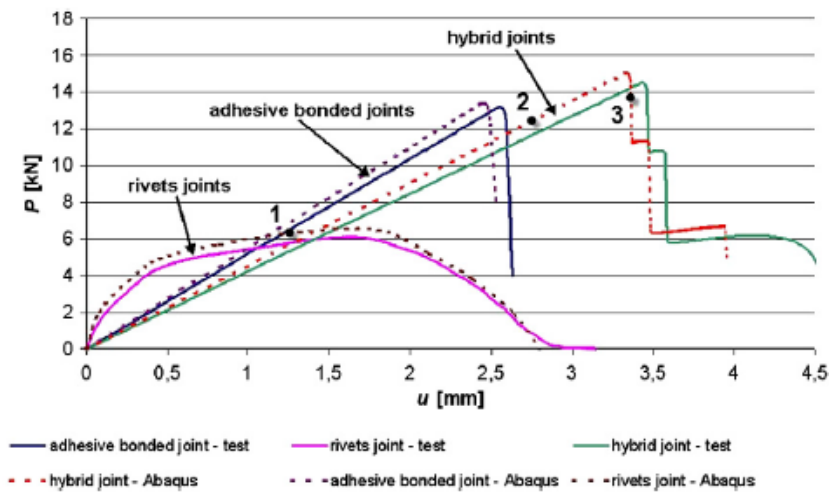


Figure 2.83: Comparison between experimental and numerical results for rivet joints, adhesive bonded joints and hybrid joints [98]

Moroni et al. [100] conducted an experimental analysis in order to compare the strength, stiffness and energy absorption of simple bonded, simple welded and hybrid structural joints. Therefore, it was observed weld bonded joints had increased strength, stiffness, energy absorption compared to simple spot welded joints (Figure 2.84) and lower dependence on temperature and ageing regarding bonded joints. For last, weld bonded joints showed more contribution of adhesive bonding, with improved mechanical properties and so performances when compared to simple fastened joints. However, similar effect of temperature and ageing was observed for both type of joints.

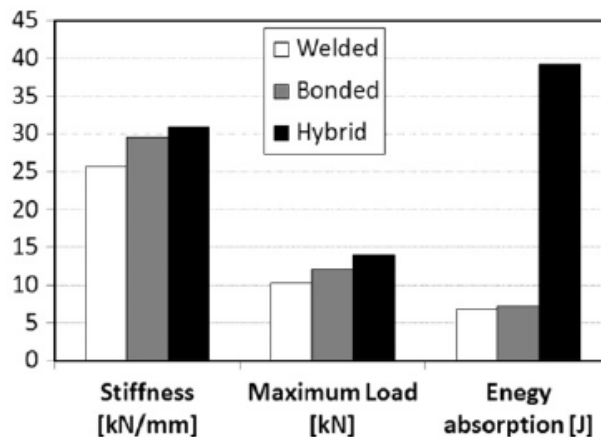


Figure 2.84: Strength, stiffness and energy absorption for homogeneous joints [100]

Meanwhile, other studies [103, 76] compared stress in weld bonded, resistance spot-welded and adhesive-bonded joints. Conclusions revealed that for welded-bonded joints, stress in the lap zone was distributed uniformly, with no high-stress zone observed (Figure 2.85). As referred before, stress concentration can be avoided by using adhesives. Plus, weld-bonded joints when considering the lap zones, basically presented the same characteristics of adhesive-bonded joints, see Figure 2.86. Adhesive bonded joints had the higher fatigue resistance. On

the other hand, fatigue strength of weld bonded joints was greater compared to that of weld spots. However, it was lower when compared to that of the adhesive layer. The big conclusion comes when it was noticed that the presence of adhesives in spot-welded joints was positive while the presence of weld spots in adhesive bonded joints had the opposite effect. It is important to understand at both ends of weld nugget, in case of spot-welded and weld bonded joints, and at the far ends of overlap area, regarding adhesive bonded joints, there are stress concentrations (Figure 2.87 and Figure 2.88) [33]. Another important statement was made [36] towards multiple welds and adhesives of high modulus: weld pitch had no influence on the stress and strain at the edges of the weld spots. Nevertheless, for adhesives with low modulus, stress and strain increased when weld pitch increased too. However, for this case there was a saturation value of weld pitch which was responsible for restraining the stress and strain values.

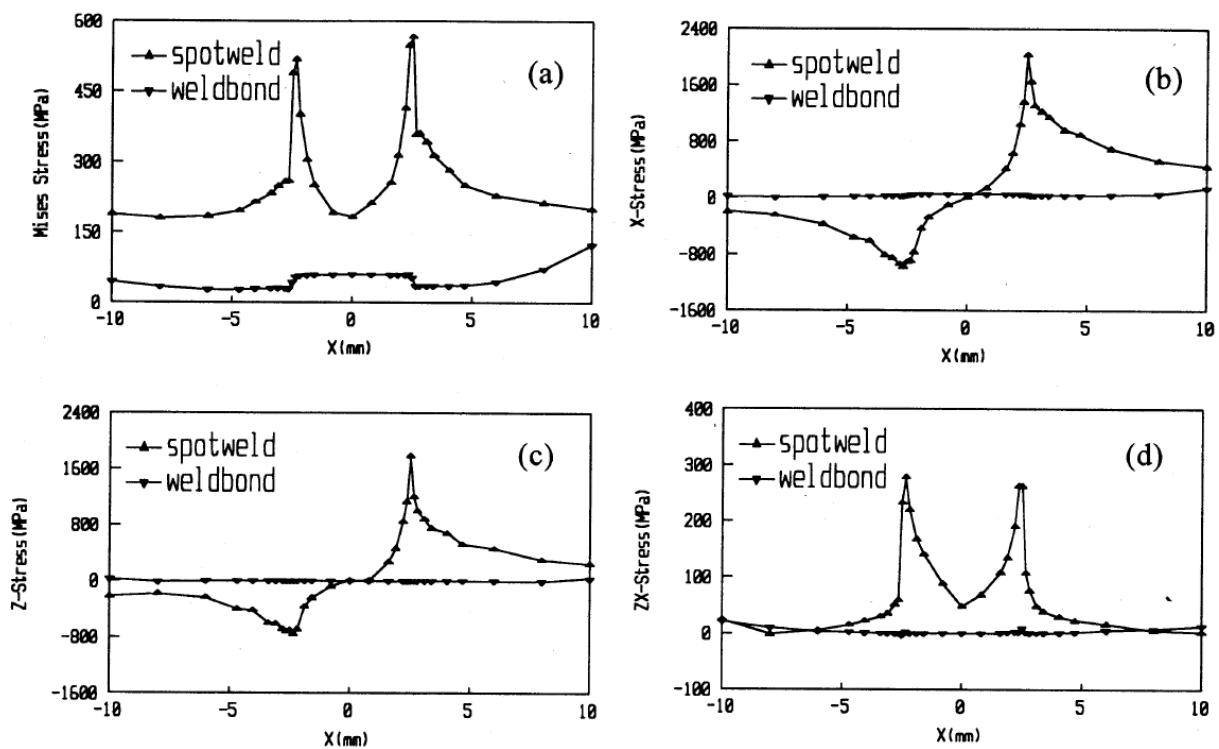


Figure 2.85: Stress distribution in the lap zone for weld bonded and spot welded joints [103]

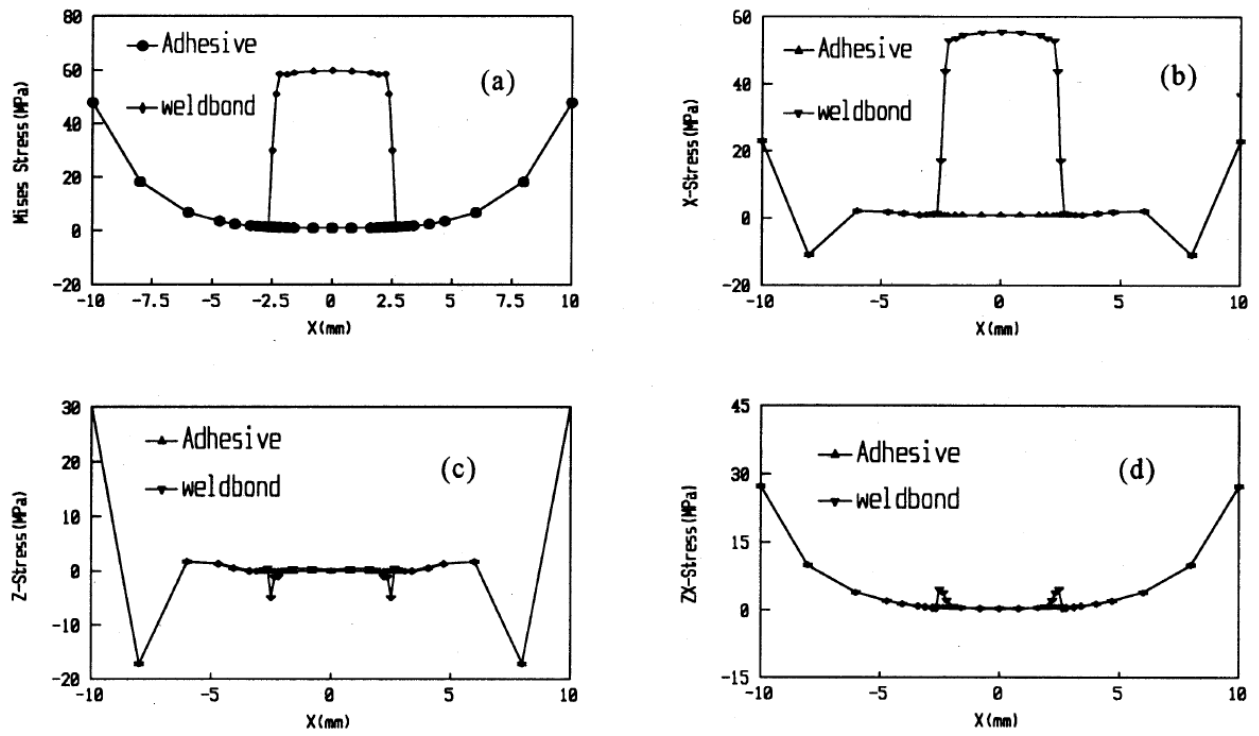


Figure 2.86: Stresses distribution over the lap length for weld bonded and adhesive bonded joints [103]

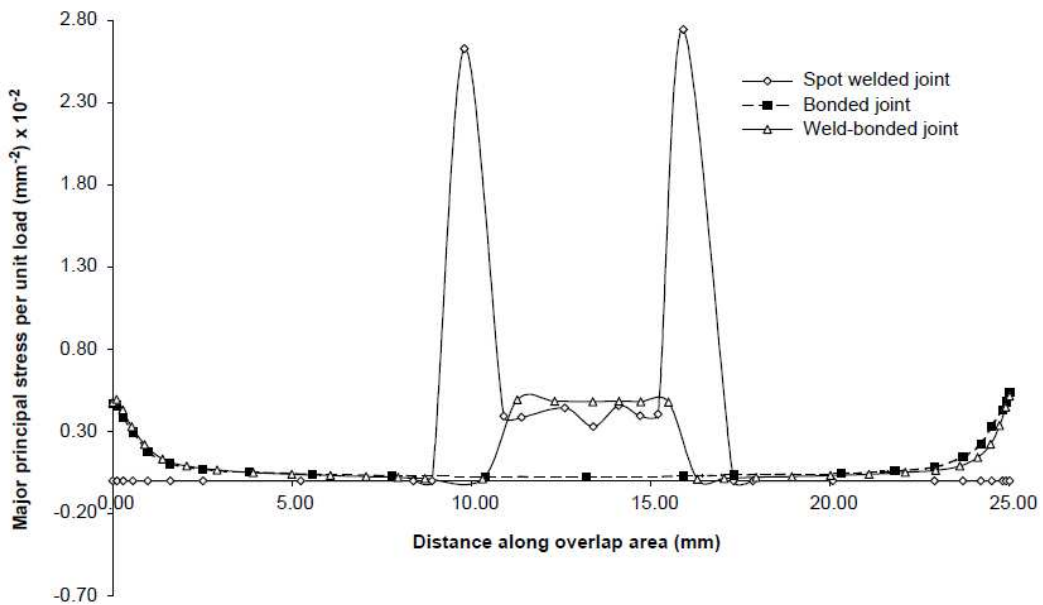


Figure 2.87: Major principal stress distribution for three models [33]

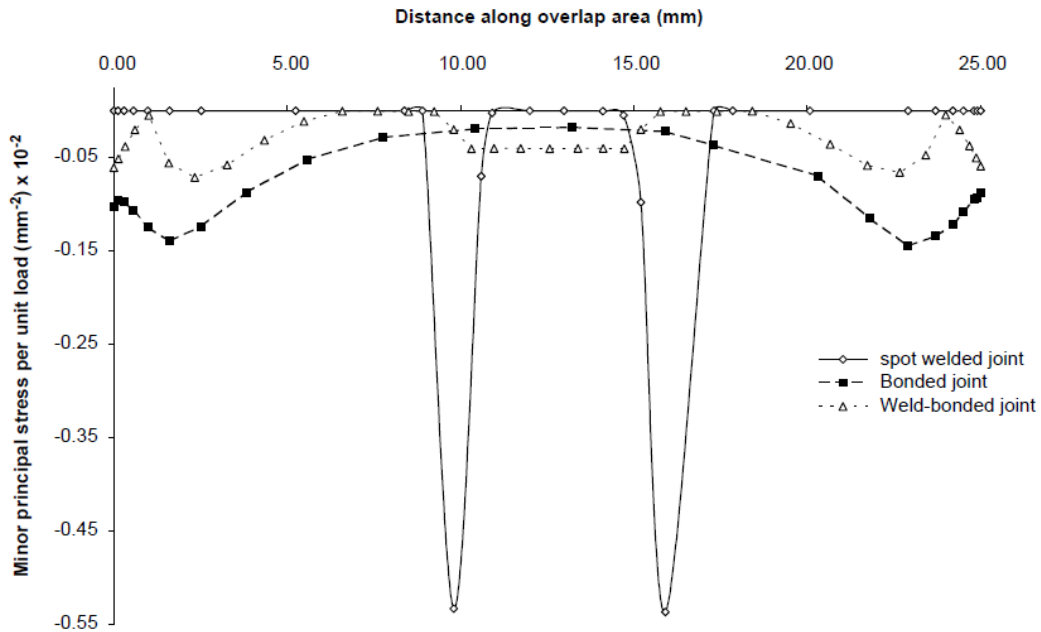


Figure 2.88: Minor principal stress distribution for three models [33]

Darwish [105] performed a study with the aim to characterize weld bonded commercial aluminium sheets and observed they presented higher tensile shear strength than spot welded joints, had higher damping capacity and noted natural frequency was independent on shear strength and on the joining technique (see Figure 2.89, Figure 2.90 and Figure 2.91). Further, Darwish and Al-Samhan [34], when studied the design rationale of weld bonded joints, concluded the strength of weld bonded joints was proportionally dependent on the elastic modulus of adherents and when maximum possible gap thickness was desired, an adhesive with lower Young's modulus should be chosen.

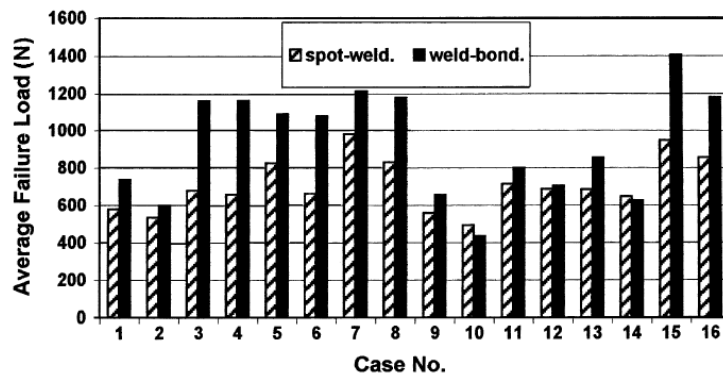


Figure 2.89: Strength comparison between spot welded and weld bonded joints [105]

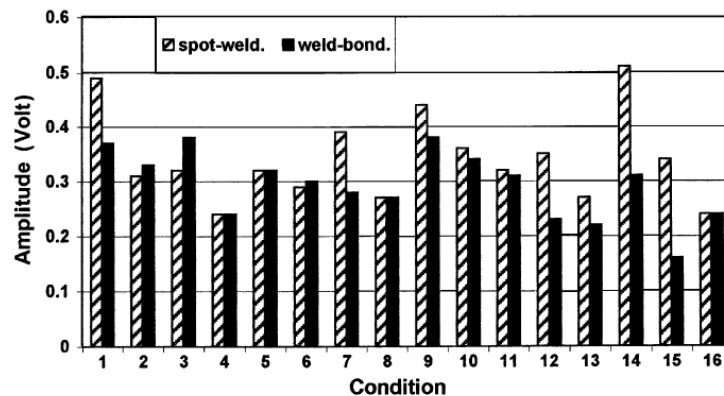


Figure 2.90: Damping capacity of spot welded and weld bonded joints [105]

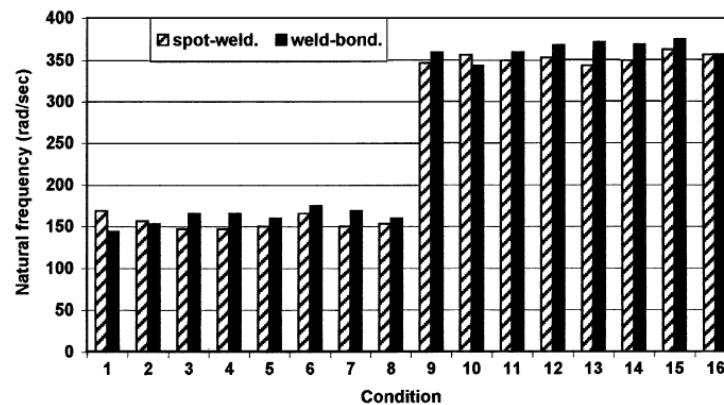


Figure 2.91: Natural frequency of spot welded and weld bonded joints [105]

An experimental investigation of the mechanical behaviour of spot welding-adhesive joints were conducted by Costa et al. [106]. Although, it was stated before hybrid joints presented higher shear strength, degradation and crack of the adhesive was found because of a possible contamination of the nugget. Its microhardness was higher than that of other regions and grain coarsening was found at the weld centre and HAZ, regarding spot welded joints. Thermal effect due to the concentration of high temperatures in a small area caused adhesive decomposition in the spot welding. Further, adhesive thickness had a great importance if good strengths were required.

Braga et. al [5] performed an experimental investigation on aluminium friction stir weld bonded joints in the lap joint configuration, developing a manufacturing process for this hybrid joint. Different types of joints were tested in order to compare the obtained results: adhesive bonding joints, friction stir welded joints and weld bonded joints. Afterwards, a FEM model was created in ABAQUS. The authors concluded that adhesive bonding joints presented higher strength when compared to that of friction stir welded joints, see Figure 2.92. However, hybrid joints presented the same strength of adhesive bonding joints but lower failure displacement. The developed FEM model showed a good correlation for both adhesive bonding and friction stir welded joints rather than hybrid joints, whose failure mechanism was not so well discretized.

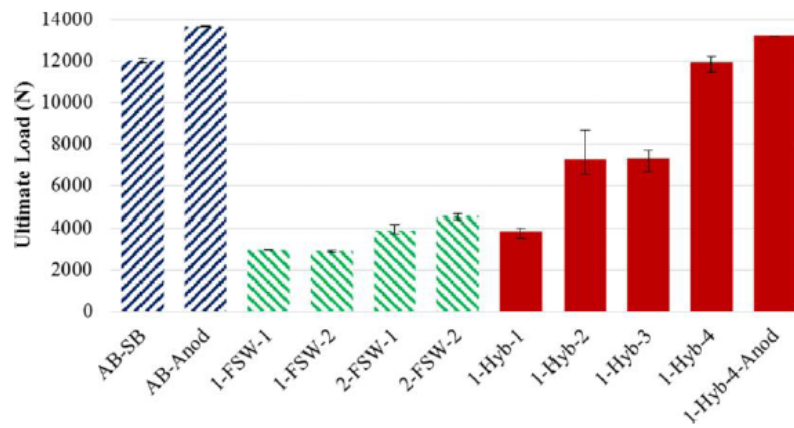


Figure 2.92: Ultimate load for the different types of joints tested [5]

Sun and Khaleel [107] evaluated the dynamic strength for self-piercing rivets and resistance spot welds joining similar and dissimilar metals, using a servo-hydraulic machine and performing test for  $4.47 \text{ m/s}$  and  $8.94 \text{ m/s}$ . The principal conclusions showed that joint strength increased with loading rate increase, with major significance to strength increase from quasi static to  $4.47 \text{ m/s}$ . Increasing loading velocity led to a decrease in displacement to failure and impact velocity was the cause for the brittleness of the joint.

## Chapter 3

# Experimental Methods Fundamentals

### 3.1 The split Hopkinson bar testing

In Sub-subsection 2.4.1.5, it was mentioned that the SHPB apparatus was first introduced by Sir Bertram Hopkinson [43] and posteriorly, modified by Davies [44] and Kolsky [45]. Davies was the first to record electrically the elastic waves propagation using a parallel-plate condenser and an oscilloscope. Although, the commonly known split Hopkinson tensile bar was a product of Kolsky's modifications.

The original split Hopkinson bar was composed by a cylindrical bar of steel suspended ballistically. On one end of the bar was applied a pressure which was then measured. At the other end, a cylindrical pellet was wrung on. Further, Kolsky introduced an apparatus composed by two elastic bars and a detonator. The stress-strain measurement was possible due to the use of two condensers and amplifier [45]. The classic SHB is constituted by three bars: the striker, the incident and the transmitted bar. These three bars are made of the same material, have the same diameter and must be sufficiently long to provide an interference-free propagation of the waves and to allow the stress-strain data record. The bars should be axially aligned, permitting free movements along the test direction. In addition, bearings with minimal friction between them and alignments fixtures should be employed. For compression tests, the striker bar has to hit the incident bar while for direct tensile tests a hollow striker is used, which hits the anvil at the end of the incident bar (Figure 2.18). The impact is achieved through a gas gun which will fire the striker in the intended direction, considering the test. In order to measure strain pulses, strain gauges on Wheatstone-bridge circuit are mounted on the incident and transmitted bar with an adequate distance towards the specimen-bar interface. To record the striker impact and the strain wave signals a data acquisition system is needed [37, 108].

High structural metals, such as AISI-SAE 4340 steel, maraging steel or Inconel are used to construct the bars. The bars must remain elastic so the selected material yield strength limits the maximum striker's velocity and therefore, the stress attainable in the deforming specimen (as will be seen in Subsection 3.1.2) [37]

For the direct tensile set up, the striker bar impacts the incident bar on its anvil and a longitudinal compression stress wave is created. This compression stress wave is transformed into a tensile stress wave because of the previous reflection on the anvil. This tensile stress wave is called the incident wave,  $\varepsilon_I$  whose shape is nearly rectangular and it is measured by the incident bar strain gauge. This wave arrives at the incident bar-specimen interface and part is reflected back as compression stress wave, due to the differences in cross sectional area and

respectively, mechanical impedances (see Sub-subsection 3.1.1.2). The reflected part of the incident wave is known as the reflected wave,  $\varepsilon_R$  and it is also measured by the incident bar strain gauge. The other remaining part of the tensile stress wave is transmitted to the specimen, causing a complex reverberation on the specimen until it achieves dynamic equilibrium [108]. The tensile wave transmitted through the specimen- transmitted bar interface is called transmitted wave,  $\varepsilon_T$ . It is measured by the strain gauge on the transmitted bar.

The measured strain waves can be used to calculate the dynamical response of the specimen, as will be further discussed in Sub-subsection 3.1.1.3.

### 3.1.1 The split Hopkinson pressure bar analysis

#### Conditions

Conditions must be strictly followed in order to determine the dynamic stress-strain behaviour of the specimen by applying the 1D propagation theory. The 1D propagation theory can only be enforced when the following conditions are fulfilled [108, 109]:

1. The striker, incident and transmitted bar are made of homogeneous and isotropic material.
2. The bars cross-section is uniform over their entire length. The bars must be perfectly aligned along the centre axis.
3. The striker bar and the bar material mechanical properties influence the striker velocity. Thus, the striker's velocity must be determined to maintain all the three bars in the elastic domain (see Subsection 3.1.2). Therefore, the incident wave causes a deformation strictly linear-elastic.
4. As the axial strain distribution is constant over the bars entire diameter, the measured strains of the surface are merely representative of the strains within the bars. To satisfy and accomplish this condition, bar-length/bar-diameter ratio should be greater than 20:

$$\frac{l_b}{d_b} > 20 \quad (3.1)$$

where  $l_b$  is the length of the bar and  $d_b$  is the diameter of the bar.

5. Bars with finite diameter are not considered to be dispersion free. However, to minimise this effect, a pulse duration ( $T$ ) (defined by Equation 3.2) 10 times larger than the transit time ( $t_t$ ) (defined by Equation 3.3) of the longitudinal wave across the bar diameter must be selected:

$$T = \frac{2l_{striker}}{c_0} \quad (3.2)$$

$$t_t = \frac{d_b}{c_0} \quad (3.3)$$

where  $l_{striker}$  is the length of the striker. With the dispersion effect minimised, the three waves measured at the strain gauges are in fact the same three waves that act on the specimen. In addition, the incident wave maintains its shape when it arrives at the incident bar-specimen interface after being measured at the incident gauge. The reflected and transmitted waves measured at the strain gauges placed in the incident and transmitted bar, also maintain their shape after their creation at the specimen-transmitted bar interface.



6. Both interfaces, the incident bar-specimen and specimen-transmitted bar interfaces, must remain plane all time. This assumption is only valid when the mechanical impedance of the specimen is lower than the mechanical impedance of the bars. If the specimen has a cylindrical shape, this assumption is only satisfied if the specimen diameter is lightly lower or equal than the bars diameter.
7. The wave velocity of the specimen material,  $c_s$ , influences its dynamic stress equilibrium which occurs after an initial “ringing-up” period (see Subsection 3.1.2).
8. Friction and inertia effects in the specimen need to be minimised with the application of Molybdenum-Disulphide,  $MoS_2$ .
9. The specimen material, follows the incompressibility condition presented in Equation 3.4, since it needs to be incompressible [108, 37].

$$A_s(t)l_s(t) = A_{s0}l_{s0} \quad (3.4)$$

### 3.1.1.1 Wave propagation in cylindrical bars

The 1-wave propagation theory is used since its application allows simplifications when compared to the 2- and the 3-wave propagation theories.

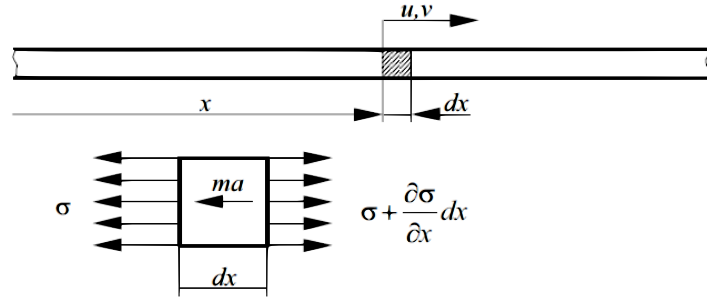


Figure 3.1: Pressure bar differential element [110]

Observing the Figure 3.1,  $x$  represents the coordinate of the bars transversal section position and  $u$  represents the displacement of that section. Applying Newton's second law to the  $dx$  element:

$$\sigma A + \left(\sigma + \frac{\partial \sigma}{\partial x} dx\right) A = \rho A dx \frac{\partial^2 u}{\partial t^2} \quad (3.5)$$

The area doesn't vary along the cross section of the bar. Assuming an elastic behaviour of the material, the Hooke's law for an uniaxial tensile state can be applied:

$$\sigma = E \varepsilon = E \frac{\partial u}{\partial x} \quad (3.6)$$

Replacing Equation 3.6 in Equation 3.5:

$$\frac{\partial^2 u}{\partial t^2} = \frac{E}{\rho} \frac{\partial^2 u}{\partial x^2} \text{ or } \frac{\partial^2 u}{\partial t^2} = c_0^2 \frac{\partial^2 u}{\partial x^2} \text{ with } c_0 = \sqrt{\frac{E}{\rho}} \quad (3.7)$$

with  $c_0$  defining the wave velocity propagation in unidirectional environments.

However, the solution of Equation 3.7 can be rewritten using the D'Alembert solution for the wave propagation equation:

$$u(x, t) = F(x - c_0t) + G(x + c_0t) \quad (3.8)$$

where  $F$  and  $G$  are non harmonic functions and propagate in opposite ways in  $x$  direction, with  $c_0$  velocity. These functions also describe the pulse shape and their shape is constant over time.

If a pulse with  $F$  amplitude propagates along the positive direction of a bar with infinite dimensions, the displacement  $u$  is given by:

$$u(x, t) = F(x - c_0t) \quad (3.9)$$

Therefore, the particulates' velocity can be described:

$$v(x, t) = \frac{\partial u(x, t)}{\partial t} = -c_0 F'(x - c_0t) \quad (3.10)$$

And its strain:

$$\varepsilon(x, t) = \frac{\partial u(x, t)}{\partial x} = F'(x - c_0t) \quad (3.11)$$

Replacing Equation 3.10 in Equation 3.11:

$$\varepsilon(x, t) = \frac{-v(x, t)}{c_0} \text{ or } \varepsilon = -\frac{v_p}{c_0} \quad (3.12)$$

being  $v_p$  the particulates' velocity. Considering an uniaxial state of stress and Equation 3.6 and Equation 3.7:

$$\sigma = -\rho c_0 v_p \quad (3.13)$$

The temporal evolution of stresses and strains regarding the particles' velocity and the material properties are described by the previous equations (Equation 3.12 and Equation 3.13).

In SHPB, the shock between the striker and the incident bar generates an impulsive force. Since it is important to relate the particulates' velocity with striker's velocity, that relation is obtained through the conservation of movement's quantity. Its values before and after the shock can be calculated by:

$$Q_{striker} = mv_{striker} = A_0 l_{striker} \rho v_{striker} \quad (3.14)$$

and

$$Q_p = mv_p = 2A_b l_{striker} \rho v_p \quad (3.15)$$

where  $Q_{striker}$  is the striker movement's quantity and  $Q_p$ , is the particulates movement's quantity. Thus, by matching the second members of the Equation 3.14 and the Equation 3.15:

$$v_p = \frac{v_{striker}}{2} \quad (3.16)$$

Hereupon, it is concluded the particulates' velocity is determined by the striker's velocity and it is always half of the latter. The shock between a moving and resting bar results in a pulse whose propagation velocity is constant and represents the propagation velocity in the continuous environments that constitutes the bars.

The impact velocity also has an important role over stresses and their amplitude. As explained before, stress and strain are obtained in the bar through the pulse action. Combining Equation 3.12 and Equation 3.13 with Equation 3.16, it is obtained:

$$\sigma_b = -\rho c_0 \frac{v_{striker}}{2} \quad \varepsilon_b = -\frac{v_{striker}}{2c_0} \quad (3.17)$$

The axial force in any bar section where a elastic deformation wave is passing can be determined by applying Hooke's law [111]:

$$\sigma = E\varepsilon \Leftrightarrow \frac{N}{A} = E\varepsilon \Leftrightarrow N = AE\varepsilon \quad (3.18)$$

The length of the measured pulse over the bar, in a system of position vs strain axis, is given by [110]:

$$A = 2l_{striker} \quad (3.19)$$

### 3.1.1.2 Mechanical Impedance

The mechanical properties of the material which the bar is made influence directly the way the bar responds when it is subjected to an elastic wave. This elastic wave carries elastic strain energy and kinetic energy due to the particles mass movement.

On one hand, the particulates' mass which moves on a determined instant of time it is proportionally related with the area and density of the material. On the other hand, the force is related with the Young's modulus.

When an incident pulse reaches a section with different mechanical impedances, a reflection and transmission will emerge, as explained previously in Section 3.1. The Equation 3.20 defines the intrinsic impedance of a material,  $Z_0$ :

$$Z_0 = \rho c_0 \quad (3.20)$$

where  $\rho$  defines the volumetric mass density of a material, while  $c_0$  defines the propagation velocity.

Thereby, the mechanical impedance of a bar is defined as the ratio between the force acting on the section and the velocity of the particulates' mass. The Equation 3.21 defines the mechanical impedance as a function of the wave velocity propagation,  $c_0$ , and the cross section area,  $A$  [111, 110, 108].

$$Z = A\rho c_0 \quad (3.21)$$

### Change in cross sectional area and impedance variation

The Figure 3.2 illustrates the wave propagation at the interface of two united bars with different cross section areas and mechanical properties.

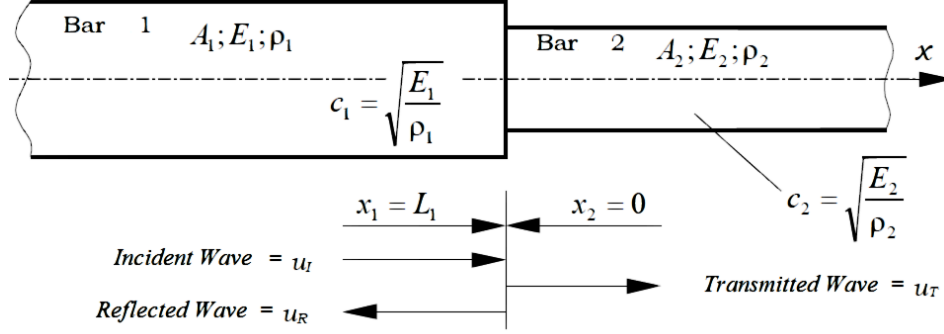


Figura 3.2: Wave propagation between two different bars [110]

The bars are characterized by their area, volumetric mass density and Young's modulus which permit the determination of the impedance of each bar. As can be seen in Figure 3.2,  $c_1$  represents the wave propagation in bar 1, while  $c_2$  represents the wave propagation in bar 2. The equilibrium and compatibility conditions must be verified in all the bar sections during the wave propagation. These conditions, at the interface of the two bars, impose equal force and displacement [110]:

$$N_1 = N_2 \Leftrightarrow N_I + N_R = N_T \quad (3.22)$$

$$u_1 = u_2 \Leftrightarrow u_I + u_R = u_T \quad (3.23)$$

Using Equation 3.24:

$$\sigma = \frac{N}{A} \quad (3.24)$$

The Equation 3.22 can be developed into Equation 3.25:

$$A_1(\sigma_R + \sigma_I) = A_2\sigma_T, \quad (3.25)$$

Thus, the stress ratios between transmitted-incident wave and reflected-incident wave are determined by matching the equation (3.25) and the equation (3.13) [108]:

$$\frac{\sigma_T}{\sigma_I} = \frac{2A_1\rho_2c_2}{A_1\rho_1c_1 + A_2\rho_2c_2} \quad (3.26)$$

$$\frac{\sigma_R}{\sigma_I} = \frac{A_2\rho_2c_2 - A_1\rho_1c_1}{A_2\rho_2c_2 + A_1\rho_1c_1} \quad (3.27)$$

The equations of stress ratios are functions of the mechanical impedance (defined by Equation 3.21), since a change in the cross section area is considered. The transmission coefficient,  $\alpha$ , is described by:

$$\alpha = \frac{2A_1\rho_2c_2}{A_1\rho_1c_1 + A_2\rho_2c_2} \quad (3.28)$$

And the reflection coefficient,  $\beta$  [112]:

$$\beta = 1 - \alpha \quad (3.29)$$

Despite providing a good understanding of the differences between mechanical impedances, the Equation 3.26 and the Equation 3.27 have limitations. The bars remain in the elastic domain, since they are deformed elastically while the specimen is deformed plastically [108].

### 3.1.1.3 Incident, reflected and transmitted pulse under the specimen in stresses and strains calculus

As seen and demonstrated in Subsection 3.1.1.2, whenever a change in impedance occurs a reflection and transmission will occur. The impedance characteristics influence directly the ratio between reflected and transmitted pulses. This phenomena is observed when the incident wave reaches the specimen, causing the reflection and transmission of the pulse (see Figure 3.3).

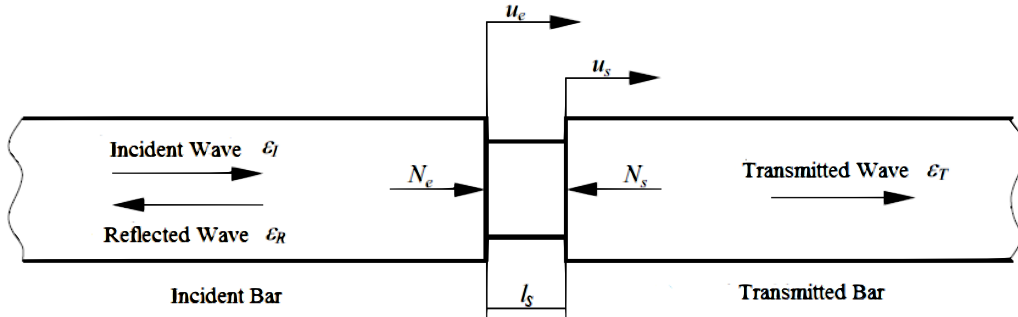


Figure 3.3: Expanded view of incident bar-specimen and specimen-transmitted bar interface [111]

The specimen's mechanical impedance might vary during the tests performed with the SHPB, specially if its rupture, plastic strain or an increase of area takes place [111].

The forces acting on the specimen are calculated by applying the Equation 3.18 to the interfaces of the bars, which are in contact with the specimen:

$$N_e(t) = A_b E_b [\varepsilon_I(t) + \varepsilon_R(t)] \quad (3.30)$$

$$N_s(t) = A_b E_b \varepsilon_T(t) \quad (3.31)$$

where  $A_b$  and  $E_b$  are the cross section area and the Young's modulus of the bars, respectively.

Assuming that the specimen is deformed uniformly, meaning that the external forces acting on it are equal and combining Equation 3.30 and Equation 3.31:

$$N_e(t) = N_s(t) \quad (3.32)$$

$$A_b E_b [\varepsilon_I(t) + \varepsilon_R(t)] = A_b E_b \varepsilon_T(t) \quad (3.33)$$

Therefore, if the bars are made of the same material and have the same diameter:

$$\varepsilon_I(t) + \varepsilon_R(t) = \varepsilon_T(t) \quad (3.34)$$

It is important to notice that the reflected strain has an opposite sign towards the incident and transmitted strains [110].

The mean stress acting on the specimen at every instant is calculated through the equilibrium condition of the forces acting on the specimen:

$$\sigma(t) = \frac{N_e(t) + N_s(t)}{2A_{s0}} \quad (3.35)$$

where  $A_{s0}$  represents the initial specimen cross section.

Combining Equation 3.30 and Equation 3.31 in Equation 3.35, the stresses that act on the specimen in their complete form, also known as 3-wave analysis, are obtained:

$$\sigma(t) = \frac{A_b E_b}{2A_{s0}} [\varepsilon_I(t) + \varepsilon_R(t) + \varepsilon_T(t)] \quad (3.36)$$

Using Equation 3.30, it is possible to calculate the stress acting on both faces of the specimen independently:

$$\sigma(t) = \frac{A_b E_b}{2A_{s0}} [\varepsilon_I(t) + \varepsilon_R(t)] \quad (3.37)$$

The Equation 3.37 is representative of the 2-wave analysis.

The 1-wave analysis is the most used by researchers, since it determines correctly the acting stress on the specimen:

$$\sigma(t) = \frac{A_b E_b}{2A_{s0}} \varepsilon_T(t) \quad (3.38)$$

The 2-wave analysis represents the stress on the incident bar-specimen interface and leads to inaccurate results, due to the lack of precision on the initial phase and oscillations due to the high-frequencies of the incident pulse. The 1-wave analysis represents the stress on the specimen-transmitted bar interface and it is also referred to as a simplification of the 3-wave analysis [111, 108].

However, if the specimens suffer a high plastic deformation, the true stress can be determined by correcting the specimen's area in relation to time,  $A_s(t)$  [110].

The true stress given by 1-wave analysis is given by Equation 3.39:

$$\sigma_{true}(t) = E_b \frac{A_0}{A_s(t)} \varepsilon_T(t) \quad (3.39)$$

Using the solution of Equation 3.8, velocity and displacements at the top of the incident bar can be calculated. At this solution,  $F$  and  $G$  are the functions which describe the shape of the incident and reflected pulse. These pulses propagate in opposite ways in the  $x$  direction, with  $c_0$  velocity:

$$u_e(x, t) = F(x - c_0t) + G(x + c_0t) \quad (3.40)$$

In this case, the strain in the  $x$  direction given by Equation 3.11 is used. Deriving Equation 3.40 in the  $x$  domain, the strain on the incident bar is obtained:

$$\varepsilon_e(t) = F'(x - c_0t) + G'(x + c_0t) = \varepsilon_I(x, t) + \varepsilon_R(x, t) \quad (3.41)$$

If Equation 3.40 is derived the time domain:

$$\dot{u}_e(x, t) = c_0[F'(x - c_0t) + G'(x + c_0t)] \quad (3.42)$$

And then replaced in Equation 3.41, the displacement velocity at the top of the incident bar, more precisely, the incident bar-specimen interface is obtained:

$$v_e(t) = c_0[-\varepsilon_I(t) + \varepsilon_R(t)] \quad (3.43)$$

The displacement velocity at the specimen-transmitted bar interface is given by:

$$v_s(t) = -c_0\varepsilon_T(t) \quad (3.44)$$

The velocities on both interfaces and the specimen initial length,  $l_{s0}$ , are used to define the nominal specimen strain rate,  $\dot{\varepsilon}_n$ :

$$\dot{\varepsilon}_n(t) = \frac{v_e(t) - v_s(t)}{l_{s0}} \quad (3.45)$$

Furthermore, the specimen strain rate can also be defined by the 3-wave analysis, combining Equation 3.44 and Equation 3.45:

$$\dot{\varepsilon}_n(t) = \frac{c_0}{l_{s0}}[-\varepsilon_I(t) + \varepsilon_R(t) - \varepsilon_T(t)] \quad (3.46)$$

Otherwise, using Equation 3.34 the specimen strain rate can be defined by the 1-wave analysis:

$$\dot{\varepsilon}_n(t) = \frac{-2c_0\varepsilon_R(t)}{l_{s0}} \quad (3.47)$$

To determine the true strain rate suffered at every instant of time, the actual length of the specimen should be used:

$$\dot{\varepsilon}_{true}(t) = \frac{-2c_0\varepsilon_R(t)}{l_s(t)} \quad (3.48)$$

In order to calculate the amount of specimen strain, the displacements at the bars-specimen interfaces or direct integration are used. So, the calculus expression for the mean strain of the specimen through the 3-wave analysis is obtained by integrating Equation 3.46 [110]:

$$\varepsilon_n(t) = \frac{c_0}{l_{s0}} \int_0^t [-\varepsilon_T(t) + \varepsilon_I(t) - \varepsilon_R(t)] dt \quad (3.49)$$

If 1-wave analysis is used, the mean strain suffered by the specimen is defined by replacing Equation 3.49 in Equation 3.34:

$$\varepsilon_n(t) = -\frac{2c_0}{l_{s0}} \int_0^t \varepsilon_R(t) dt \quad (3.50)$$

In addition, the true strain suffered by the specimen at every instant of time is obtained through the accounting of its actual length:

$$\varepsilon_{true}(t) = -2c_0 \int_0^t \frac{\varepsilon_R(t)}{l_s(t)} dt \quad (3.51)$$

The three different wave analysis might conduct to slightly different results. The incident bar signal may contain noise or high frequencies which lead to the presence of oscillations in the results. In this case, 1-wave analysis is more suitable, since the specimen behaves as a low filter when the testing material has a low Young's modulus or when there's a significant plastic deformation. Although, 2-wave analysis allows the verification of the specimen forces equilibrium during the test [110].

### 3.1.2 Practical Aspects of The Split Hopkinson Pressure Bar

The correct striker's velocity is responsible for maintaining the bars in their elastic domain and for determining also the specimen strain and strain rate. Knowing that velocity, the strain gauge mounted on the incident bar can determine the striker stress,  $\sigma_{striker}$ , and the incident bar stress, represented by Equation 3.17.

Remembering Equation 3.32 which assumes the specimen is deformed uniaxially and the equality of the external forces acting on it and noticing the stress pulse is transmitted and reflected at the incident bar-specimen interface:

$$A_b \sigma_T(t) = A_{s0} \sigma(t) \quad (3.52)$$

and

$$\sigma_T(t) = \frac{A_{s0} \sigma(t)}{A_b} \quad (3.53)$$

$$\sigma_R(t) = E_b \varepsilon_R(t) \quad (3.54)$$

where  $\sigma_T$  represents the transmitted stress and  $\sigma_R$  the reflected stress.

Equation 3.54 can be combined with Equation 3.47:

$$\sigma_R(t) = \frac{E_b l_{s0}}{-2c_0} \dot{\varepsilon}_n(t) \quad (3.55)$$

And Equation 3.34 can be transformed, using Equation 3.24:

$$\sigma_I(t) + \sigma_R(t) = \sigma_T(t) \quad (3.56)$$

Then, mixing Equation 3.53 and Equation 3.55 with Equation 3.56:



$$\sigma_I(t) = \frac{A_{s0}\sigma(t)}{A_b} + \frac{E_b l_{s0}}{2c_0} \dot{\varepsilon}_n(t) \quad (3.57)$$

Replacing Equation 3.57 in Equation 3.17:

$$v_{striker} = \frac{2}{\rho c_0} \left( \frac{A_{s0}}{A_b} \sigma(t) + \frac{E_b l_{s0}}{2c_0} \dot{\varepsilon}_n(t) \right) \quad (3.58)$$

As mentioned several times previously, the bars must remain in the elastic domain. Therefore, the yield strength of the bars material cannot be surpassed. Replacing the incident stress,  $\sigma_I(t)$  in Equation 3.57 with the yield strength of the bars material,  $\sigma_{yb}$  :

$$v_{striker\ max} = \frac{2\sigma_{yb}}{\rho c_0} \quad (3.59)$$

Thus, Equation 3.59 enables the definition of the maximum striker's velocity without deforming plastically the bars [109].

After defining the specimen length, the maximum strain achieved by it can be predicted with Equation 3.60 and Equation 3.61:

$$\varepsilon = 2\dot{\varepsilon}_n(t) \frac{l_{striker}}{c_0} \quad (3.60)$$

$$\dot{\varepsilon}_n(t) = \frac{v_{striker}}{l_{s0}} \quad (3.61)$$

It should be noted that Equation 3.61 provides an overestimation of the strain rate, since it considers a momentum conservation between the striker and incident bar. However, it also provides a good first approximation for soft metals, such as aluminium [37].

The geometry defined for the specimen should ensure that the specimen itself deforms uniformly. Nevertheless, the specimen only achieves dynamic equilibrium after an initial "ringing-up" period. To determine the length of this period, 1-wave (Equation 3.38) and 2-wave (Equation 3.37) (or even 3-wave) analysis are compared. To validate the test, the 2-wave stress must oscillate equally above and below the 1-wave stress [37]. A sample of a 304 stainless steel was examined [37] and the true stress vs. true strain was plotted (Figure 3.4), regarding 1- and 2-wave analysis. The sample reached dynamic equilibrium after 2% of true strain, approximately.

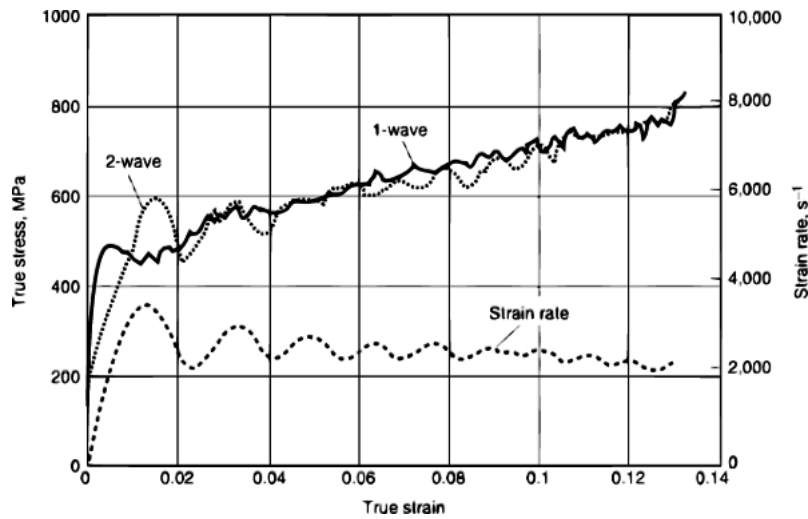


Figure 3.4: 1-wave and 2-wave stress curves for the response of 304 stainless steel [37]

In contrast, if the 2-wave stress is divergent and also exceeds the values for the 1-wave stress, it means that the sample couldn't achieve a uniform stress state. Such an event can be observed in Figure 3.5, for a high-purity lead. It should be noted that the sample didn't achieve a dynamic equilibrium state.

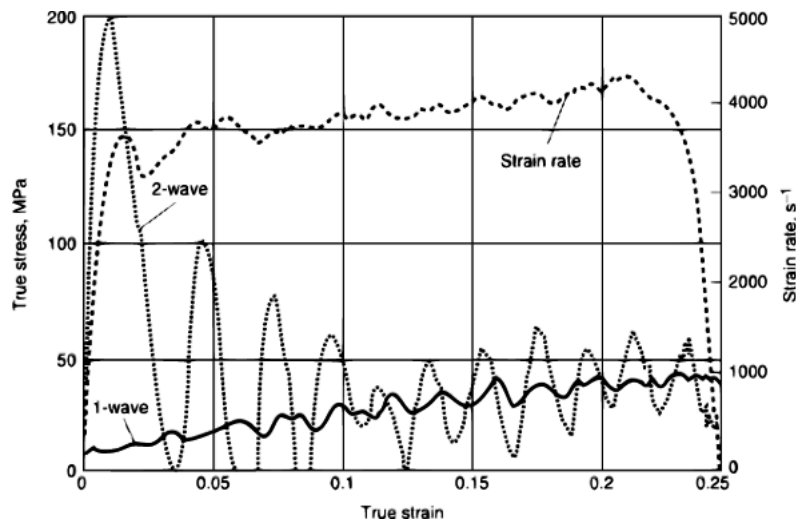


Figure 3.5: True stress-true strain curve for a high-purity lead, comparing the 1- and 2-wave analysis [37]

The measurement of the materials' compressive Young's modulus at high strain rates using the SHPB results in inaccurate values. The stress equilibrium isn't achieved under 1% plastic strain [37, 108].

In order to obtain reliable data to characterize the dynamic plastic material behaviour, the duration of the incident pulse defined with Equation 3.2 must be sufficiently long to surpass the transit time of specimen's longitudinal wave,  $t_s$ , defined with Equation 3.62.

$$t_s = \frac{l_{s0}}{c_s} \quad (3.62)$$

where  $l_{s0}$  represent the specimen initial length and  $c_s$  the velocity of the specimen longitudinal wave [108].

### 3.1.3 Pulse time-shifting

To enable the application of equations presented in Sub-subsection 3.1.1.3, the incident, reflected and transmitted pulses need to be determined separately. Furthermore, incident and transmitted pulses have opposite directions and interference close to the specimen on the incident bar occurs. Close to the specimen and at a distance inferior to half the pulses length, there will always be interference. In order to achieve this, strain gauges must be placed at a distance superior to half the pulse length to allow the independent record of the three pulses. Therefore, the incident pulse is recorded before arriving to the specimen and the reflected and transmitted pulses are recorded after the specimen deformation. A correct positioning is defined with the Lagrange-diagram, as exemplified in Figure 3.6.

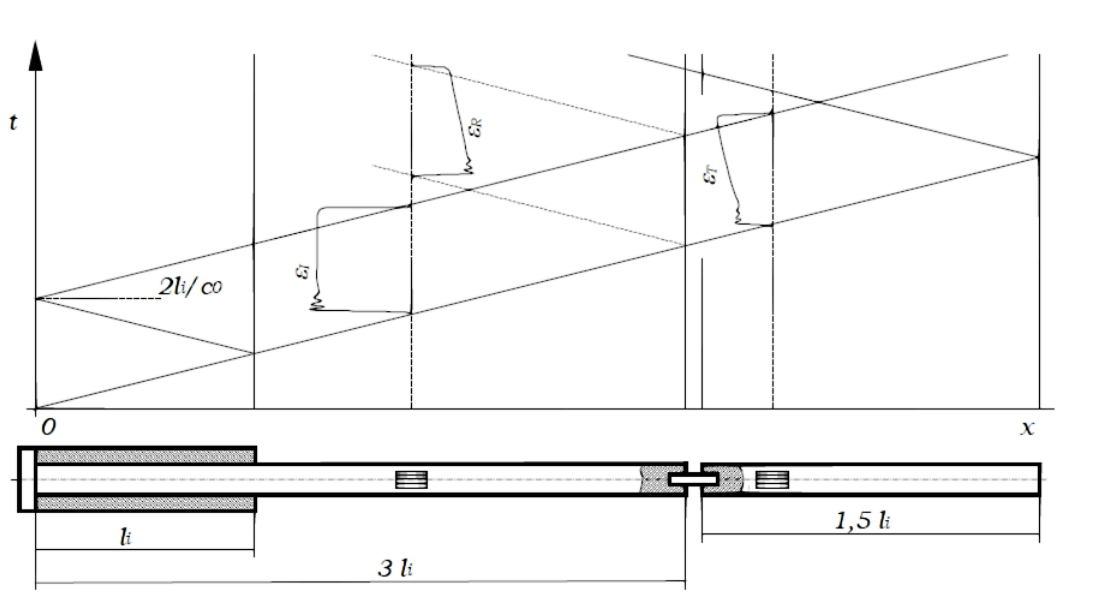


Figure 3.6: Lagrange-diagram for FEUP's SHPB TD16 [110]

Further, this diagram takes in account the temporal evolution of the pulses.

Time-shifting the recorded pulses with precision is necessary in order to use the equations referred in Sub-subsection 3.1.1.3. The Equation 3.30, Equation 3.31 and Equation 3.34 allow the verification of a correct time-shift, since a good equilibrium of the forces acting on the specimen is only possible with a correct time-shift [111]. The three pulses are time-shifted to the time at which they actuated simultaneously on the specimen. To the incident wave, a forward time-shift is applied and therefore, it is determined the time that the incident wave reached the specimen,  $t_{\varepsilon_I}^{specimen}$  (Equation 3.63). To the reflected wave, a backward time-shift is applied to determine the time that the reflected wave actuated on the specimen  $t_{\varepsilon_R}^{specimen}$  (Equation 3.64). Likewise, a backward time-shift is also applied to determine the time the transmitted wave actuated on the specimen,  $t_{\varepsilon_T}^{specimen}$  (Equation 3.65).

$$t_{\varepsilon_I}^{specimen} = t_{SG1} + \frac{\Delta l_{SG1}}{c_0} \quad (3.63)$$

$$t_{\varepsilon_R}^{specimen} = t_{SG1} - \frac{\Delta l_{SG1}}{c_0} \quad (3.64)$$

$$t_{\varepsilon_T}^{specimen} = t_{SG2} - \frac{\Delta l_{SG2}}{c_0} \quad (3.65)$$

where  $t_{SG1}$  represents the time of the signal of the incident bar strain gauge,  $\Delta l_{SG1}$  represents the geometrical distance between the incident bar strain gauge and the specimen and  $\Delta l_{SG2}$  represents the geometrical distance between the specimen and the transmitted bar.

Since both strain gauges record in simultaneous, it is assumed  $t_{SG1} = t_{SG2}$  [108]. Figure 3.7 illustrates a time-shift example.

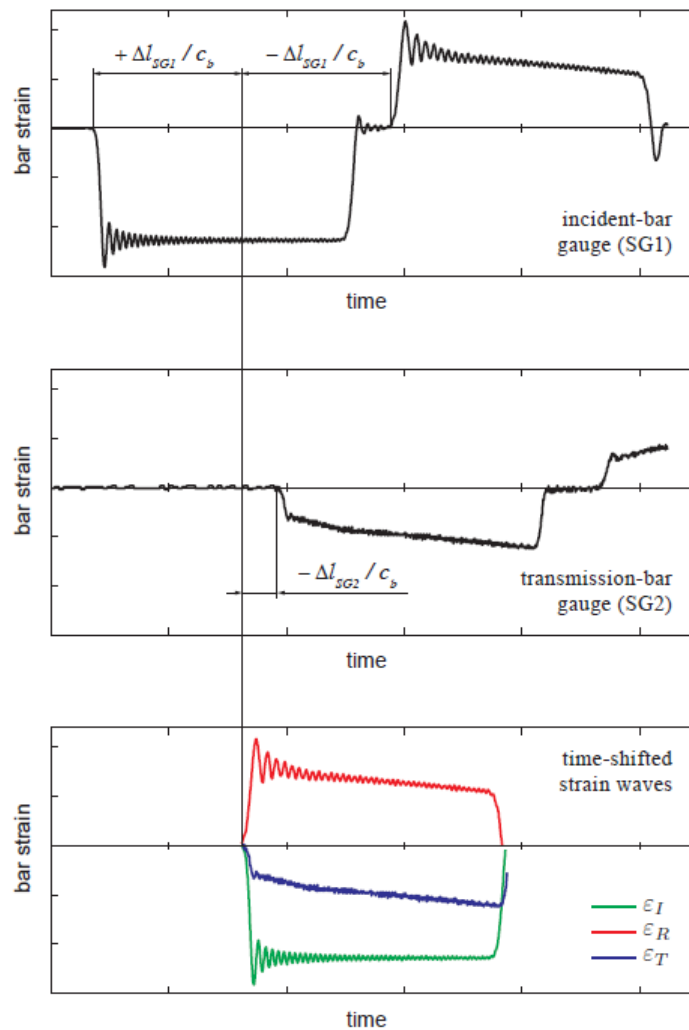


Figure 3.7: Time-shifting of the bars strain waves [108]

### 3.1.4 Wave dispersion

A pulse whose propagation occurs along the bar suffers the dispersion phenomena which begins when the incident pulse produced by the impact of the striker does not rise immediately

into a square-wave with fixed amplitude but instead, rings-up. The incident pulse recorded on the incident bar strain gauge suffers dispersion until it propagates itself to the specimen. In addition, the transmitted and reflected pulses also suffer dispersion until they propagate to the transmitted bar and incident bar strain gauges, respectively. Further, several differences between the measured pulses and those acting on the specimen emerge. Only after the wave has propagated a length of about 10 bar diameters this effect quickly dampens [37].

Besides proceeding to the time-shift correction, it is necessary to correct the wave dispersion to apply the equations presented in Subsection 3.1.1.3.

The equation of motion in an infinite cylindrical solid fully describes the wave propagation behaviour and was first established by Pochhammer and Chree, and then solved by Bancroft [110, 37, 111].

Knowing the bars diameter, Poisson's ratio and the pulse shape, it is possible to reconstruct it in time and space, making use of the Bancroft's table [113]. For that, it is necessary to first identify the frequencies and amplitudes of the components of the pulse. Therefore, any pulse may be decomposed on a sinusoidal summation, applying Fourier transform. At any position along the pressure bar,  $z$ , the wave may be represent by Fourier series expansion,  $f(t)$ :

$$f(t) = \frac{A_0}{2} + \sum_{n=1}^{\infty} D_n \cos(nw_0t - \delta) \quad (3.66)$$

where  $nw_0$  is the angular frequency,  $\delta$  is the phase angle and,  $A_0$  and  $D_n$  are Fourier coefficients.

Since dispersion alters the phase angle, a new one at  $z + \Delta z$  position can be determined:

$$\delta(z + \Delta z) = \delta(z) + \frac{nw_0\Delta z}{c_0} \left( \frac{c_0}{c_n} - 1 \right) \quad (3.67)$$

where  $c_0$  is the velocity of the longitudinal wave while  $c_n$  is the velocity of component  $nw_0$ .

The  $c_n$  value depends on the wave length and on the vibration mode. The SHPB case is characterized by the fundamental mode [37, 114, 113]. Therefore, the Equation 3.66 and Equation 3.67 represent the dispersion correction for mode 1.

Figure 3.8 shows the first three vibrational modes regarding the Pochhammer-Chree solution for a material with a Poisson's ratio of 0,29 [114].

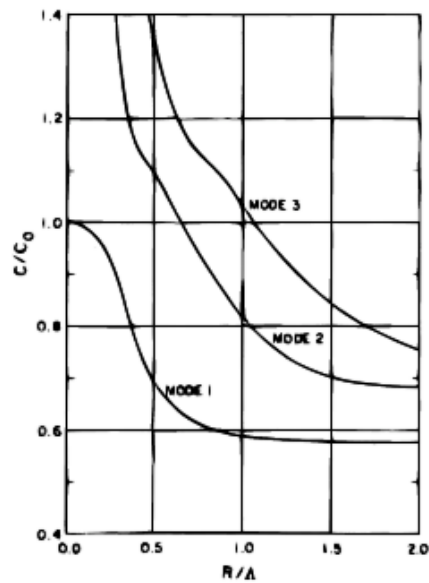


Figure 3.8: Solution of Pochhammer-Chree's equation showing the variation of phase velocity with wavelength for the first three vibrational modes for a material with Poisson's ratio of 0.29 [114]

Observing Figure 3.7, the instants of time to correct the wave dispersion are the same considered to correct the pulse time-shift.

However, some cases require an incident pulse with a higher rise-time so the contact surfaces of the bar-specimen can be adjusted to permit a lower and a progressive application of the incident force [110]. Brittle and fragile materials are examples of those cases. Experimental techniques such as Pulse shaping can be employed to increase the rise time of the incident wave. The technique consists on placing a soft and deformable metal between the striker and the incident bar before the impact, e.g.: copper. The incident pulse has a trapezoidal shape, eliminating high-frequencies and oscillations and hence, dispersion. The advantage of this technique relies on a more uniform strain rate during the test [37]. Gerlach et al. [115] developed a new method for pulse shaping the split hopkinson tensile bar, using a rod shaped geometrically between loading and incident bar (see Figure 3.9 B=2).

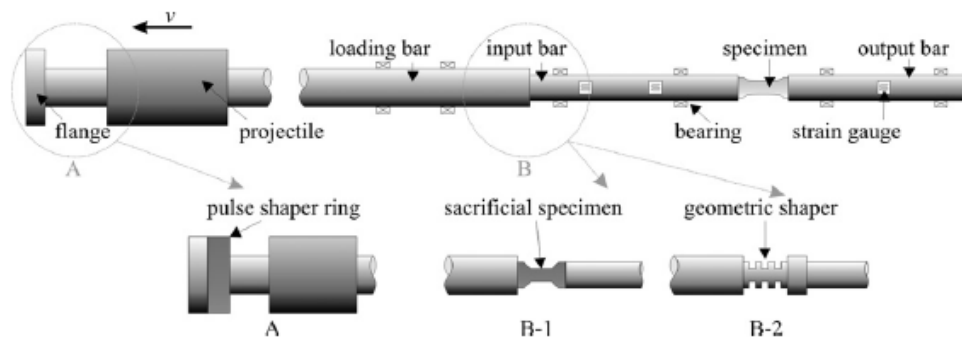


Figure 3.9: Scheme of the possible forms to employ the pulse shaping technique on a tensile apparatus [115]

### 3.1.5 Data acquisition

With the temporal record of the measured signals of the deformed bars, it is possible to obtain the dynamic properties of a material.

However, the waves propagation occurs at high-speeds. Hence, it is required the use of equipments to measure and storage the signal capable of the acquisition speed [37]. Those equipments include two strain gauge signal conditioners and a device to record the signals, e.g.: an oscilloscope. Thus, the two strain gauge conditioners should have an adequate data resolution which can be achieved if they have a frequency response of 1 MHz, at minimum. Further, signal conditioners with gains in the order of 1000 retain high signal-to-noise levels.

Formerly, the dynamic stress-strain curve of the specimen was obtained through the use of an oscilloscope which, in its turn, recorded the strain gauge signal pulses and it was fed with the transmitted and integrated reflected wave. If the reflected wave was fed with an operational amplifier, a signal directly proportional to the strain was yielded in the specimen, without dispersion correction. Nowadays, high-speed data-acquisition computer modules are used [37]. They are directly connected to a computer and posteriorly, the data is processed and numerically treated with a specialized software. Accordingly, the software should identify the beginning and duration of each pulse. It also should effectuate the translation and dispersion correction and traces the dynamical behaviour curves [110].

In Chapter 4 it is exposed the signal conditioner and acquisition used in this work.

## 3.2 Digital Image Correlation

The strain gauge method is widely established and has been used to measure mechanical and thermal loadings throughout the years, being an important resource of experimental mechanics. This method requires the contact between the strain gauge and the surface of the object in study. However, it only provides the values of average strain if the object in study is a specimen, more precisely over its gauge length. The traditional strain gauge measures the strain between two different points and therefore, provides an average strain [116, 117]. Besides, the measurement of large strains with foil strain gauges must be corrected because of the transverse sensitivity of the measurement grid and non-linearity errors, despite the non existence of consensus regarding the latter. The strain that foil strain gauges can measure is limited to 5% of strain [108].

Several non-contact optical techniques have been developed to allow full-field measurement, such as interferometry techniques: holography interferometry, speckle interferometry, moiré interferometry and non-interferometry techniques such as: the grid method and digital image correlation [118]. On one hand, the interferometry techniques require precise set ups, low vibrational environments, coherent light sources, are more expensive and more difficult to use outside the laboratory [119]. On the other hand, compared with DIC, interferometry techniques have a higher performance regarding spatial resolution [108] and better strain measurement accuracy [118].

The DIC method was first introduced in the early 1980s at the University of South Carolina and its application has been increasing in the field of experimental and solid mechanics over the years due to its flexibility, robustness and ease of use. Nonetheless, only after massive developments in computer hardware the demands of calculating correlation were satisfied [120]. The method allows strain measurements between 0.01% and 100%, in-plane and out of plane measurements, no corrections are necessary because the measured strain is the true strain, images taken by camera show if there are deformation and failure mechanisms and the data obtained

towards displacement and strain field can also be used to verify the data obtained by finite element simulations [108].

### 3.2.1 DIC fundamentals

This method is based on the comparison of a set of images of the specimen surface taken before and after deformation occurs, particularly the tracking of the same pixels between images. The 2D DIC method is used for measuring in plane-deformation of planar surfaces while the 3D DIC method is used for measuring general deformation of planar and curved surfaces on the three-dimensional spaces [121]. As LOME only has a 2D camera, more precisely PHOTRON Fastcam SA4, the author will focus on the 2D DIC method. Information about the 3D DIC method can be consulted on [120, 119, 121, 117].

The 2D method uses a single fixed charge-coupled device (CCD) which is a camera to record the specimen images. To allow these records, the specimen surface must have a random pattern, natural or artificial. Further, white source lights are required to illuminate the specimen surface. The CCD sensor should be parallel to the surface of the specimen (see Figure 3.10). After, the images will be exported to a PC and processed using a proper software, so the displacement and strain informations are obtained [108].

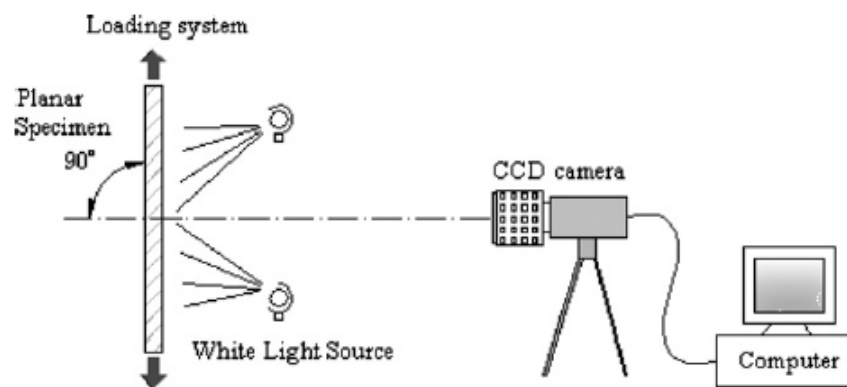


Figure 3.10: 2D DIC method set up [118]

The specimen surface must have a random grey intensity distribution/pattern which will produce dissimilar intensities of diffusely reflected light [121]. The speckle pattern, usually black on white and produced by aerosol spray painting, will deform along with the specimen surface and will be responsible for transmitting the deformation information [118]. In addition, the pattern should have high contrast to provide an efficient image correlation and its roughness should be minimal in a way the specimen surface roughness is practically unaltered. Also, the speckle size is chosen considering the resolution of the camera, the application and therefore, the desirable strain, displacement field resolution and the object size. It should be noticed that by adjusting the intensity of the white light sources and/or the aperture of the camera lens, the grey intensity distribution can be regulated [108, 122].

The digital images are divided into facets or subsets, equally spaced from each other. The facets size should be defined having regard to the specimen size, the speckles size, the desirable strain gradients and the related loading conditions. It is important to consider facets greater than speckles dots so that small displacements are able to be measured. In contrast, their size should not be large to the point which there's loss of resolution. Accordingly, each



facet contains a horizontal and vertical defined number of pixels and the distance between two consecutive facets is known as grid spacing (see Figure 3.11 (a) ). So, if the grid space is too small, there are more consecutive facets and therefore, a higher computational cost. However, grid spacing has not a great influence on the accuracy of the computed data. In addition, overlapping facets provide more precision and accuracy of the strain field obtained through the software. Further, for different kind of tests a different density of the measurement points is applied. Larger spacing grids are preferred when uniform strain is expected, contrarily to strain gradients where a small spacing grid is the most suitable [122].

As each facet has a different grey intensity distribution, it can be easily identified towards the others in the deformed state. To compute the displacements, a point centred on a facet from the reference image is compared to its location in the deformed image (see Figure 3.12). The choice of the point instead of a pixel lies on a wide variation of the grey distribution, providing a better and a more unique identification of the facets in the deformed image [118]. Hereafter, different correlation criterias can be applied to evaluate the similarity between the reference facet and the deformed facet. Different criterias are provided by Pan et. al [118] and Sutton et. al [123]. The vector which defines the displacement in-plane is the result of the difference between the position of the reference facet centre and the deformed facet centre (Figure 3.11 (b)).

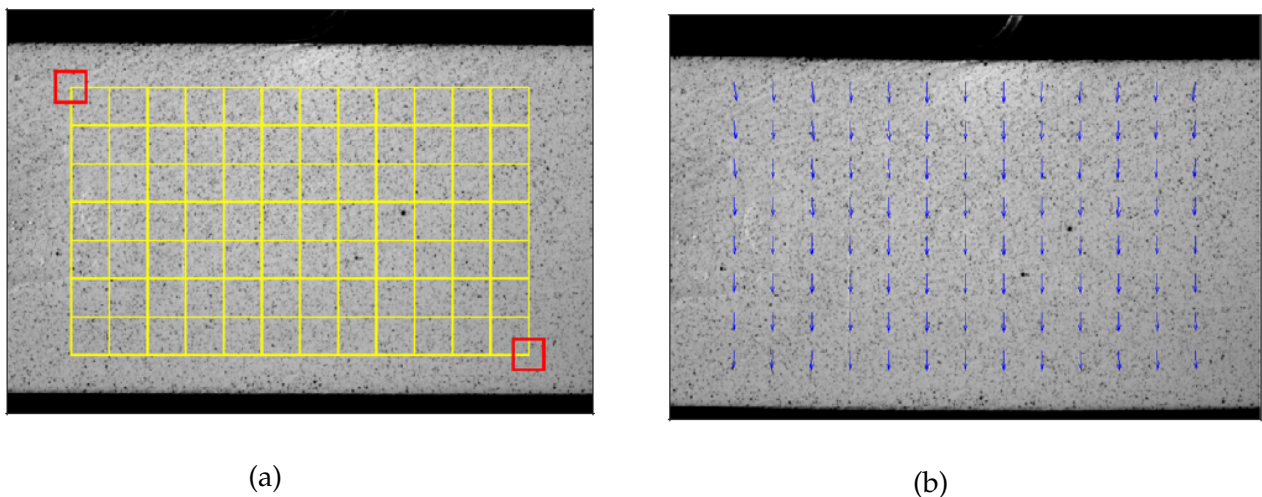


Figure 3.11: Reference image with red facet used to track its centre point motion and yellow grid intersection points represent the points to be calculated (a) and the calculated displacement vectors to impose on the deformed image (b) [118]

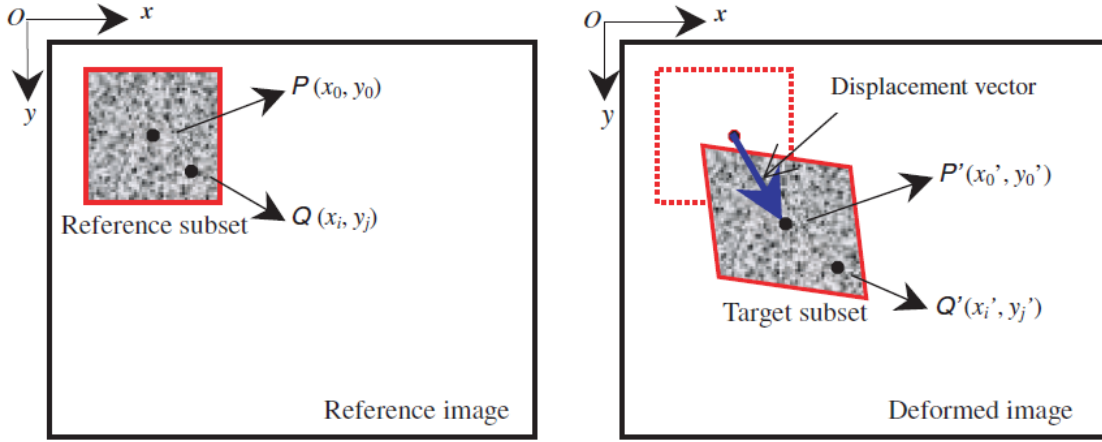


Figure 3.12: Reference facet (reference subset) and deformed facet (target subset) [118]

Shape functions are used in order to map any point  $Q(x_i, y_j)$  around the facet centre  $P(x_0, y_0)$  in the reference facet to point  $Q'(x'_i, y'_j)$  in the deformed facet.

$$\begin{aligned} x'_i &= x_i + \xi_1(x_i, y_j) \\ y'_j &= y_j + \eta_1(x_i, y_j) \end{aligned} \quad (i, j = -M : M) \quad (3.68)$$

where  $M$  represents a square reference facet of  $(2M + 1) \times (2M + 1)$  pixels centred at point  $P(x_0, y_0)$  from the reference image.

If there's only rigid body translation in the reference and deformed facets, the displacements are the same in both facets. So, a zero-order shape function is used:

$$\xi_0(x_i, y_j) = u \quad \eta_0(x_i, y_j) = v \quad (3.69)$$

In Equation 3.69,  $u$  and  $v$  are the  $x$  and  $y$  directional displacement components of the reference facet centre.

However, since the zero-order shape function only describes the translation movement its use isn't suitable when situations of rotation and/or shear occurs. Thus, first-order shape functions which allow translation, rotation, shear, normal strains and their combinations of the facet are used [118]:

$$\begin{aligned} \xi_1(x_i, y_j) &= u + u_x \Delta x + u_y \Delta y \\ \eta_1(x_i, y_j) &= v + v_x \Delta x + v_y \Delta y \end{aligned} \quad (3.70)$$

where  $\Delta x = x_i - x_0$ ,  $\Delta y = y_j - y_0$ ,  $u_x, u_y, v_x, v_y$ , are the first-order displacement gradients of the reference facet.

If more complex deformation states are observed on the deformed facet, second-order shape functions can be used and are also presented by Pan et. al [118].

After determining the deformation field, the strain field can be obtained using a facet of points in the displacement fields, called the computation size. Remembering what  $M$  represents, the minimal computation size attainable is  $3 \times 3$  and should be sufficient enough to

compute the local strain. To attenuate the noise from the strain field, larger windows should be employed. Still, this may result in attenuation of existing strain gradients when the specimen has a irregular geometry [122].

Other important aspects such as validity quote and filtering are listed by Palanca et. al [122]. The aperture and correspondence problem, images matching methods, facet shape functions, optimization criteria for pattern matching, efficient solution methods and also statistical errors analysis are presented by Sutton et. al [123]. Likewise, the calibration process for the subject method is described by Sutton et. al [121], PI et. al [117] and Jabłoński and Březina [120].



## Chapter 4

# The Experimental Test Set Up

The experimental test set up for the split Hopkinson tensile bar is introduced in this chapter in order to perform tensile tests. Initially there was an apparatus developed in LOME facilities by [110]. The author of this work introduced major developments and renewed the whole set up. These developments are described along the chapter.

The split Hopkinson pressure bar technique was developed to measure the materials mechanical response when subjected to high strain rate loading. It was first develop for compressive tests and then, different modifications were made to apply this technique for tensile tests.

The signals are registered with the strain gauges which are placed on both bars at a distance wherein the waves don't interfere with each other. The three waves must be acquired close to the specimen, to minimize dispersion effects. Next to the impact and interfacial zones, the pulses nature is complex and the existing friction between bars and specimen results in restrictions on the radial direction. The use of specimens with smaller diameters than the bars' causes misalignments responsible for the appearance of waves with spherical shape or dilatations. As seen in Chapter 3, this effect disappears after a distance ten times greater than bars diameter, being correctly describe with the 1-wave analysis.

In addition, the recorded signals allow the temporal evolution of forces and the displacements on specimen extremes reconstruction. After suffering an adequate treatment, this data gives the materials mechanical properties and their response to such kind of loading [110].

### 4.1 Tensile Split Hopkinson Pressure Bar

To perform a tensile test in a SHB there are barriers which need to be outweighed, such as the tensile pulse generation and the specimen attachment to the bars. Further, this attachment should minimize as much as possible the impedance variation and thereafter, reflections.

To generate a tensile pulse, the incident bar must be loaded in tensile. For that, there are two solutions. The first solution uses a tubular striker (Figure 4.1) while the second is based on the compressive pulse reflection on a free end [2]. In order to apply the first solution, the impedance of the striker and the bars should be identical. The incident bar must have an anvil on its free end to receive the impact.

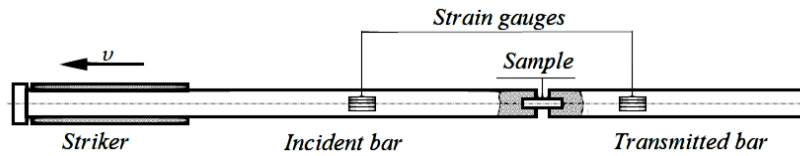


Figure 4.1: Tensile split Hopkinson bar with a tubular striker [110]

Although, as the striker has a tubular form its manufacturing is complex as well as the anvil construction which must resist the striker shock and shouldn't alter or even interfere with the incident wave form. Also, this solution requires the use of bars with greater length. In Figure 3.6 it is shown that the incident bar length includes the striker length.

This configuration has a total length of  $4.5 l_i$ , being  $l_i$  the striker length. Moreover, this solution required a complex gas gun design and respective breech which must be provided with an orifice to allow the incident bar slide and a radial air feeding. On the other hand, the striker must possess bushings to allow its slide over the incident bar and in the intern surface of the barrel with a good sealing [110].

## 4.2 Experimental Set Up Design

The old solution introduced by Ferreira in [110] is illustrated in Figure 4.2. Since the support structure is already mounted, the old parts were dismantled in order to assemble the new ones. The support structure was constructed using *Bosch* modular commercial profiles with an available length of 9000 mm.

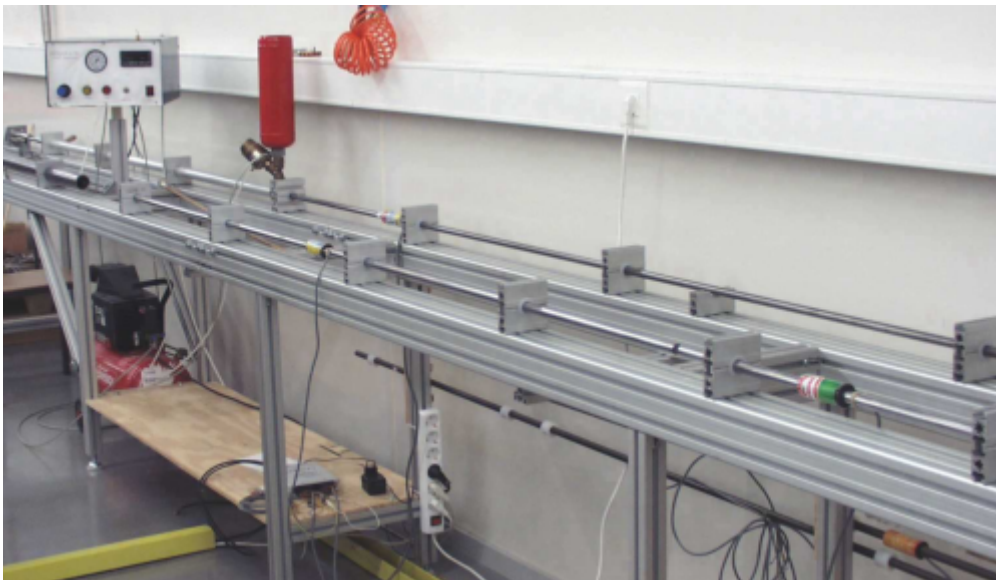


Figure 4.2: Original SHPB apparatus [110]

The new solution, in Figure 4.3, was specially designed for testing aluminium alloys and its joints. It is suitable for testing three different types of specimens: dog bone, butt joint and overlap joint specimens. Also, the design of the bars allows the use of different gripping systems making possible the use of others specimens geometries or even testing other materials.

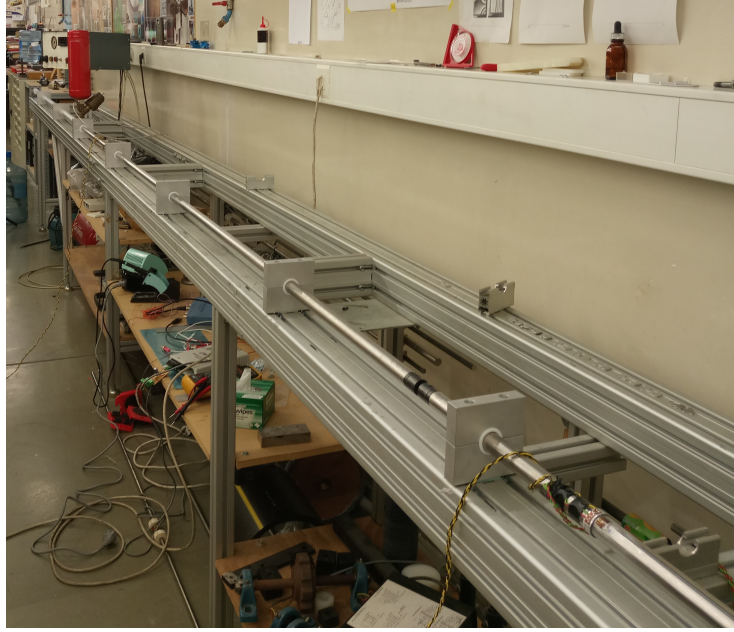


Figure 4.3: LOME split Hopkinson tensile bar developed

### 4.2.1 Gas gun

The gas gun is used over a mechanic actuation, since it doesn't generate deformation waves. Therefore, the striker has a uniform acceleration, free of vibrations.

The gas gun is composed of four parts: air chamber, valve, breech and barrel. The air chamber used by Ferreira [110] will be used. For its design, the desired range of velocities and the striker's mass were considered. The barrel must have a low residual pressure when the impact occurs so the desired impact velocity can be reached. Hence, the striker should not possess a great acceleration at the impact time, since it causes deviations in velocity measurement.

The valve is pneumatically actuated with a fast overture and large debit. This quick overture allows the use of barrels with lower length because it guarantees a higher effective mean pressure over the striker.

A trigger controller (Figure 4.4) is used to control the trigger pressure, the principal pneumatic valve overture and to record the impact velocity. This controller is responsible for pressuring the air chamber, for initiating the trigger and for measuring the striker velocity immediately before the impact. Since the impact velocity depends directly on the pressure, by controlling the latter great ranges of selected velocities can be reached, concerning the calibration curve. The desirable pressure can be determined with Equation 4.1, proposed by Berggren and Reynolds using Newton's motion equations [124].

$$v_{striker} = \left[ \frac{2P}{\rho_{striker}} \frac{l_{bar}/d_{bar}}{l_{striker}/d_{bar}} \right] \quad (4.1)$$

where  $P$  is the desirable pressure,  $l_{bar}$  is the length of the barrel,  $l_{striker}$  is the length of striker,  $\rho_{striker}$  is the density of the striker and  $d_{bar}$  is the barrel diameter.

To maximize the striker's velocity it is necessary to increase the pressure and  $l_{bar}/d_{bar}$ , while minimizing the density of the striker and  $l_{striker}/d_{bar}$ . If the bore of the barrel is held at a specific diameter, the striker's velocity increases with an increase in the length of the barrel [124]. The

chosen barrel is made from aluminium, has an exterior diameter of 40 mm, an interior diameter of 36 mm and length of 2000 mm. Further, the desirable pressure determined with Equation 4.1 and Equation 3.59 is 640 KPa (see Subsection 4.2.2 for the striker velocity).

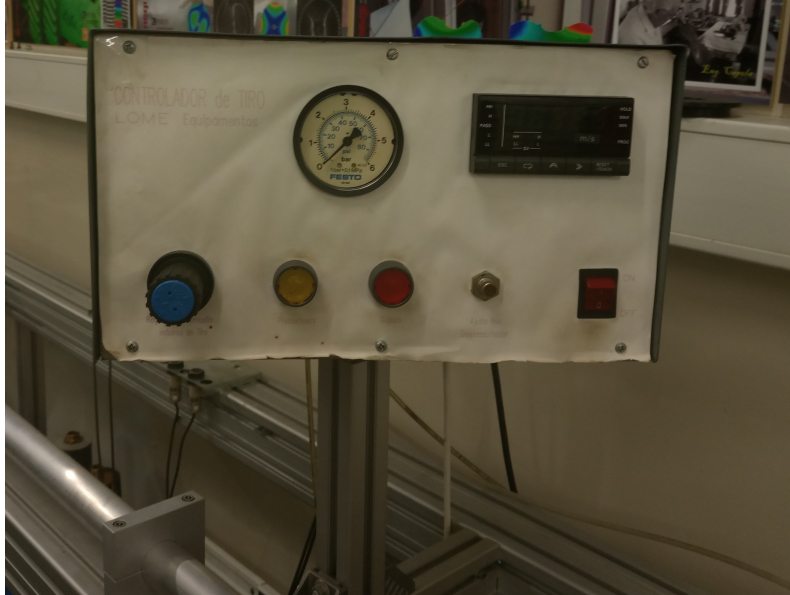


Figure 4.4: Trigger controller

However, it should be noticed that impact velocities higher than  $15 \text{ m/s}$  result in the collapses of the strain gauges. So, this value is considered the reference value for the upper limit of velocity.

#### 4.2.1.1 Breech and bushing

These two components are responsible for transmitting the air supplied by the air chamber to barrel and consequently, the bars. The breech is made of steel and has a threaded orifice on its top where the air chamber is plugged in through the use of a special threaded part, see Figure 4.5. One of the extremes of the breech is connected to the barrel (Figure 4.6) while other is connected to the incident bar through the bushing. The orifice allows the air to pass inside the barrel.



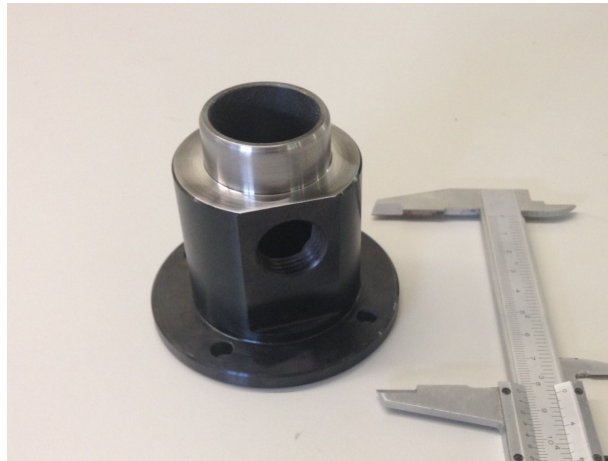


Figure 4.5: Breech



Figure 4.6: Breech and barrel

The bushings mounted on the striker (see Subsection 4.2.2) will cause its slide over the incident bar until it reaches the anvil. The breech bushing (4.7) is responsible for the alignment of the incident bar inside the breech, with the help of the striker. It only allows the air to pass on one direction, the direction of the striker sliding. Therefore, the air supplied by the gas chamber only travels inside the barrel, causing the impact of the striker on the anvil. Such can be achieved due to the larger exterior diameter of the bushing that fits inside the breech. Thus, the bushing serves as a sealing. The bushing section with a smaller exterior diameter was purposely designed to provide its support through the holders (see Figure 4.8). In addition, the bushing is made of Polytetrafluoroethylene (Teflon), a material known to have a low friction coefficient, providing a good bar sliding on its inside.

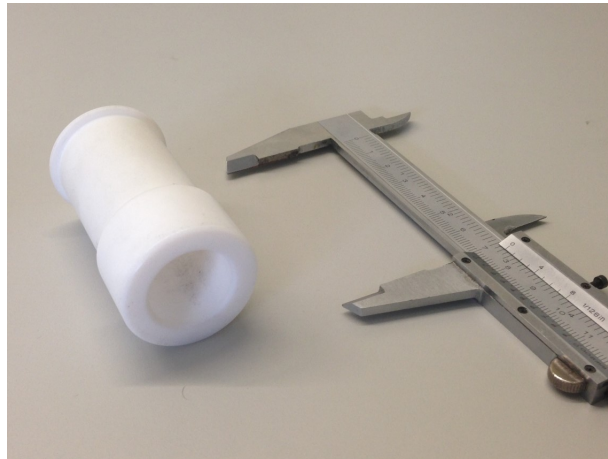


Figure 4.7: Breech bushing

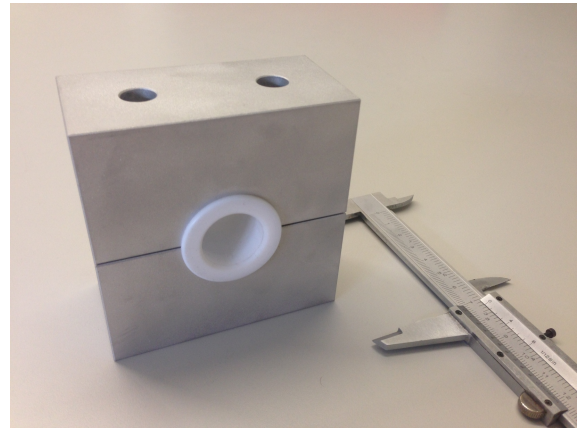
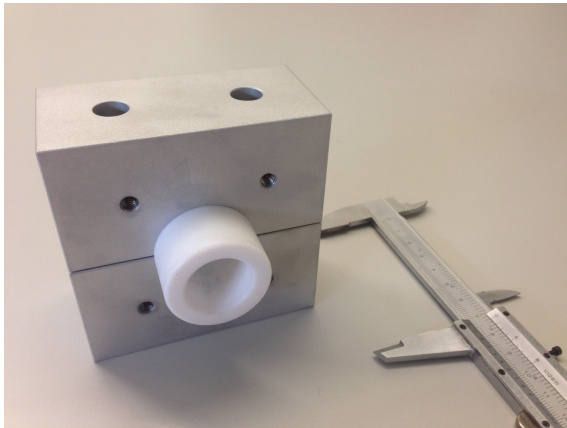


Figure 4.8: Bushing assembled on breech holders

Since the breech needs to be fixed, there are four through holes equally and radially spaced to allow its assembly with M6 screws on the breech holders.

#### 4.2.1.2 Holders

Holdings made of aluminium were developed to support the breech and subsequently, the gun barrel. It is important to notice that the alignment must be done towards the centre axis and therefore, this fact was taken into consideration when designing the holders.

The breech holders are composed by two symmetric supports. Each support has two holes for dowels and two through holes for M6 screws on the top as shown in Figure 4.9. The front face has two holes to fix the breech with the use of M6 screws and it also has a half hole in the middle, with chamfers on its extremes. This half hole forms a complete hole when both supports are assembled and it is responsible for supporting the bushing. On its turn, the chamfers have the purpose to compensate any misalignments caused by the manufacturing process. Thus, a good positioning of the bushing in the assembled hole can be accomplished. When placing the holders at the defined position, the dowels will be responsible for aligning both. After assembling the holders, its fixation to the modular structure is accomplished due to the

two through holes of each support. Since the holders are symmetric, the two through holes are concentric. These holes have lowered counterbored sinks, considering the lengths of the M6 screws available. Their placement was strategically done, in a way there's a match between them and the guides of the modular profiles. Nuts with hammer heads are placed in those guides to complete the modular fixation.

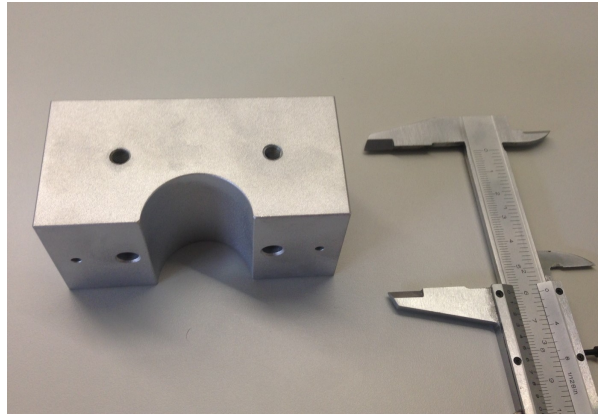


Figure 4.9: Breech holders

The gun barrel holders are not symmetric due to the diameter of the barrel which avoids the use of matching through holes to fix the assembled holders to the structure. The upper support, contrarily to the breech holders, only has two through holes and a half hole in the middle. On the other hand, the lower support has two threaded holes placed at an equal distance of the two through holes of the upper support to allow the fixation between both and a half hole in the middle (Figure 4.10). Both half holes have chamfered extremes, for the same reason described previously regarding the breech holders. When the holders are assembled, the hole formed is responsible for supporting directly the barrel (Figure 4.11). The holders are fixed to the modular structure with the use of two M6 on lowered counterbored sinks for through holes and two nuts with hammer head placed on the modular structure guides. Though, there's an order that should be followed. The first holders to be mounted are the lower holders, directly on the structure. Then, the barrel can be placed over them. The upper holders are placed over the barrel and fixed to the lower holders.

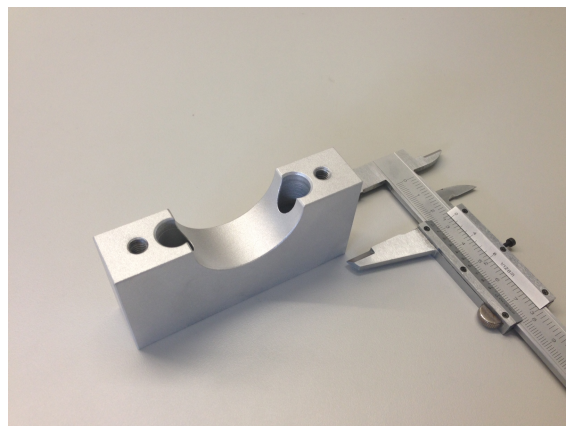


Figure 4.10: Barrel lower support

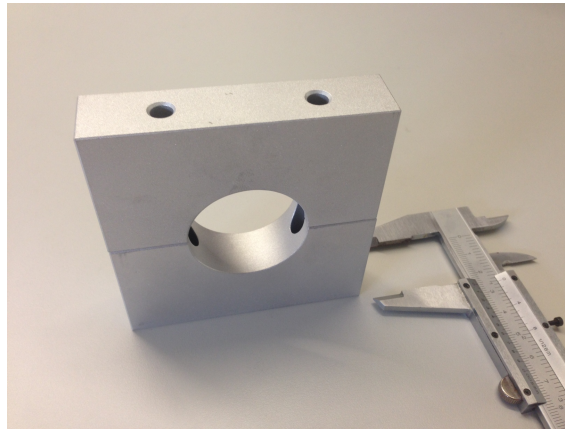


Figure 4.11: Holders assembled

### 4.2.2 Striker

Chapter 3 presents all the necessary conditions to design the striker and bars, and to verify if they follow the conditions and restrictions imposed. Since their length is predefined due to the modular structure length, verifications are made to check if the chosen diameter fits the conditions. The striker dimensions are dependent on the bars dimensions as seen before. In its turn, the bars dimensions are dependent on the proposed gripping system whose major concern is to avoid a significance change in impedances.

Thereby, the striker has a length of 1900 mm due to the length available of the modular structure, an external diameter of 28 mm and an internal diameter of 22 mm. The internal diameter was selected to allow the incident bar slide inside the striker (see Subsection 4.2.3). The striker must have a good impact resistance to not suffer plastic deformation. It was machined from a round bar of AISI 303 steel, dependent on the materials availability of the manufacturing company for such lengths. The chemical composition of the AISI 303 steel is presented in Table 4.1 while its mechanical properties are listed in Table 4.2.

Grade designation	Carbon	Manganese	Silicon	Chromium	Nickel	Sulphur
AISI 303	0.15 % max	2 % max	1 % max	17-19 %	8-10 %	0.15 % min

Table 4.1: AISI 303 Steel chemical composition [125]

Mechanical Properties at 20°C		
Young's Modulus (GPa)	193	
Volumetric mass density( $g/cm^3$ )	7.8	
Brinell Hardness	Annealed	130-180
	Strain hardened	180-330
Rockwell Hardness	Annealed	70-90
	Strain hardened	-
Ultimate tensile Rm ( $N/mm^2$ )	Annealed	530-700
Yield Strength Rp(0,2) ( $N/mm^2$ )	Annealed	205-340
	Strain hardened	350-900
Rp(1) ( $N/mm^2$ ) minimum annealed	255	
Elongation 50mm. A(%)	60	

Table 4.2: AISI 303 Steel mechanical properties [125]

Remembering Equation 3.1 and Equation 3.7, the pulse duration is:

$$T = 7.68815 \times 10^{-4} \text{ s} \quad (4.2)$$

With Equation 3.19, its length:

$$\Lambda = 3.8 \text{ m} \quad (4.3)$$

Observing Table 4.2 and using Equation 3.59, the striker maximum velocity can be determined:

$$v_{striker \max} = 13.06 \text{ m/s} \quad (4.4)$$

According to the statement made before, the striker maximum velocity is lower than 15 m/s. It is noticed that this velocity causes the strain gauges collapse [110].

#### 4.2.2.1 Striker bushings

During the test, the use of a striker with a constant cross section results in an incident wave with a rectangular shape. It is desired that the pulse is as regular as possible in order to ignore the deviations caused by noise. Also, the rectangular shape allows a better interpretation of the results obtained.

The striker has four similar bushings made of Teflon with the purpose of guiding it along the barrel, avoiding misalignments towards the centre axis (Figure 4.12). Ferreira [110] studied two forms of connecting the bushings with the striker. The author concluded that bushings mounted rigidly on the striker caused a localized increase of the total impedance, aggravated due to the use of two different materials and geometries variation. As the materials were different, the wave velocity propagation was different too. Thereafter, the incident wave form suffered an alteration and no linear level was observed. Also, these factors generated shear waves that propagated on the radial direction through the bushings.

To minimise such effects, the bushings have an appropriate design and a reduced mass (see Figure 4.13). They are mounted with a small interference on the striker, avoiding a rigid connection. The application of a gummed tape layer on the bar surface immediately before and after the bushings leads to their immobilization.

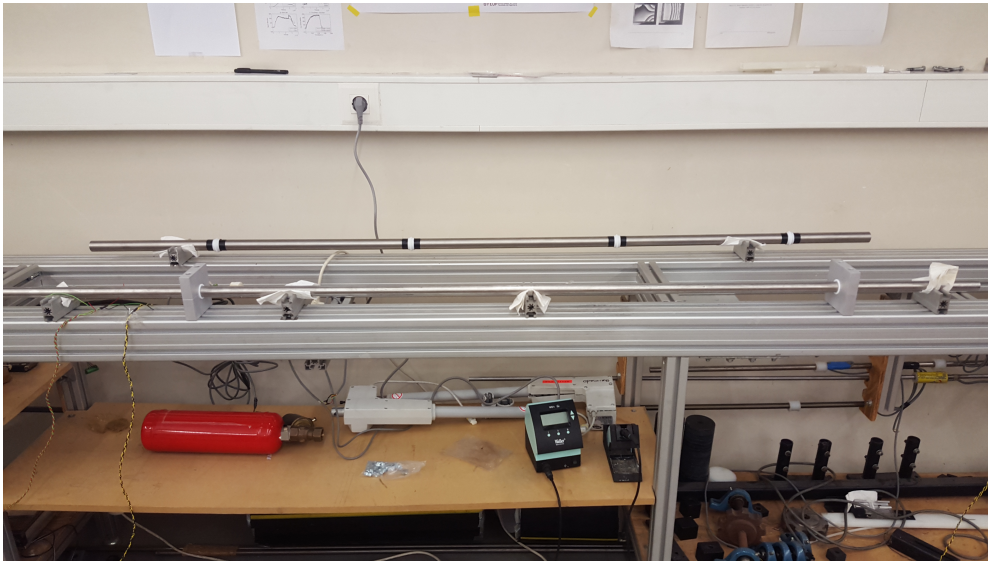


Figure 4.12: Striker with the four bushings assembled

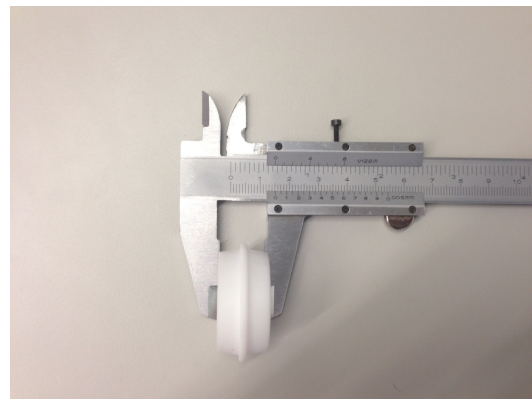
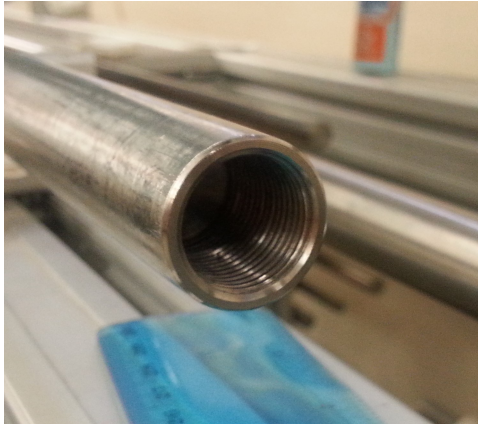


Figure 4.13: Striker's bushings

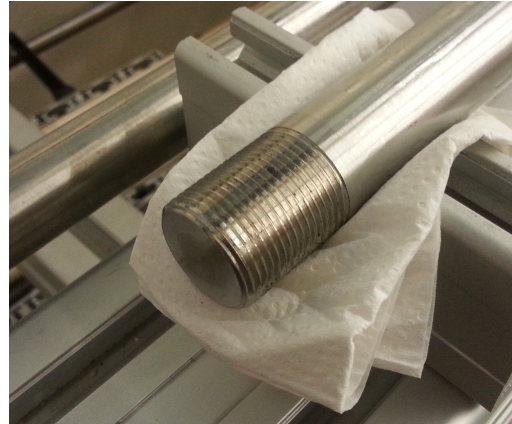
### 4.2.3 Bars

To assure the wave propagates with the same velocity along the bars, the incident and transmitted bar are made of the same material of the striker. The materials chemical and mechanical properties are listed in Table 4.1 and Table 4.2. As aforementioned, the striker has a length of 1900 mm. As such, to accomplish the statements withdrawn from Figure 3.6, the incident bar has a length of 5700 mm while the transmitted bar has a length of 2850 mm. This is an important statement because the length of the three bars must allow an interference free record of the three waves, with the respective placement of the strain gauges. Both bars have a diameter of 22 mm imposed by the materials availability and manufacturing constrains. To allow the attachment of the grips, both bars have a M18×1.5 threaded hole on one end. The other end of the incident bar was threaded with M22× 1.5, considering the bars diameter (Figure 4.14). This thread has the purpose of attaching the anvil, responsible for transforming the compressive stress wave into a tensile stress wave due to the reflection phenomena. Since the diameter of the energy dissipation system's tube is equal to the barrel's (see Sub-section 4.2.5), a standard lock nut can not be used as an anvil. Accordingly, the anvil is composed of two non standard

nuts (Figure 4.15) specially designed to form a lock-nut with a  $M22 \times 1.5$  threaded hole to fit the threaded end of the incident bar. Besides, the anvil should possess a reduced mass in order to not alter impedances and to be able to transmit the impact force.



(a)

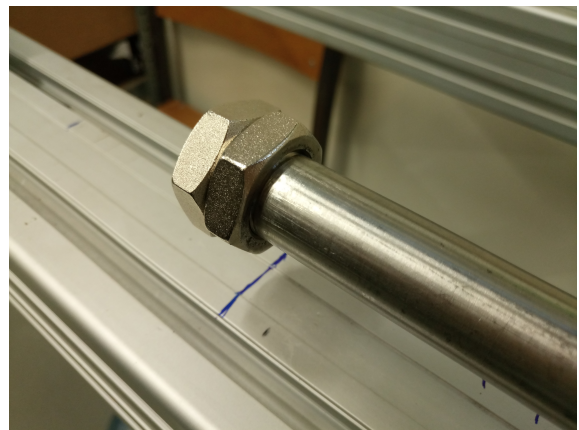


(b)

Figure 4.14: Threaded hole to attach the grip (a) and threaded end (b)



(a)



(b)

Figure 4.15: Non standard lock nuts (a) and their attachment to the threaded end of the incident bar (b)

To ensure that the axial strain distribution is constant over the bars entire diameter, Equation 3.1 is applied to the incident bar:

$$\frac{5700}{22} = 259.1 > 20 \quad (4.5)$$

And to the transmitted bar:

$$\frac{2850}{22} = 129.4 > 20 \quad (4.6)$$

The transit time calculated with equation (3.3) validates the condition to minimise the dispersion effect, since the pulse duration (Equation 4.2) should be 10 times larger than the transit time:

$$t_t = 4.05 \times 10^{-6} \text{ s} \quad (4.7)$$

Using Equation 3.17, the bars stress and strain can be determined:

$$\sigma_b = 254.9 \text{ MPa} \quad (4.8)$$

$$\varepsilon_b = 0.0013 \quad (4.9)$$

As the striker's velocity was determined considering the yield strength of the bars material, Equation 4.8 proves that the bars remain elastic during the test and the deformation caused by the incident wave is strictly linear-elastic. Thus, it can be concluded that both bars assure the 1-wave propagation theory described in Section 3.1, which is the base of the SHPB analysis.

With the dimensions of the bars known, consulting Appendix A for the specimen dimensions and using Equation 3.28, the transmission coefficient can be determined:

$$\alpha = 0.68 \quad (4.10)$$

#### 4.2.3.1 Bars holders and bushings

The bars holders are composed of two symmetric parts made of aluminium, with half hole in the middle of each (see Figure 4.16). As the other holders, the bars' holders also have chamfers on the extreme of each half hole. This configuration enables a better positioning of the bars, easing the process. The good positioning is accomplished with the use of dowels, since both parts have two holes located at a equal distance for the dowels. Therefore, the dowels serve as a guidance mechanism.

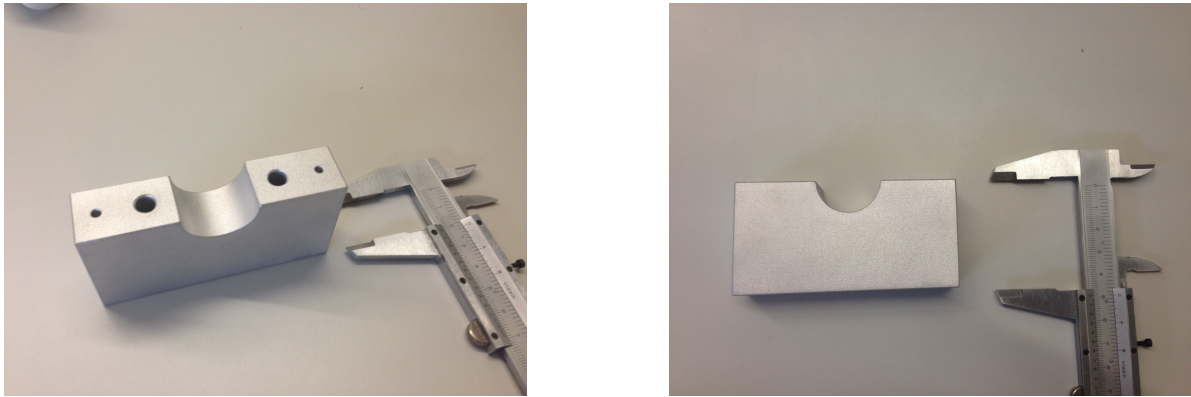


Figure 4.16: Bars holders

The complete middle hole formed with the assembly of both holders supports the bushing without any problem, due to the chamfers. The holders also have two through holes in order to fix them to the modular structure. Continuing, the holders are fixed to the *Bosch* modular structure with M6 screws and nuts with hammer head, enabled by the lowered counterbored holes and the guides on the modular structure. Furthermore, the bushings were designed with the aim to align the bars on the centre axis, providing a concentric and coaxial configuration of the equipment. The bushings are made of Teflon, so both bars move with low friction on the bushings surface. Thus, the bars are able to slide on the bushings interior diameter.





Figure 4.17: Bar's bushing (a) and assembled holders with bushing (b)

#### 4.2.4 Gripping System

One of the most discussed difficulties of the SHPB in tensile configuration is how to attach the specimen to be tested on the bars. The gripping system dimensions and the bars diameter are directly connected. Therefore, the specimen geometry depends directly on them. Furthermore, the grips must be designed to transmit the tensile force without the slipping of the contact surfaces and failure must not occur in the grip section. The variation of the mechanical impedance due to the introduction of the gripping system should be low so the incident wave propagation isn't affected [126, 110].

Axially symmetric specimens with threaded ends which engage on the threaded holes on the end of the bars can be used [53, 56, 54, 59], see Figure 4.18. Fine threads should be used to maximize the load transfer between the bars and the specimen. However, the threads cause wave reflections. Failure when removing the specimen is responsible for open gaps in the loading path since this connection results in an uneven loading of the specimen [126]. Nevertheless, this solution is not adequate for sheet metals since this kind of materials don't have any axial symmetry. Besides, it is incompatible with 2D DIC method use due to its curved surface.

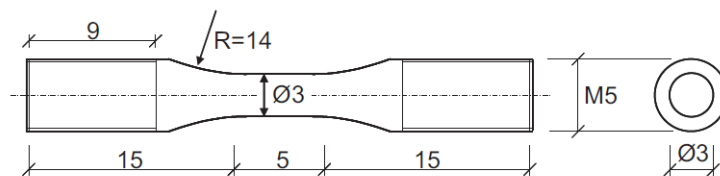


Figure 4.18: Axis symmetric specimen with threaded ends used by Chen et. al [56]

Other system consists on dog bone specimens with holes, so screws can be used to fix them in the bars slots, as presented in Figure 4.19 [127, 68]. Screws with small size should be used to minimize the mechanical impedance variation and to transfer the maximum possible load to the specimen. Despite this system being suitable for sheet metals, drilling holes in such a small specimen can lead to increase in stress concentrations. Also, there are stress concentrations created on the screws. The specimen design should be carefully studied to ensure it breaks away from the gripping zone. Furthermore, the air gap between the screw may lead to fluctuation and time delay, regarding the reflected wave. Thus, to minimize this effect a variant of this

system emerged wherein an epoxy adhesive is applied to seal the gap [87]. This system also may also be adapted to metallic endcaps, generally of the same material of the bars. In its turn, the endcaps have holes to screw the specimen. Thereafter, the endcaps are screwed into the bars [128].

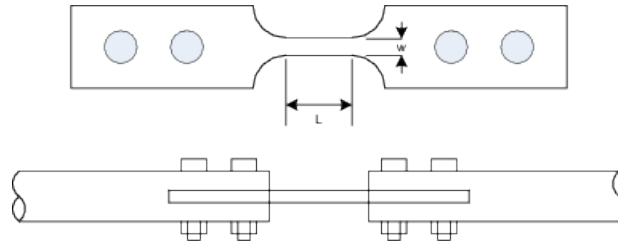


Figure 4.19: Specimen and gripping system used by Huh et. al [127]

Another technique dismisses the use of screws to fix the specimen in the slotted bars. The specimen fixation is accomplished through the use of adhesives, see Figure 4.20 [129]. Moreover, an alternative appeared wherein the specimen is adhesively bonded to threaded metallic endcaps, see Figure 4.21. These endcaps with the bonded specimen are screwed into the bars [128]. However, both of these techniques require time for the adhesive to cure before the test. After the test, the adhesive must be burnt so another specimen can be tested. This technique is more suitable for composite materials.

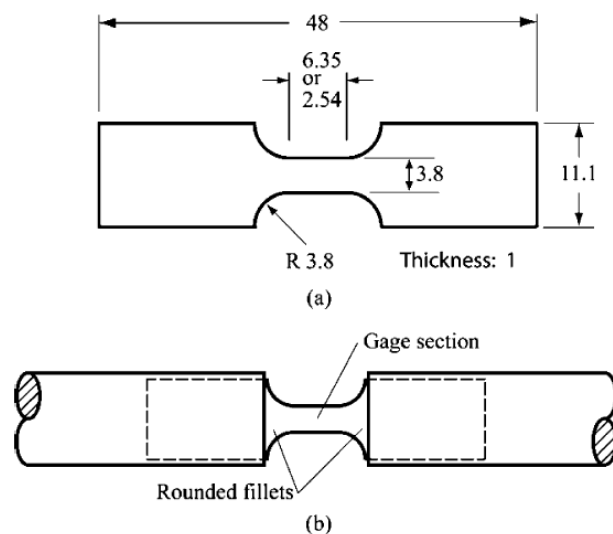


Figure 4.20: Tensile specimen (a) and its positioning at SHPB (b) [129]



Figure 4.21: Adhesively bonded specimen to threaded metallic endcaps [128]

#### 4.2.4.1 Development of the gripping system

Initially, three different gripping solutions were taken into account and were developed to design the gripping system. The first solution is based on the system used by Ferreira [110], where the grips are welded to the bars through the metal inert gas (MIG) technique to avoid significant variations of impedance. Specimens up to 2 mm of thickness are allowed to be tested (Figure 4.22). Thus, the grips possess a serrated surface, oriented  $87^\circ$  with the test direction, a pitch of 0,5 mm and an indentation angle of  $90^\circ$  as shown in Figure 4.23. The specimen's fastening is possible due to the use of six M4 screws whose clamping force is enough. Also, there are few mass alterations because the bars have a chamfer composed of three progressive chamfers and the distance between the welded grips on each bar is slowly reduced due to the groove's existence. However, if the welding between the bars and the grips is not precisely done some porosities or even significant mass alterations avoided by their geometry will probably appear.



Figure 4.22: Gripping system which uses screws to fix specimens with respective holes

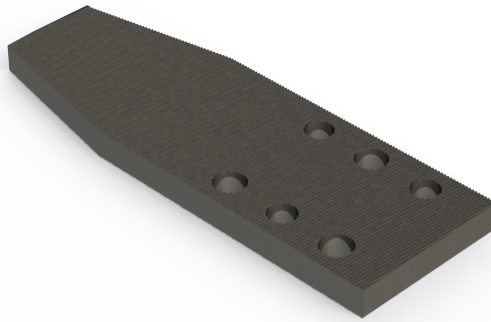


Figure 4.23: Grip serrated surface detail

The second solution is based on a form-fit gripping (Figure 4.24). The gripping system is composed by three different parts: the grip, the grip cover and a M4 screw. This solution requires strict geometric tolerance of the machined parts, specially the slot that supports the specimen and the cover. The depth and height of the respective parts mentioned are interlinked since the plates to cut the specimens present thickness variations. This solution also allows the specimens with thickness of 2 mm to be tested.

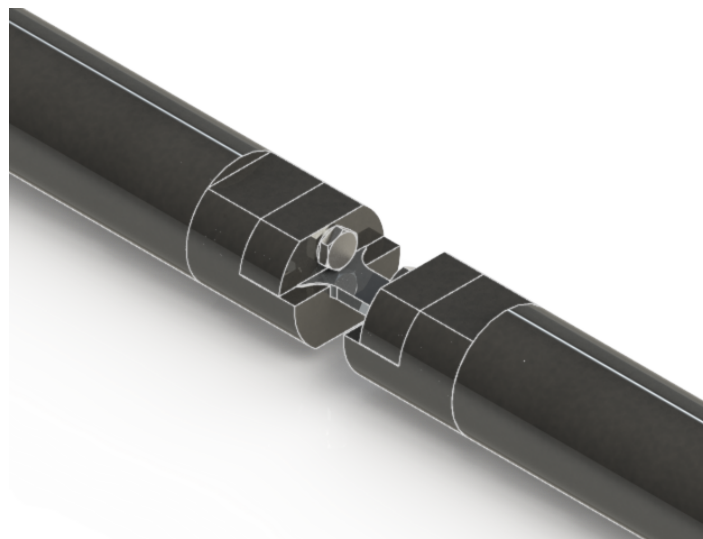


Figure 4.24: Form-fit gripping system

The third solution is based on the adhesively bonded specimen, described earlier. The bars have a threaded hole in order to match the threaded metallic grips which are shown in Figure 4.25. The grips attachment is made through the use of a wrench. However, this technique requires time to cure the adhesive and to burn it after the test, increasing the time of preparation and exchange of the specimen. Further, it doesn't provide a good alignment of the specimen between the bars and has a higher cost compared to the other two systems considered. Nevertheless, the external diameter of the grips is smaller than the bars diameter to allow the attachment. This will cause a variation of mechanical impedance, aggravated due to the threaded connection. As the other two solutions mentioned previously, this allows specimens with 2 mm of thickness to be tested.

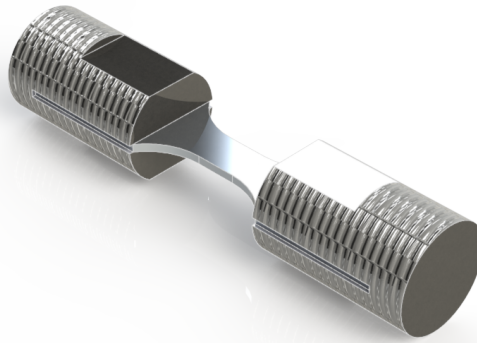


Figure 4.25: Adhesively bonded specimen with threaded metallic grips

The choice of the gripping system was based on Ledford et. al [128] investigation. These authors studied the influence of the specimen mounting and its design on high strain rate tests, using SHTB and DIC. The authors considered three different mounting systems: adhesively bonded endcaps, metallic endcaps with holes to screw the specimen and form-fit grips.

The nominal stress and nominal strain were plotted for the three methods, see Figure 4.26.

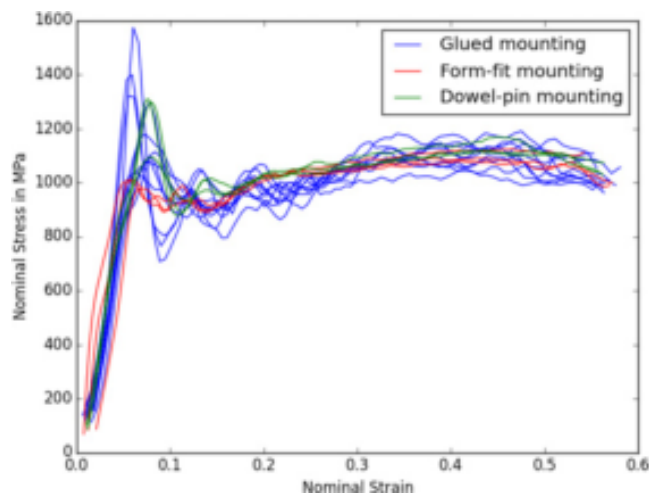


Figure 4.26: Nominal stress strain curves for the three different mounting systems considered [128]

Observing Figure 4.27, there were different amounts of oscillation for each method, being the form fit mounting the method with less oscillation. The authors also studied the strain rate of the measured specimens strain, with a striker velocity of  $12\text{ m/s}$ . It was noticed that during the test there was a drop of the strain rate, with the form-fit having the higher drop. Possibly, it might be due to mounting deformations.

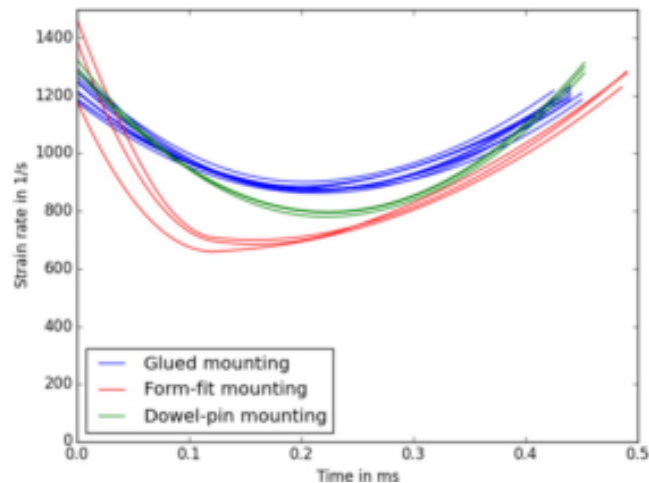


Figure 4.27: Strain rate with the different systems [128]

All the three methods studied by Ledford et. al were assumed to give reliable results. Although the form fit had the higher drop of strain rate, the best results were obtained with this method. Also, it was cost effective and gave the best signal for sheet metals.

Thus, after this important research became clear that the author of this thesis should focus on the improvement of the second gripping system: form fits grips. Regarding this system, three variants emerged. The first variant, which is shown in Figure 4.28, consists on a grip with two planar surfaces placed diametrically so a wrench can be used to attach it to the bar. Further, the cover lies on the entire top of the machined slot who supports the specimen. It is attached to the grip through the use of a M4 screw on its front face. Accordingly, the machined slot has a depth of 1.8 mm and allows specimens with 2 mm of thickness to be tested. Such is possible due to the height of the cover which permits some fluctuations regarding the thickness of the plate which is used to cut the specimens. Although, a good positioning of the grip cover can't be accomplished due to the location of the screw responsible for attaching both grip and grip cover if variations of the specimens thickness appear. Also, there are only two back faces between parts.

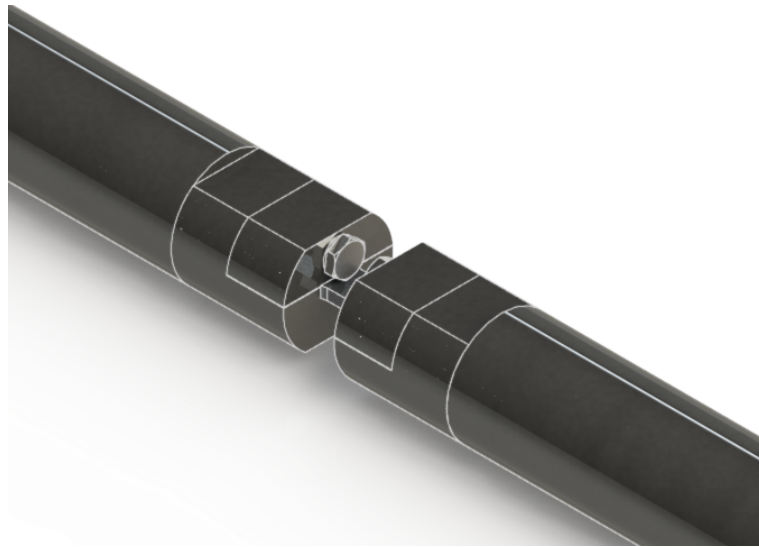


Figure 4.28: First variant of the chosen gripping system

So, in order to solve the problem exposed, a second variant emerged. This variant introduced a different form of the grip cover where the attachment of it to the grip is made on its top through the use of a M4 screw. Figure 4.29 presents an illustration of the system. The attachment of the grips to the bars is made as explained for the other systems, using a wrench. Nevertheless, to enable the use of this system, demanding geometric tolerances must be applied to guarantee a good back between the grip and grip cover, since there are three back faces.

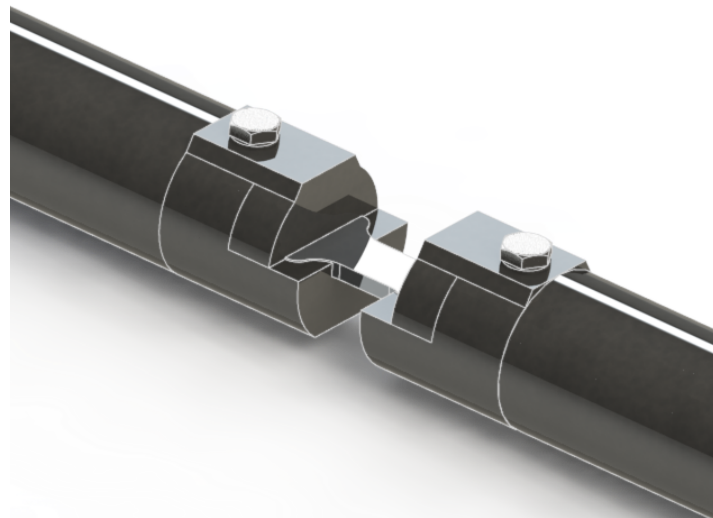


Figure 4.29: Second variant of the chosen gripping system

Not satisfied with the second variant because of the existence of only three back faces between the grip and grip cover, the last and third variant appeared. Further, it presents a different form of the grip cover which aimed to overcome the problems generated due to the back between parts. Therefore, a step is designed on the grip after the machined slot to assure that despite of the variations of the specimens thickness, a good positioning and back between

parts exist. After the step, dimensions of the slot are precisely thought to enable the grip attachment through the use of a wrench. Such is possible because there is another slot placed opposed diametrically. The grip cover has one slot and two steps with the appropriate dimensions to meet the grip step and the slot after it, respectively. Thus, a good back between parts, with the application of the required geometric tolerances is achieved. Accordingly, the part of the grip cover which is in direct contact with the specimen has a height which allows significant variations of the cut specimens. Thereafter, this system can overcome the problems caused by the thickness variation of the plates used to cut the specimens and a good positioning between parts can be accomplished.

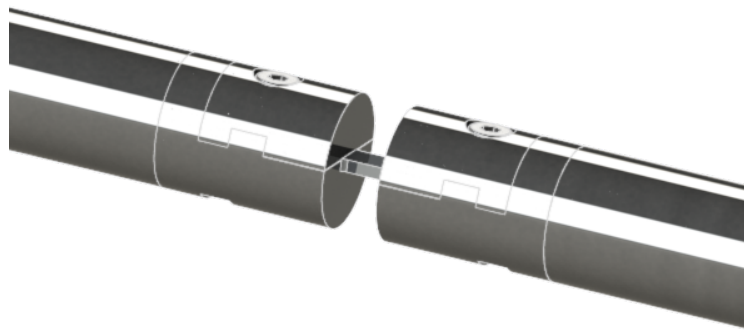


Figure 4.30: Third variant of the chosen gripping system

Hereupon, the third variant was considered for the development of the gripping system and it is followed by a detailed description. Hence, the grip has a cylindrical shape with the same diameter and the same material of the bars (Figure 4.31). Therefore, the mechanical impedance variations are minimised and the wave propagates with the same velocity, since the material is the same. The grip has a machined slot according to the non-gage dimensions of the specimen as shown in 4.32. Grip, grip cover and specimens must be precisely machined because the tapered section of the grip transfers all the load to the tapered section of the specimen. It is evident that this will create stress concentrations and the geometry of the parts is very important for a successful use and so, good results. The grip cover (see Figure 4.32) plays a very important role, since it prevents the specimen from coming out of the grip machined slot and it is also made from the same material of the bars. Further, the depth of the machined slot and the height of the grip cover were made to support specimens with 2 mm of thickness, seeing that the plates to cut the specimens to be tested might suffer thickness variations as aforementioned. The dimensions were planned to coincide the centre axis of the bars with the axis of the specimen. Geometric tolerances were applied to both grip and grip cover to assure the parts meet without any gaps, responsible for generating variations of the mechanical impedance. The grip cover has a through hole, enabling its connection to the grip with a small screw, M4, for the same reason of the application of the geometric tolerances: minimise variations towards mechanical impedance. The grips have a threaded end with a smaller diameter,



M18×1.5, which permits the attachment to the bars and also serves as a sealing. Each grip has two slots placed diametrically, positioned at such a distance to allow the use of a wrench to attach it to the bar. One of the slots is coincident with the face where the grip cover lies.

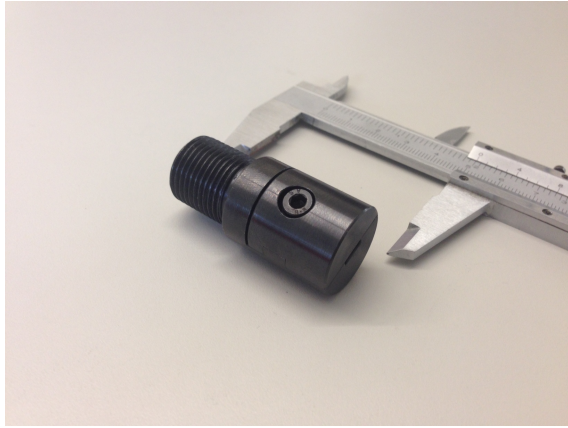
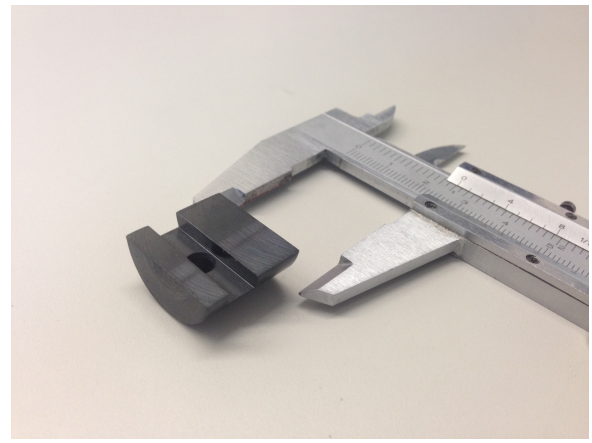


Figure 4.31: Grippings



(a)



(b)

Figure 4.32: Gripping (a) and grip cover (b)

This system allows the use of grips with different geometries from those described. This flexibility may be considered an advantage. Also, the gripping system can be improved to test different kinds of materials. So, in order to test the specimens with overlap joints, the gripping system was adapted to provide the use of thickness compensators (see Figure 4.33). These thickness compensators align the axis of the specimen with the centre axis of the bars. The depth of the machined slot is machined to support specimens up to 4.2 mm of thickness due to the thickness of the plates and adhesive. The height of the grip cover is also planned to be aware of the variations of the plate and adhesive thickness. The connection of the grip and the grip cover is made through the use of a M4 screw, too. Further, the grip also possesses two slots placed diametrically with the same intent of the previous grips.

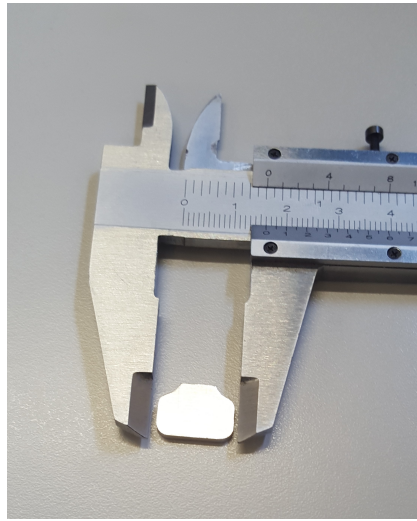
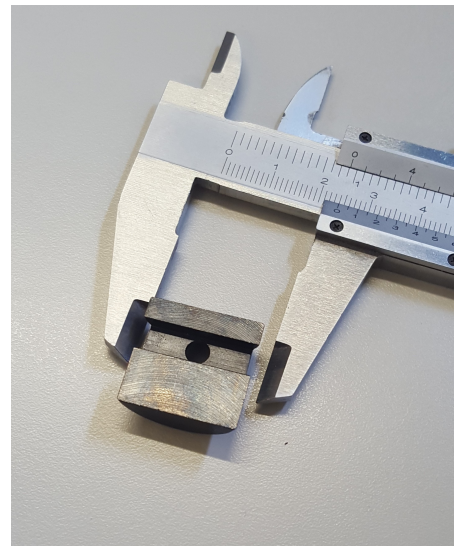


Figure 4.33: Compensator



(a)



(b)

Figure 4.34: Gripping (a) and grip cover (b) for overlap joints

#### 4.2.5 Energy dissipation system

The energy dissipation system is responsible for absorbing the kinetic energy and the stress waves. This happens because the energy supplied by the gas gun is greater than the energy absorbed by the specimen deformation. Although the test ends after the first passage of the incident wave, the residual energy of the three pulses is stored in the bars.

Also, the energy dissipation system has the purpose to interrupt the test if it surpasses the predetermined strain rate, maintaining the bars in the elastic domain. This way, only the first tensile loading is applied to the specimen. Accordingly, the system is composed by five parts. A tube with the same exterior diameter and material of the barrel in order to maintain impedances, with 2 mm of thickness is welded to a plate. The plate has four through holes in

order to enable the fixation to a *Bosch* profile with the use of M6 screws. Inside the tube there are layers of cork, with 1.5 mm of thickness. After the cork, a round piston made of Nylon is placed. This piston has an exterior diameter equal to the interior diameter of the tube and slides inside it when receives the impact of the anvil and incident bar.

### 4.3 Strain gauges design

Using the 1-wave propagation theory, it is correct to say that the strain measured on the bar surface is the same strain on the bar centre. Placing strain gauges at the bars surface, it is possible to determine the amplitude of the incident, reflected and transmitted waves. However, the strain gauges placement should be extremely careful so the measured amplitudes are not under the influence of parasitic capacitance effects. In turn, these amplitudes are employed to determine the specimen strain and stress.

The bars instrumentation is done using electric strain gauges, in half Wheatstone bridge. The strain gauges per bar are employed and bonded to the grid surface on the same section. Strain gauges are placed diametrically opposed with the grid parallel to the bar axis. To minimize the noise and cable effect, the cables correspondent to the axial and transversal strain gauges were braided respectively, concerning each bar.

The selected strain gauges are from HBM, with reference 1-XK51E-3/350, have a resistance of 350  $\Omega$  and a gauge factor of 2.06. This value of resistance is suitable for dynamic applications, allows the use of greater excitation stresses and has a greater output signal. Further, its value enables the use of the most part of signal conditioners to attain the equilibrium of the Wheatstone bridge. The strain gauges are bonded to the bars with HBM Z70 adhesive. The distance from the bridge to the specimen in the incident bar is 2400 mm, while the distance from the specimen to the bridge in the transmitted bar is 330 mm. For recording signals with a good ratio of signal/noise, it is necessary a good ground connection.

After the installation, the strain gauges were checked with the *Strain Gage Installation Tester Vishay Model 1300* and with the multimeter.

### 4.4 Signal processing

It is very important to process the signal with extreme precision, since the tests have a very short duration in the order of milliseconds. Thus, the signal conditioners should operate on a range of frequency compatible to those of the tests. The quality of the signal is crucial for a good application of this technique.

#### 4.4.1 Signal conditioners

As explained before in Subsection 3.1.5, the signal conditioners must possess a band width of 100 *KHz*, at minimum. The operate frequency of the signal conditioners should be compatible with the duration of the test, which it is of the order of milliseconds.

The *Vishay 2200 model* was the signal conditioner considered to be used in this work. It has a band width of 100 *KHz* to -3 *dB* and a gain from 1 up to 3300, allows the use of 350  $\Omega$  strain gauges and feeds the measuring bridge with voltages up to 10 *V*. However, after following all the instructions given in the manual and due to laboratory conditions such as high levels of noise, it was impossible to achieve the circuit balance. Initially, the impossibility of achieving circuit balance was thought to happen because of an inappropriate determination of the gain

and consequent setting. Thus, the determined gain value was verified and it was properly determined. Also, the impossibility to achieve the circuit balance could be caused by a wrong connection of the wires to the proper input pin. Hereupon, all the connections were verified too and they were correct. As stated before, there were high levels of noise in the laboratory since there were several operating equipments. It was tried to increase the gain slightly, since it should be able to offset noise effects but there were no improvements. Posteriorly, the major part of the operating equipments were turned off but it wasn't enough. Proceeding, it is known that the circuit balance can be obtained with the Auto Bal Switch reset. During the auto balance interval, by reducing the amplifier output, the instrument tries to achieve the circuit balance. After, a red light appeared in the led indicator meaning that *the bridge unbalance is outside the range of the balance circuit* [130]. After this event, proper data can't be obtained. Therefore, there weren't any results to analyse.

After, another solution was put to test regarding the *National Instrument 9237* module. This module has four channels with  $50\text{ kS/s}$  per channel, an analog input resolution of 24 bits, an accuracy of  $0.0375\text{ mV/V}$ , simultaneous sampling, allows different values of excitation voltage from  $2\text{ V}$  to  $10\text{ V}$ , provides bridge configurations for full, half and quarter bridge and has anti-aliasing filter, bridge completion and voltage excitation. Once again, it was impossible to record any signals of the designed SHTB as the noise level was higher than the signals recorded with the strain gauges.

Hereafter, with the collaboration of engineer Jorge Reis, a circuit was built from scratch in a breadboard with the aim to filter the high noise levels of the laboratory, with the differential to unipolar characteristic. This circuit possesses its own linear voltage power supply (Figure 4.36), with its own noise filter, which is then converted to current power supply. Any temperature effects regarding the strain gauges are eliminated. It provides bridge completion and its gain was properly setted considering the used filters. Figure 4.35 shows the used circuit to acquire proper data.

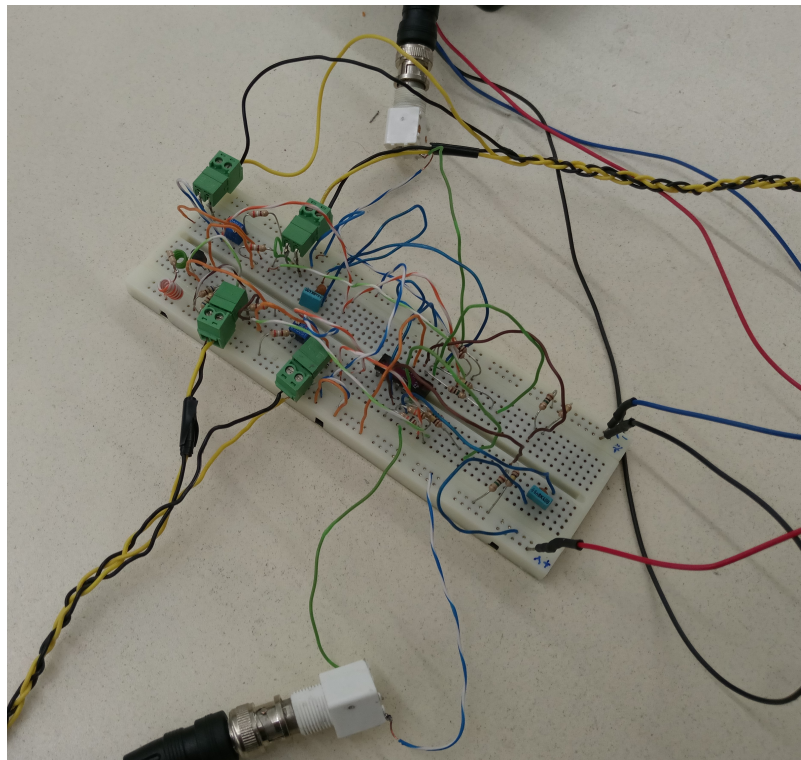


Figure 4.35: Used breadboard circuit to acquire data

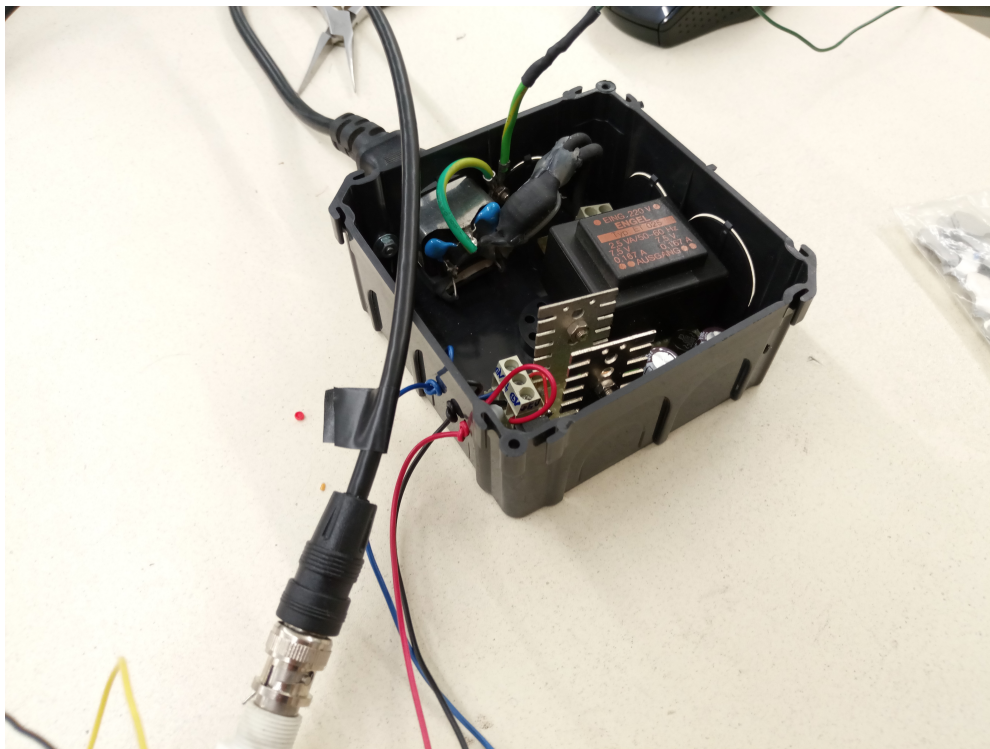


Figure 4.36: Voltage power supply

#### 4.4.2 Data acquisition

Since the tests are performed at high frequencies and have short duration, the data acquisition is made using oscilloscopes. If the events had long duration and low frequency, the use of data acquisition cards placed at personal computers were more suitable. In contrast, the oscilloscopes have low pass filters and offer different values for the input impedance. The low filters have the function to eliminate noises. If a low value for the input impedance is chosen, there's a bigger trigger stability and a noise filtering. However, the signal conditioner should debit an electric current in the range of  $20\text{ mA}$ , regarding the signal voltage. If a high value for the input impedance is chosen, signal conditioner with low power can be used, providing an operation with greater gains.

The oscilloscope used in this work is the *PicoScope* USB oscilloscope 4224 model with two channels, bandwidth of 20 MHz, has a 12 bit resolution, a sampling rate of 80 MS/s and buffer memory of 32 MS (Figure 4.37).



Figure 4.37: *PicoScope* USB oscilloscope

However, despite being brand new, the *PicoScope* showed mechanic problems, more specifically with the input probes. These probes were a bit loose which affected the connections with the BNC cables, since any movement of each cable itself affected strongly the signal which was being read.

#### 4.4.3 Trigger

The trigger is directly done by the incident wave pulse, with an adequate value for the pre trigger. This value takes in consideration the inherent noise of the laboratory and the circuit sensibility.

The bars length and their slide on the respective bushings generate electrostatic loadings. In its turn, these loadings generate peak voltage. Thereupon, these effects can be minimised and controlled if the bars are previously discharged, if a ground connection of the three bars is made, using a low pass filter or using an input impedance of  $1\text{ M}\Omega$  [110].

# Chapter 5

## Experimental Work

### 5.1 Introduction

This Chapter aims to present the experimental results obtained with the designed split Hopkinson tension bar set up introduced in Chapter 4. Results were analysed for base material, overlap joints and butt joints obtained through FSW. The AA6082-T6 alloy was the chosen material to be tested due to its increasing use in the several industries mentioned in Section 2.1 and Section 2.2 and due to current ongoing research within the workgroup on friction stir welds using this alloy. Its chemical composition and mechanical properties are presented in the Table 5.1 and Table 5.2, respectively.

Chemical Element	% Present
Aluminium	95.2-98.3
Manganese	0.40-1.00
Iron	0.0-0.50
Magnesium	0.60-1.20
Silicon	0.70-1.30
Copper	0.0-0.10
Zinc	0.0-0.20
Titanium	0.0-0.10
Chromium	0.0-0.25
Residuals	0.0-0.15

Table 5.1: Chemical composition of AA6082-T6 aluminium alloy [131]

Properties	Values
Volumetric mass density	2.71 g/cm <sup>3</sup>
Young's Modulus	71 GPa
Ultimate tensile strength	140-330 MPa
Yield Strength	90-280 MPa
Thermal expansion	23.1 $\mu\text{m}/\text{m}\cdot\text{K}$
Solidus	575 °C

Table 5.2: Properties of AA6082-T6 aluminium alloy [131]

The tested butt joints and overlap joints were welded in parallel and perpendicularly to the rolling direction. The welds were performed in the ESAB LEGIO<sup>TM</sup> 3UL machine, with a pin of 5 mm of diameter and a shoulder with 11 mm of diameter. In one hand, the butt joints welds were performed with the following welding parameters: 1000 rpm, 150 mm/min and 260 kgf. On the other hand, the overlap joints were performed with the following welding parameters: 1000 rpm, 200 mm/min and 450 kgf.

In order to validate the experimental set up results and to adjust parameters such as the compressor pressure and therefore, air chamber pressure, divers specimens were cut from a shot blasting plate supplied by LOME. Using the PHOTRON *Fastcam SA4*, high speed videos were recorded for later inspection, analysing the specimen rupture and to determine the adequate pressure for the failure occurrence on the first impact. In other words, to avoid a small recovery of the material in the elastic domain. This procedure also allowed the determination of the correct positioning of the incident bar along the modular structure. All the results were obtained with a sampling rate of 80 MS/s and 16 bits of resolution.

Thereafter, a threaded part was used to verify if the wave propagation was similar on both bars, more precisely to confirm if the strain gauges were properly mounted in order to allow an interference free record of the waves. This part had the feature to unite both bars so that a single bar is formed and its length is equal to both grips lengths, see Figure 5.1. Its dimensions are shown in Figure 5.2. Figure 5.3 provides an illustration of the wave recorded with the incident bar and transmitted bar strain gauges.



Figure 5.1: Threaded part



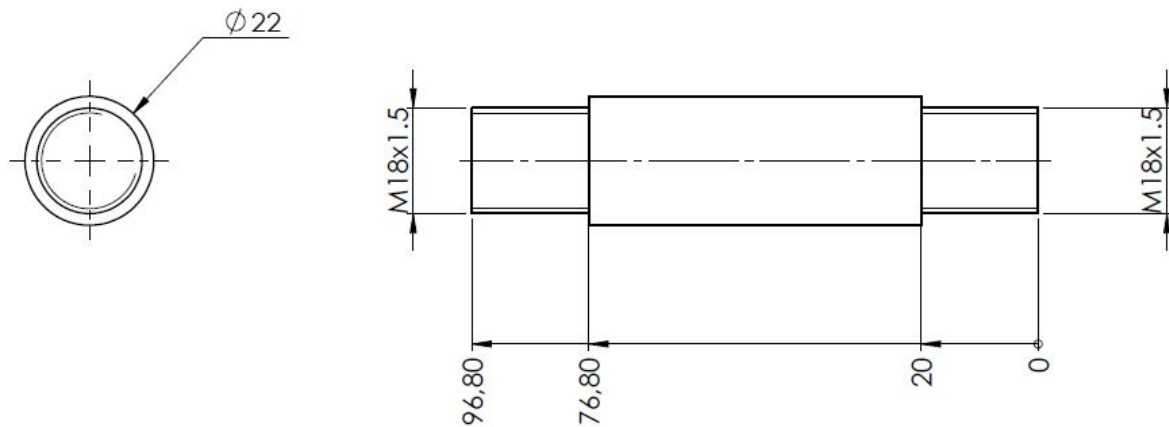


Figure 5.2: Threaded part dimensions

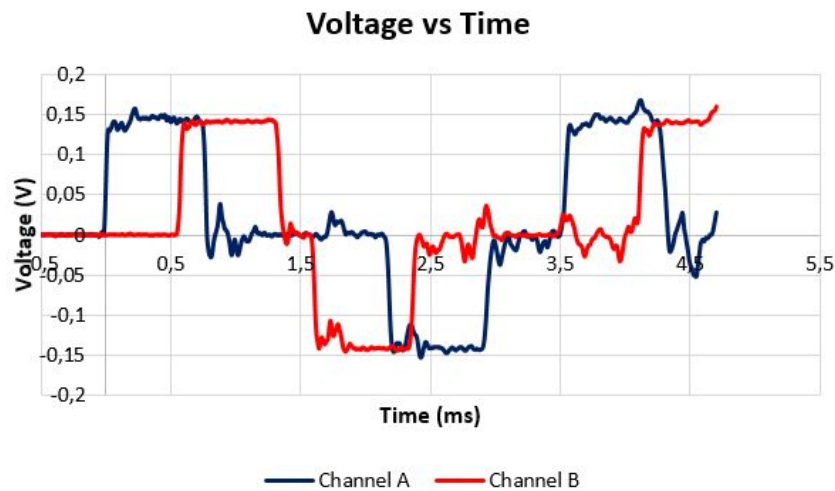


Figure 5.3: Wave recorded with the calibration part

As expected, the wave recorded with both bars strain gauges were similar. After checking the correct assembly of the strain gauges, it was necessary to proceed to the calibration of the experimental set up. This calibration consisted on the determination of the real elastic wave velocity. The value of the elastic wave velocity is obtained taking into account the Young's modulus of the bar and its density. However, that value can only be properly calculated if the time, that the incident wave takes to reach the specimen and to reflect until the respective strain gauge,  $\Delta t$ , is well determined. Nevertheless, the reliability of the determination of that period depends on the experimentalist. Thus, the calibration of the Young's modulus which is one of the most important parameters in the SHPB analysis can be determined with Equation 5.1 [132].

$$c_0 = \frac{2\Delta l_{SG1}}{\Delta t} \quad (5.1)$$

After calculating the real value of the elastic wave velocity, the real Young's modulus is determined consulting Equation 3.7. Any small deviations of this important parameter can lead

to significant discrepancy of the obtained results, since its directly connected to the calculus of the stress, strain rate and finally, strain. Thus, good judgement strongly influences the ability of choosing the start and end of each wave [133].

Subsequently, the data acquired with the initial specimens was recorded and analysed with an open source software, the *SUREPulse* software.

## 5.2 Data analysis with the *SUREPulse* software

For the analysis stage, first it was necessary to learn how to work with the *SUREPulse* software. Its menu is composed of four parts: *Bar Setups*, *New Sample*, *Analyze Results* and *Change/Create* to alter the workspace as shown in Figure 5.4.

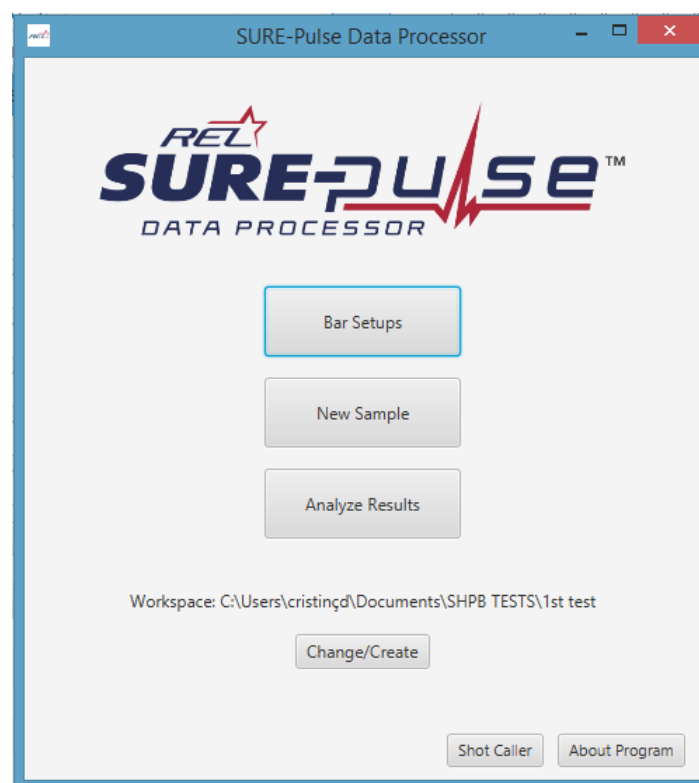
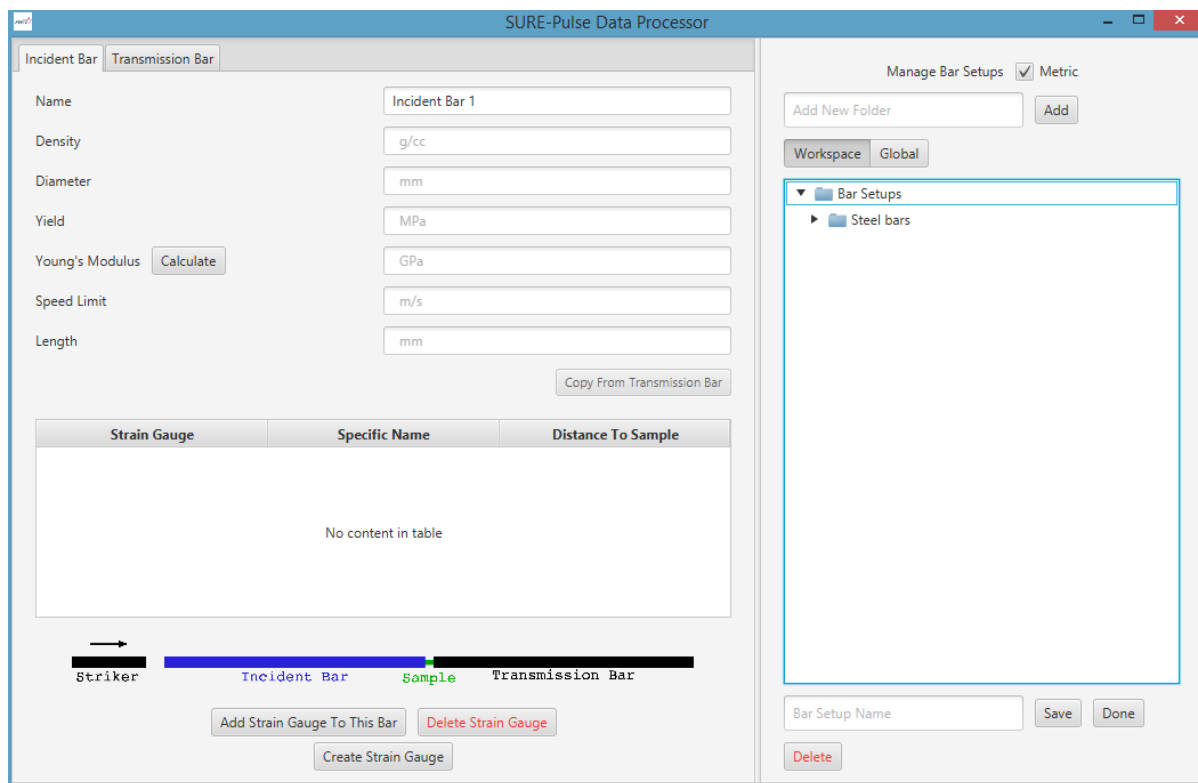


Figure 5.4: *SUREPulse* menu

First, a bar setup had to be created selecting the *Bar Setups* option where the mechanical properties of both incident and transmitted bars used were entered as shown in Figure 5.5. Following, strain gauges had to be added to each bar. But first, it was necessary to create one with the *Create Strain Gauge* option where the values of the respective resistance, grid length, voltage calibrated, gauge factor and shunt resistance were put. Continuing, with the *Add Strain Gauge To This Bar* option, the intended strain gauges were added to the bars according to their distance to the sample. With these steps, the created bar set up was ready to be saved by selecting a folder and a name for the set up on the author's preference.

Figure 5.5: Creating a bar setup in *SUREPulse*

Thereby, the author was ready to select the *New Sample* option where the mechanical properties of the tested sample were requested in the *Sample Parameters* tab. On the *Bar Setup* tab, the set up in which the sample was tested was selected. Afterwards, the data acquired with the *PicoScope* was loaded in the *Load Data* tab where the columns correspondent to time, incident bar voltage and transmitted bar voltage were selected, taking into account the measuring units. It should be noticed that an interpreter can be saved to automatically choose the type of each column. With the *Trim Data* tab, the beginning and ending of each pulse was selected with the help of proper zoom. Subsequently, there are other options such as the zero of each wave which must be done before selecting its beginning and ending. If there is too much noise a lowpass filter can also be applied. With all the sample parameters correctly entered and with the data properly trimmed, the author was ready to save the sample in the *Save Sample* tab and continue to the *Analyze Results* option. In Figure 5.6 all the tabs mentioned for the *New Sample* option may be observed.

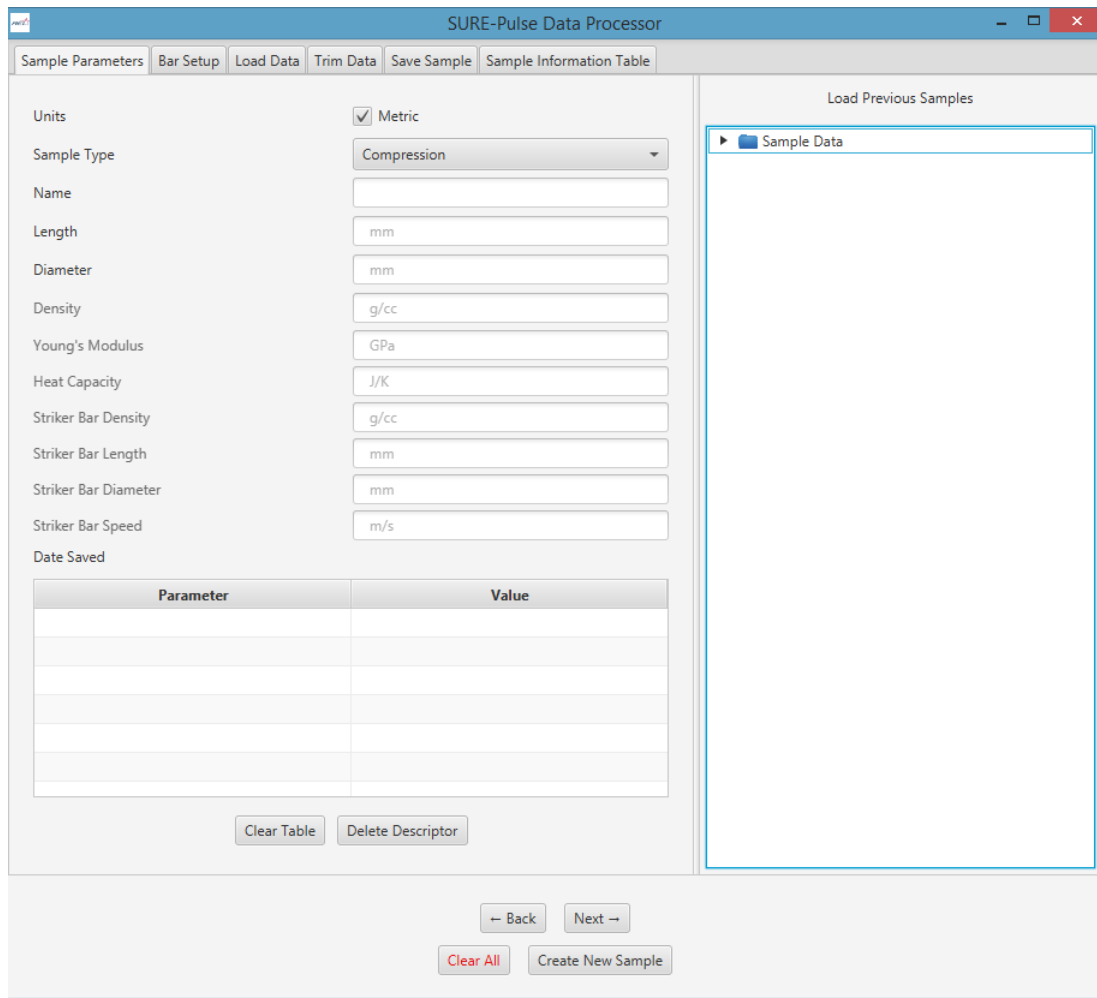


Figure 5.6: Creating a sample on *SUREPulse*

In order to analyse the results, the sample or samples to analyse should be selected. When the selected sample or samples appeared on the left side correspondent to *Currently Loaded Samples*, it should be verified if the samples to be analysed were with a check. Only then the author could proceed to the *Charting*, Figure 5.7, where the graphics of *Stress Vs Strain*, *Stress Vs Time*, *Strain Vs Time*, *Strain Rate Vs Time*, *Face Force Vs Time* and *Load-Displacement* graphics were shown according to the author's preferences. It should be noticed that the *Stress Vs Strain* graphic was the most relevant, since the others were only used to confirm if the waves were well selected. Also, *Data Modifiers* and *Region of Interest* can be applied. Assuming that the results were obtained, they were exported with the *Export* option to an excel or *csv* file.

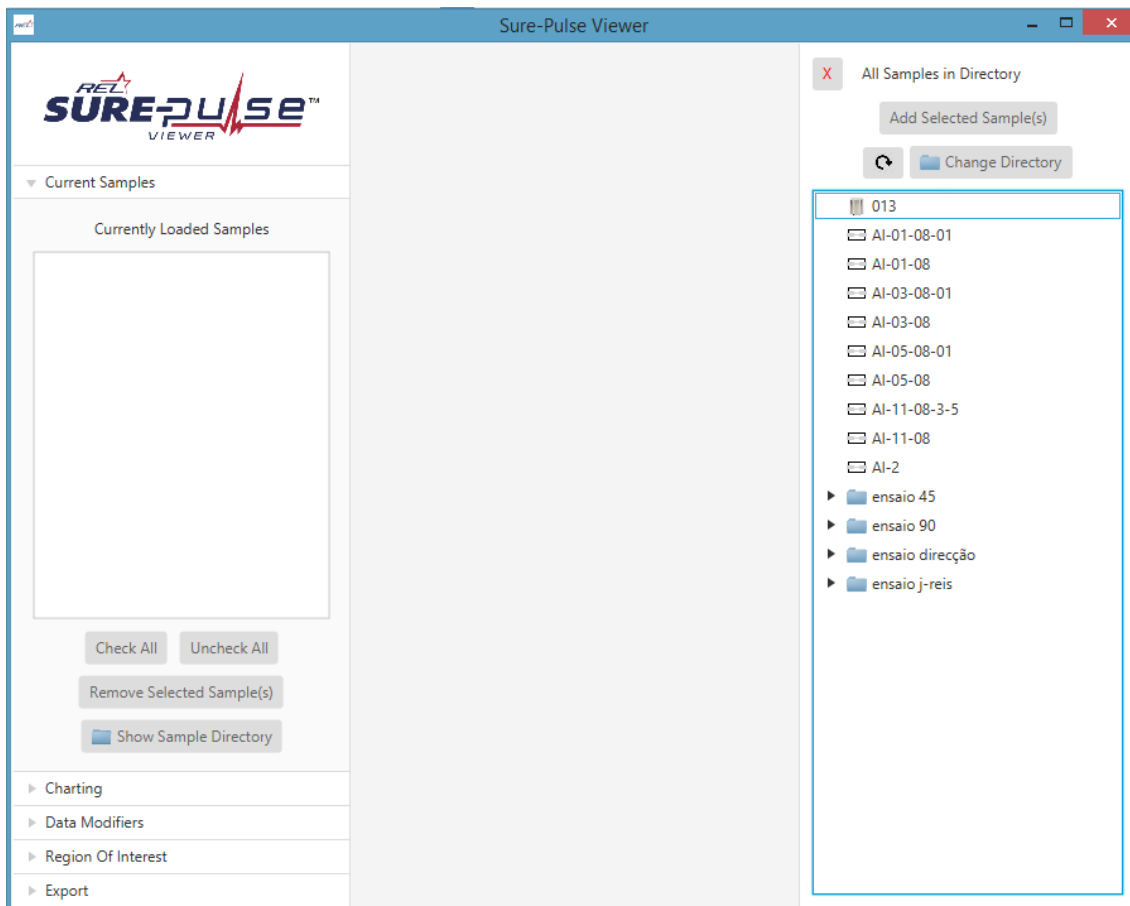


Figure 5.7: Analyzing samples on *SUREPulse*

For further details, the *SUREPulse* instruction manual should be consulted [134].

### 5.3 Considerations and Results

As aforementioned, several experiments were performed so the values of the parameters such as the compressor and the gas gun pressures, the incident bar positioning along the modular structure, the necessary torque to tighten the grips screws and the necessary and proper electrical potential difference trigger value could be ascertained. For that, the specimens cut from a AA6082-T6 plate were used and the data obtained was recorded for posterior analysis. Figure 5.8 shows the specimen used in this work while figure 5.9 shows its dimensions.



Figure 5.8: Specimen

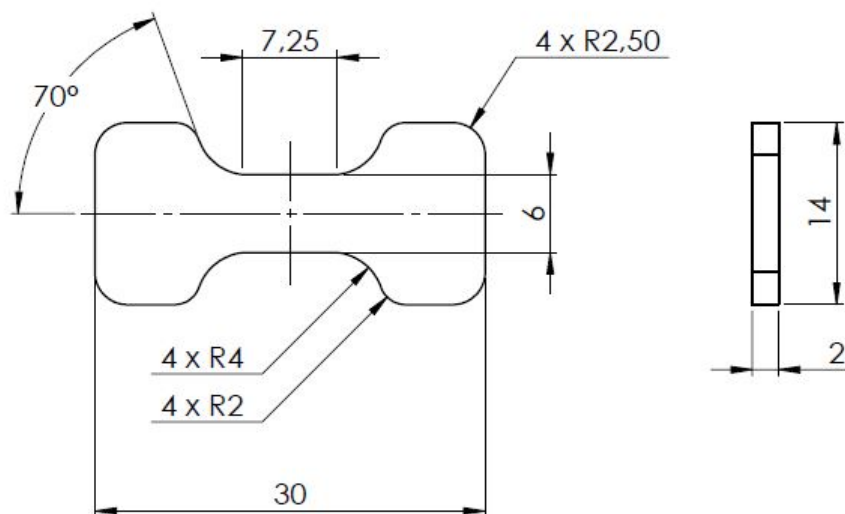


Figure 5.9: Specimen dimensions

Its geometry should provide the failure occurrence out of the gripping section, favoured by the specimen gage (see Subsection 4.2.4). Only this way, the test is valid. Thus, several specimens were placed on the grips with the respective covers and screws (Figure 5.10) in order to be tested. Further, the parameters were being varied until the optimum value for each one was reached. Afterwards, tests with all the optimum parameters combined were performed and a good match between all of them was observed. It is noteworthy that all the signals obtained after ascertain all the parameters were repetitive.

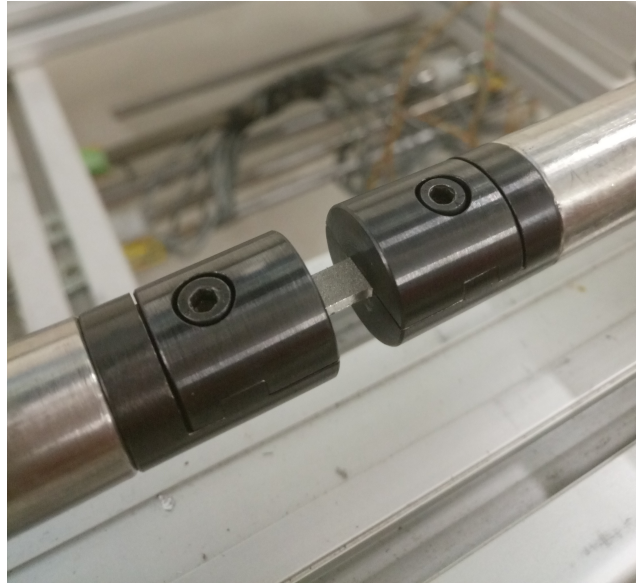


Figure 5.10: Specimen to be tested after the parameters determination

Therefore, it was concluded that the compressor needs to be loaded with 6 bar before performing every test, while the air chamber needs 3.5 bar at least. This value is the minimum value for the failure to occur in the first impact of the striker on the anvil of the incident bar. It was verified that for pressures greater than 4 bar, the grips tend to loosen up of the bars and they need to be attached again with the proper wrench. This event is responsible for causing some oscillations in the incident wave. Since the signal conditioner amplifier was very sensitive, it was recommended to load both compressor and air chamber before setting the single trigger event on the software of the *PicoScope* whose recommended value is 75 mV at 10 %. The amplifier is capable of sensing the vibrations induced by the compressor. The length of the transmitted bar cables were reduced in order to lower the noise level. In some experiments, it was noticed that the screws tend to get loose. Therefore, such occurrence was prevented by tightening the screws with 3 N.m using a torque wrench, as shown in Figure 5.11.

Finally, it was necessary to calculate the shunt resistance so the voltage values could be converted to strain. Therefore, its value was calculated with Equation 5.2 [135].

$$V_s = \frac{250}{\frac{R_s}{R_b} + 0.5} \quad (5.2)$$

where  $V_s$  defines the simulated output at signal leads,  $R_s$  is the shunt resistance value and  $R_b$  is the bridge resistance.

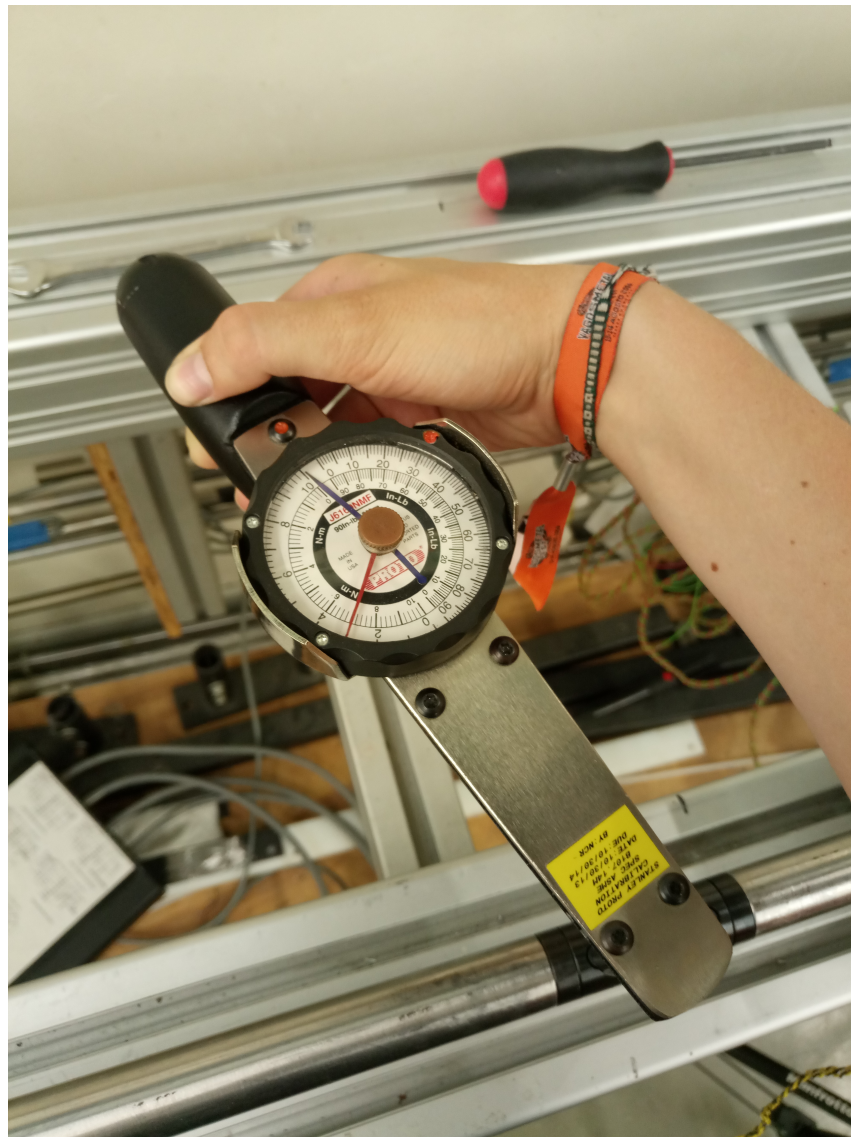


Figure 5.11: Torque wrench used for tighten the screws

With all the parameters ascertained, the first results concerning the first samples were acquired and analysed following the steps presented in Section 5.2.

An example of a recorded signal with the oscilloscope is shown in Figure 5.12. The signals obtained with both strain gauges can be observed. It is important to remember that the signal obtained with the incident strain gauge represents the incident and reflected wave and the signal obtained with the transmitted bar strain gauge represents the transmitted wave. Some oscillations on the rectangular shape of the incident wave were noticed, with a particular peak at 0.2 V and 0.19 ms, while a peak between the incident and transmitted pulse appeared at 0.033 V and 0.93 ms. This last peak shouldn't exist, being its normal form linear. The first peak may be caused due to the threaded connection between the incident bar and its grip. The second peak may be caused by the lock nut. Such happened due to the mechanical impedance variation towards the lock nut outside dimension and the bar diameter.



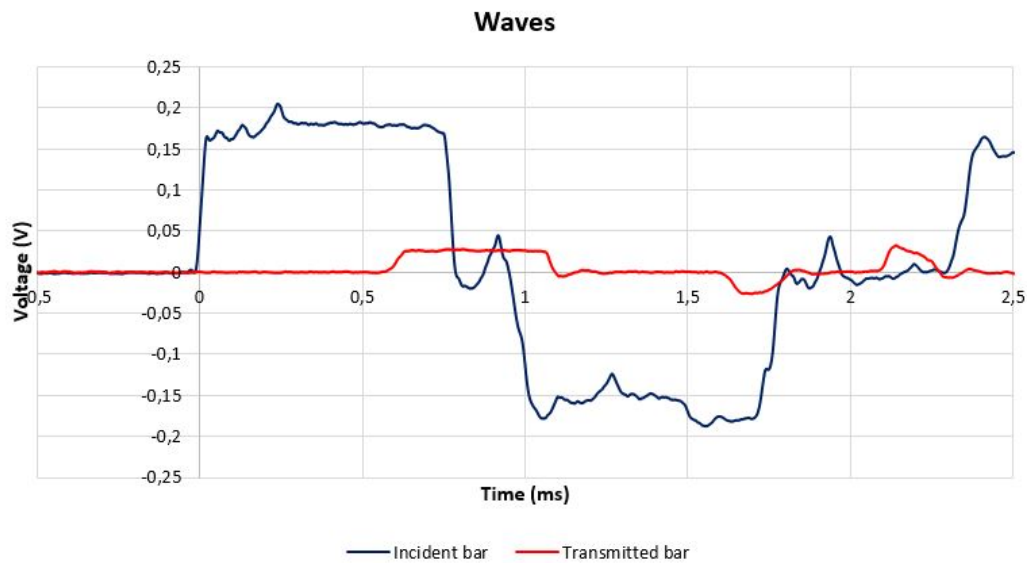


Figure 5.12: Recorded waves for the first test

Following the steps introduced in Section 5.2, the first graphic for stress vs strain was obtained as can be seen in Figure 5.13. The achieved strain rate was in the order of  $560.8 \text{ s}^{-1}$ , while the ultimate engineering stress was in the order of 348 MPa.

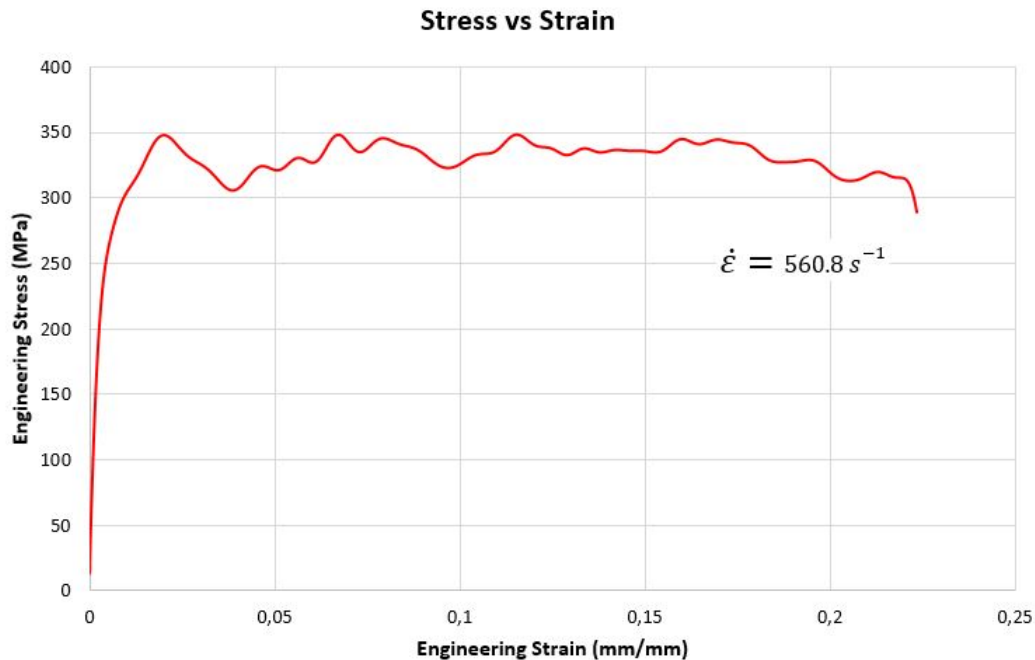


Figure 5.13: Stress vs strain curve obtained for one of the first samples

Nevertheless, the results obtained through the software were verified. The signals were zeroed and cut properly, considering the time of the impulse (see Equation 4.2) and the point that each one crossed the horizontal axis (see Figure 5.14). Therefore, using Equation 3.38,

Equation 3.47, Equation 3.51 and Equation 5.3 as follows, the values for stress, strain rate and strain were respectively determined.

$$\text{Strain} = \text{Voltage reading} \times \frac{\text{Gauge Resistance}}{\text{Voltage calibrated} \times \text{Gauge factor} \times (\text{Gauge resistance} + \text{Calibration resistance})} \quad (5.3)$$

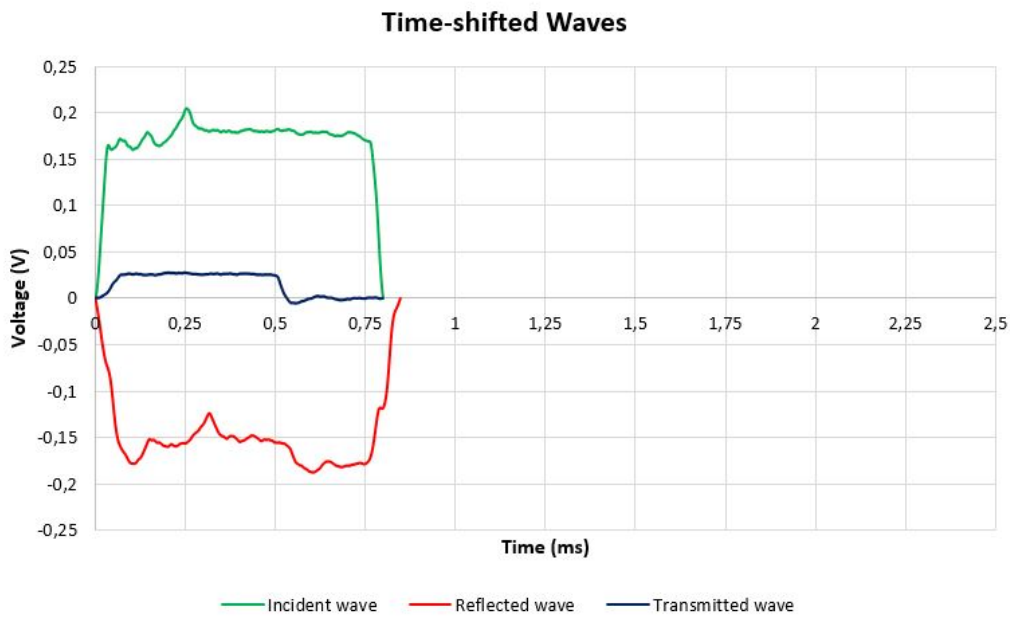


Figure 5.14: Time-shifted waves

With the values represented in Figure 5.14, it was possible to verify the statement presented by Equation 3.34, meaning that all the acting forces are in equilibrium. The stress vs strain graphic obtained through calculated values is shown in Figure 5.15. Thereafter, the results given by the software and by the calculations are compared in Figure 5.16.

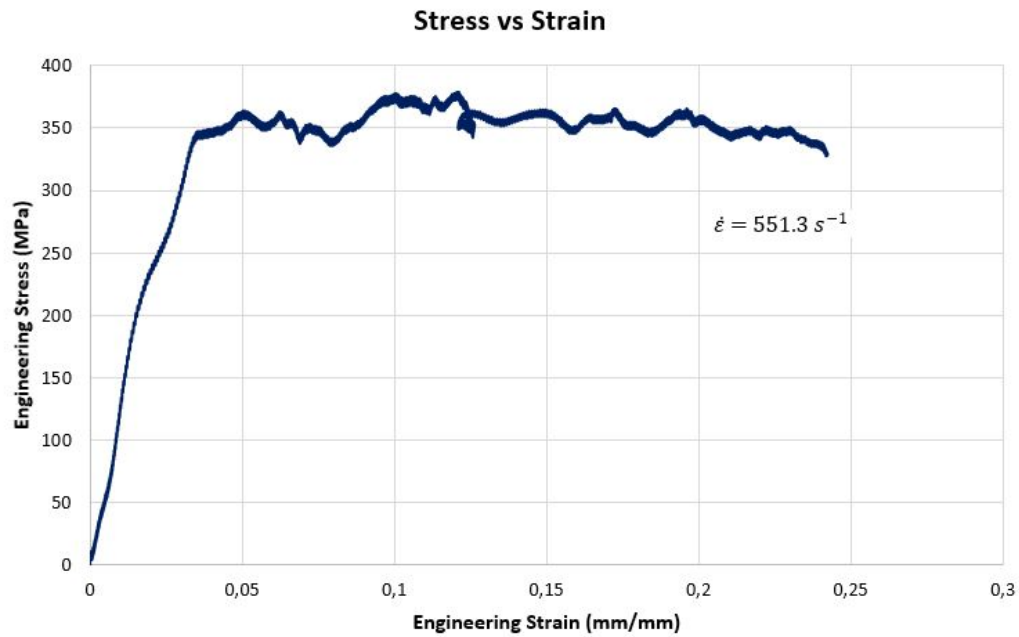


Figure 5.15: Stress vs strain curve for the calculated results

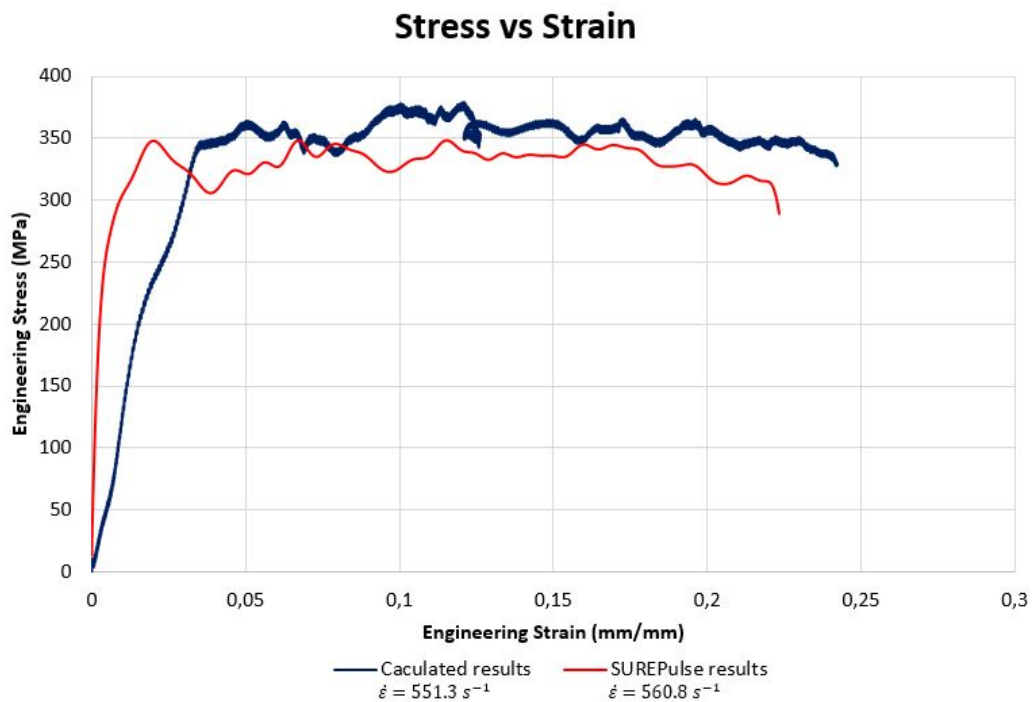


Figure 5.16: Comparison between the software and the calculated results

As presented in Figure 5.15 and Figure 5.16, the respective values for the calculated strain rate and stress were  $551.3 \text{ s}^{-1}$  and  $378.9 \text{ MPa}$ . Comparing the values of the software with the values calculated, an error of  $1.69 \%$  was determined for the strain rate and an error of  $8 \%$

was determined for the stress. These errors were probably related with the definition of the starting and ending of the reflected and transmitted pulses which, in its turn, were implicit in the calculation of the strain and stress. Therefore, it can be concluded that a good correlation between the software and the calculated values were observed. Thereby, the use of the software was seen as a plus due to the time it can save on the data analysis.

After a few preliminary tests, noise was detected in the recorded wave signals. This problem was related to the striker bushings which are mounted with a small interference and immobilized with gummed tape, see Subsubsection 4.13. The pressure input on the striker also caused damage on the gummed tape layer on striker bushings by twisting them. Due to that damage, the bushings are able to slide over the tape. In order to solve this problem, the striker was disassembled and another layer of gummed tape was applied. Nevertheless, bushings must be verified after a couple of tests so the noise caused by this phenomena are eliminated.

Figure 5.17 shows with the detail the specimen rupture which is fragile and occurs at  $45^\circ$ . It should be pointed that the distance between the grips is not the real distance after the performed test.

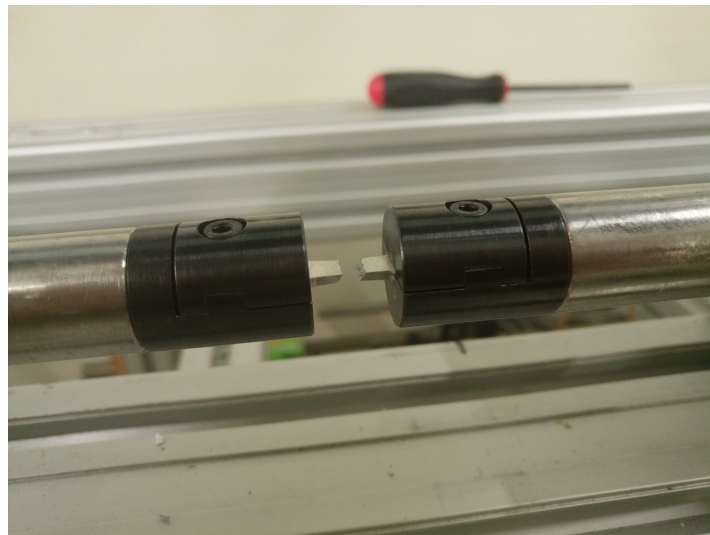


Figure 5.17: Specimen rupture

Since there are few researches considering this aluminium alloy on the high strain rate field, the only way that the author of this thesis had to confirm the results was to resort to the information gathered in Chapter 2, more specifically Subsection 2.4.2. Furthermore, it is important to remember that aluminium has low sensitivity towards strain rate variations.

## 5.4 Dynamic characterisation of materials

As the preliminary results presented in Section 5.3 showed good consistency despite some small level of noise mentioned previously, it was possible to take the next step. Hence, this section aims to give an exposure and a brief analysis of the results obtained for the base material, butt joints and overlap joints obtained through FSW.

### 5.4.1 Dynamic characterisation of base material

In order to characterise the AA6082-T6 aluminium alloy, several tests considering the different rolling directions were performed. Thereafter, specimens were cut from a plate with 2 mm of thickness for 0°, 45° and 90° rolling directions. To perform the tests, the air chamber was loaded with a pressure of 3.5 bar which corresponded to a striker velocity of 5.5 m/s.

Figure 5.18 shows the base material placement on the grips and Figure 5.18 shows the results obtained for the three different rolling directions tested.

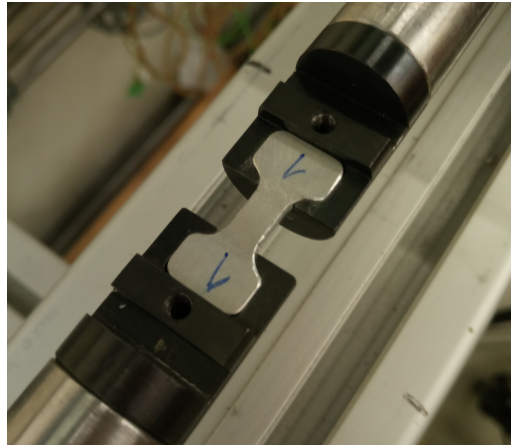


Figure 5.18: Base material specimen placed on the grips

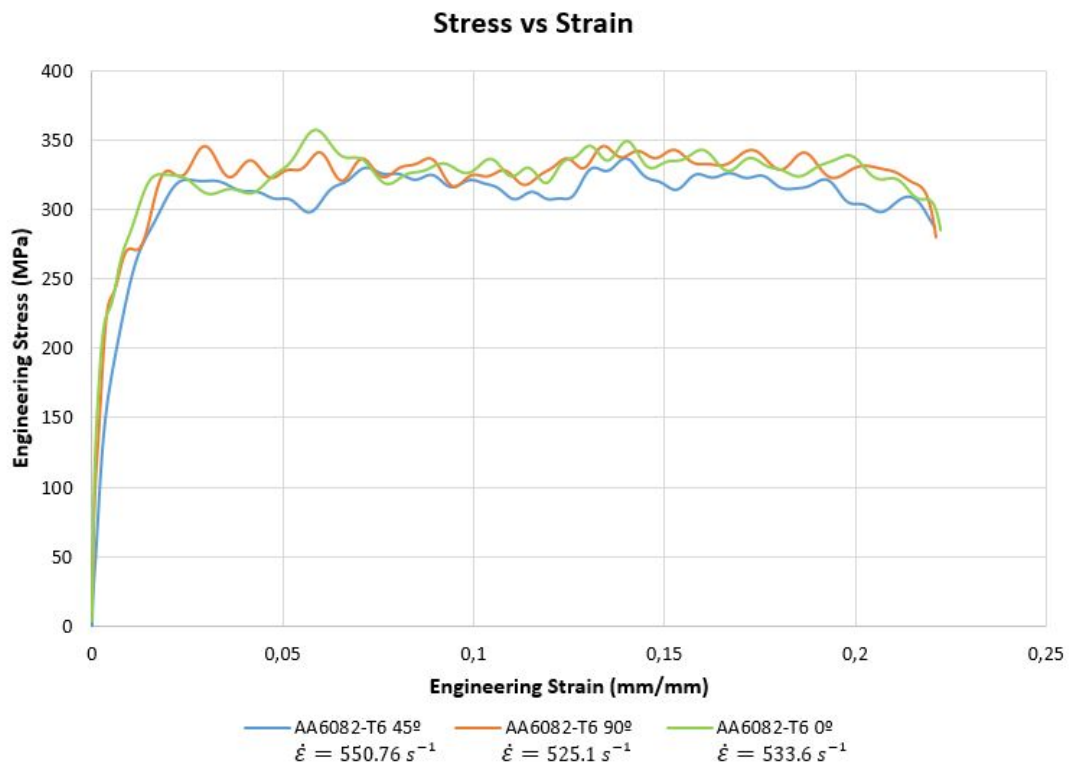


Figure 5.19: Stress vs strain curves for the 0°, 45°, 90° rolling directions

For the specimen with the rolling direction of  $0^\circ$ , the stress achieved was 349 MPa with a deviation of 11.65 and the strain rate was  $533.6 \text{ s}^{-1}$ , with a deviation of 26.23. Further, for the rolling direction of  $90^\circ$  the stress value was 349 MPa, with 4.9 of deviation and the achieved strain rate value was  $525.1 \text{ s}^{-1}$ , with 27.69 of deviation. Last, for the specimen with the rolling direction of  $45^\circ$  the stress and strain rate achieved were 348 MPa, with 7.67 as a deviation value and  $550.76 \text{ s}^{-1}$ , with a respective value of deviation of 2.29. Also, observing Figure 5.15, it can be stated that the rolling direction had no influence on the stress strain curve. The small variations in the results obtained from these tests were most probably due to uncertainties related with mechanical losses on the compressor and subsequently, air chamber loading. Likewise, they may appear due to the loose screws of the grip cover, the oscillations caused by the threaded connection between bars and grips, or even the loose of grips towards the bar.

In Figure 5.20 the rupture of a specimen can be observed and it occurred at the middle section of the specimen gage, fragile at  $45^\circ$ .

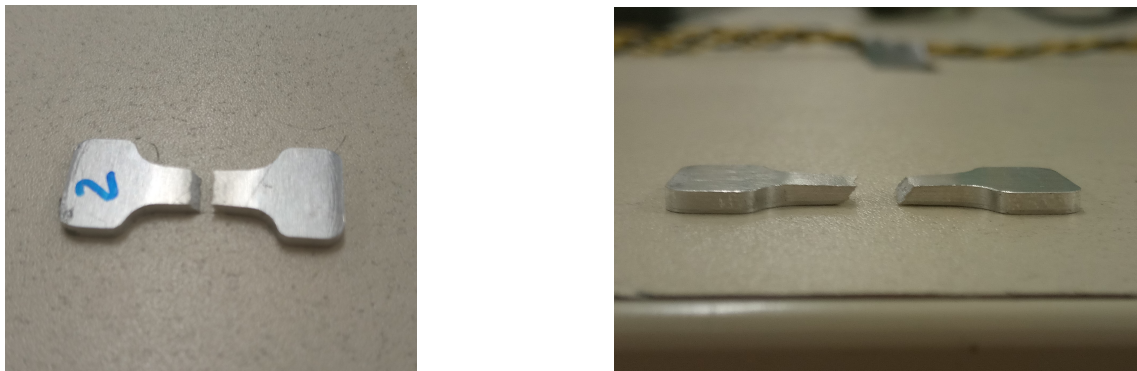


Figure 5.20: Base material specimen rupture at  $45^\circ$

Having performed the high strain rate tests for the base material, comparison with the quasi static stress strain curve was performed. Such comparison is shown in Figure 5.21.

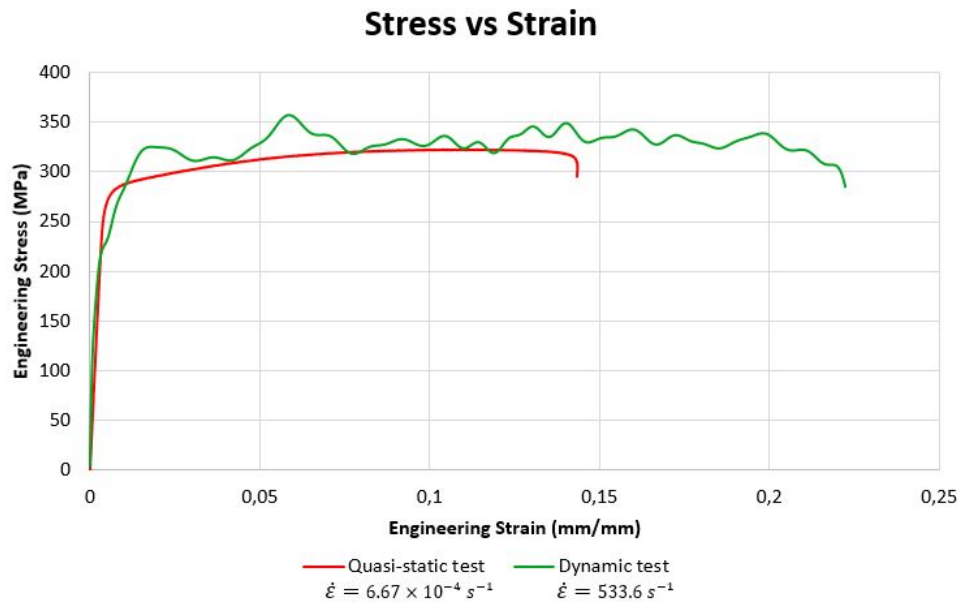


Figure 5.21: Comparison between quasi-static [136] and dynamic results for base material

As expected, the stress and strain achieved for the specimen submitted to the dynamic test were slightly higher than those achieved in the quasi-static test. Therefore, it also states the low strain rate sensitivity of this aluminum alloy. This important comparison is not only in accordance with the literature results but also validates the results obtained, being an important remark.

#### 5.4.2 Dynamic characterisation of butt joints obtained through FSW

The dynamic characterisation of FS welded butt joints was based on two different kind of specimens. Therefore, butt joints were performed on a plate in two different rolling directions. After, that plate was used to cut specimens aligning first the welding axially and then, crosswise. The butt joint specimens had the same dimensions of the base material specimens. The tests were performed with an air chamber pressure of 3.5 bar and a striker velocity of 5.5 m/s, likewise.

Accordingly, the tests which involved specimens with the welding crosswise to their gage were first performed with the advancing side directed to the incident bar and subsequently, with the retreating side directed to the incident bar. In Figure 5.22 it is visible the specimen placement on the grips, positioned with the advanced side directed to the incident bar, whereas in Figure 5.23 the specimen was placed with the retreating side to the incident bar.

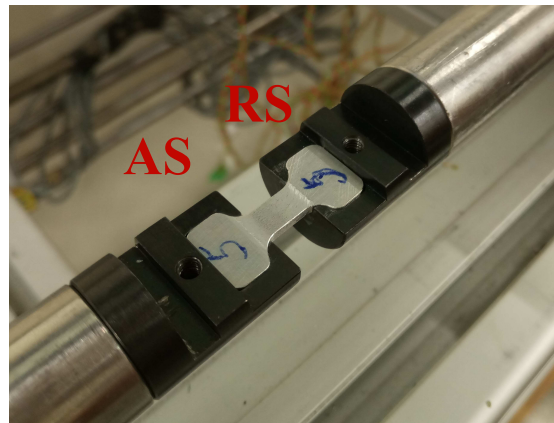


Figure 5.22: Butt joint specimen with the welding crosswise and its placement on the grips, positioned with the AS to the incident bar

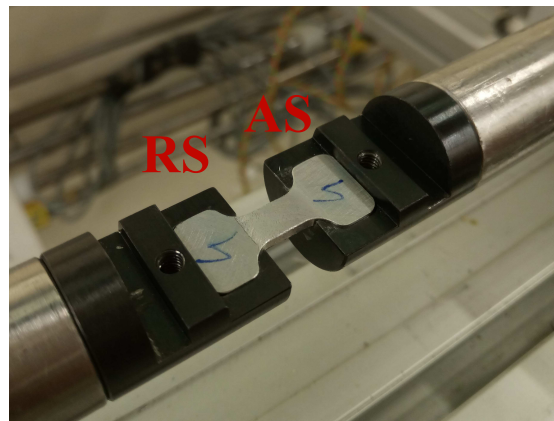


Figure 5.23: Butt joint specimen with the welding crosswise and its placement on the grips, positioned with the RS to the incident bar

The stress vs strain curves for these specimens are presented in Figure 5.24. The specimen which had its retreating side directed to the incident bar showed lower strain rate value,  $530.9 \text{ s}^{-1}$ , towards the specimen which had its advancing side directed to the incident bar,  $542.4 \text{ s}^{-1}$ . The deviations calculated were 5.19 and 29.39 for the strain rate values mentioned, respectively. In contrast, the specimen with its advancing side directed to the incident bar presented lower stress with a value of 210.7 MPa and 25 of deviation, whereas the specimen with its retreating side directed to the incident bar showed a value of 216 MPa and deviation of 16.19. Therefore, by comparing those values and their small differences, it can be concluded that the positioning of the advancing side had no influence in the obtained results.



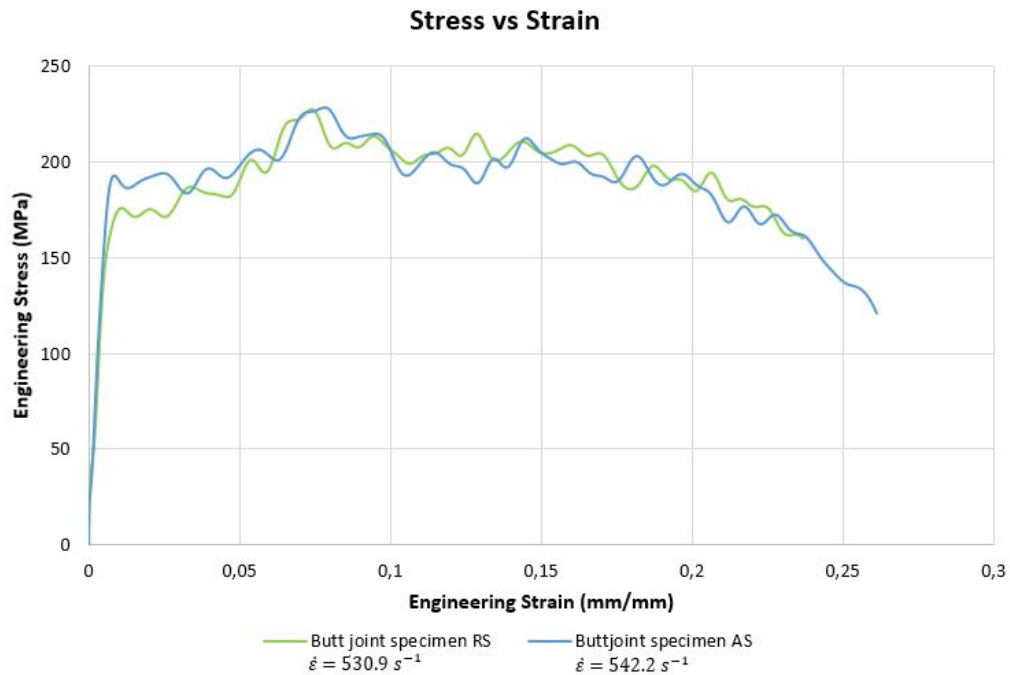


Figure 5.24: Stress vs strain curves for the specimens with the cross wise weld

The tests in which specimens whose welding was placed axially on their length were performed first with the advancing-retreating side and posteriorly, with the retreating-advancing side. Figure 5.25 illustrates a specimen placed on the grips, in detail for the welding where the advancing side can be noticed on the upper part and the retreating side on the lower part. On the other hand, the retreating side can be noticed on the upper part, whereas the advancing side can be noticed on the lower part (see Figure 5.26).

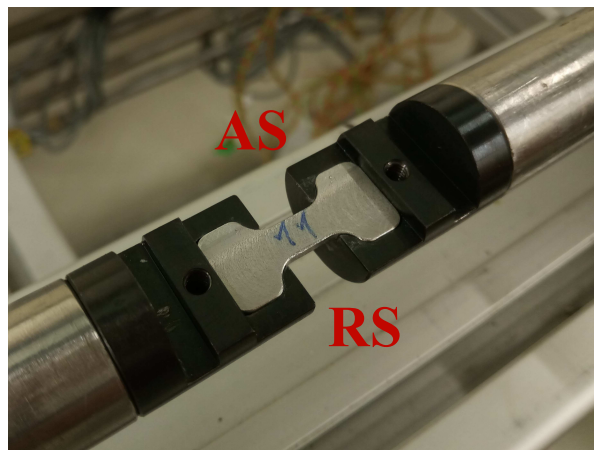


Figure 5.25: Butt joint specimen with axial welding placement on the grips, advancing-retreating side

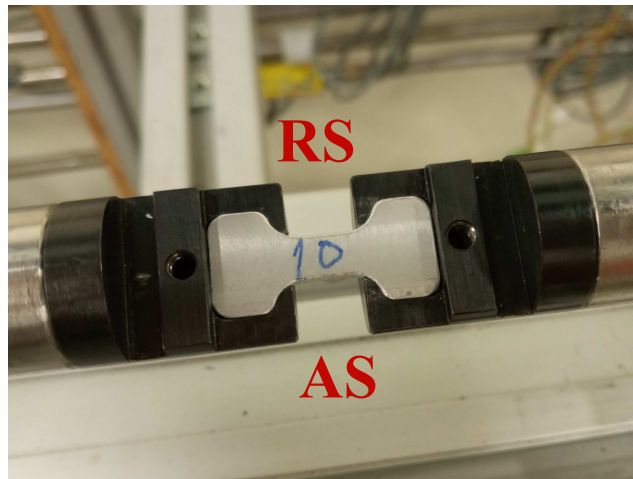


Figure 5.26: Butt joint specimen with axial welding placement on the grips, retreating-advancing side

For this case Figure 5.27 exhibits the stress vs strain curves. Observing them, one can notice that the butt joint specimen with the retreating side on the upper part and the advancing side on the lower part showed a strain rate of  $552.8 \text{ s}^{-1}$  and stress of 186.2 MPa. In its turn, the butt joint specimen with the advancing side on the upper part and retreating side on the lower presented a strain rate of  $548.7 \text{ s}^{-1}$  and a stress of 185 MPa. Nevertheless, observing that graphic, bigger oscillations can be noticed for the butt joint specimen AS-RS as a gap between the two curves. Hereupon, that gap and oscillations may be the result of a decentralization of the weld on the specimen. As the specimen as reduced dimensions, it can be difficult to proceed to the alignment. Figure 5.28 shows the broken specimens of this last test, in which the weld is visible and doesn't cover all the specimen surface.

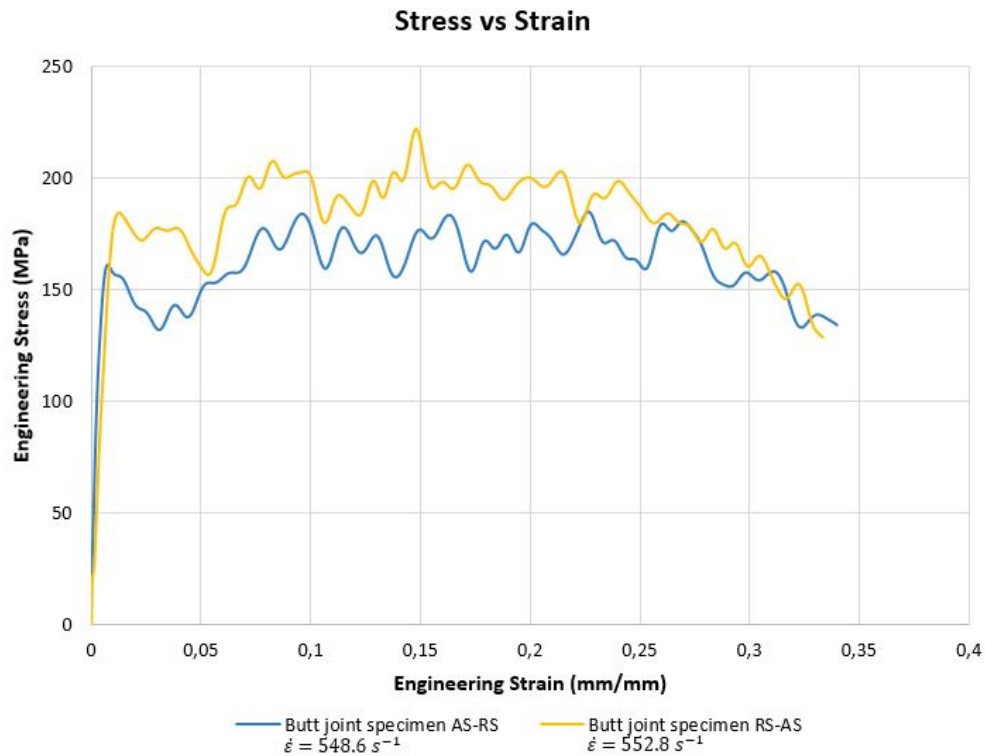


Figure 5.27: Stress vs strain curves for the specimens with the axial weld

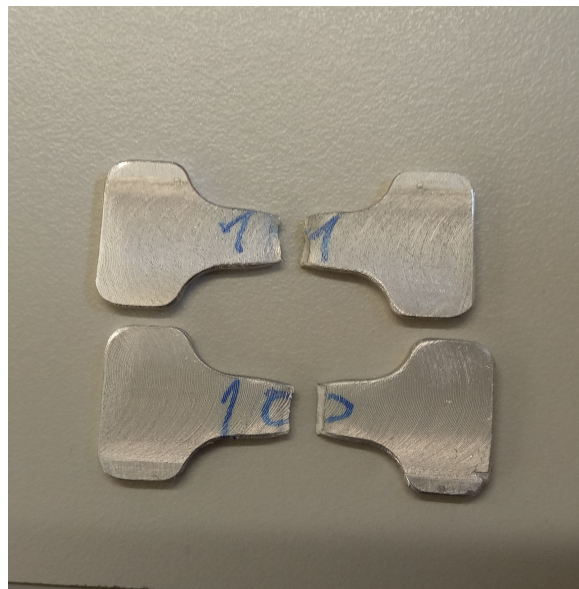


Figure 5.28: Broken butt joint specimens for the second kind of tests

After, the dynamic results were compared with the quasi-static results as shown in Figure 5.29. It can be observed that there was almost no strain rate sensitivity concerning butt joints, since the studied aluminium alloy has low strain rate sensitivity.

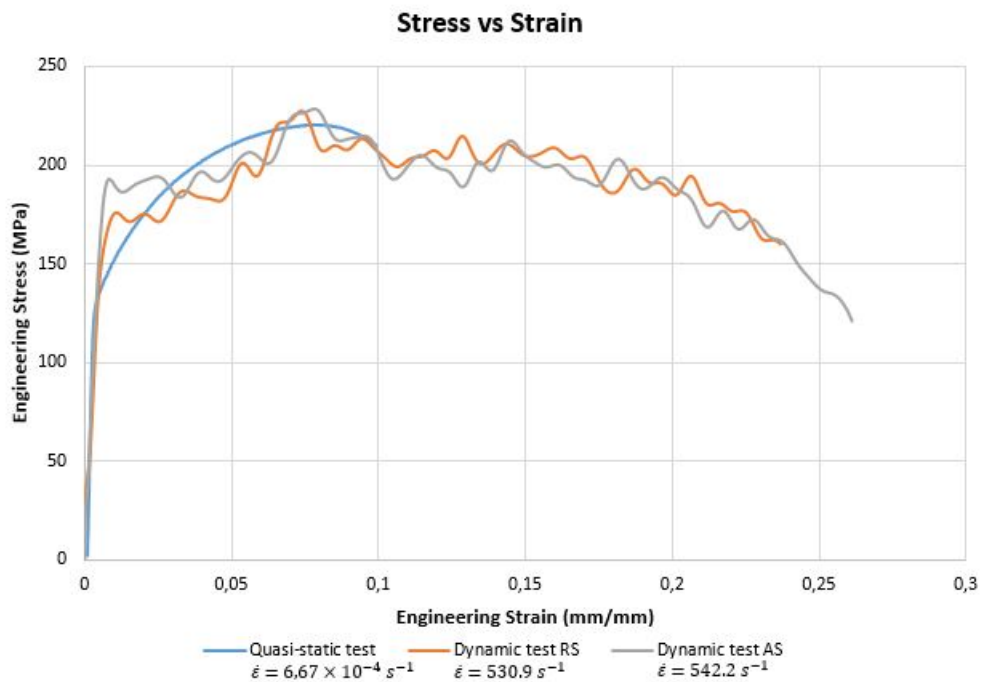


Figure 5.29: Comparison between quasi-static [136] and dynamic results for FS welded butt joints

Furthermore, Figure 5.30 presents the dynamic comparison between base material and butt joint specimens results wherein base material showed the high value of stress. Regarding the butt joint specimens, it was concluded that the weld placement had no influence in the obtained stress values. On the other hand, the butt joint specimens whose weld was placed axially achieved higher values of strain.

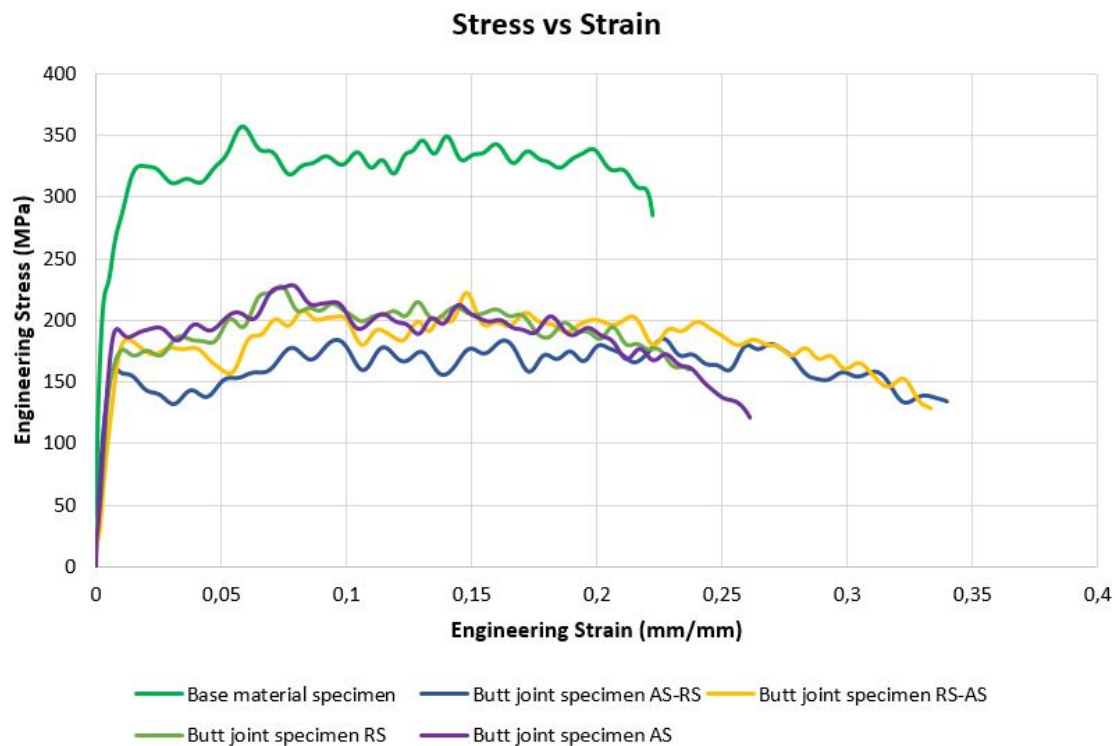


Figure 5.30: Comparison between FS welded butt joints and base material

### 5.4.3 Dynamic characterisation of overlap joints obtained through FSW

Overlap joints obtained through FSW have been gaining ground on the last years. Specially, when this technique can be combined with others such as AB in order to produce joints whose final mechanical properties are improved. This combination is usually known as Weldbonding and it has seen its importance increasing towards the aeronautical industry, where the external impact of strange objects and its effect on mechanical properties is a major concern. Nevertheless, before proceeding to the dynamic characterisation of overlap joints obtained through WB, it is necessary to characterise overlap joints obtained through FSW. As far as the author of this thesis knows, such has never been done before.

To perform the overlap joints tests, the grips used for the previous tests were dismantled so the grips for the overlap joints could be assembled. Figure 5.31 shows the overlap joints grips assembled on the bars.

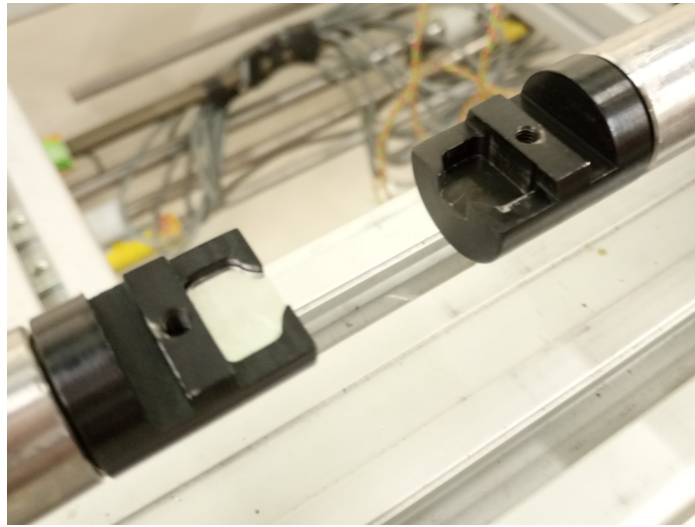


Figure 5.31: Grips for testing overlap joints assembled on the bars

The specimens used for these tests were cut from standard specimens, as well as the thickness compensators (see Appendix B). Their total length was 50.80 mm and their overlap length was 20 mm as shown in Figure 5.32. In Figure 5.33, it can be noticed that the advancing side was placed directed to the incident bar. Accordingly, specimen and both compensators were placed on the grips with respective screws and grip covers as shown in Figure 5.34 .

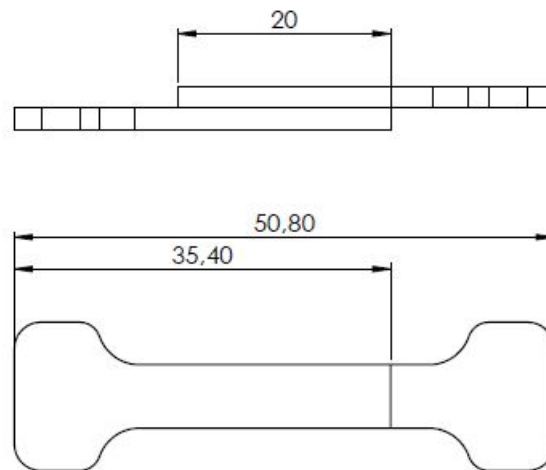


Figure 5.32: FSW overlap specimen dimensions

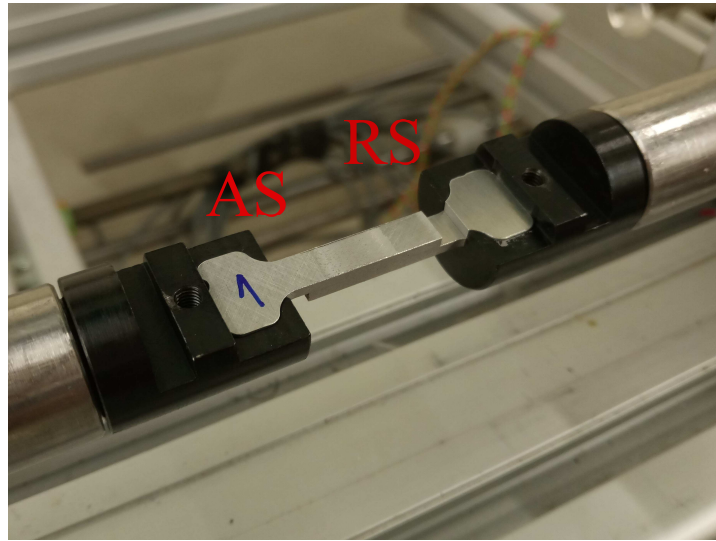


Figure 5.33: Overlap joint specimen on the grips

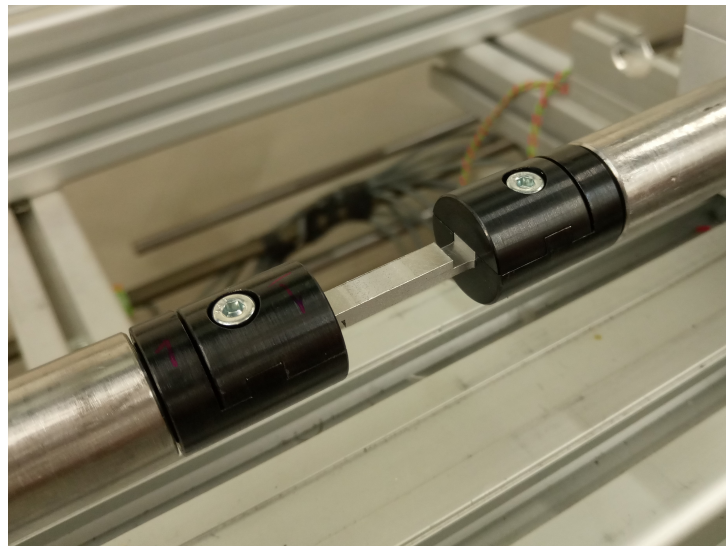


Figure 5.34: Overlap joint specimen placement on the gripping system

Hereafter, the air chamber was loaded with a pressure of 4 bar. The remote stress vs displacement curve obtained for the overlap joints obtained through FSW is presented in Figure 5.35. This curve was obtained using the remote area of the overlap joint specimen. Thus, the stress achieved was 139.7 MPa with a deviation of 4.18 and the strain rate was  $228.93 \text{ s}^{-1}$ , with 0.14 of deviation.

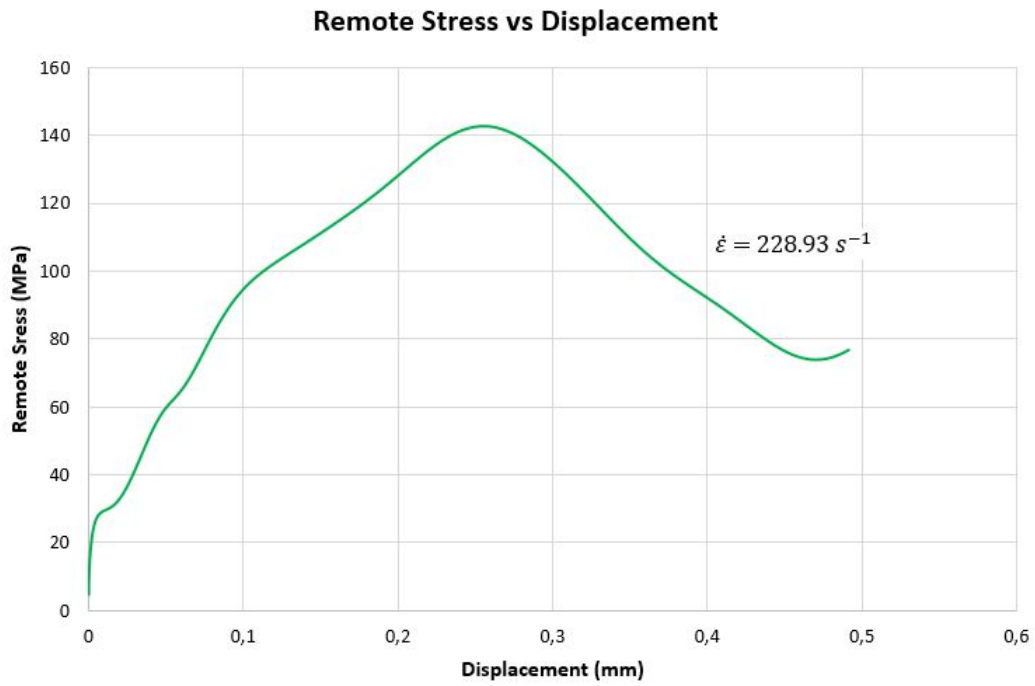


Figure 5.35: Remote stress vs displacement curve for overlap joints obtained through FSW

The quasi-static results were compared with the dynamic results, as shown in Figure 5.36.



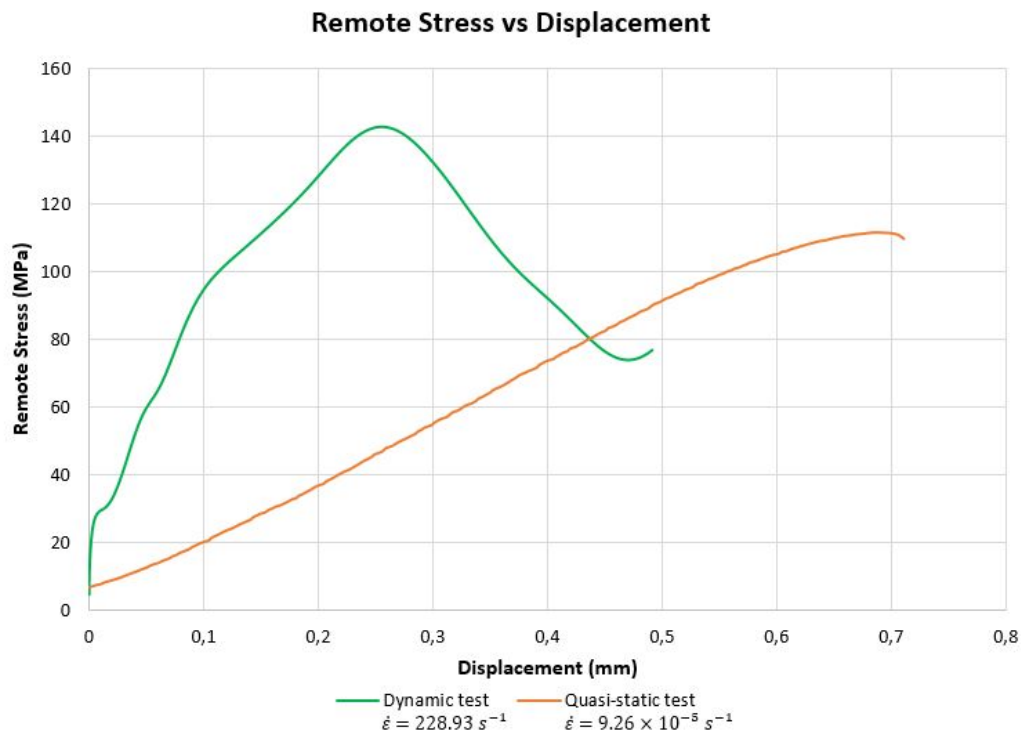


Figure 5.36: Comparison between the quasi-static and dynamic results for overlap joints obtained through FSW

Observing it, the specimen submitted to the dynamic tests achieved a higher strain rate with small displacement towards the quasi-static specimen. The discrepancy between results can be explained with the reduced dimensions of the dynamic specimen which has a great influence on the overlap joints tests, unlike the other tests aforementioned. The length of the dynamic specimen arm, more precisely the free length, was extremely reduced regarding the quasi-static specimen arm, since smaller specimens can achieve higher strain rates. The reduced free length was responsible for forcing the specimen to be more loaded to shear than to peel. The specimen rupture is shown in Figure 5.37.



Figure 5.37: Overlap specimen rupture



## Chapter 6

# Concluding Remarks

The possibility to work in the experimental field was one of the major motivations and one of the reasons that this master thesis theme was chosen. Principally, when it was possible to characterise materials obtained through manufacturing processes that were never characterised before and whose application has been growing exponentially in the most varied industries. Industries which require impact resistance without the decrease of mechanical properties.

Initially, the main goal was to realize tests on base material, butt joints and overlap joints obtained through FSW. Those tests were assumed to be performed on the old SHPB that was installed in LOME and analysed resorting to the SHPB analysis and DIC analysis. Afterwards, the obtained results would be compared in future to study if WB was an employable manufacturing process and worthy for the aeronautical industry. Thus, a new window with immeasurable possibilities could be opened with that being the first step in the field. Although, this old set up didn't allow tests involving overlap joints due to its gripping system. In other words, only tests for base material could be performed since the admissible thickness was 2 mm. Therefore, the execution of tests which implicates overlap joints wouldn't take into consideration the use of thickness compensators to align the axis of the specimen with the axis of the bars. As thickness compensators wouldn't be used, when the tests were performed the bars wouldn't be aligned towards their axis centre. Such would disable the use of the SHPB analysis which assumes that the bars are perfectly aligned towards their axis centre.

Hence, there was a need to develop a new set up so that base material, butt joints and overlap joints could be tested. The first strategy, after the initial conclusions presented on the previous paragraph, was outlined. This strategy includes lots of researches wherein a small part is introduced in the second chapter of this thesis, the design of a whole and brand new set up, the performance of tests using the SHPB theory and DIC, with posterior analysis which might lead to interesting conclusions. Despite of the existence of diverse papers concerning the use of the SHB, there was almost no information about the necessary conditions to design the principal elements. Only after an extensive research on that area, the necessary conditions specially when it comes to design important elements such as the bars, gripping system and specimen were met. Thereby, the final drawings of the parts used in the first part of this work were obtained after six versions. These drawings include the striker and its bushings, the bars and its bushings, the breech and its bushing, the bars, barrel and breech holders, the gripping system, the anvil, the momentum trap and the specimen. The next step was to design the gripping system for the overlap joints which was much faster than the other, since this was achieved with only one version of technical drawings. When the bars arrived, the strain gauges instrumentation was done while the wait for the other parts continued for almost a month. During the wait for the parts of the set up, it was necessary to learn how to work with the

signal amplifier conditioner available in LOME, more precisely, *Vishay 2200 model*. Designing only the set up wouldn't be enough to reach all the initial goals. It was necessary to obtain results and to validate them.

However, problems regarding the delay on the delivery of the parts were not enough. Problems with the signal amplifier conditioner emerged since it was impossible to obtain the bridge balance which allows the acquisition of data. With the help of engineer Jorge Reis and after huge attempts, it was concluded that the *Vishay 2200* signal amplifier condition was not working in its best conditions. Also, the inherent noise level in LOME was responsible for precluding the bridge balance. It was necessary to determine where all that noise came from. But, due to the existence of other works in LOME, it was impossible to eliminate that high level of noise. In order to proceed with this work and with all the parts correctly assembled, the only thing missing was a signal amplifier conditioner capable of reading and recording the signal in the middle of such noise. Other solutions were tried without any success. It took almost two months of work and failed attempts to finally reach a working solution that is capable of filtering all the noise existing in the laboratory. It is extremely important to notice that there were huge amounts of noise.

After overcoming these barriers encountered throughout this work, the author was finally able to advance to the next section of the strategy outlined. However, due to the lack of time, it wasn't possible to employ the DIC method. First tests started to be performed in order to ascertain the principal parameters. Then, with all the parameters properly setted, results were obtained and validated. This validation was accomplished by comparing the results with those in the literature and by comparing the software results with the calculated results. There was an error of 1.69 % for the strain rate and an error of 8 % for the stress. These errors may be caused for differences on zeroing the signals. Nevertheless, the software was considered a plus.

With the previous tests validated, tests for 0°, 45° and 90° rolling directions were performed and it can be concluded that the rolling direction presented no influence on the values achieved for stress and strain concerning each one of them. However, the higher values of deviations were observed for the specimens tested on the rolling direction. Finally, by comparing the results of the dynamic tests with the quasi-static tests, it was observed that base material showed no strain rate sensitivity.

Posteriorly, test with butt joints specimens obtained through FSW were performed. These tests were divided in two. The first tests were performed on the specimens which had the welding placed crosswise. Thus, specimens with the retreating side and after, with the advancing side directed to the incident bar were tested. It was concluded that the placement of the advancing or retreating side had no influence on the results. Proceeding, the second tests were performed on specimens whose weld was placed axially. Specimens with the retreating side and with the advancing side on the upper part were tested. These specimens achieved higher strain than the specimens used in the first tests. Small differences for the stress value were observed. Furthermore, these differences were reflected on the gap between the curves for the latter specimens. Such difference was thought to be caused due to existing oscillations due to the grips screws loosen or due to the loosen of the grips on the bars. Besides, some losses concerning the loading of compressor and air chamber could also be responsible. When it comes to compare the butt joint results with the base material results, all the butt joint specimens showed lower stress. However, the specimens with the weld placed axially achieved higher values of strain than the base material.

Concerning the overlap joints specimens obtained through FSW, they showed the lowest value for stress when compared to the base material and butt joint specimens tested. Continuing, they achieved the lowest value of strain rate. Major differences were observed when

the results between quasi-static tests and dynamic tests were compared. For this type of connection, the specimen arm plays a very important role. However, the smaller the specimen length, the greater the strain rate achieved. The reduced free length was responsible for forcing the specimen to be more loaded to shear than peel. Also, a specimen with larger dimensions wouldn't be able to receive the load transmitted by the tapered section of the grips.



## Chapter 7

### Future Work

Due to the delays aforementioned, time lacked for using DIC. Therefore, it was impossible to use DIC in order to analyse the results and compare them with the SHPB analysis. As future works, tests using overlap joints obtained through FSW with the retreating side directed to the incident bar, AB and WB may be performed so that the results can be compared with the others already obtained in this work. Obviously these tests and all the others should be performed using DIC at the same time. Nevertheless, quasi static test results should be used to point a better observation of the strain rate sensitivity. Notwithstanding, numerical simulations should be performed for the SHPB to define the best dimensions and parameters. Beyond these simulations, others should be done for the stress vs strain curve to afterwards compare with the experimental results. Also, the work hardening rate as the strain hardening rate should be studied. Moreover, it would be interesting performing tests with temperature variation.

At last, bars with higher yield stress must be used so higher velocities can be achieved. Therefore, higher strain rates can be achieved too. On the other hand, bars with smaller diameter should be employed in order to reduce mechanical impedance variations towards the specimen geometry used in this work. To reduce oscillations, the gripping system can also be improved to originate lower reflections due to the existence of threading connections. For the same reason, a barrel with greater length should be considered since the striker would have a larger length to be guided in, maintaining the same number of bushings but with a larger spacing. The increasing of the barrel length provides greater velocity too. Also, the oscillations may be minimised if striker bushings have a smaller width and if the non standard locknut was replaced with a standard locknut or a square nut with smaller dimensions. As the circuit for the data acquisition was placed on open space and it was not armoured, further electromagnetic signals could be captured and overlap the bars signal, provoking oscillations. Notwithstanding, this circuit was a provisional solution to record data, within the available time.





# Bibliography

- [1] L. Goglio, L. Peroni, M. Peroni, and M. Rossetto, "High strain-rate compression and tension behaviour of an epoxy bi-component adhesive," *International Journal of Adhesion and Adhesives*, 2008.
- [2] T. Nicholas, "Tensile testing of materials at high rates of strain," *Experimental Mechanics*, vol. 21, no. 5, pp. 177–185, 1981.
- [3] R. Smerd, "Constitutive behavior of aluminum alloy sheet at high strain rates," Master's thesis, 2005.
- [4] R. Talwar, "Method for joining at least two adjoining work-pieces by friction stir and/or friction stir spot welding," Patent, Jul. 10, 2007, uS Patent 7,240,821.
- [5] D. F. Braga, L. de Sousa, V. Infante, L. F. da Silva, and P. Moreira, "Aluminium friction stir weld-bonded joints," *The Journal of Adhesion*, no. just-accepted, 2015.
- [6] U. Reisgen, A. Schiebahn, M. Essers, A. Naumov, and M. Harraz, "Feasibility study on the use of adhesive fixation in conjunction with friction stir welding," vol. 3, no. 2 (February-2014), 2014.
- [7] R. Cobden and A. Banbury, "Aluminium: physical properties, characteristics and alloys," *Talal lecture*, vol. 1501, pp. 19–26, 1994.
- [8] D. V. Wilson, "Aluminium versus steel in the family car - the formability factor," *Journal of Mechanical Working Technology*, vol. 16, pp. 257 – 277, 1988.
- [9] G. Cole and A. Sherman, "Light weight materials for automotive applications," *Materials characterization*, vol. 35, no. 1, pp. 3–9, 1995.
- [10] W. Miller, L. Zhuang, J. Bottema, A. Wittebrood, P. De Smet, A. Haszler, and A. Vieregge, "Recent development in aluminium alloys for the automotive industry," *Materials Science and Engineering: A*, vol. 280, no. 1, pp. 37–49, 2000.
- [11] Y. Muraoka and H. Miyaoka, "Special issue on aluminium forming development of an all-aluminum automotive body," *Journal of Materials Processing Technology*, vol. 38, no. 4, pp. 655 – 674, 1993. [Online]. Available: <http://www.sciencedirect.com/science/article/pii/0924013693900425>
- [12] R. Donahue and P. A. Fabiyi, "Manufacturing feasibility of all-aluminum automotive engines via application of high silicon aluminum alloy," *SAE Transactions: Journal of Materials & Manufacturing*, vol. 109, pp. 16–26, 2000.

- [13] E. Starke and J. Staley, "Application of modern aluminum alloys to aircraft," *Progress in Aerospace Sciences*, vol. 32, no. 2, pp. 131–172, 1996.
- [14] J. C. Williams and E. A. Starke, "Progress in structural materials for aerospace systems," *Acta Materialia*, vol. 51, no. 19, pp. 5775–5799, 2003.
- [15] F. M. Mazzolani, "Structural applications of aluminium in civil engineering," *Structural engineering international*, vol. 16, no. 4, pp. 280–285, 2006.
- [16] T. Stump and J. Vatauvuk, "A construção naval em liga de alumínio," *Revista Mackenzie de Engenharia e Computação*, vol. 1, no. 1, 2010.
- [17] E. K. center, "Understanding the aluminum alloy designation system," 2014, consulted 2016. [Online]. Available: [http://www.aalco.co.uk/datasheets/Aluminium-Alloy-6082-T6T651-Plate\\_148.ashx](http://www.aalco.co.uk/datasheets/Aluminium-Alloy-6082-T6T651-Plate_148.ashx)
- [18] W. Thomas, M. Murch, E. Nicholas, P. Temple-Smith, J. Needham, and C. Dawes, "Improvements relating to friction welding," Patent, 1995.
- [19] S. Tiwari, D. K. Shukla, and R. Chandra, "Friction stir welding of aluminum alloys: A review," *International Journal of Mechanical, Aerospace, Industrial and Mechatronics Engineering*, vol. 7, p. 12, 2013.
- [20] J. Adamowski and M. Szkodo, "Friction stir welds (fsw) of aluminium alloy aw6082-t6," *Journal of Achievements in Materials and Manufacturing Engineering*, vol. 20, no. 1-2, pp. 403–406, 2007.
- [21] A. Elrefaey, M. Gouda, M. Takahashi, and K. Ikeuchi, "Characterization of aluminum/steel lap joint by friction stir welding," *Journal of materials engineering and performance*, vol. 14, no. 1, pp. 10–17, 2005.
- [22] R. S. Mishra and Z. Ma, "Friction stir welding and processing," *Materials Science and Engineering: R: Reports*, vol. 50, no. 1, pp. 1–78, 2005.
- [23] M. S. Sidhu, S. S. Chatha *et al.*, "Friction stir welding—process and its variables: a review," *Int J Emerg Technol Adv Eng*, vol. 2, no. 12, pp. 275–279, 2012.
- [24] P. Threadgill, A. Leonard, H. Shercliff, and P. Withers, "Friction stir welding of aluminium alloys," *International Materials Reviews*, vol. 54, no. 2, pp. 49–93, 2009.
- [25] S. Sattari, H. Bisadi, and M. Sajed, "Mechanical properties and temperature distributions of thin friction stir welded sheets of aa5083," *International Journal of Mechanics and Applications*, vol. 2, no. 1, pp. 1–6, 2012.
- [26] R. Nandan, T. DebRoy, and H. Bhadeshia, "Recent advances in friction-stir welding—process, weldment structure and properties," *Progress in Materials Science*, vol. 53, no. 6, pp. 980–1023, 2008.
- [27] S. K. K. Aditya Kumar, Sushant Tripath, "A critical review on friction stir welding and its applications in automobile industries," 2014.
- [28] F. M. B. Pinto, "Caraterização de juntas de alumínio soldadas por fricção linear," Ph.D. dissertation, UNIVERSIDADE DO PORTO, 2013.

- [29] W. Thomas and R. Dolby, "Friction stir welding developments," *Proceedings of the sixth international trends in welding research*, pp. 203–211, 2003.
- [30] A. H. Landrock and S. Ebnesajjad, *Adhesives technology handbook*. William Andrew, 2008.
- [31] L. F. da Silva, A. Öchsner, and R. D. Adams, *Handbook of adhesion technology*. Springer Science & Business Media, 2011.
- [32] A. Pizzi and K. L. Mittal, *Handbook of adhesive technology, revised and expanded*. CRC press, 2003.
- [33] A. Al-Samhan and S. Darwish, "Strength prediction of weld-bonded joints," *International journal of adhesion and adhesives*, vol. 23, no. 1, pp. 23–28, 2003.
- [34] S. Darwish and A. Al-Samhan, "Design rationale of weld-bonded joints," *International journal of adhesion and adhesives*, vol. 24, no. 5, pp. 367–377, 2004.
- [35] L. F. da Silva, A. Pirondi, and A. Öchsner, *Hybrid adhesive joints*. Springer Science & Business Media, 2011, vol. 6.
- [36] B. Chang, Y. Shi, and S. Dong, "Studies on a computational model and the stress field characteristics of weld-bonded joints for a car body steel sheet," *Journal of Materials Processing Technology*, vol. 100, no. 1, pp. 171–178, 2000.
- [37] H. Kuhn, D. Medlin, and A. I. H. Committee, *Mechanical Testing and Evaluation*, ser. ASM Handbook: Mechanical Testing and Evaluation. ASM International, 2000. [Online]. Available: <https://books.google.pt/books?id=fdU6AQAIAAJ>
- [38] M. Kutz, *Eshbach's Handbook of Engineering Fundamentals, 4th Edition*, B. D. Tapley, Ed. A Wiley-interscience publication, 1990.
- [39] INSTRON, "Vhs 8800 high strain rate systems," consulted 2016. [Online]. Available: <http://www.instron.us/en-us/products/testing-systems/dynamic-and-fatigue-systems/8800-high-strain-rate>
- [40] E. ASM, "208-95a: Standard test method for conducting drop-weight test to determine nil-ductility transition temperature of ferritic steels," *Annual Book of ASTM Standards*, vol. 3.
- [41] J. Davis, *Tensile Testing, 2nd Edition*. A S M International, 2004. [Online]. Available: <https://books.google.pt/books?id=5uRlb3emLY8C>
- [42] INSTRON, "Ceast 9350 drop tower impact system," consulted 2016. [Online]. Available: <http://www.instron.us/en-us/products/testing-systems/impact-systems/drop-weight-testers/9350-drop-tower>
- [43] B. Hopkinson, "A method of measuring the pressure produced in the detonation of high explosives or by the impact of bullets," *Philosophical Transactions of the Royal Society of London. Series A, Containing Papers of a Mathematical or Physical Character*, vol. 213, pp. 437–456, 1914.
- [44] R. Davies, "A critical study of the hopkinson pressure bar," *Philosophical Transactions of the Royal Society of London A: Mathematical, Physical and Engineering Sciences*, vol. 240, no. 821, pp. 375–457, 1948.

- [45] H. Kolsky, "An investigation of the mechanical properties of materials at very high rates of loading," *Proceedings of the Physical Society. Section B*, vol. 62, no. 11, p. 676, 1949.
- [46] D. H. Korber, "Material behavior under high strain rates," 2016, consulted 2016. [Online]. Available: <http://www.lcc.mw.tum.de/en/research-groups/material-behavior-and-testing/material-behavior-under-high-strain-rates/>
- [47] U. Lindholm and L. Yeakley, "High strain-rate testing: tension and compression," *Experimental Mechanics*, vol. 8, no. 1, pp. 1–9, 1968.
- [48] M. Shi and D. Meuleman, "On certain aspects of strain rate sensitivity of sheet metals," *Journal of materials engineering and performance*, vol. 4, no. 3, pp. 321–333, 1995.
- [49] S. Timothy, "The structure of adiabatic shear bands in metals: a critical review," *Acta metallurgica*, vol. 35, no. 2, pp. 301–306, 1987.
- [50] M. Da Silva and K. Ramesh, "The rate-dependent deformation and localization of fully dense and porous ti-6al-4v," *Materials Science and Engineering: A*, vol. 232, no. 1, pp. 11–22, 1997.
- [51] W.-S. Lee, J.-C. Shyu, and S.-T. Chiou, "Effect of strain rate on impact response and dislocation substructure of 6061-t6 aluminum alloy," *Scripta Materialia*, vol. 42, no. 1, pp. 51–56, 1999.
- [52] L. D. Oosterkamp, A. Ivankovic, and G. Venizelos, "High strain rate properties of selected aluminium alloys," *Materials Science and Engineering: A*, vol. 278, no. 1, pp. 225–235, 2000.
- [53] O. Lee and M. Kim, "Dynamic material property characterization by using split hopkinson pressure bar (shpb) technique," *Nuclear Engineering and Design*, vol. 226, no. 2, pp. 119–125, 2003.
- [54] T. Masuda, T. Kobayashi, L. Wang, and H. Toda, "Effects of strain rate on deformation behavior of a6061-t6 aluminum alloy," in *Materials Science Forum*, vol. 426. Trans Tech Publ, 2003, pp. 285–290.
- [55] Y. Chen, A. Clausen, O. Hopperstad, and M. Langseth, "Stress–strain behaviour of aluminium alloys at a wide range of strain rates," *International Journal of Solids and Structures*, vol. 46, no. 21, pp. 3825–3835, 2009.
- [56] —, "Application of a split-hopkinson tension bar in a mutual assessment of experimental tests and numerical predictions," *International Journal of Impact Engineering*, vol. 38, no. 10, pp. 824–836, 2011.
- [57] X. Fan, T. Suo, Q. Sun, and T. Wang, "Dynamic mechanical behavior of 6061 al alloy at elevated temperatures and different strain rates," *Acta Mechanica Solida Sinica*, vol. 26, no. 2, pp. 111–120, 2013.
- [58] X. Tang, V. Prakash, and J. Lewandowski, "Dynamic tensile deformation of aluminum alloy 6061-t6 and 6061-0a," *Journal of Experimental Mechanics*, vol. 22, no. 3, p. 4, 2007.
- [59] S. Lemanski, N. Petrinic, and G. Nurick, "Experimental characterisation of aluminium 6082 at varying temperature and strain rate," *Strain*, vol. 49, no. 2, pp. 147–157, 2013.

- [60] D. Ng, M. Delich, and L. Lee, "Yielding of 6061-t6 aluminum tubings under dynamic biaxial loadings," *Experimental Mechanics*, vol. 19, no. 6, pp. 200–206, 1979.
- [61] K. G. Hoge, "Influence of strain rate on mechanical properties of 6061-t6 aluminum under uniaxial and biaxial states of stress," *Experimental Mechanics*, vol. 6, no. 4, pp. 204–211, 1966.
- [62] A. Dorbane, G. Ayoub, B. Mansoor, R. Hamade, G. Kridli, and A. Imad, "Observations of the mechanical response and evolution of damage of aa 6061-t6 under different strain rates and temperatures," *Materials Science and Engineering: A*, vol. 624, pp. 239–249, 2015.
- [63] G. Owolabi, D. Odoh, A. Peterson, A. Odeshi, and H. Whitworth, "Measurement of the deformation of aluminum alloys under high strain rates using high speed digital cameras," 2013.
- [64] R. Bobbili, V. Madhu, and A. K. Gogia, "Tensile behaviour of aluminium 7017 alloy at various temperatures and strain rates," *Journal of Materials Research and Technology*, 2016.
- [65] K. Higashi, T. Mukai, K. Kaizu, S. Tsuchida, and S. Tanimura, "Strain rate dependence on mechanical properties in some commercial aluminum alloys," *Le Journal de Physique IV*, vol. 1, no. C3, pp. C3–341, 1991.
- [66] W.-S. Lee and C.-F. Lin, "High-temperature deformation behaviour of ti6al4v alloy evaluated by high strain-rate compression tests," *Journal of Materials Processing Technology*, vol. 75, no. 1, pp. 127–136, 1998.
- [67] K. Ishikawa, H. Watanabe, and T. Mukai, "High strain rate deformation behavior of an az91 magnesium alloy at elevated temperatures," *Materials Letters*, vol. 59, no. 12, pp. 1511–1515, 2005.
- [68] R. Smerd, S. Winkler, C. Salisbury, M. Worswick, D. Lloyd, and M. Finn, "High strain rate tensile testing of automotive aluminum alloy sheet," *International Journal of Impact Engineering*, vol. 32, no. 1, pp. 541–560, 2005.
- [69] H. Zhang, K. Ramesh, and E. Chin, "High strain rate response of aluminum 6092/b 4 c composites," *Materials Science and Engineering: A*, vol. 384, no. 1, pp. 26–34, 2004.
- [70] L. Barker, C. Lundergan, and W. Herrmann, "Dynamic response of aluminum," *Journal of Applied Physics*, vol. 35, no. 4, pp. 1203–1212, 1964.
- [71] D.-H. Park, S.-W. Choi, J.-H. Kim, and J.-M. Lee, "Cryogenic mechanical behavior of 5000- and 6000-series aluminum alloys: Issues on application to offshore plants," *Cryogenics*, vol. 68, pp. 44–58, 2015.
- [72] E. El-Magd and M. Abouridouane, "Characterization, modelling and simulation of deformation and fracture behaviour of the light-weight wrought alloys under high strain rate loading," *International Journal of Impact Engineering*, vol. 32, no. 5, pp. 741–758, 2006.
- [73] P. Yibo, W. Gang, Z. Tianxing, P. Shangfeng, and R. Yiming, "Dynamic mechanical behaviors of 6082-t6 aluminum alloy," *Advances in Mechanical Engineering*, vol. 5, p. 878016, 2013.

- [74] I. Torca, A. Aginagalde, J. Esnaola, L. Galdos, Z. Azpilgain, and C. Garcia, "Tensile behaviour of 6082 aluminium alloy sheet under different conditions of heat treatment, temperature and strain rate," in *Key Engineering Materials*, vol. 423. Trans Tech Publ, 2010, pp. 105–112.
- [75] C. Dharan and F. Hauser, "Determination of stress-strain characteristics at very high strain rates," *Experimental Mechanics*, vol. 10, no. 9, pp. 370–376, 1970.
- [76] Y. Chao, Y. Wang, and K. Miller, "Effect of friction stir welding on dynamic properties of aa2024-t3 and aa7075-t7351," *Welding journal*, vol. 80, no. 8, pp. 196s–200s, 2001.
- [77] T. Yokoyama and K. Ogawa, "Impact tensile properties of 6061 aluminium alloy to sus 304 stainless steel friction-welded butt joints," *Welding international*, vol. 17, no. 7, pp. 514–523, 2003.
- [78] T. Yokoyama and K. Nakai, "High strain-rate compressive response of friction stir welded aa7075-t651 joints," in *Applied Mechanics and Materials*, vol. 7. Trans Tech Publ, 2007, pp. 251–256.
- [79] T. Yokoyama, K. Nakai, and K. Katoh, "High strain-rate compressive response of friction stir welded aa6061-t6 joints: Effect of welding parameter," *????*, vol. 10, no. Special\_Issue, pp. s168–s173, 2010.
- [80] G. Le Louëdec, F. Pierron, M. Sutton, C. Siviour, and A. Reynolds, "Identification of the dynamic properties of al 5456 fsw welds using the virtual fields method," *Journal of Dynamic Behavior of Materials*, vol. 1, no. 2, pp. 176–190, 2015.
- [81] Y. Morisada, T. Imaizumi, and H. Fujii, "Determination of strain rate in friction stir welding by three-dimensional visualization of material flow using x-ray radiography," *Scripta Materialia*, vol. 106, pp. 57–60, 2015.
- [82] S. Mallon, B. Koohbor, A. Kidane, and A. P. Reynolds, "On the effect of microstructure on the torsional response of aa7050-t7651 at elevated strain rates," *Materials Science and Engineering: A*, vol. 639, pp. 280–287, 2015.
- [83] R. Adams and J. Harris, "A critical assessment of the block impact test for measuring the impact strength of adhesive bonds," *International journal of adhesion and adhesives*, vol. 16, no. 2, pp. 61–71, 1996.
- [84] M. Martínez, I. Chocron, J. Rodriguez, V. S. Gálvez, and L. Sastre, "Confined compression of elastic adhesives at high rates of strain," *International Journal of Adhesion and adhesives*, vol. 18, no. 6, pp. 375–383, 1998.
- [85] C. Sato and K. Ikegami, "Strength of adhesively-bonded butt joints of tubes subjected to combined high-rate loads," *The Journal of Adhesion*, vol. 70, no. 1-2, pp. 57–73, 1999.
- [86] T. Yokoyama, "Experimental determination of impact tensile properties of adhesive butt joints with the split hopkinson bar," *The Journal of Strain Analysis for Engineering Design*, vol. 38, no. 3, pp. 233–245, 2003.
- [87] X. Chen and Y. Li, "An experimental technique on the dynamic strength of adhesively bonded single lap joints," *Journal of Adhesion Science and Technology*, vol. 24, no. 2, pp. 291–304, 2010.

- [88] G. Challita, R. Othman, P. Casari, and K. Khalil, "Experimental investigation of the shear dynamic behavior of double-lap adhesively bonded joints on a wide range of strain rates," *International Journal of Adhesion and Adhesives*, vol. 31, no. 3, pp. 146–153, 2011.
- [89] O. Sen, S. A. Tekalur, and C. Jilek, "The determination of dynamic strength of single lap joints using the split hopkinson pressure bar," *International Journal of Adhesion and Adhesives*, vol. 31, no. 6, pp. 541–549, 2011.
- [90] G. Haugou, B. Bourel, F. Lauro, B. Bennani, D. Lesueur, and D. Morin, "Characterisation and modelling of structural bonding at high strain rate," in *EPJ Web of Conferences*, vol. 26. EDP Sciences, 2012, p. 04012.
- [91] T. Yokoyama and K. Nakai, "Determination of the impact tensile strength of structural adhesive butt joints with a modified split hopkinson pressure bar," *International Journal of Adhesion and Adhesives*, vol. 56, pp. 13–23, 2015.
- [92] S. Hayashida, T. Sugaya, S. Kuramoto, C. Sato, A. Mihara, and T. Onuma, "Impact strength of joints bonded with high-strength pressure-sensitive adhesive," *International Journal of Adhesion and Adhesives*, vol. 56, pp. 61–72, 2015.
- [93] J. Neumayer, P. Kuhn, H. Koerber, and R. Hinterhölzl, "Experimental determination of the tensile and shear behaviour of adhesives under impact loading," *The Journal of Adhesion*, no. just-accepted, 2015.
- [94] R. Gerlach, C. Kettenbeil, and N. Petrinic, "A new split hopkinson tensile bar design," *International Journal of Impact Engineering*, vol. 50, pp. 63–67, 2012.
- [95] G. Challita and R. Othman, "Finite-element analysis of shpb tests on double-lap adhesive joints," *International Journal of Adhesion and Adhesives*, vol. 30, no. 4, pp. 236–244, 2010.
- [96] T. Gao, A. J. Kinloch, B. R. Blackman, F. R. Sanchez, S.-k. Lee, C. Cho, H.-j. Bang, S. S. Cheon, and J. U. Cho, "A study of the impact properties of adhesively-bonded aluminum alloy based on impact velocity," *Journal of Mechanical Science and Technology*, vol. 29, no. 2, pp. 493–499, 2015.
- [97] X. He, "A review of finite element analysis of adhesively bonded joints," *International Journal of Adhesion and Adhesives*, vol. 31, no. 4, pp. 248–264, 2011.
- [98] T. Sadowski, P. Golewski, and E. Zarzeka-Raczkowska, "Damage and failure processes of hybrid joints: adhesive bonded aluminium plates reinforced by rivets," *Computational Materials Science*, vol. 50, no. 4, pp. 1256–1262, 2011.
- [99] W. Xu, D. Chen, L. Liu, H. Mori, and Y. Zhou, "Microstructure and mechanical properties of weld-bonded and resistance spot welded magnesium-to-steel dissimilar joints," *Materials Science and Engineering: A*, vol. 537, pp. 11–24, 2012.
- [100] F. Moroni, A. Pironi, and F. Kleiner, "Experimental analysis and comparison of the strength of simple and hybrid structural joints," *International Journal of Adhesion and Adhesives*, vol. 30, no. 5, pp. 367–379, 2010.
- [101] G. Marques, R. Campilho, F. da Silva, and R. Moreira, "Adhesive selection for hybrid spot-welded/bonded single-lap joints: Experimentation and numerical analysis," *Composites Part B: Engineering*, vol. 84, pp. 248–257, 2016.

- [102] R. Campilho, A. Pinto, M. D. Banea, and L. F. da Silva, "Optimization study of hybrid spot-welded/bonded single-lap joints," *International Journal of Adhesion and Adhesives*, vol. 37, pp. 86–95, 2012.
- [103] B. Chang, Y. Shi, and S. Dong, "Comparative studies on stresses in weld-bonded, spot-welded and adhesive-bonded joints," *Journal of Materials Processing Technology*, vol. 87, no. 1, pp. 230–236, 1999.
- [104] T. Fujii, K. Tohgo, Y. Suzuki, T. Yamamoto, and Y. Shimamura, "Fatigue strength and fatigue fracture mechanism of three-sheet spot weld-bonded joints under tensile–shear loading," *International Journal of Fatigue*, vol. 87, pp. 424–434, 2016.
- [105] S. Darwish, "Characteristics of weld-bonded commercial aluminum sheets (bs 1050)," *International journal of adhesion and adhesives*, vol. 23, no. 3, pp. 169–176, 2003.
- [106] H. R. Costa, J. M. Reis, J. P. Souza, P. M. Pacheco, R. A. Aguiar, and S. De Barros, "Experimental investigation of the mechanical behaviour of spot welding–adhesives joints," *Composite Structures*, vol. 133, pp. 847–852, 2015.
- [107] X. Sun and M. A. Khaleel, "Dynamic strength evaluations for self-piercing rivets and resistance spot welds joining similar and dissimilar metals," *International journal of impact engineering*, vol. 34, no. 10, pp. 1668–1682, 2007.
- [108] H. Körber *et al.*, "Mechanical response of advanced composites under high strain rates," 2012.
- [109] K. Young, "Development of a tensile split hopkinson pressure bar testing facility," 2015.
- [110] F. J. Ferreira, "Análise do comportamento dinâmico de componentes estruturais sob solicitações generalizadas," 2012.
- [111] J. M. C. d. F. Justo, "Estudo do comportamento ao impacto de alta velocidade de estruturas em materiais compósitos," 2013.
- [112] H. Berger-Pelletier, "Modelling of split hopkinson pressure bars," Master's thesis, Université Laval, 2013.
- [113] J. Gong, L. Malvern, and D. Jenkins, "Dispersion investigation in the split hopkinson pressure bar," *Journal of Engineering Materials and Technology*, vol. 112, no. 3, pp. 309–314, 1990.
- [114] P. Follansbee and C. Frantz, "Wave propagation in the split hopkinson pressure bar," *Journal of Engineering Materials and Technology*, vol. 105, no. 1, pp. 61–66, 1983.
- [115] R. Gerlach, S. K. Sathianathan, C. Siviour, and N. Petrinic, "A novel method for pulse shaping of split hopkinson tensile bar signals," *International Journal of Impact Engineering*, vol. 38, no. 12, pp. 976–980, 2011.
- [116] M. A. V. Joaquim Silva Gomes, *Análise Experimental de Tensões*. FEUP, 2002.
- [117] L. Y. PI, L. Smith, M. A. Gotheekar, and M. X. Chen, "Measure strain distribution using digital image correlation (dic) for tensile tests," 2010.



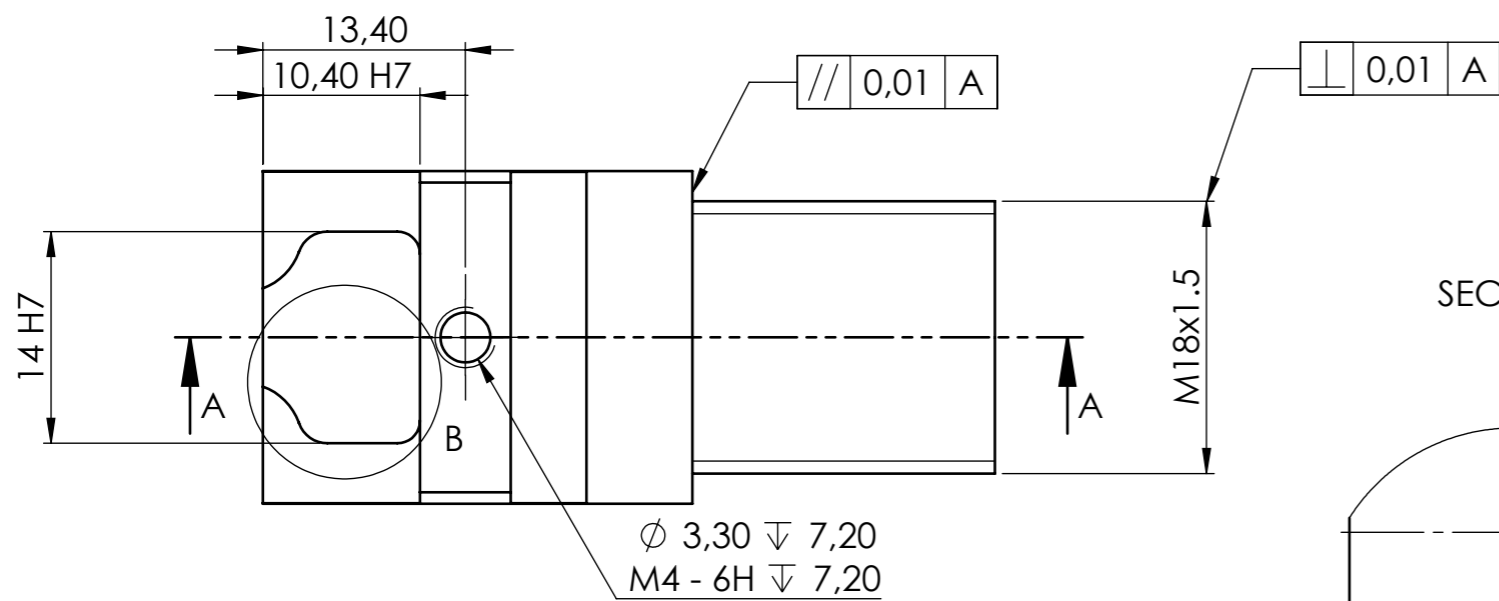
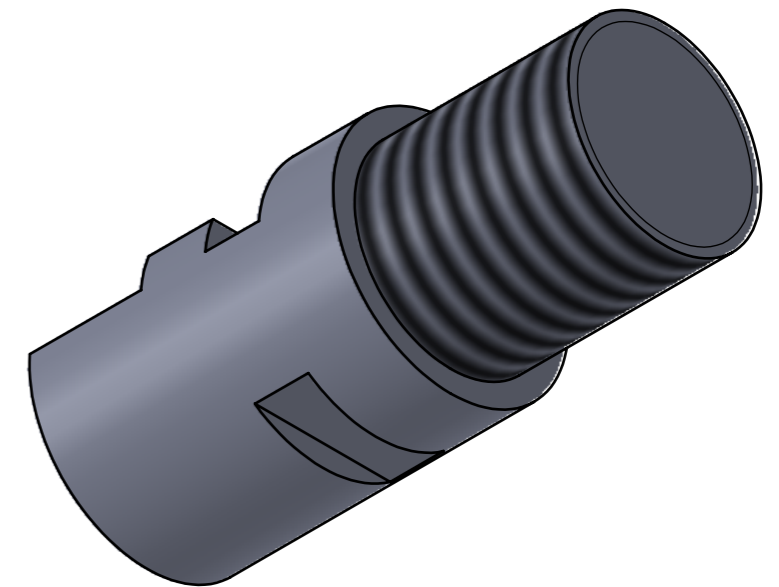
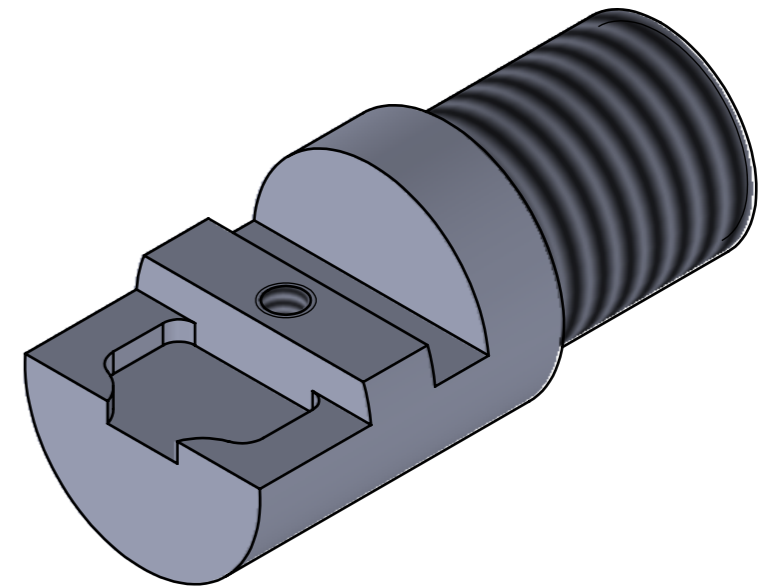
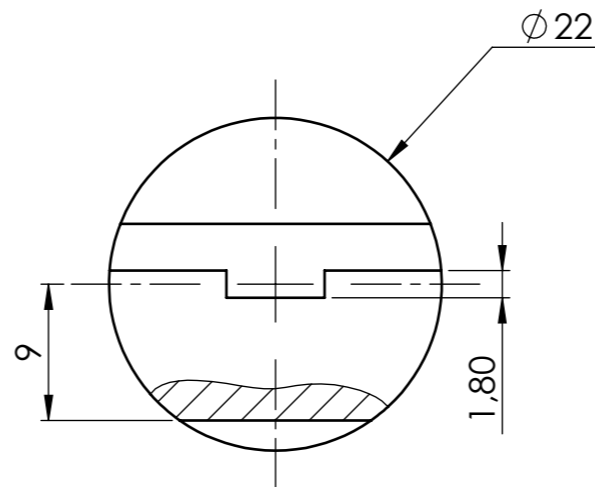
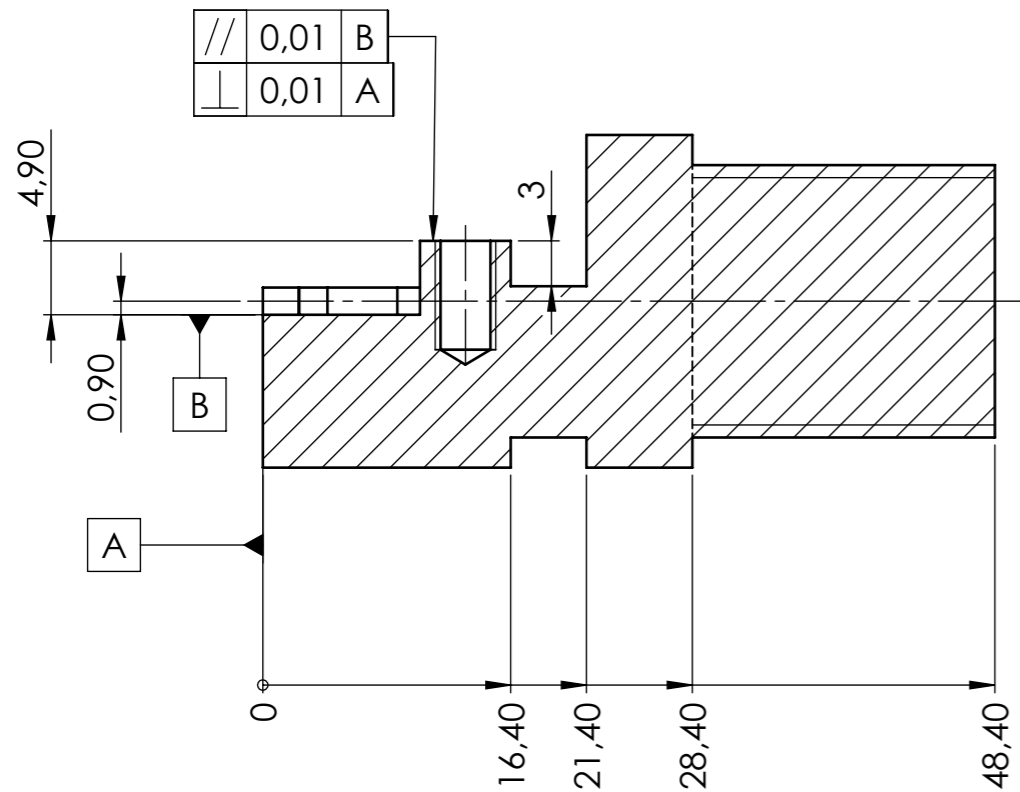
- [118] B. Pan, K. Qian, H. Xie, and A. Asundi, "Two-dimensional digital image correlation for in-plane displacement and strain measurement: a review," *Measurement science and technology*, vol. 20, no. 6, p. 062001, 2009.
- [119] N. McCormick and J. Lord, "Digital image correlation," *Materials today*, vol. 13, no. 12, pp. 52–54, 2010.
- [120] R. Jabłoński and T. Březina, *Mechatronics: Recent Technological and Scientific Advances*. Springer Science & Business Media, 2011.
- [121] M. A. Sutton, S. R. McNeill, J. D. Helm, and Y. J. Chao, "Advances in two-dimensional and three-dimensional computer vision," in *Photomechanics*. Springer, 2000, pp. 323–372.
- [122] M. Palanca, G. Tozzi, and L. Cristofolini, "The use of digital image correlation in the biomechanical area: a review," *International Biomechanics*, vol. 3, no. 1, pp. 1–21, 2016.
- [123] M. A. Sutton, J. J. Orteu, and H. Schreier, *Image correlation for shape, motion and deformation measurements: basic concepts, theory and applications*. Springer Science & Business Media, 2009.
- [124] R. E. Berggren and R. M. Reynolds, "The light-gas-gun model launcher," *Ballistic Range Technology*, pp. 9–54, 1970.
- [125] Tecnogial, *Tabela de características técnicas de aco inoxidavel*.
- [126] J. F. Acosta, "Numerical and experimental studies on the use of a split hopkinson pressure bar for high strain rate tension testing," 2012.
- [127] H. Huh, W. Kang, and S. Han, "A tension split hopkinson bar for investigating the dynamic behavior of sheet metals," *Experimental Mechanics*, vol. 42, no. 1, pp. 8–17, 2002.
- [128] N. Ledford, H. Paul, G. Ganzenmüller, M. May, M. Höfemann, M. Otto, and N. Petrinic, "Investigations on specimen design and mounting for split hopkinson tension bar (shbt) experiments," in *EPJ Web of Conferences*, vol. 94. EDP Sciences, 2015, p. 01049.
- [129] A. Gilat, T. Schmidt, and A. Walker, "Full field strain measurement in compression and tensile split hopkinson bar experiments," *Experimental Mechanics*, vol. 49, no. 2, pp. 291–302, 2009.
- [130] M.-M. D. of Vishay Precision Group, *2200 SYSTEM Signal Conditioning System- Instruction Manual*, May 2011.
- [131] Alcoa, "Aluminium alloy - commercial alloy - 6082 - t6 t651 plate." [Online]. Available: [http://www.aalco.co.uk/datasheets/Aluminium-Alloy-6082-T6T651-Plate\\_148.ashx](http://www.aalco.co.uk/datasheets/Aluminium-Alloy-6082-T6T651-Plate_148.ashx)
- [132] J. Lifshitz and H. Leber, "Data processing in the split hopkinson pressure bar tests," *International Journal of Impact Engineering*, vol. 15, no. 6, pp. 723–733, 1994.
- [133] R. N. W. Eriksen, *High Strain Rate Characterisation of Composite Materials*. DTU Mechanical Engineering, 2014.
- [134] R. INC., *Instruction Manual SUREPulse Software Version 1.9.x*, February 2016.
- [135] L. Clegg, "Shunt calibration for dummies; a reference guide," August 2005.

- [136] P. Moreira, T. Santos, S. Tavares, V. Richter-Trummer, P. Vilaça, and P. De Castro, "Mechanical and metallurgical characterization of friction stir welding joints of aa6061-t6 with aa6082-t6," *Materials & design*, vol. 30, no. 1, pp. 180–187, 2009.

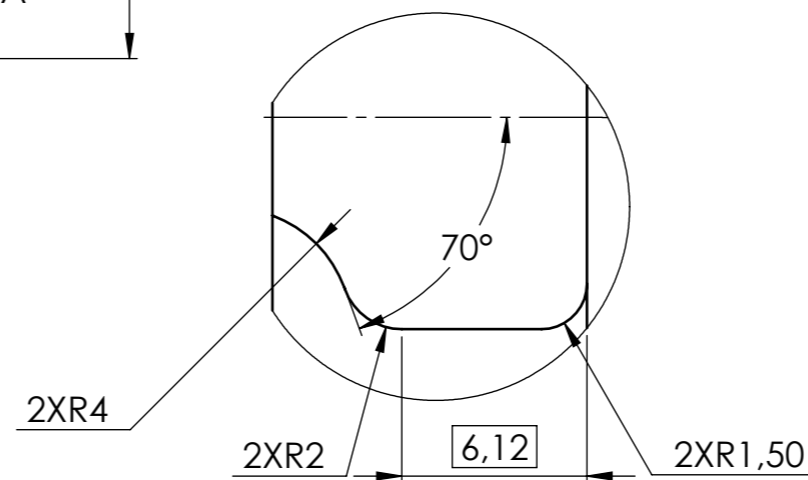
## **Appendix A**

# **Technical drawings of the SHTB components**

SECÇÃO A-A



SECÇÃO B

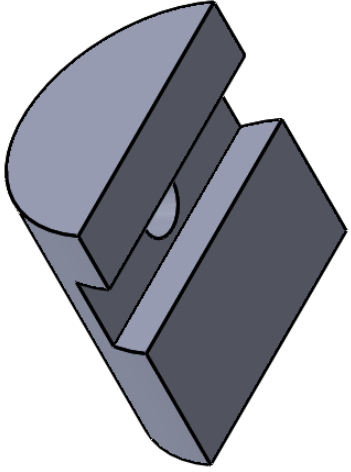
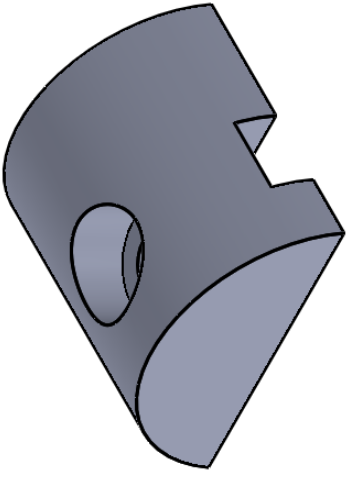
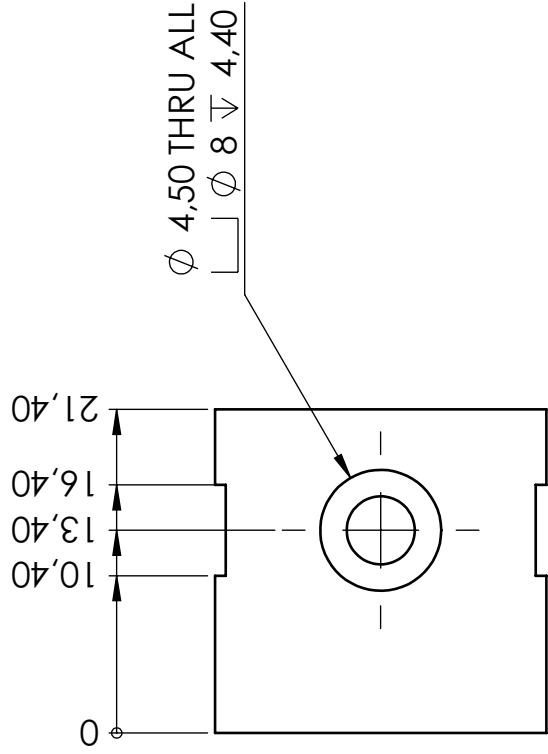
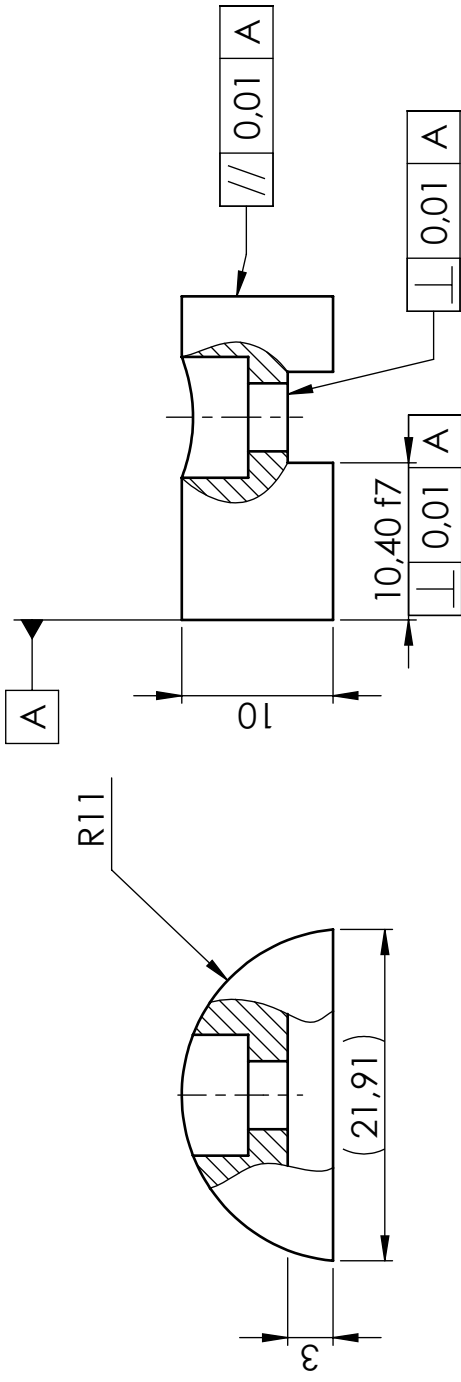


**DIMENSÕES GLOBAIS:**  
Ø22x48,40

		TÍTULO:	
		Amarras	
MATERIAL:		DSNH N:	
AÇO		SHPB 01.06.05.16	
PESO: ± XXX g	ESCALA: 2:1	QUANTIDADE: 2	A3 mm FOLHA 1 DE 1

1 2 3 4 5 6

A B C



**DIMENSÕES GLOBAIS:**  
Ø22x21,40



# Tampa amarra

MATERIAL: AÇO

DSNH Nº:

**SHPB 02.06.05.16**

PESO: ± XXX g

ESCALA:2:1

UNIDADES:2

A4

mm

FOLHA 1 DE 1

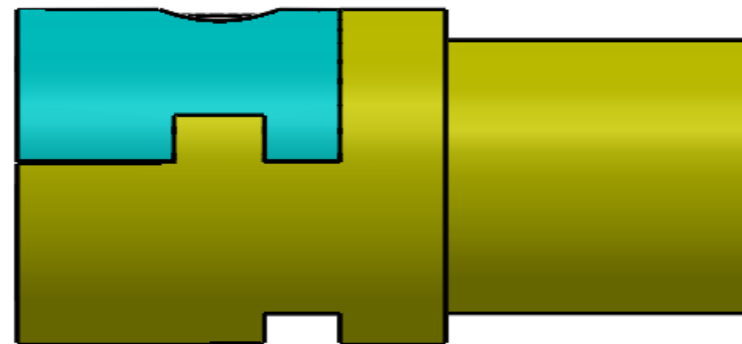
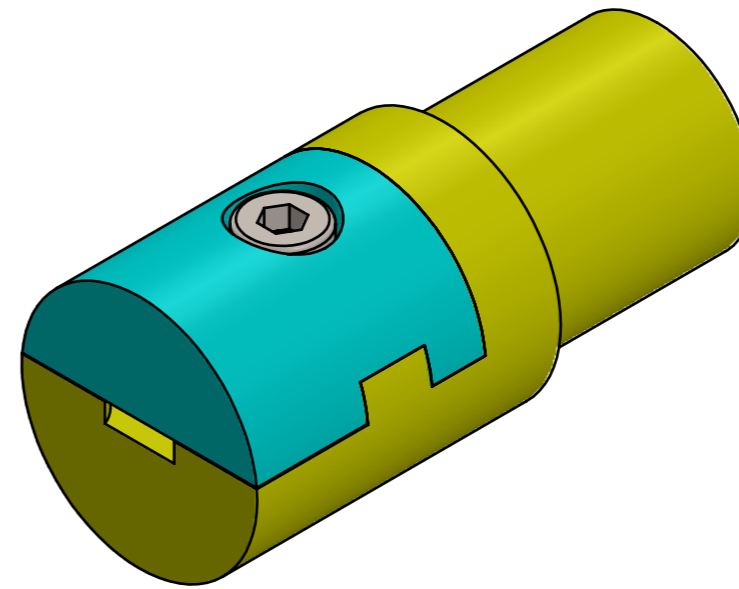
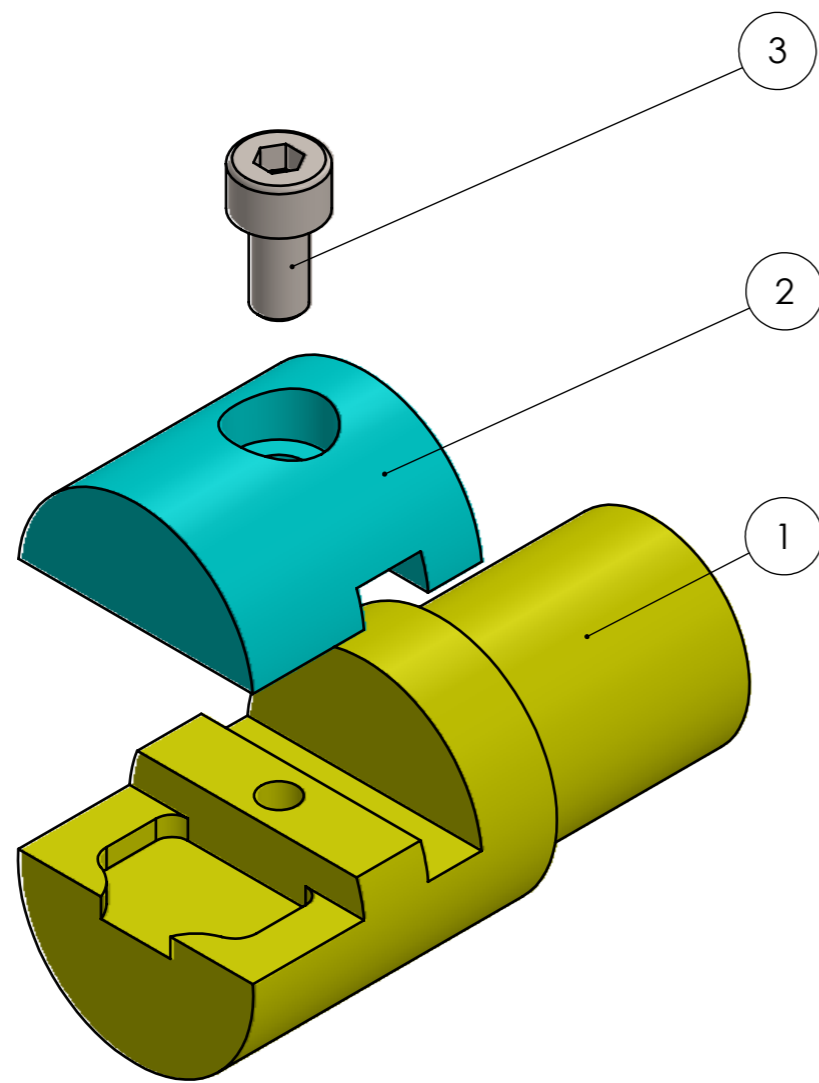
1 2 3

A

B


C

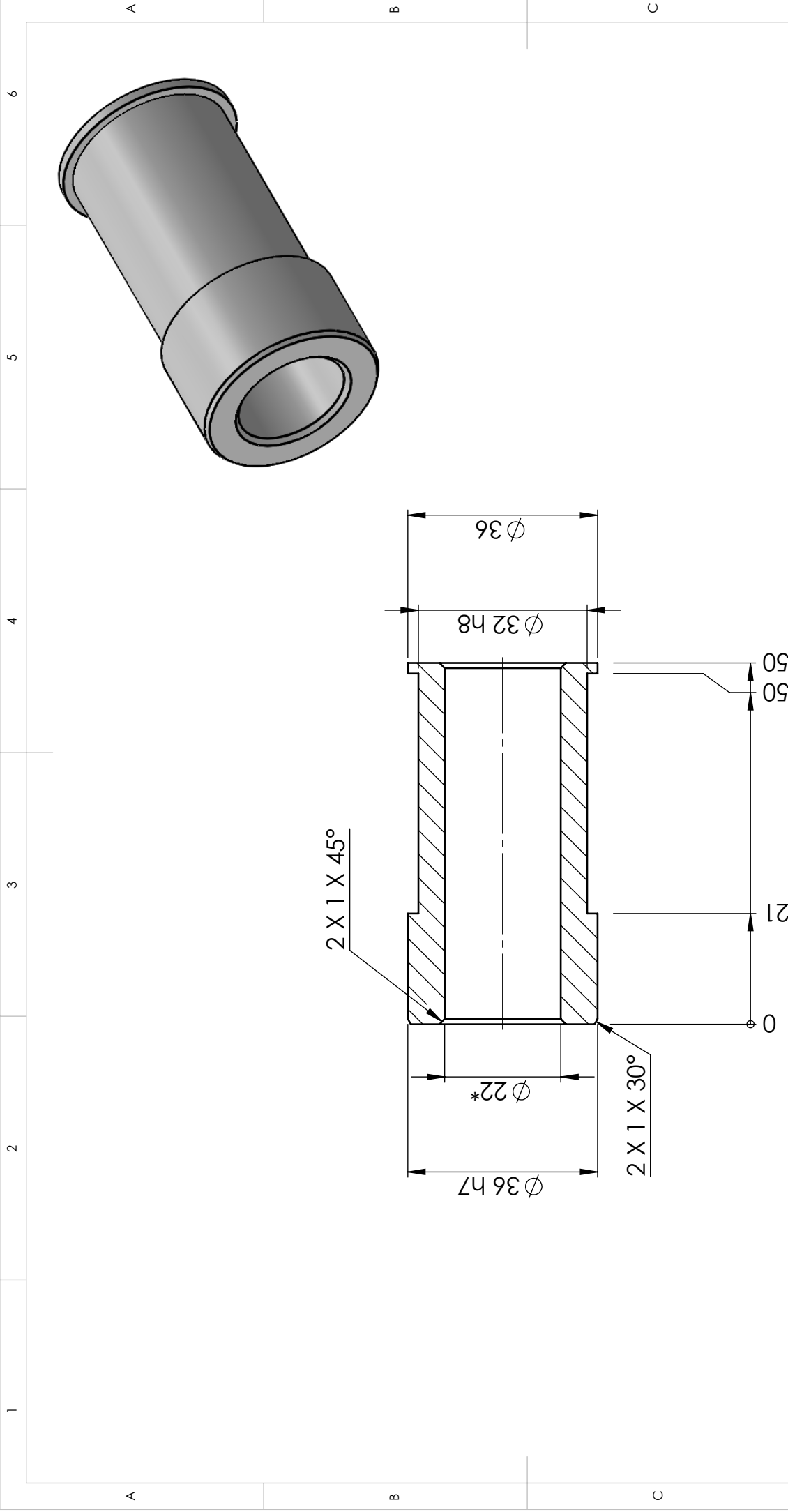
D



**DIMENSÕES GLOBAIS:**  
- X - X -


Nº	Designação	Quantidade
1	SHPB 01.06.05.16 - amarras	1
2	SHPB 02.06.05.16 - tampa amarra	1
3	DIN 912 M4 x 8 --- 8N	1

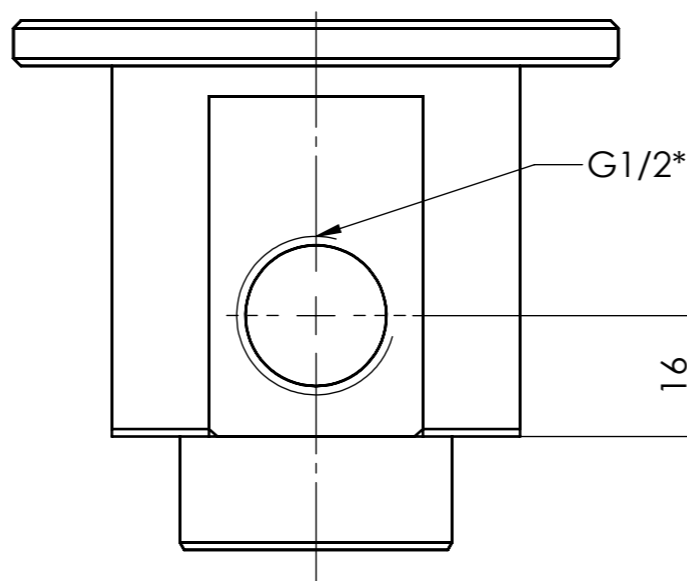
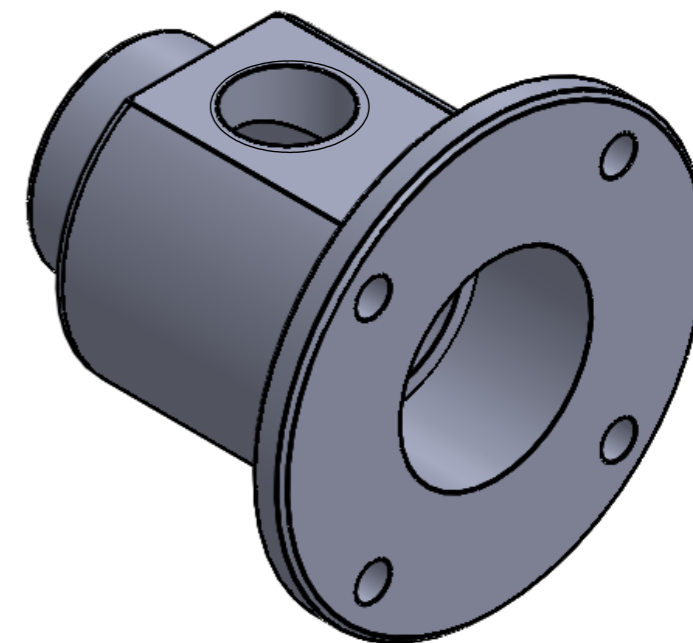
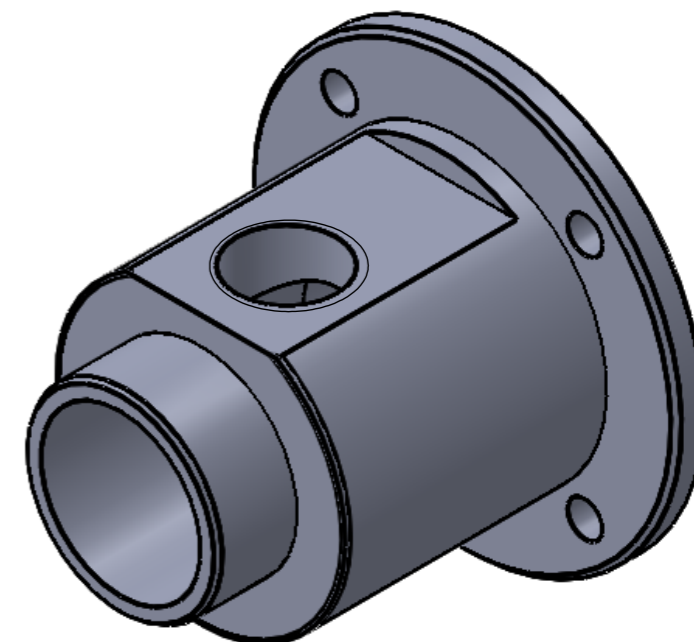
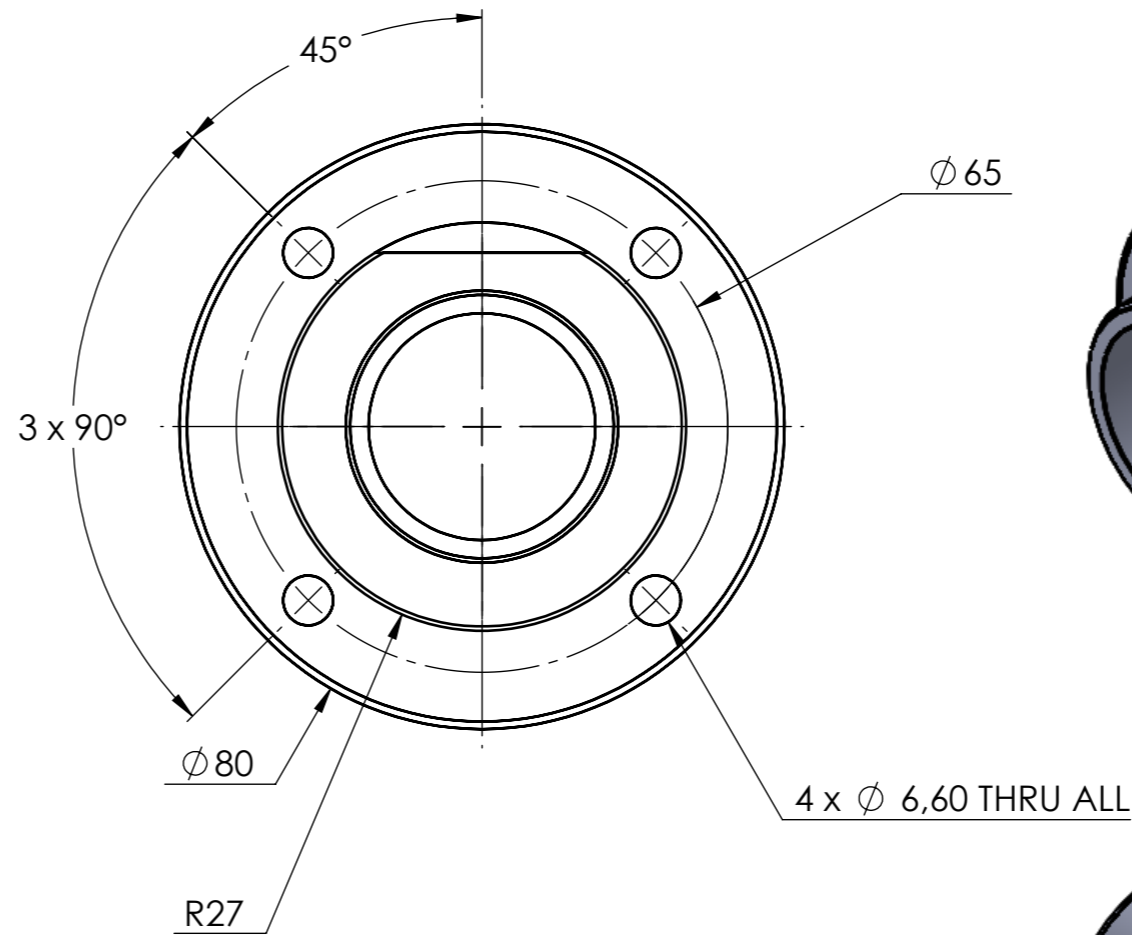
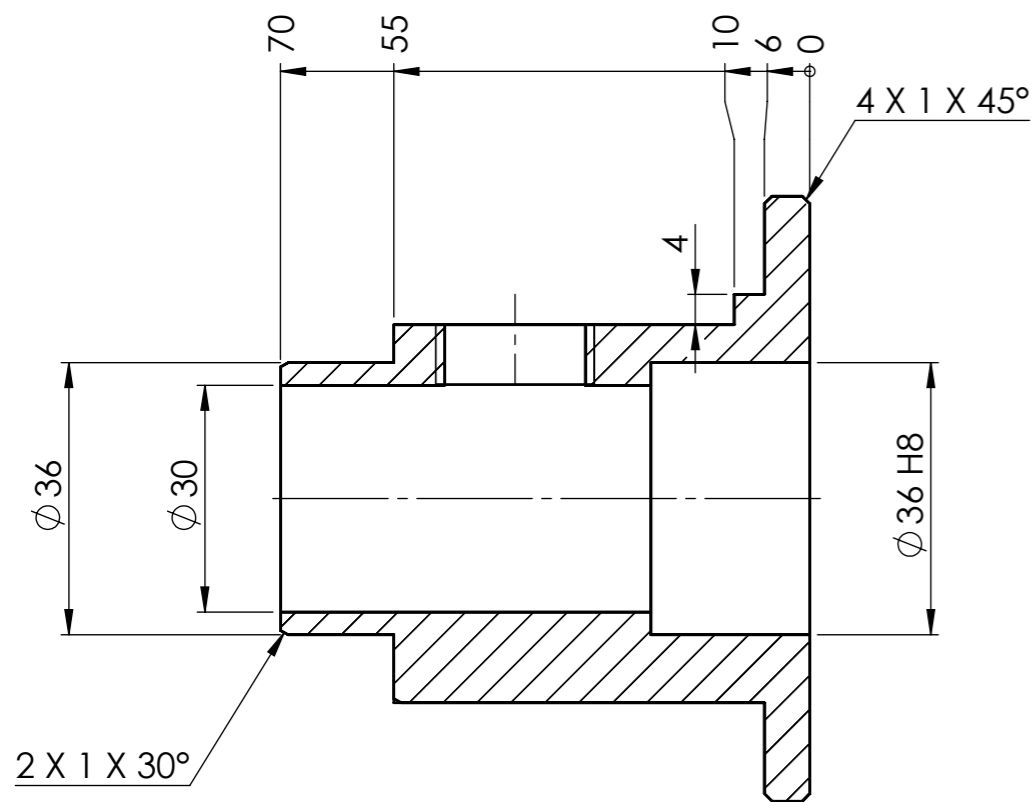
		TÍTULO:			
		<h1>Conjunto amarras</h1>			
MATERIAL:		DSNH N:			
		<h2>SHPB 001.06.05.16</h2>			
PESO: ± XXX g	ESCALA:2:1	QUANTIDADE: 2	A3	mm	FOLHA 1 DE 1



**DIMENSÕES GLOBAIS:**  
 $\phi 36 \times 68,5$


\*Nota: furo deslizante para barra de referência SHPB 10.06.05.16

	TÍTULO:  <b>Casquilho culatra</b>
MATERIAL: <b>TEFLON</b>	DSNH N°: <b>SHPB 03.06.05.16</b>
PESO: ± xxx g	UNIDADES: 1
ESCALA: 1:1	mm
3	A4
1	FOLHA 1 DE 1

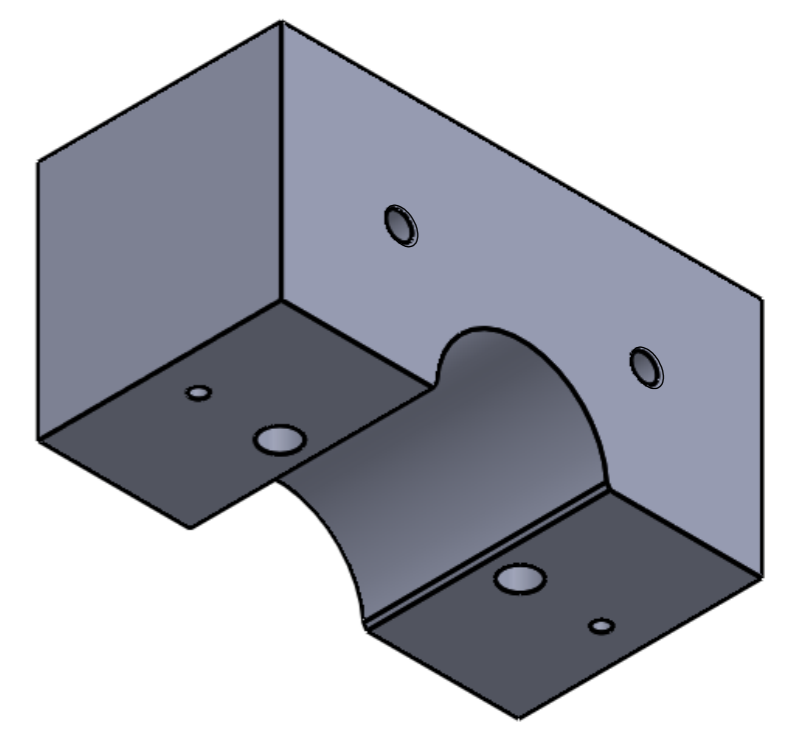
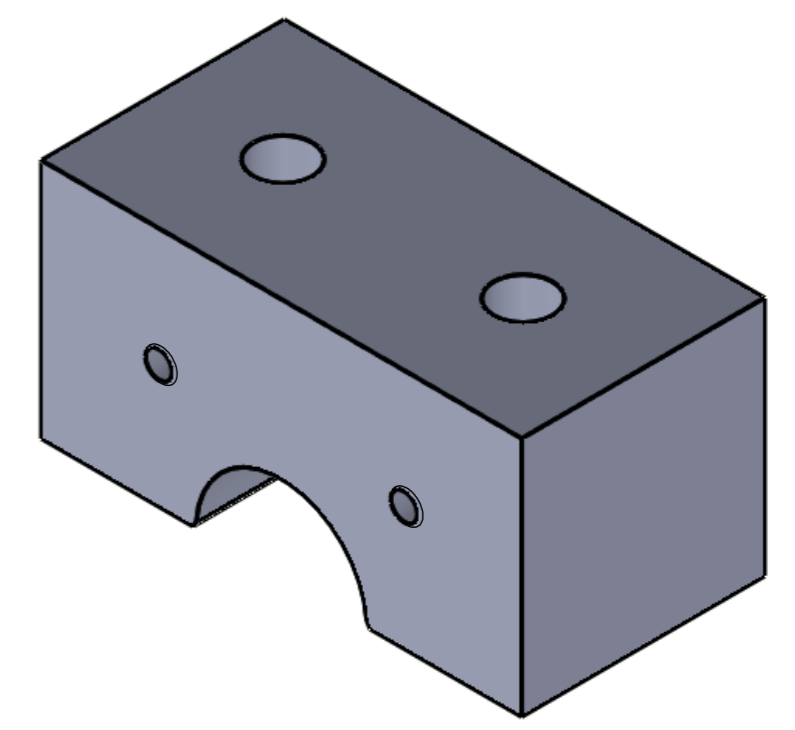
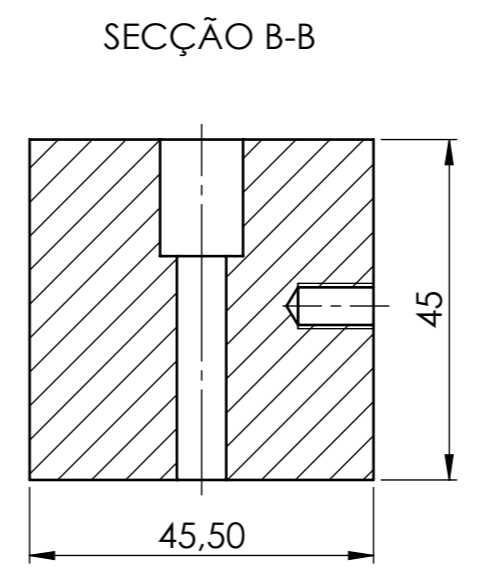
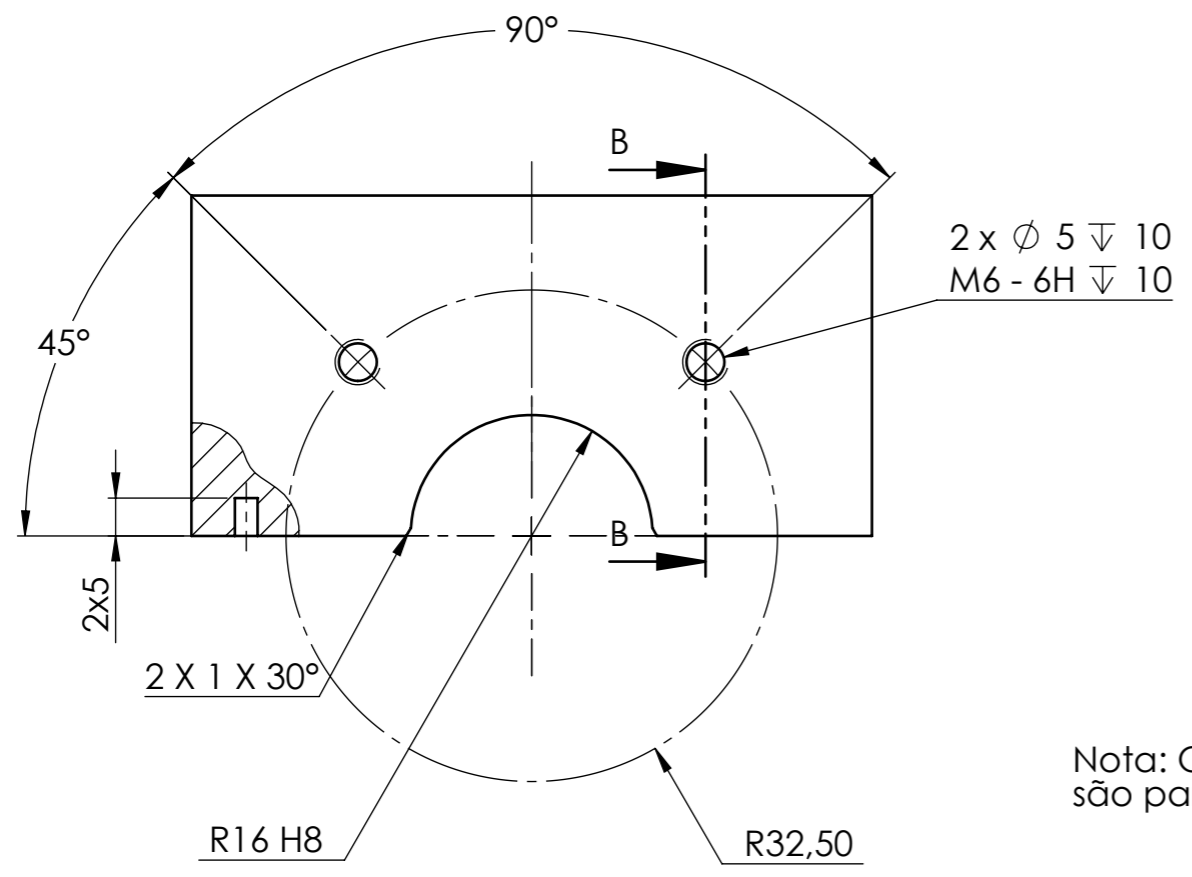
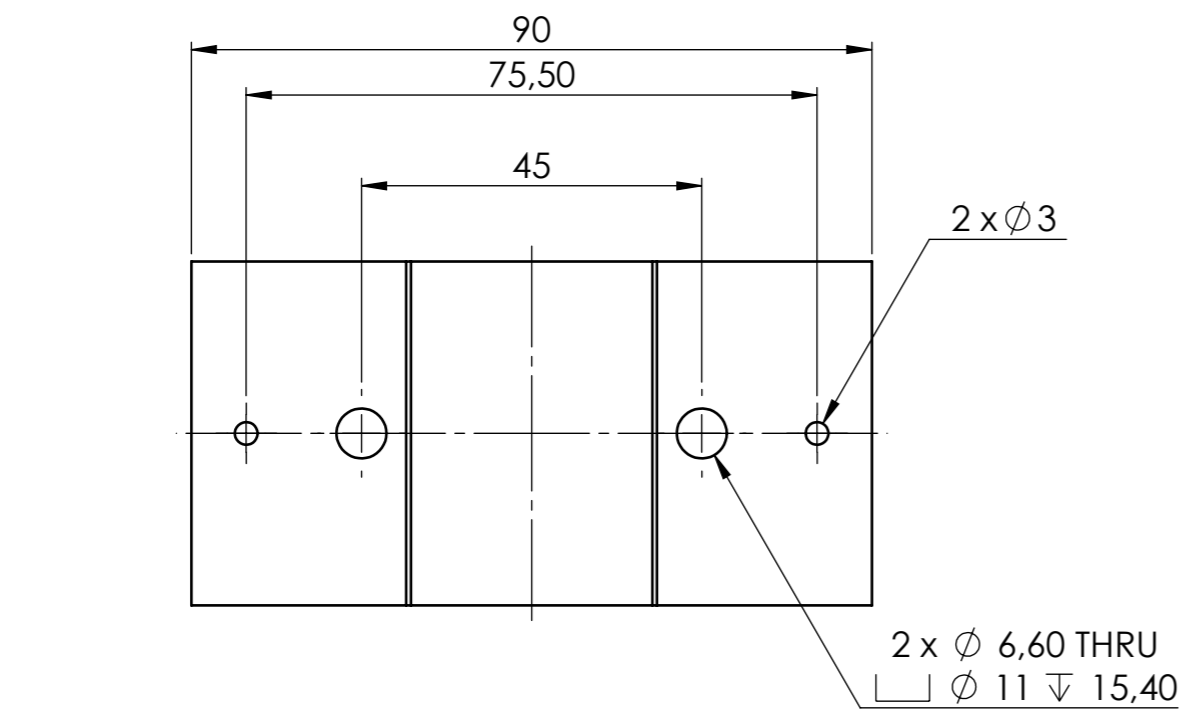


\*Nota: Rosca para componente fornecido pelo LOME

**DIMENSÕES GLOBAIS:**  
Ø 80x70

		TÍTULO:	
		Culatra	
MATERIAL:		DSNH N:	
AÇO		SHPB 04.06.05.16	
PESO: ± XXX g	ESCALA: 1:1	QUANTIDADE: 1	A3 mm FOLHA 1 DE 1

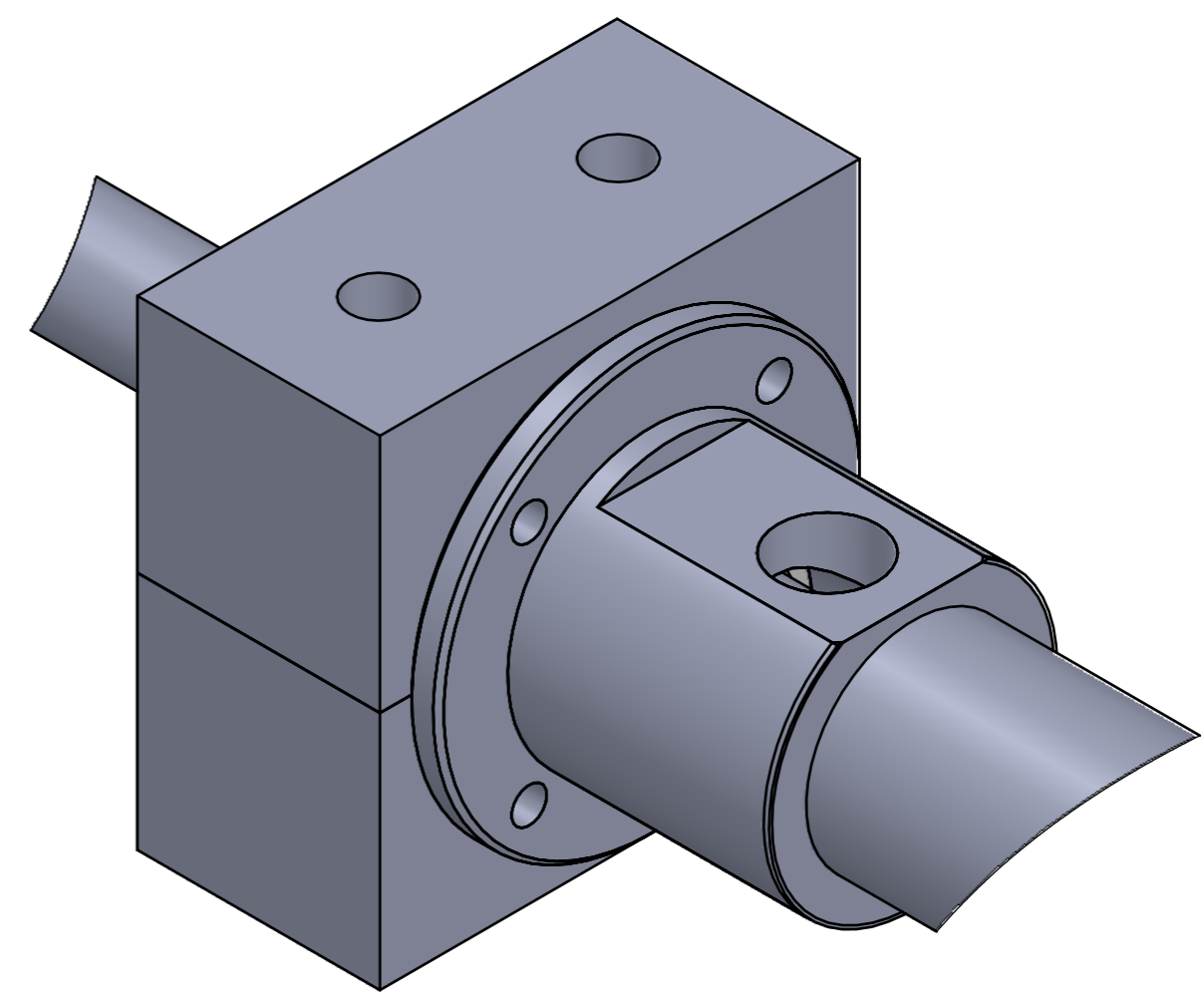
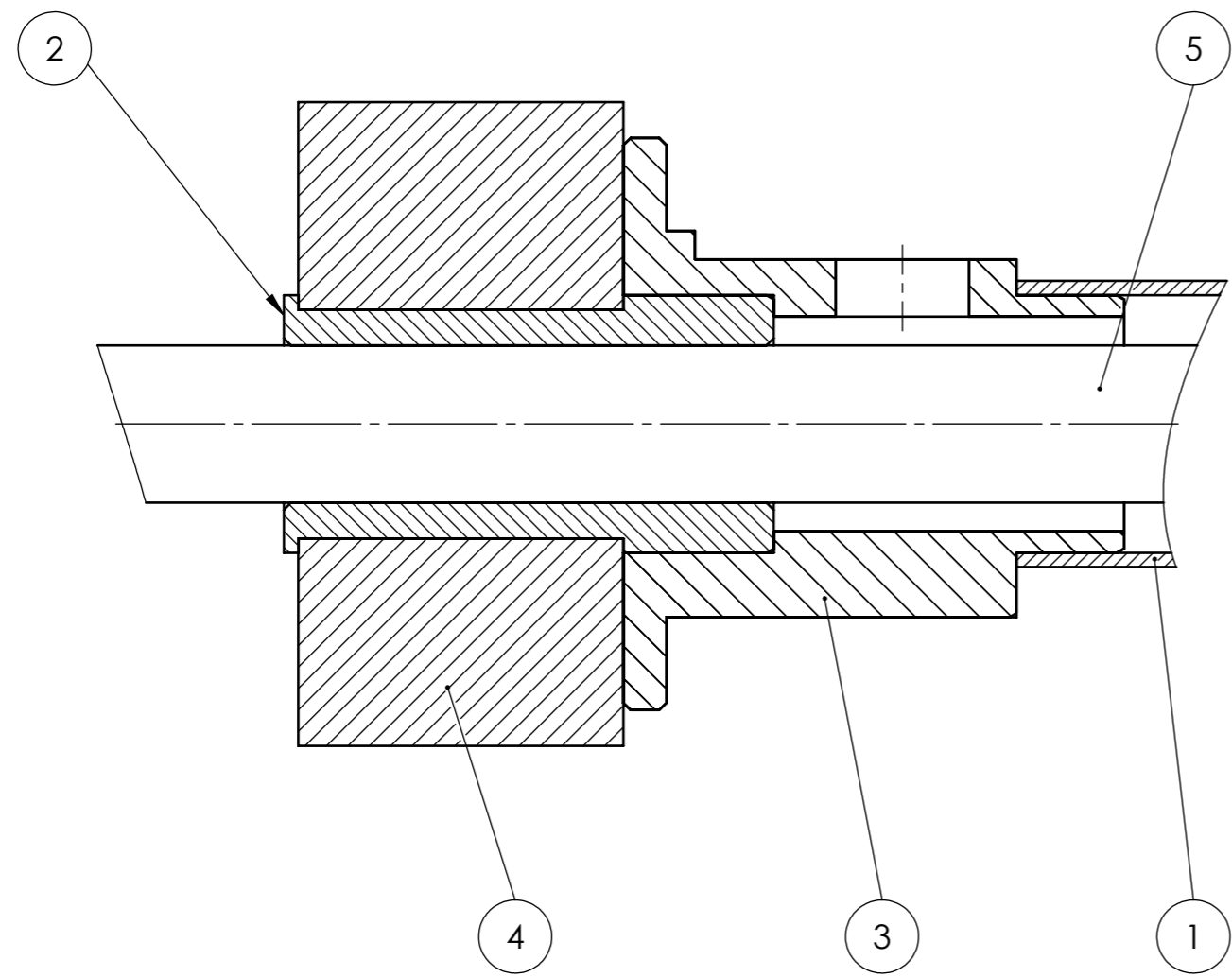




Nota: Os furos de  $\phi$  3mm com profundidade 5mm são para permitir a entrada de cavilhas fornecidas pelo LOME


**DIMENSÕES GLOBAIS:**  
90x45x45,5

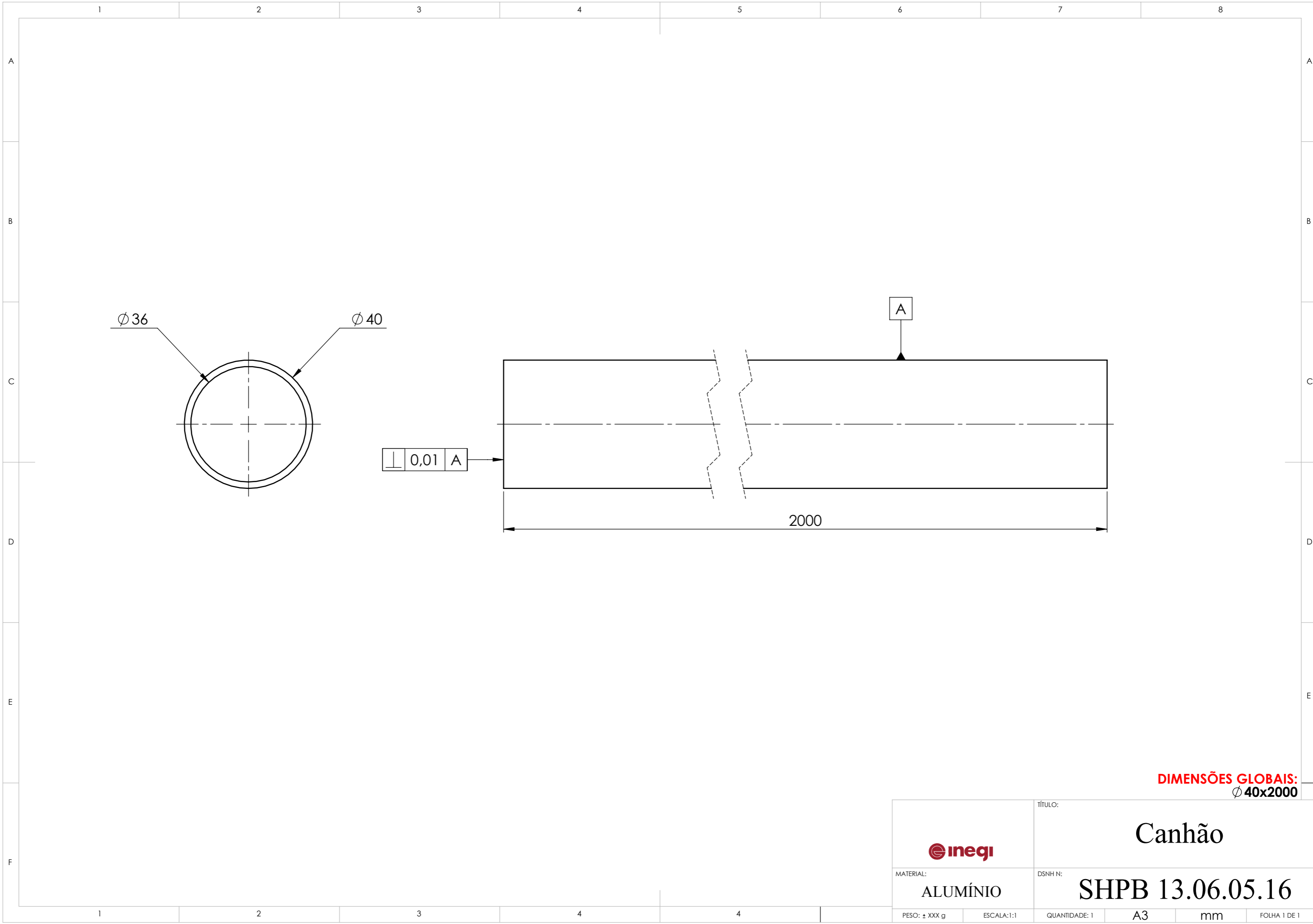
		TÍTULO:	
		Apoio casquilho culatra	
MATERIAL:		DSNH N°:	
ALUMÍNIO		SHPB 07.06.05.16	
PESO: ± XXX g	ESCALA: 1:1	UNIDADES: 2	A3 mm FOLHA 1 DE 1




**DIMENSÕES GLOBAIS:**  
- x - x -

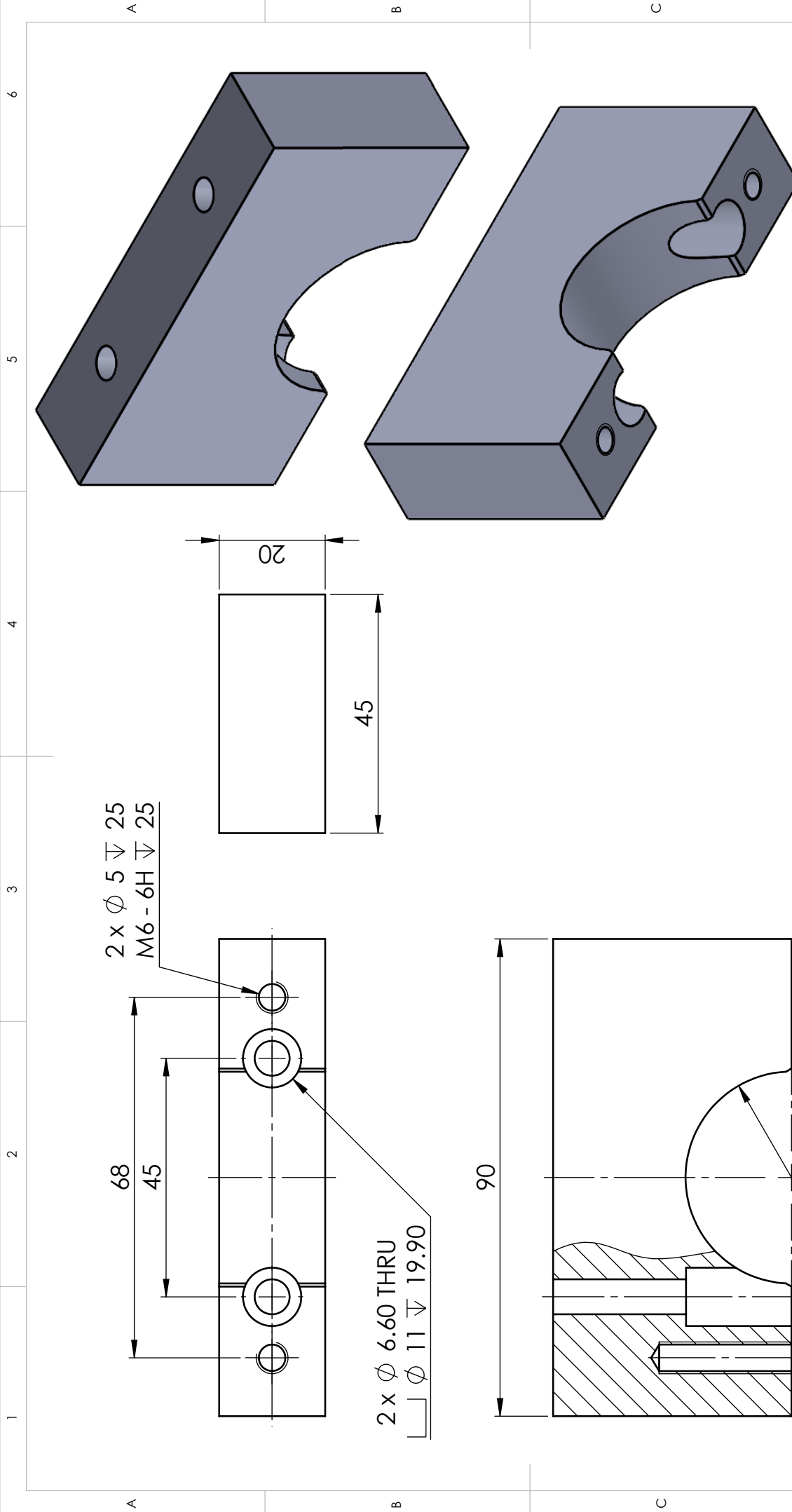
Nº	Designação
1	SHPB 13.06.05.16 - canhão
2	SHPB 03.06.05.16 - casquilho culatra
3	SHPB 04.06.05.16 - culatra
4	SHPB 07.06.05.16 - apoio casquilho culatra
5	SHPB 10.06.05.16 - barra de entrada

		TÍTULO:	
		<h1>Conjunto culatra</h1>	
MATERIAL:		DSNH N:	
		<h2>SHPB 002.06.05.16</h2>	
PESO: ± XXX g	ESCALA: 1:1	QUANTIDADE: 1	FOLHA 1 DE 1



**DIMENSÕES GLOBAIS:**  
 $\varnothing 40 \times 2000$

		TÍTULO:			
		<h1>Canhão</h1>			
MATERIAL:		DSNH N°:			
<h2>ALUMÍNIO</h2>		<h1>SHPB 13.06.05.16</h1>			
PESO: ± XXX g	ESCALA: 1:1	QUANTIDADE: 1	A3	mm	FOLHA 1 DE 1



**DIMENSÕES GLOBAIS:**  
90x45x20

TÍTULO:

# Apoio inferior canhão



MATERIAL: ALUMÍNIO

DSNH N°:

## SHPB 05.06.05.16

PESO: ± XXX g ESCALA: 1:1

UNIDADES: 2

A4

mm

FOLHA 1 DE 1

1

2

3

4

5

6

A

B

C

D

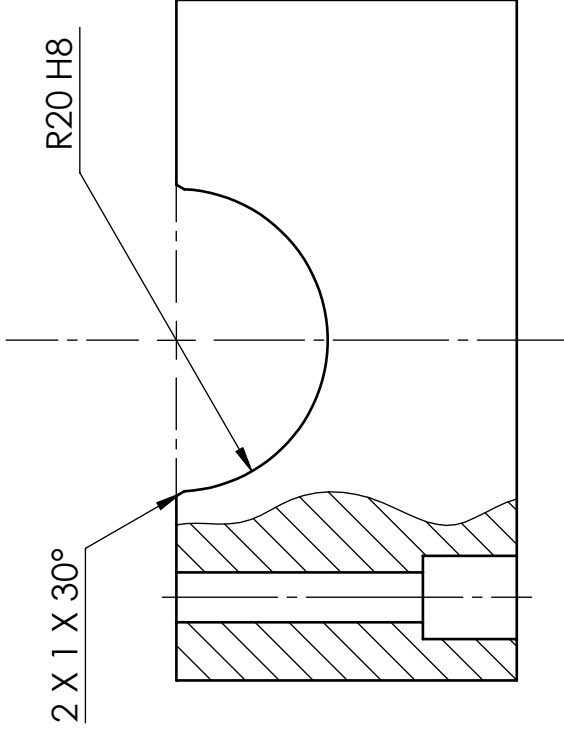
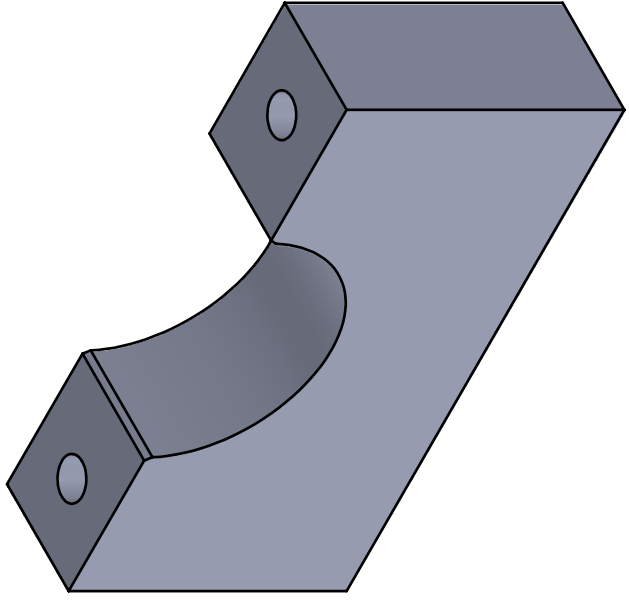
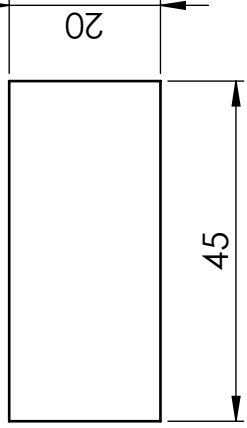
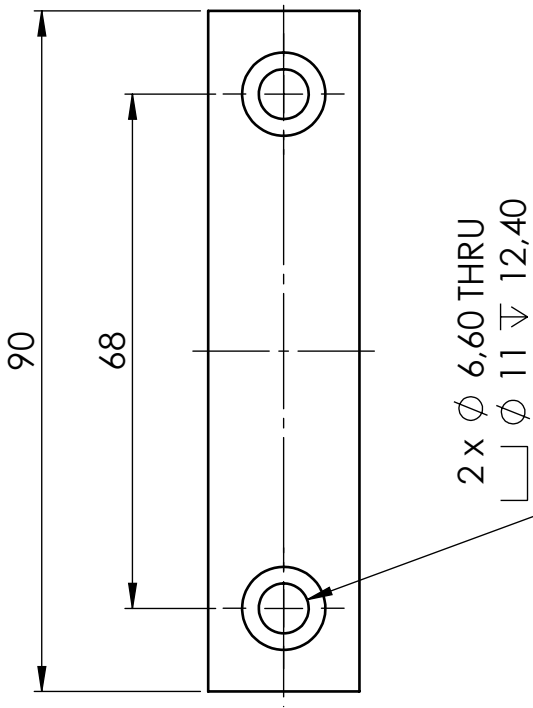
1

2

3

1 2 3 4 5 6

A B C D



**DIMENSÕES GLOBAIS:**  
**90x45x20**

TÍTULO:

**Apoio superior canhão**



MATERIAL:

**ALUMÍNIO**

DSNH Nº:

**SHPB 06.06.05.16**

PESO: ± XXX g

ESCALA: 1:1

A4

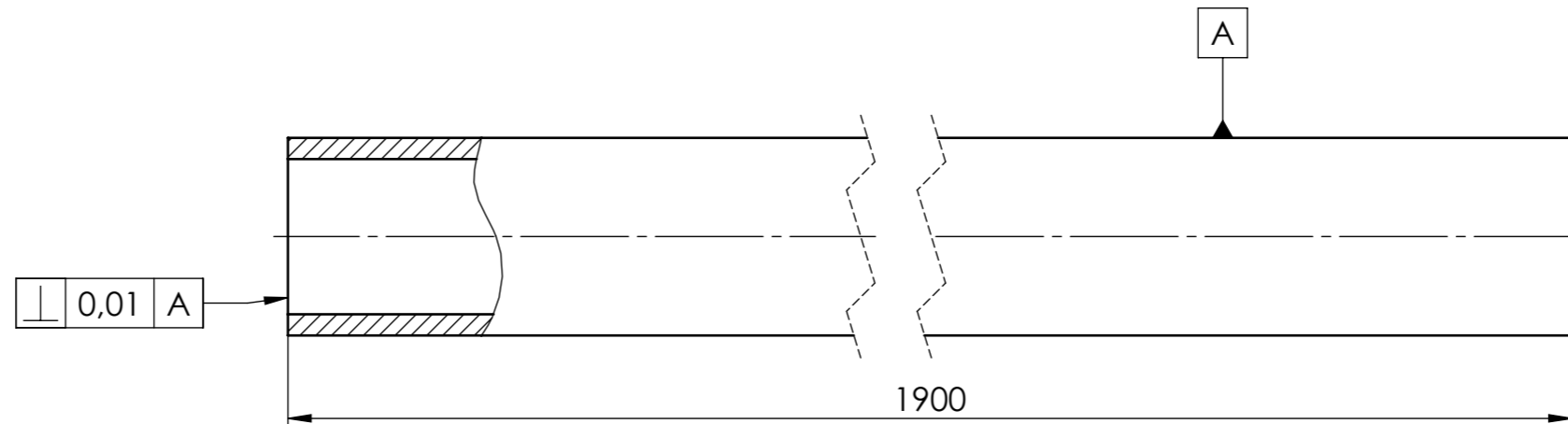
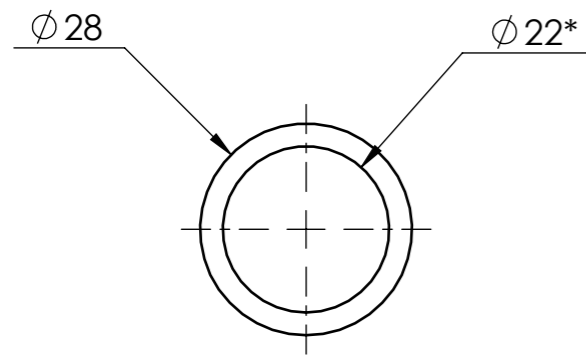
mm

FOLHA 1 DE 1

3


2

1



\*Nota: Deslizante na barra de referência SHPB 10.06.05.16

**DIMENSÕES GLOBAIS:**  
 $\phi 28 \times 1900$

		TÍTULO:			
		<h1>Impactor</h1>			
MATERIAL:		DSNH N:			
<h2>AÇO</h2>		<h1>SHPB 12.06.05.16</h1>			
PESO: ± XXX g	ESCALA: 1:1	QUANTIDADE: 1	A3	mm	FOLHA 1 DE 1

1 2 3 4 5 6

A

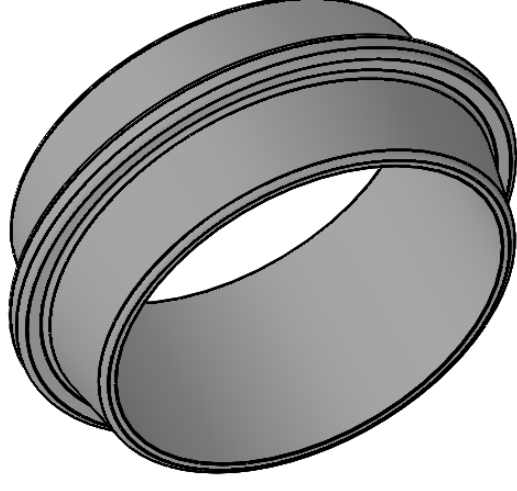
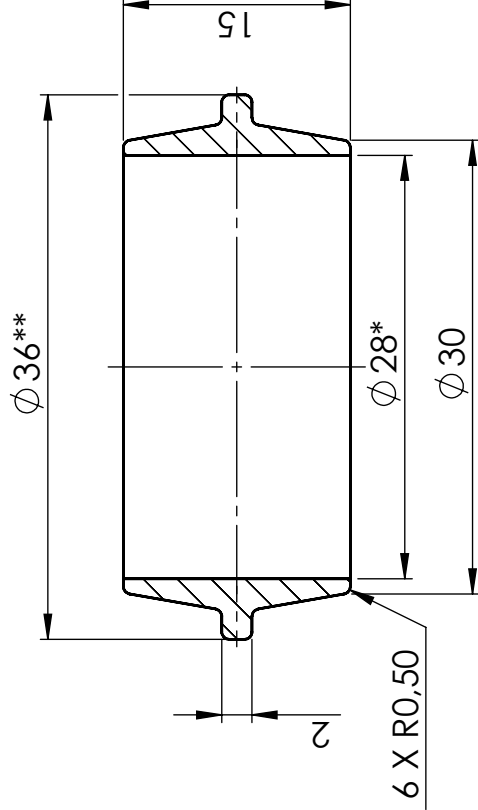
A

B

B

C

C



**DIMENSÕES GLOBAIS:**  
 $\phi 36 \times 15$

Nota\*: Montado com interferência na barra de referência SHPB 12.06.05.16  
 Nota\*\*: Deslizante no tubo de referência SHPB 13.06.05.16

TÍTULO:

# Casquilho impactor



MATERIAL:

TEFLON

DSNH Nº:

## SHPB 14.06.05.16

PESO: ± XXX g

ESCALA: 2:1

UNIDADES: 2

A4

mm

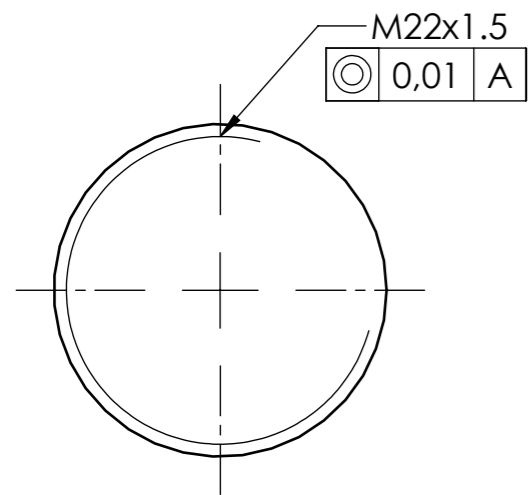
FOLHA 1 DE 1

1

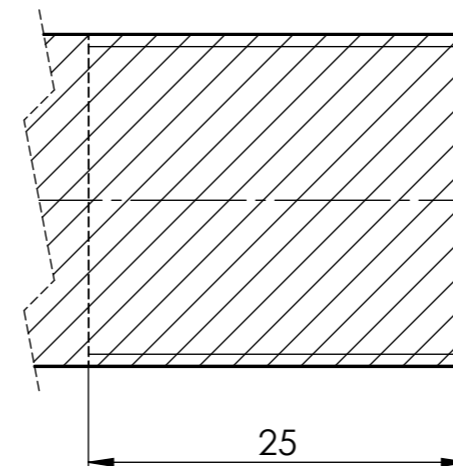
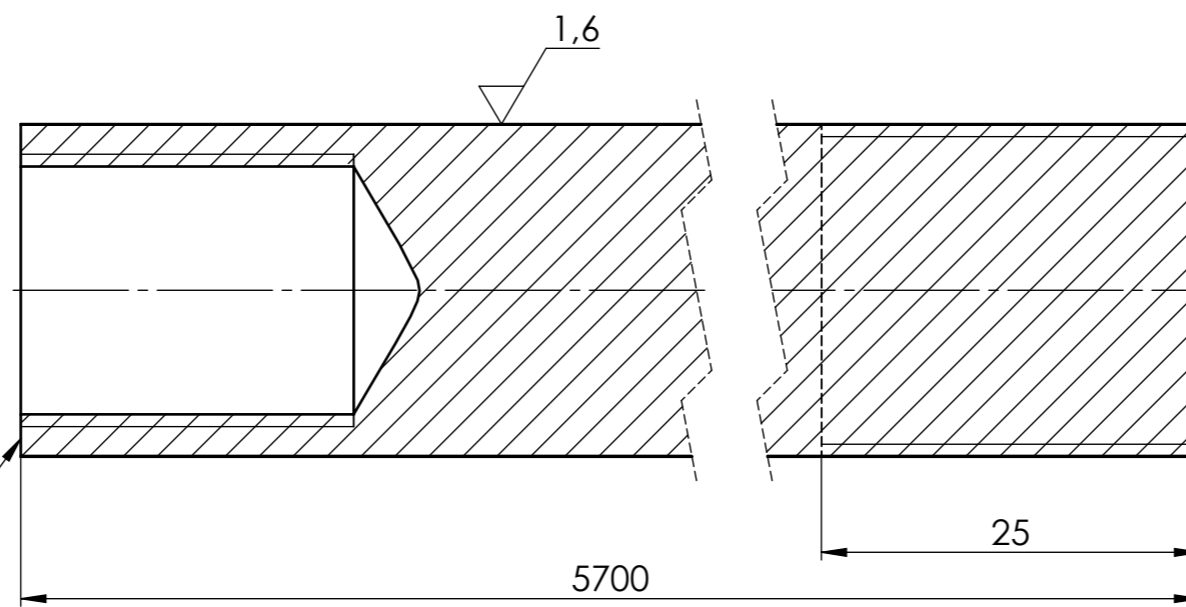
2

3

D

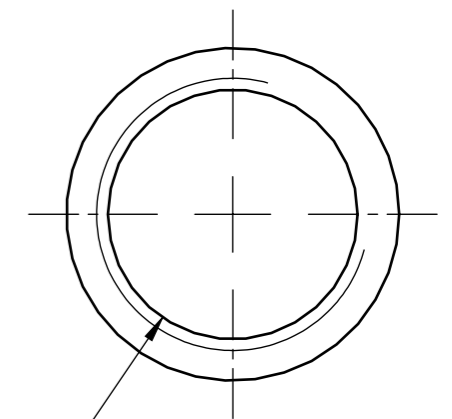


⊥ 0,01 A




$\phi 22$

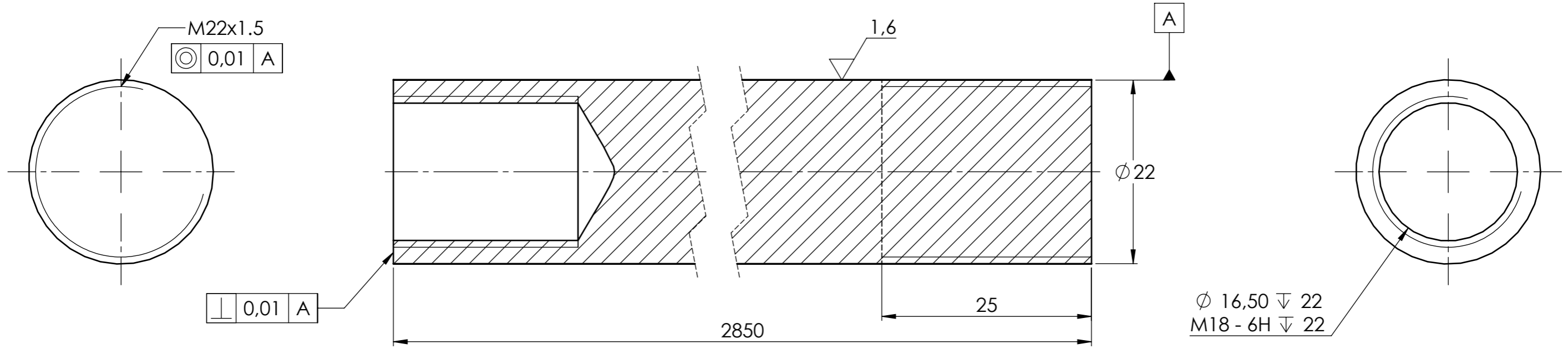
$\phi 16,50 \nabla 22$   
M18 - 6H  $\nabla 22$



**DIMENSÕES GLOBAIS:**  
 $\phi 22 \times 5700$

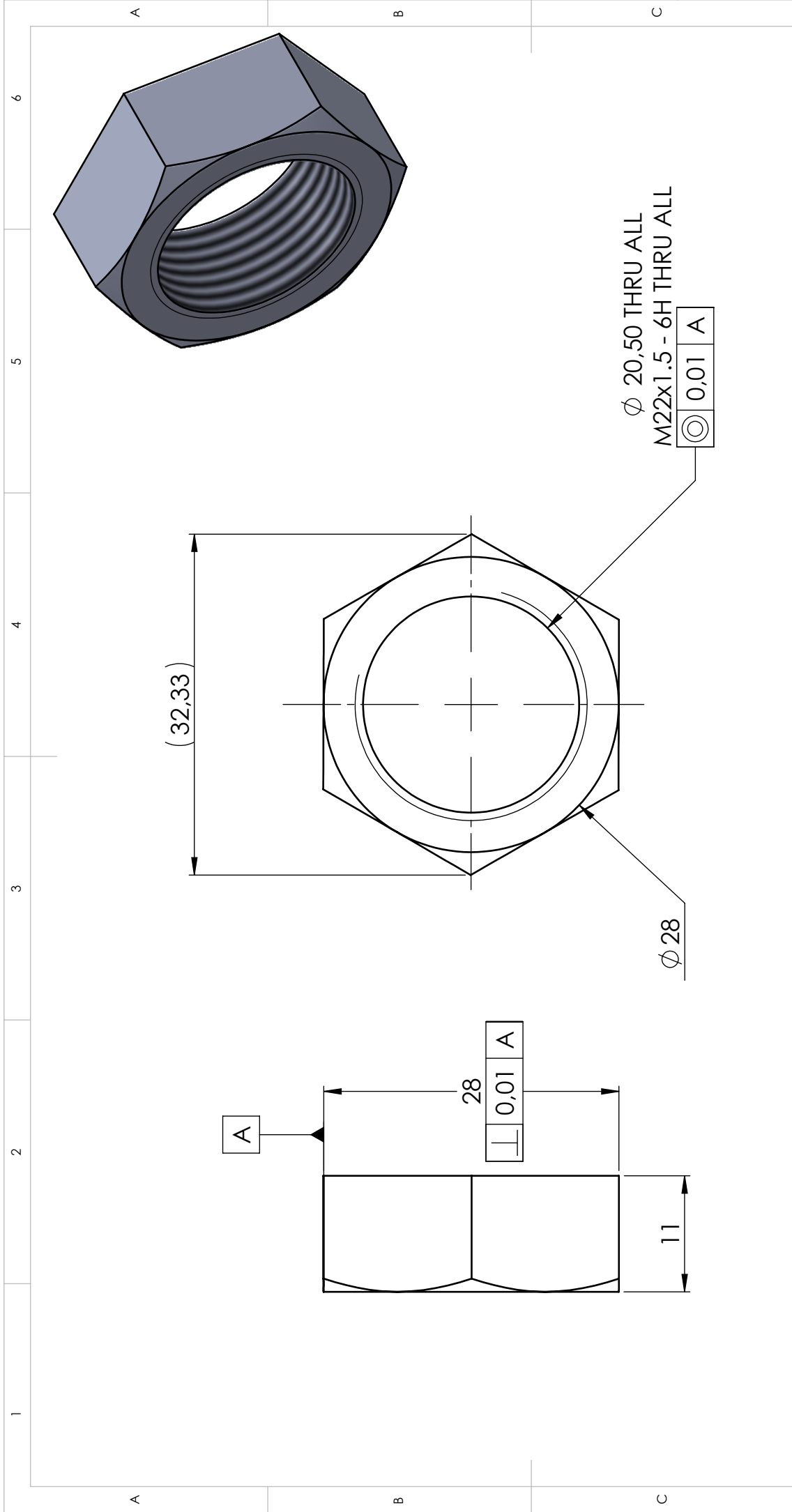
		TÍTULO:			
		Barra de entrada			
MATERIAL:		DSNH N:			
AÇO		SHPB 10.06.05.16			
PESO: ± XXX g	ESCALA: 2:1	QUANTIDADE: 1	A3	mm	FOLHA 1 DE 1





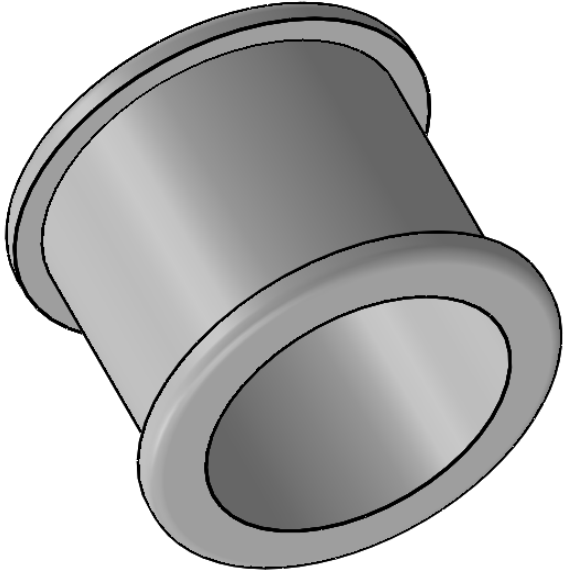
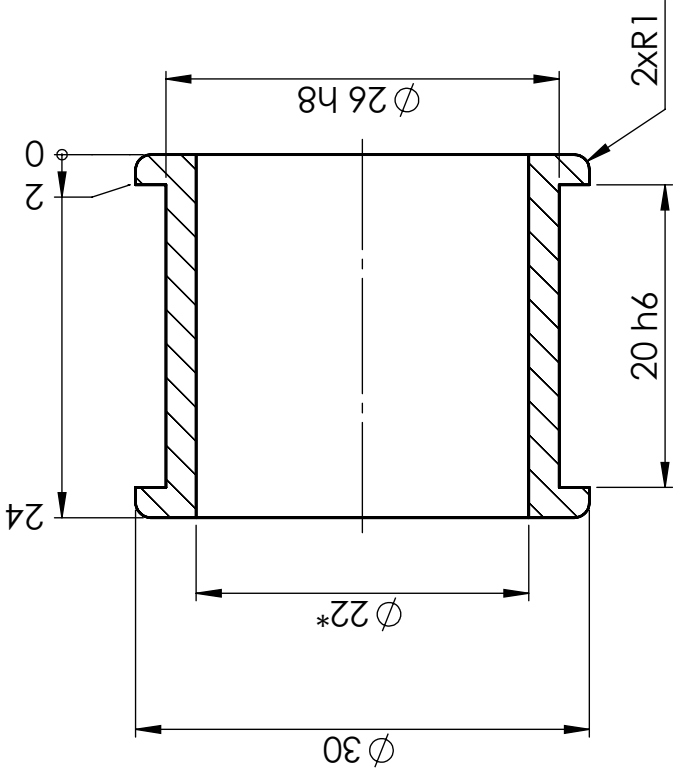
**DIMENSÕES GLOBAIS:**  
 Ø 22x2850

		TÍTULO:		
		<h1>Barra de saída</h1>		
MATERIAL:		DSNH N:		
<h2>AÇO</h2>		<h1>SHPB 11.06.05.16</h1>		
PESO: ± XXX g	ESCALA: 2:1	QUANTIDADE: 1	A3	FOLHA 1 DE 1



**DIMENSÕES GLOBAIS:**  
 $\phi 33 \times 11$

		TÍTULO:		Porca M22x1,5	
		MATERIAL:		AÇO	
DSNH N°:		ESCALA:2:1		UNIDADES:2	
SHPB 19.06.05.16		PESO: ± XXX g		A4	
FOLHA 1 DE 1		3		mm	



**DIMENSÕES GLOBAIS:**  
 $\varnothing 30 \times 24$

\*Nota: Furo deslizante nas barras de referência  
 SHPB 10.06.05.16 e SHPB 11.06.05.16



MATERIAL:  
 TEFLON BRANCO

PESO: ± xxx g ESCALA: 2:1

TÍTULO:

Casquilho barras

DSNH N°:

SHPB 09.06.05.16

UNIDADES: 7

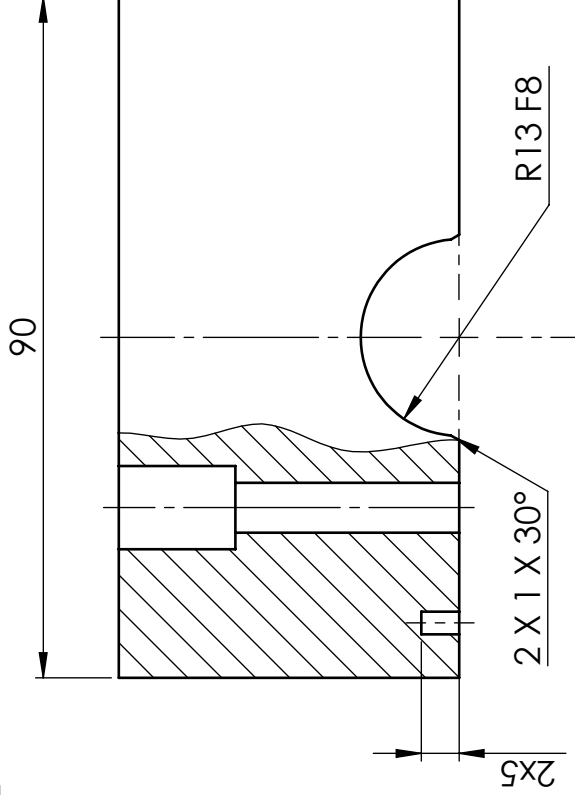
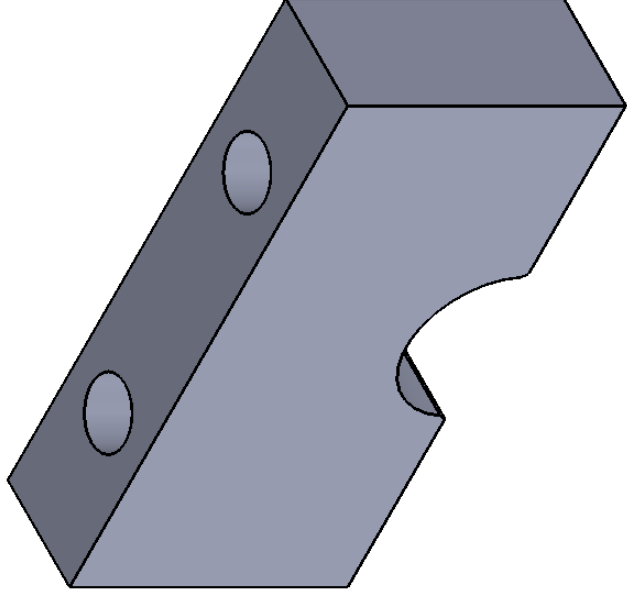
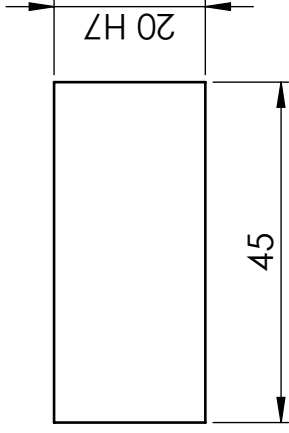
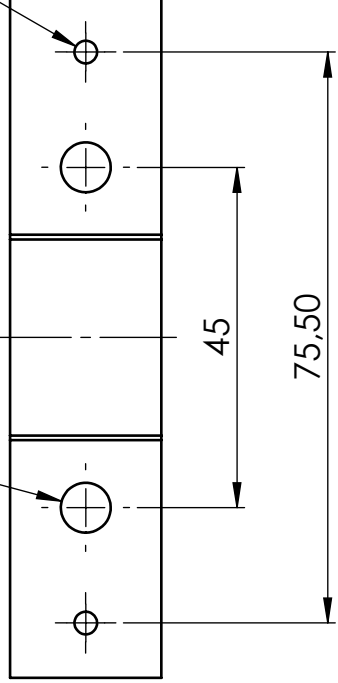
A4

mm

FOLHA 1 DE 1

2 x Ø 6,60 THRU  
 □ Ø 11 ▽ 15,40

2 x Ø 3



**Nota:** os furos de Ø 3mm com profundidade 5mm são para permitir a entrada de cavilhas fornecidas pelo LOME

**DIMENSÕES GLOBAIS:**  
 90x45x20



MATERIAL:  
 ALUMÍNIO

PESO: ± XXX g ESCALA: 1:1

TÍTULO:

Apoios barras

DSNH Nº:

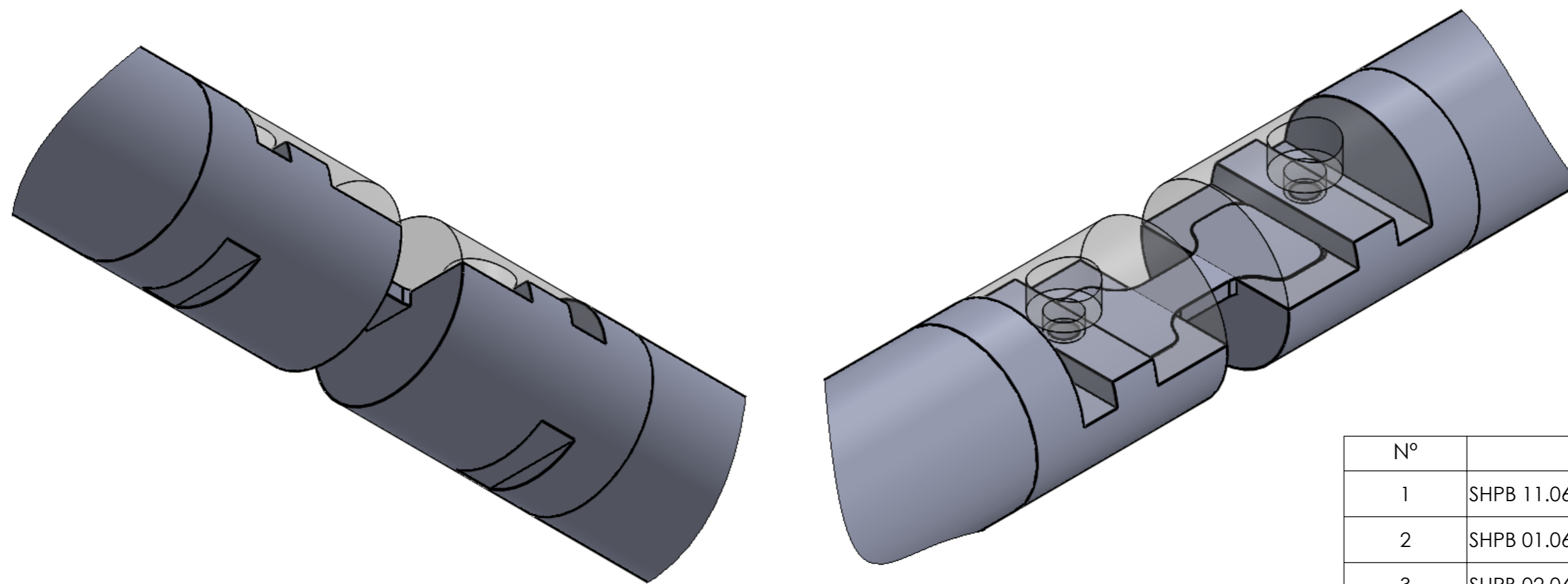
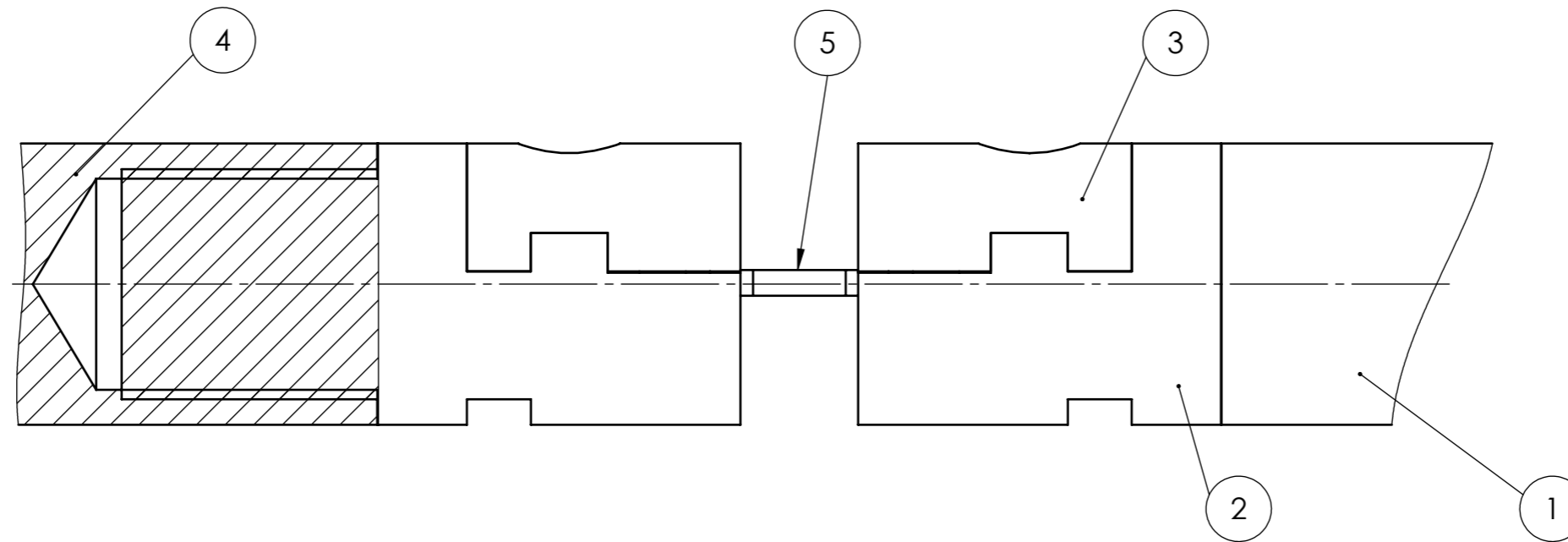
**SHPB 08.06.05.16**

UNIDADES: 14

A4


mm

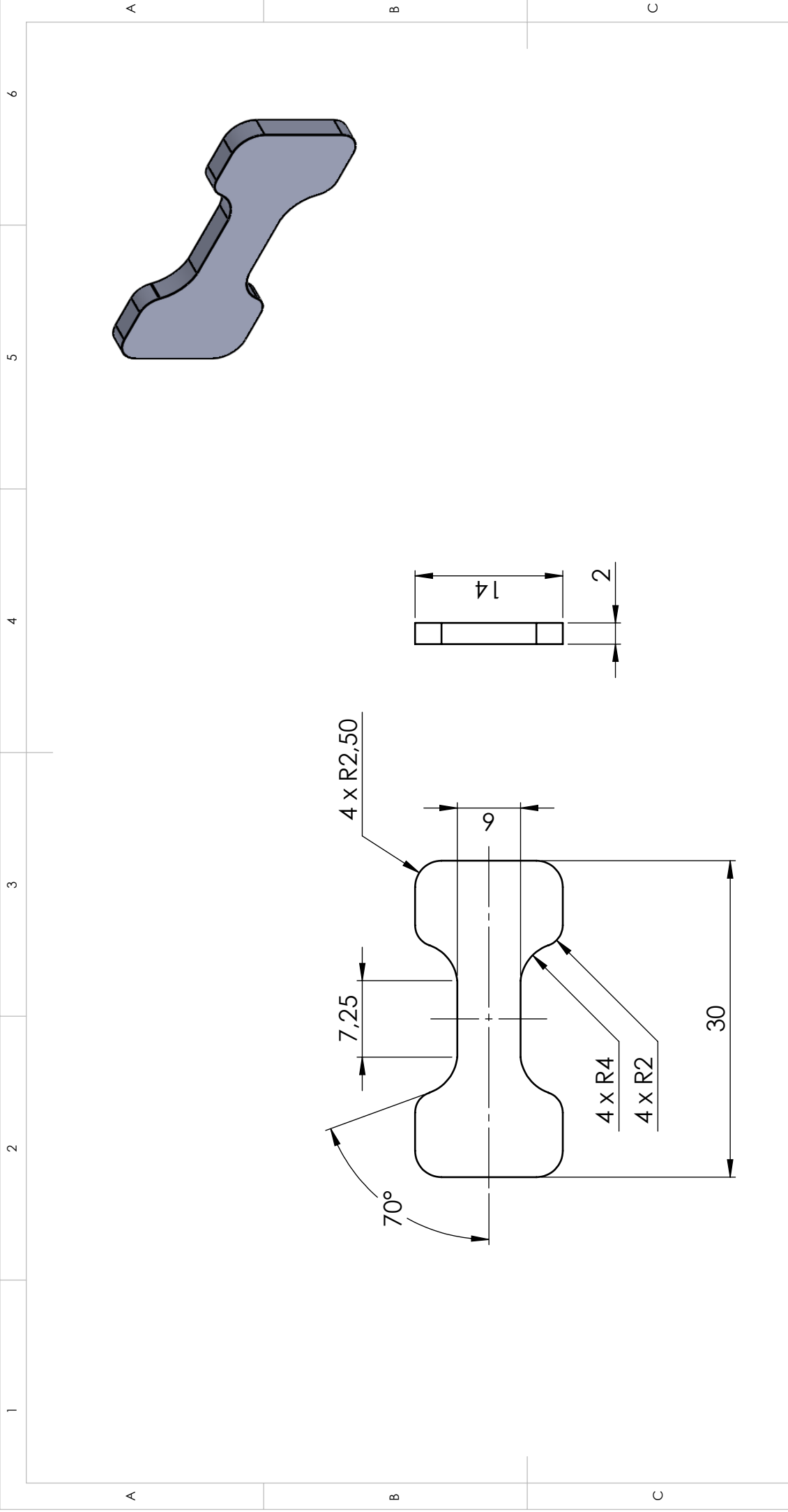
FOLHA 1 DE 1




**DIMENSÕES GLOBAIS:**  
- x - x -

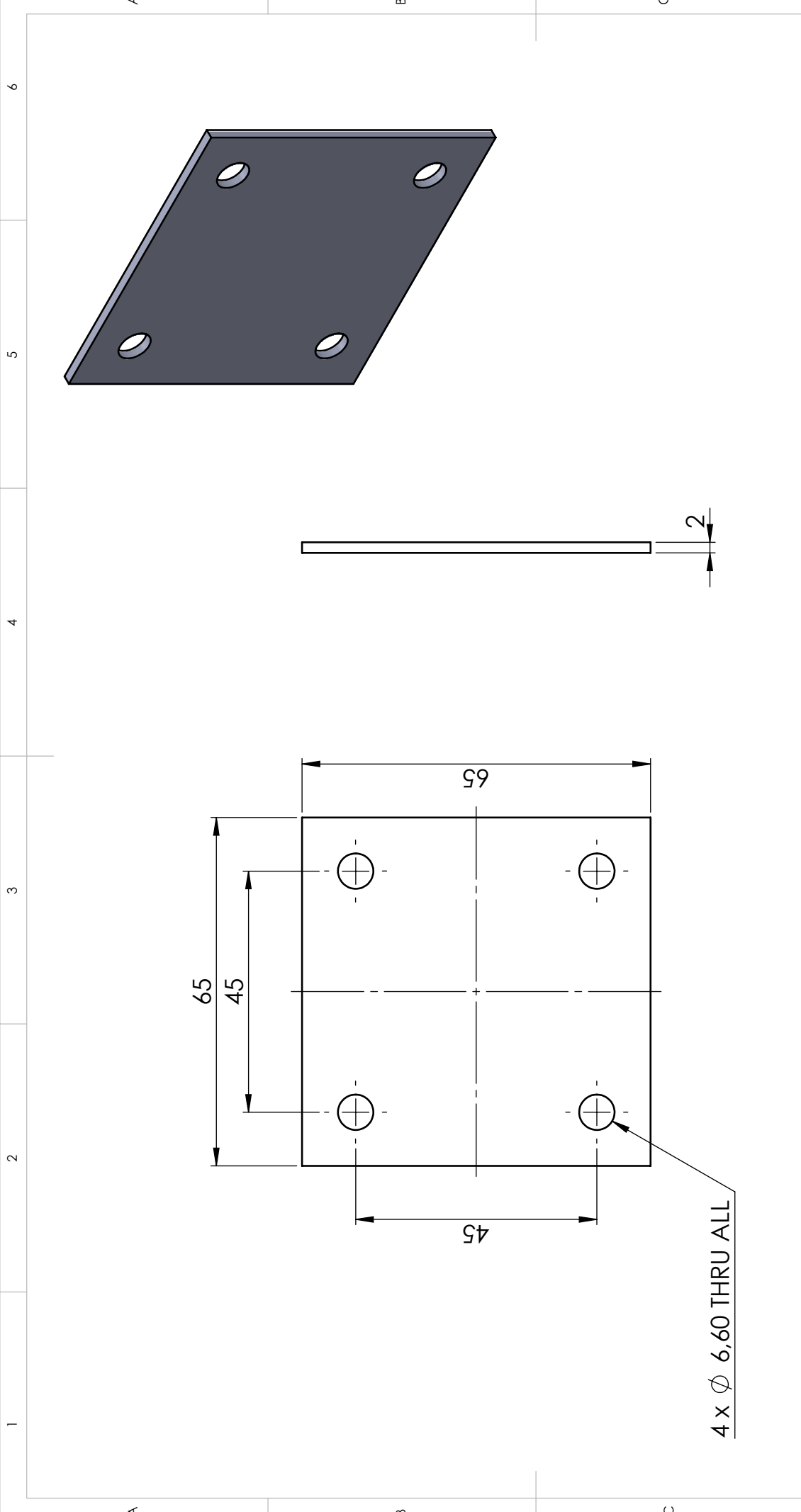
Nº	Designação
1	SHPB 11.06.05.16 - barra de saída
2	SHPB 01.06.05.16 - amarras
3	SHPB 02.06.05.16 - tampa amarra
4	SHPB 10.06.05.16 - barra de entrada
5	SHPB 15.06.05.16 - provete

	TÍTULO:	<b>Barras, amarras e provete</b>		
	MATERIAL:	DSNH N:	<b>SHPB 004.06.05.16</b>	
PESO: ± XXX g	ESCALA: 2:1	QUANTIDADE: 1	A3	mm
		FOLHA 1 DE 1		



**DIMENSÕES GLOBAIS:**  
30x14x2

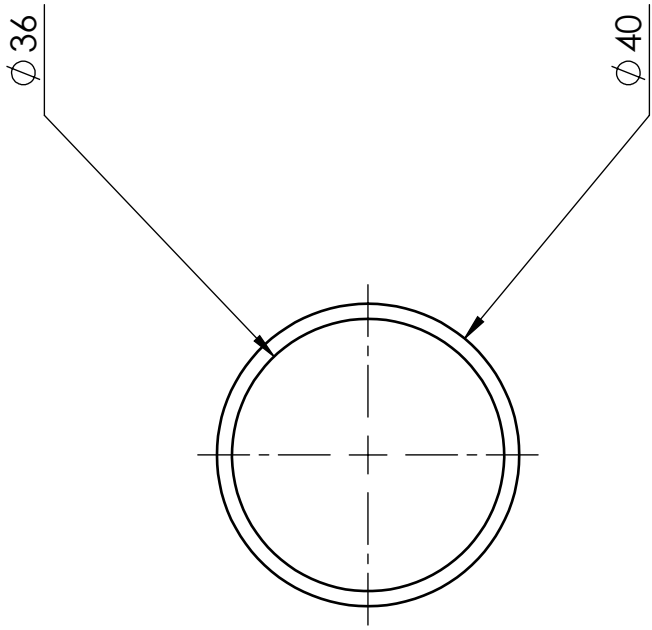
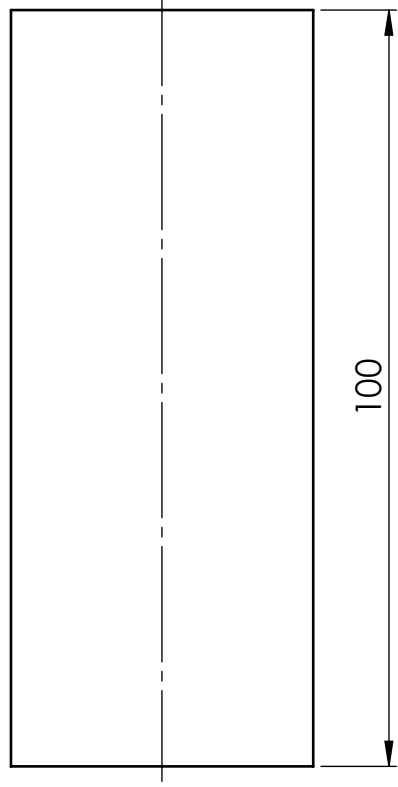
		TÍTULO:		Provete	
		MATERIAL:		ALUMÍNIO	
PESO: ± XXX g		ESCALA: 2:1		UNIDADES: 9	
3		A4		mm	
1		DSNH N°:		SHPB 15.06.05.16	
2		FOLHA 1 DE 1			



**DIMENSÕES GLOBAIS:**  
65x65x2

	TÍTULO:  <h1>Chapa absorsor</h1>
MATERIAL: ALUMÍNIO	DSNH N°: <h2>SHPB 16.06.05.16</h2>
PESO: ± XXX g    ESCALA: 1:1	UNIDADES: 1    A4    mm    FOLHA 1 DE 1

4 x Ø 6,60 THRU ALL



**DIMENSÕES GLOBAIS:**  
 $\phi 40 \times 100$



MATERIAL: ALUMÍNIO

PESO: ± XXX g ESCALA: 1:1

TÍTULO:

**Tubo absorSOR**

DSNH N°:

**SHPB 17.06.05.16**

UNIDADES: 1

A4

mm

FOLHA 1 DE 1

1 2 3 4 5 6

A A

B B

C C

D

1

2

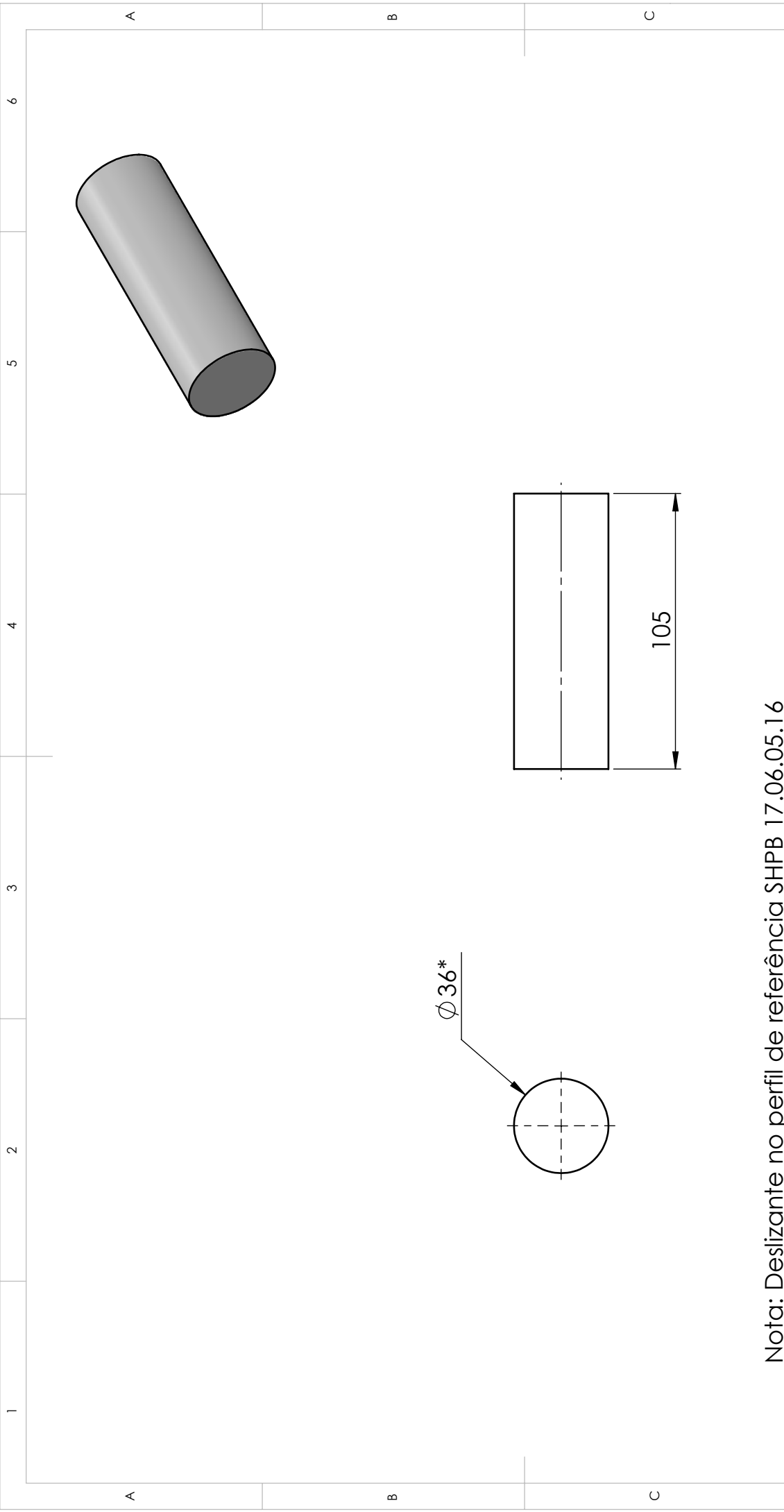
3

100

$\phi 36$


$\phi 40$

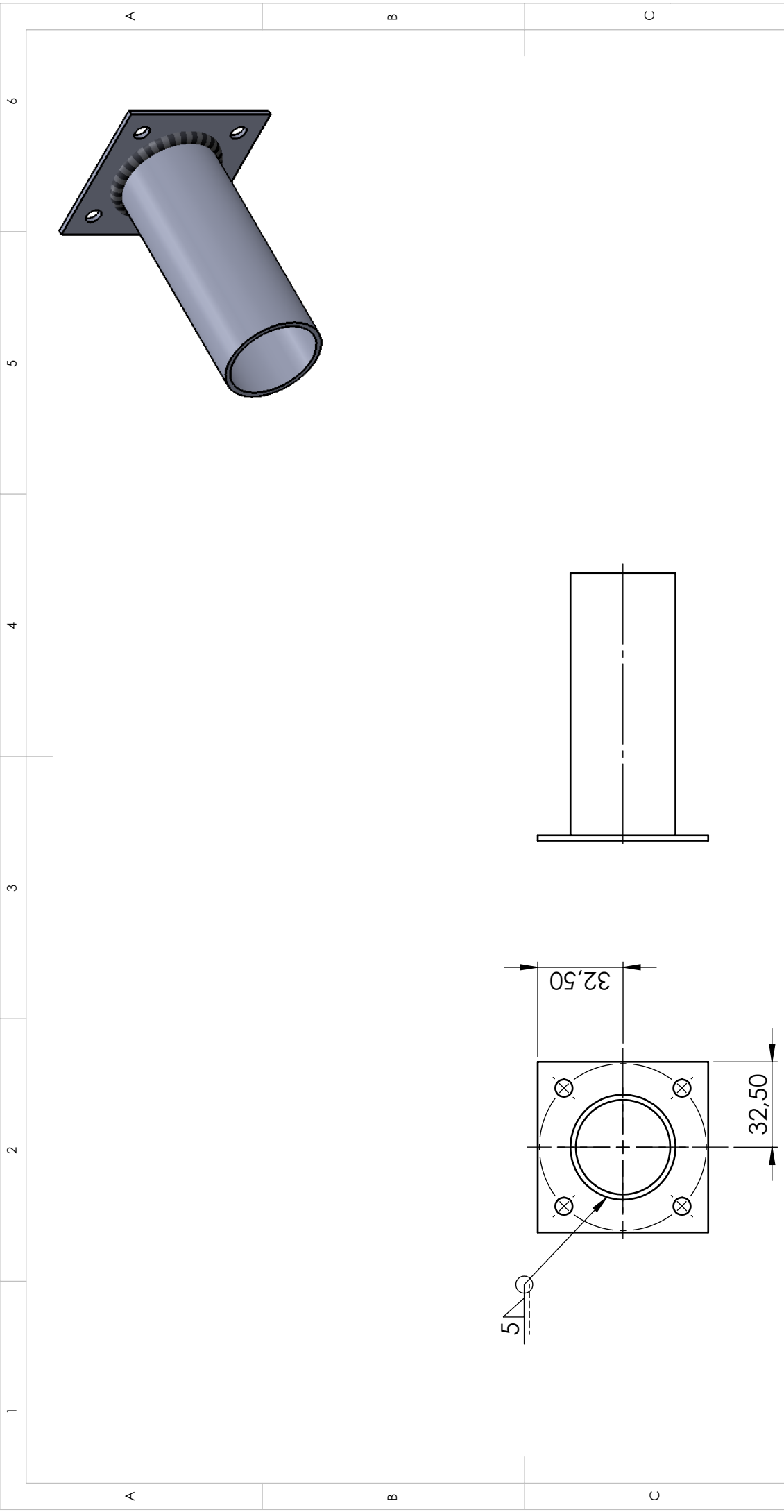




Nota: Deslizante no perfil de referência SHPB 17.06.05.16

**DIMENSÕES GLOBAIS:**  
 $\phi 36 \times 105$

		TÍTULO:				Tubo Nylon					
		MATERIAL: NYLON		DSNH N°:		SHPB 18.06.05.16		UNIDADES: I		A4	
PESO: ± xxx g		ESCALA: 1:2		3		2		1		FOLHA 1 DE 1	



**DIMENSÕES GLOBAIS:**  
- X- X -



TÍTULO:

**Chapa e tubo absorsor**

MATERIAL:

DSNH N°:

**SHPB 005.06.05.16**

PESO: ± XXX g

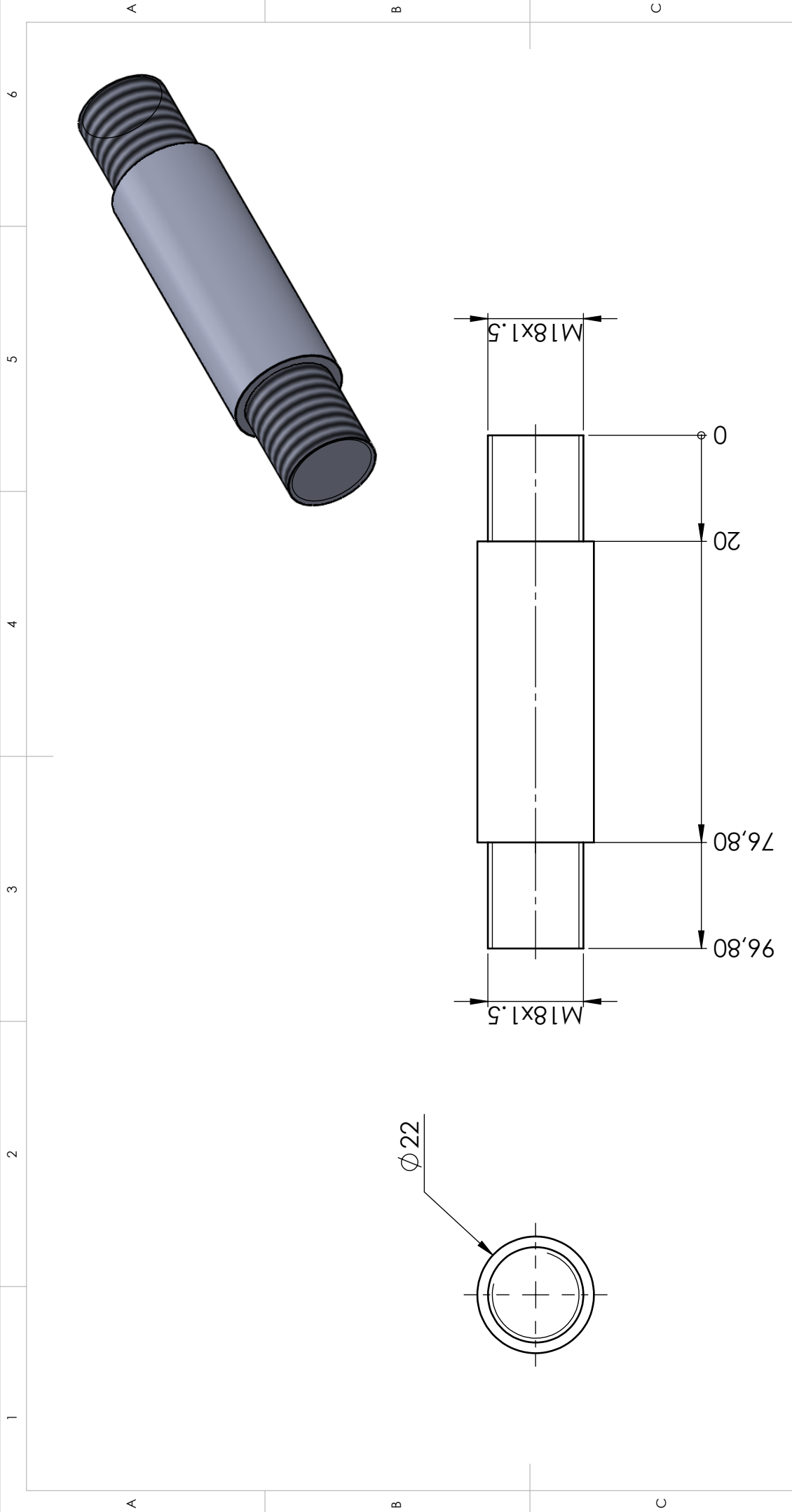
ESCALA:1:2

UNIDADES: I


A4

mm

FOLHA 1 DE 1



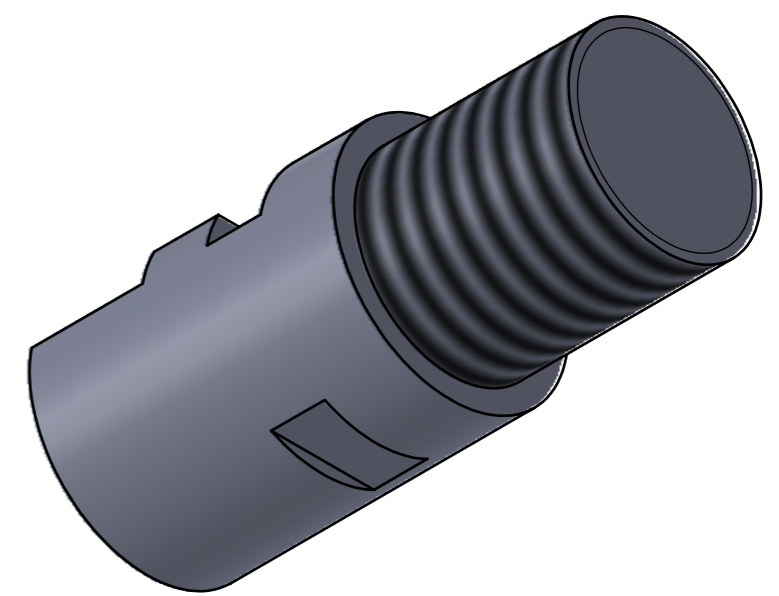
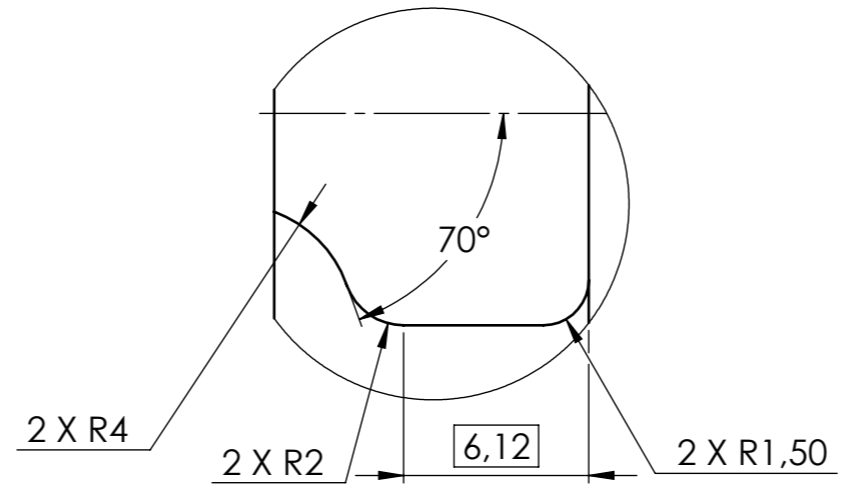
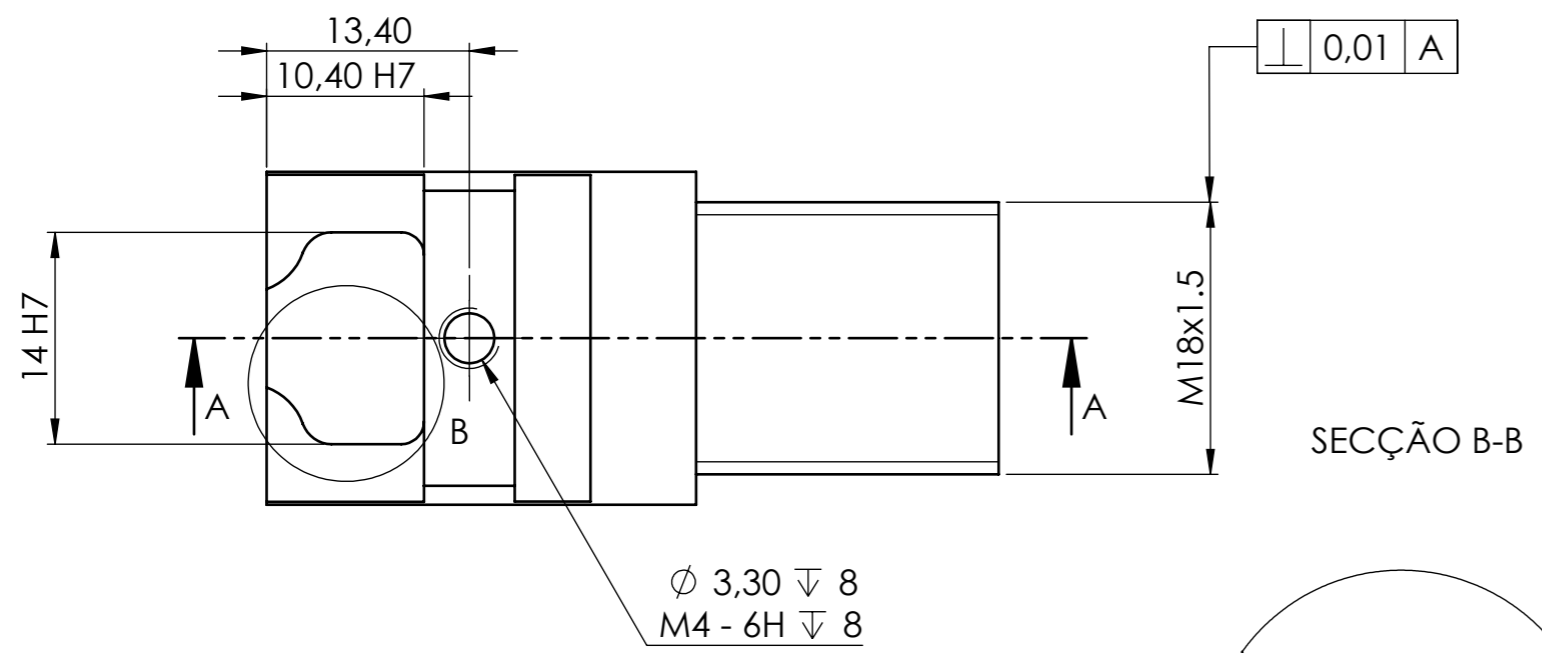
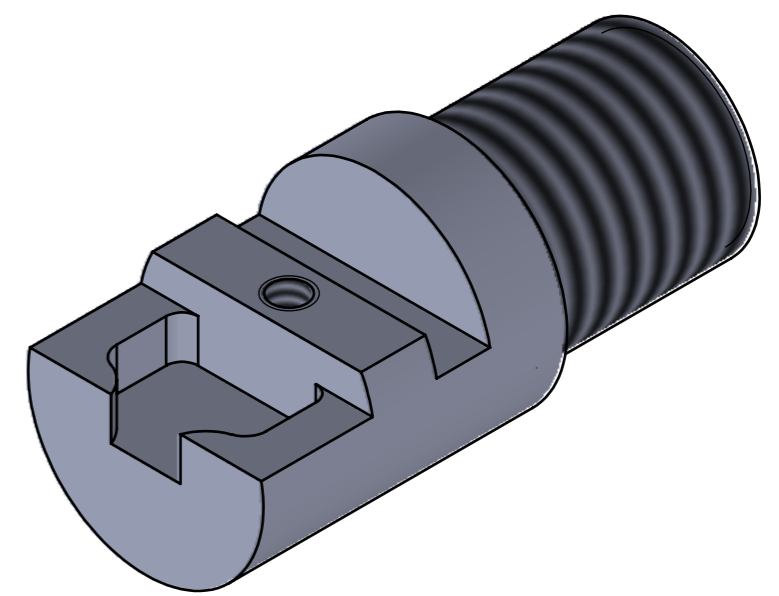
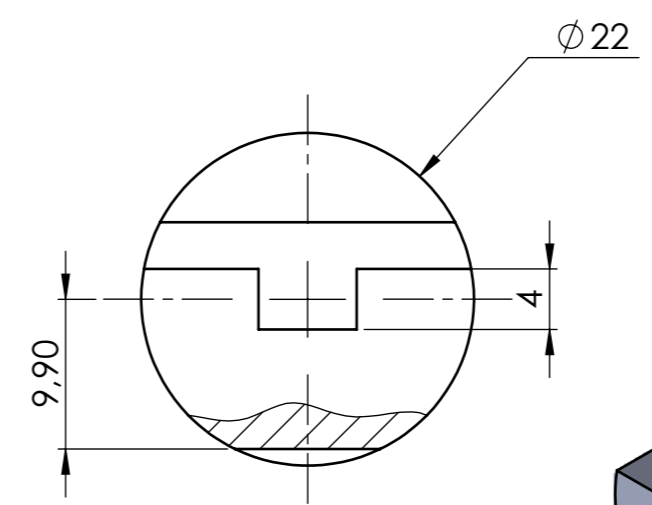
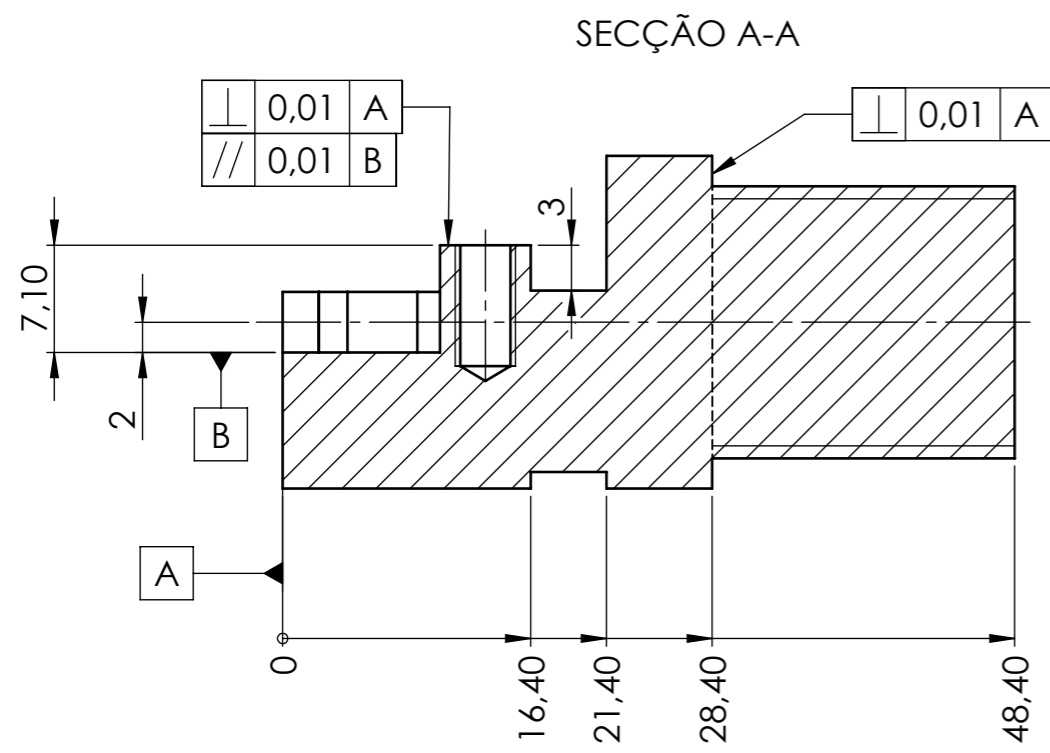
**DIMENSÕES GLOBAIS:**  
 $\varnothing 20 \times 96,80$

		TÍTULO:		Peça calibração	
		MATERIAL:		AÇO	
PESO: ± XXX g		ESCALA: 1:1		UNIDADES: I	
3		A4		mm	
2		DSNH N°:		SHPB 20.06.06.16	
1		FOLHA 1 DE 1			



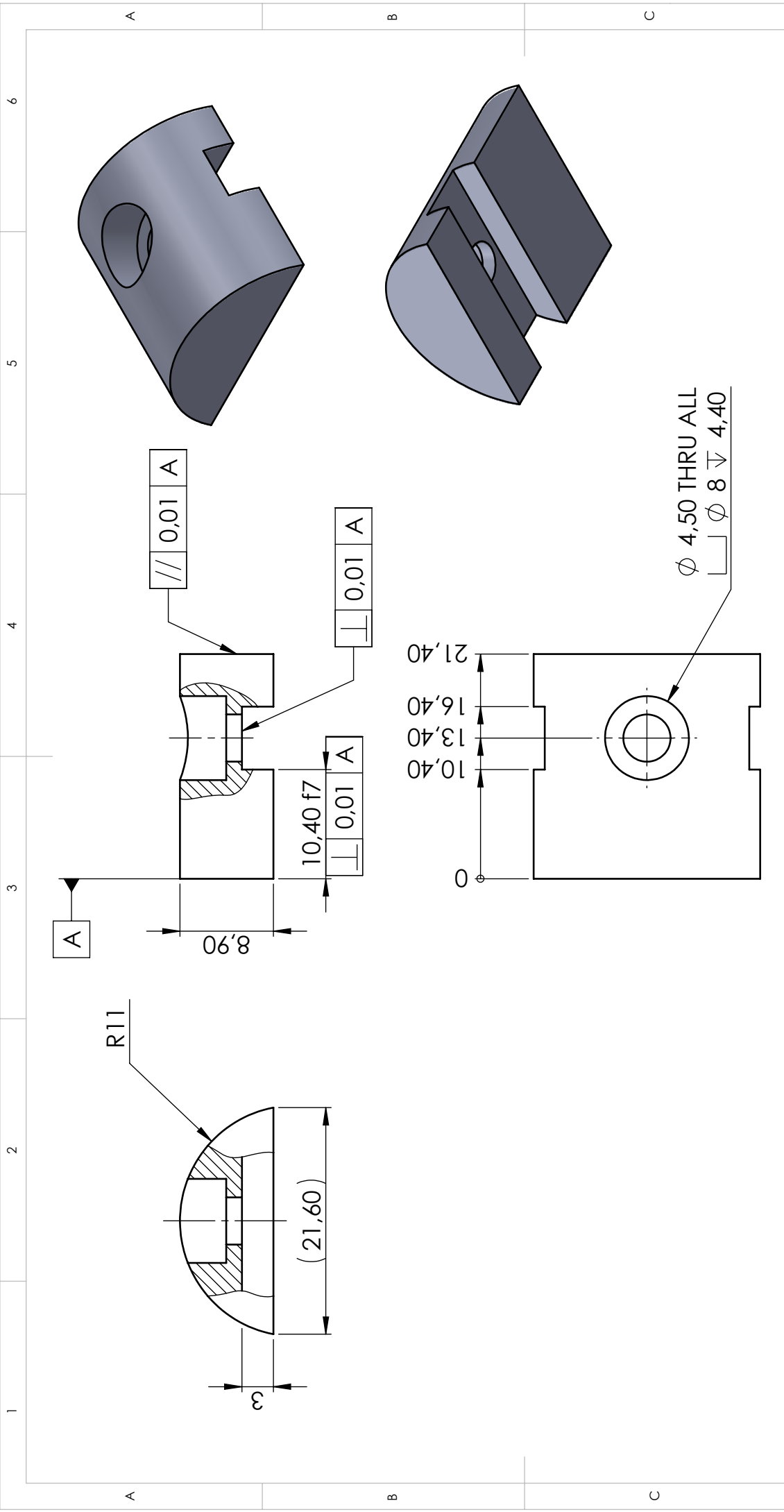
## **Appendix B**

# **Technical drawings of the SHTB components for testing single lap joints**



**DIMENSÕES GLOBAIS:**  
 Ø 22x48,40

		TÍTULO: <b>Amarras</b>		
		DSNH N: <b>SHPBJS 01.01.05.16</b>		
MATERIAL: <b>AÇO</b>	PESO: ± XXX g	ESCALA: 2:1	QUANTIDADE: 2	A3
		mm	FOLHA 1 DE 1	



**DIMENSÕES GLOBAIS:**  
 $\varnothing$  22x21,40

		TÍTULO: <b>Tampa amarra</b>	
MATERIAL: <b>AÇO</b>	DSNH N.º: <b>SHPBJS 02.01.05.16</b>	UNIDADES: 2	mm
PESO: ± XXX g	ESCALA: 2:1	A4	FOLHA 1 DE 1

6

5

4

3

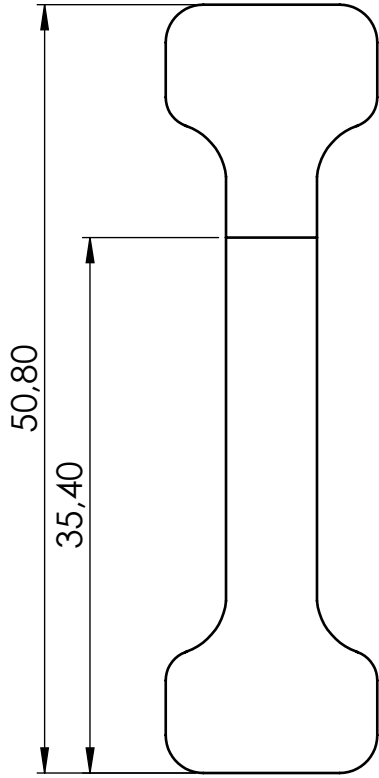
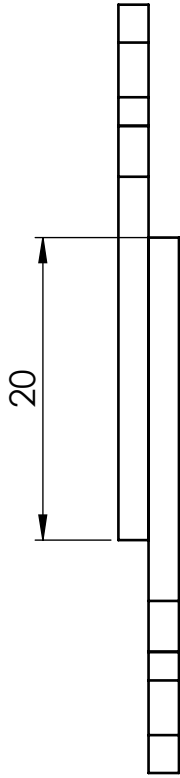
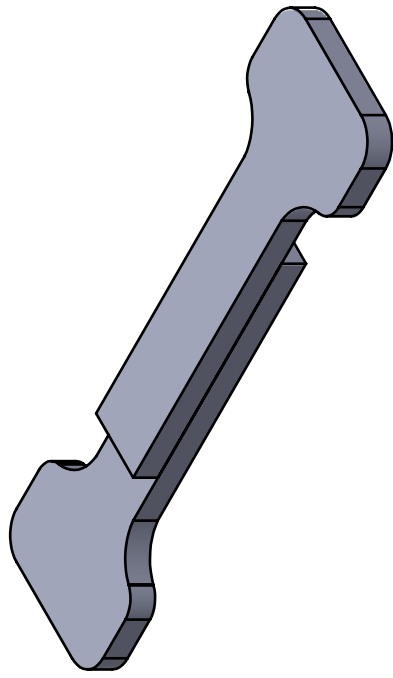
2

1

A

B

C



**DIMENSÕES GLOBAIS:**  
- X - X -

TÍTULO:

**Provete overlap joint**  
**20 mm**



MATERIAL:

**ALUMÍNIO**

DSNH N.º:

**SHPBJS 06.01.05.16**

PESO: ± XXX g

ESCALA: 2:1

UNIDADES: 3

A4

mm

FOLHA 1 DE 1

3

2

1

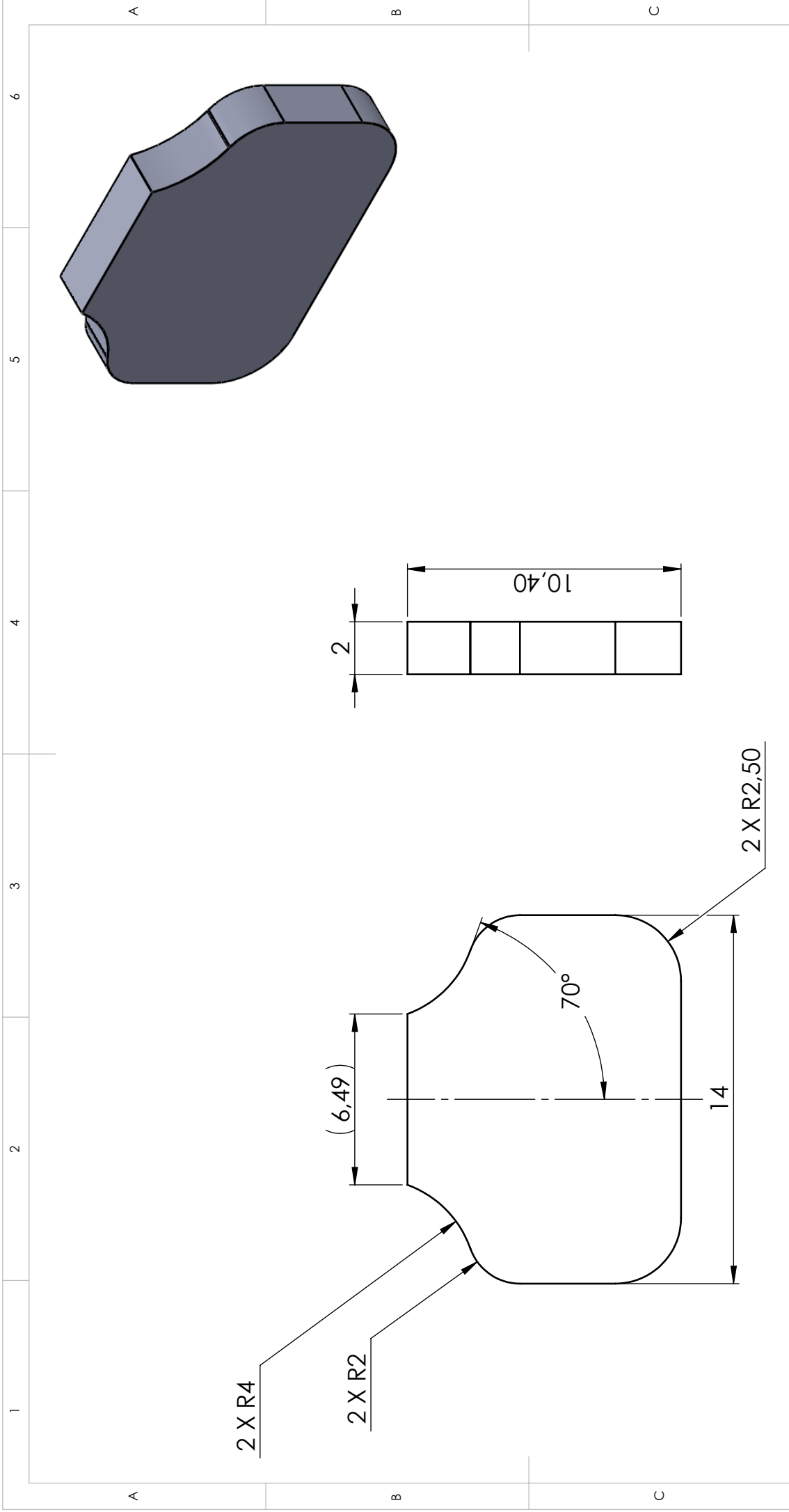
A

B


C

D





**DIMENSÕES GLOBAIS:**  
14x10,40x2

		TÍTULO:	
		<h1>Compensador</h1>	
MATERIAL: ALUMÍNIO		DSNH N.º:	SHPBJS 05.01.05.16
PESO: ± XXX g	ESCALA: 5:1	UNIDADES: 2	A4 mm

A

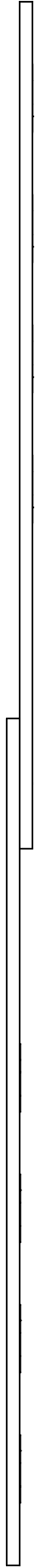
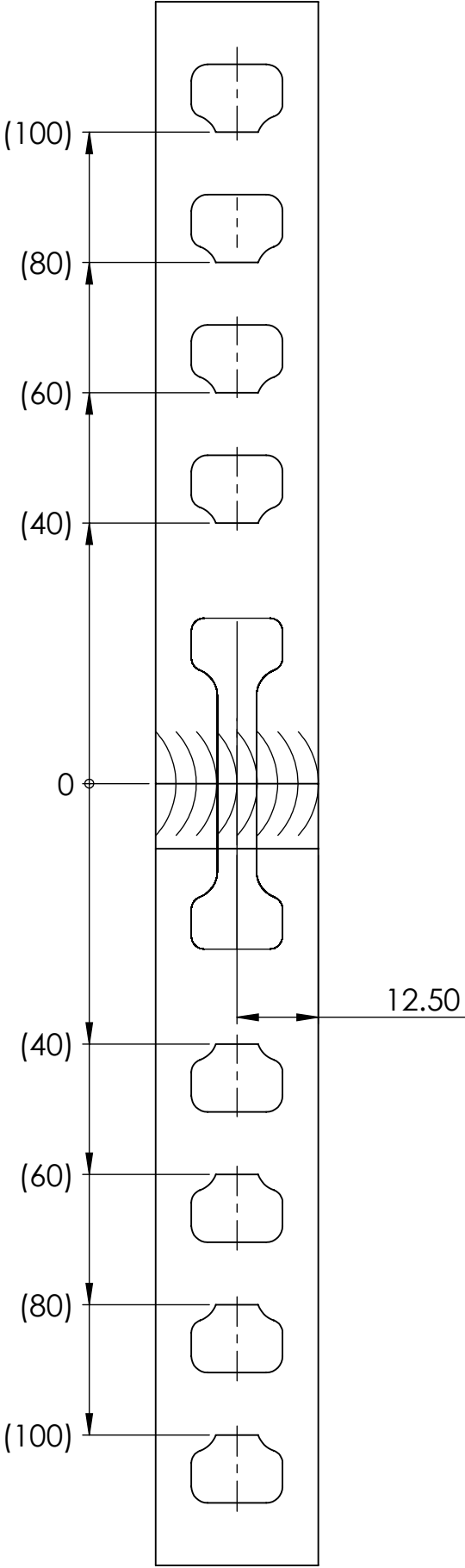
B

C


D

E

F



**DIMENSÕES GLOBAIS:**  
**240 x 25 x 4**

		TÍTULO: <h1>Provetes SPHB</h1>			
		MATERIAL: <h2>ALUMÍNIO</h2>		DSNH Nº: <h1>PSPHB 01.01.05.16</h1>	
PESO: ± XXX g	ESCALA: 1:1	UNIDADES: 1	A4	mm	FOLHA 1 DE 1